# River flood inundation under climate change: assessment of the relative effects of changes in plant growth and flood regime on conveyance


Thesis submitted in accordance with the requirements of the University of Liverpool for the degree of Doctor in Philosophy by Simon David Anthony Clark

June 2021

# Table of Contents

# Abstract

Aquatic vegetation are major controls of river flow. In-stream vegetation located in river channels increase local channel resistance by reducing flow velocities which, in turn, raises river levels and exaggerates flood magnitudes. In the UK, climate change is expected to increase the amount of in-stream vegetation occupying river channels whilst delaying the occurrence of peak biomass to coincide with intensified storms which are predicted to occur during the autumn and winter months. This creates a ‘perfect storm’ where high river flow interacts with high vegetation coverage with the potential to exacerbate flooding. This thesis has investigated the interaction between in-stream vegetation and river flow for a natural chalk river during flood events. To estimate future flow-vegetation interactions during flood events a three-dimensional numerical model was developed which was representative of the natural topography of the River Blackwater, UK. The model used double-averaged Navier-Stokes equations to simulate the influence of vegetation drag on flow conveyance. The model was calibrated using measurements of in-stream vegetation-flow interactions and compared against values reported in the literature and those produced with coefficients set to unity. The model was shown to be able to successfully simulate complex flow structures reported in the field data. A scenario-based approach was used to simulate changes to peak flow, seasonal flow regimes, and the changing channel cover of in-stream vegetation. The results consider the impact of vegetation on flow conveyance in terms of flow depth, flow velocity, turbulence generation, and vegetation geometry. The results showed that future increases in vegetation patch size will have a considerable impact of mean flood levels. The extent to which vegetation patches influence flood levels was found to change with flow rates; in-stream vegetation exhibited a greater impact on flood-water conveyance at lower flow rates. The morphological differences between the studied vegetation species *Sparganium erectum* and *Sparganium emersum*, resulted in different distributions of the local velocity and turbulence and the trailing morphology particular to the *S. emersum* species was shown to have a greater impact on mean flood levels. This study provides a detailed characterisation of the effects of vegetation on flood events under climate change. The results are finally discussed in terms of implications for river management strategies future research.

# Acknowledgements

I need to thank my partners at the Centre for Ecology and Hydrology, Ramesh and Pam, for providing guidance throughout the duration of the PhD. My academic supervisors James, Ming, and Janet for their help in producing a fully formed thesis. My parents and brother for their unwavering support. Ben Curnow for housing me during the more turbulent times of the pandemic, and Lemon for the accompanying boops. Given that most of my best ideas came to me whilst I either slept or was at the gym it would be remiss of me not to thank Apollo and my mad gains for the gift of prophecy. There are many more folk who have endured this journey with me and are due thanks for the unyielding support given: Maria Mendoza-Puchades, Sara Owczarczak-Garstecka, Dan Tudor, Francis Belmont de Oliveria, Hazel Phillips, Fiona Russell, Hannah Barnett, Maddy Moyle, Grace Skirrow, James Lea, Vanessa Laber, Alice Walker, Scott Smith, Elf Elmahdi, Sam Felvus, and lasty, myself. This one’s for me.

# List of Tables

# List of Figures

# Notation

| | | |
|---|---|---|
| $A$ | area | ($m^2$) |
| $ad$ | dimensionless cylinder array density | |
| $A_{px}$ | average projected area of gravel in the x-direction | ($m^2/m^3$) |
| $AP$ | projected area | ($m^2$) |
| $A_{PGR}$ | grass projected area | ($m^2$) |
| $A_{PT}$ | tree projected area | ($m^2$) |
| $A_{py}$ | average projected area of gravel in the y-direction | ($m^2/m^3$) |
| $A_s$ | average surface area | ($m^2/m^3$) |
| $AS$ | average surface area of tree trunk diameter | ($m^2$) |
| $A_t$ | characteristic area | ($m^2$) |
| $A_{TGR}$ | grass surface area | ($m^2$) |
| $C_f$ | dimensionless friction coefficient | |
| $C_{vf}$ | dimensionless friction coefficient for vegetation | |
| $C_d$ | bulk drag coefficient | |
| $C_{dn}$ | bulk drag coefficient related to the cylindrical surface area | |
| $C_{dg}S_{fg}$ | gravel-bed bulk drag coefficient | |
| $C_{DGR}S_{fGR}$ | grass bulk drag coefficient | |
| $C_{DGR}S_{fGR}A_{PGR}$ | composite bulk drag coefficient for grass | |

| | | |
|---|---|---|
| $C_{DT}S_{fT}$ | tree bulk drag coefficient | |
| $C_{dv}S_{fv}$ | vegetation bulk drag coefficient | |
| $C_{d0}$ | bulk drag coefficient for a patch with an aspect ratio of near zero | |
| $D$ | width | (m) |
| $\boldsymbol{D}$ | strain rate tensor of average motion | |
| $DT$ | average tree trunk circular diameter | (m) |
| $E_f$ | Nash-Sutcliffe efficiency index | |
| $F_{bi}$ | berm drag force | (kg/m$^3$) |
| $F_s$ | grid convergence index factor of safety | |
| $F_i$ | total drag force per unit volume | (kg/m$^3$) |
| $F_{vi}$ | vegetation friction term | |
| $F_x$ | total drag force per unit volume in the x-direction | (kg/m$^3$) |
| $F_y$ | total drag force per unit volume in the y-direction | (kg/m$^3$) |
| $F_z$ | total drag force per unit volume in the z-direction | (kg/m$^3$) |
| $\vec{F}$ | external force directly applied to the fluid | |
| $f_*$ | flow quantity of interest | |
| $g$ | acceleration due to gravity | (m/s$^2$) |
| $G$ | source term due to gravitational forces | |
| $\vec{g}$ | external force due to gravity | |

| | | |
|---|---|---|
| $h$ | water depth | (m) |
| $h_i$ | mesh resolution (edge length) | (m) |
| $i$ | vegetation patch identifier | |
| $I$ | turbulence intensity | |
| $ip$ | identified plane | |
| $k$ | turbulent kinetic energy | (J/kg) |
| $k_s$ | grain roughness size | (m) |
| $L$ | length | (m) |
| $L_t$ | characteristic size of vortices | |
| $n$ | Manning's roughness coefficient | s/[$m^{1/3}$] |
| $nt$ | number of trees | |
| $np$ | number of planes | |
| $\vec{n}_s$ | vector normal to the free surface | |
| $\vec{n}_f$ | vector normal to the bottom | |
| $p$ | pressure | (Pa) |
| $P$ | production of turbulent energy | |
| $Prt$ | Prandtl number | |
| $px$ | order of convergence | |
| $Q$ | flow rate (discharge) | ($m^3$/s) |

| | | |
|---|---|---|
| $Q_{10}$ | flow rate which was equalled or exceeded for 10% of the time | |
| $Q_{95}$ | flow rate which was equalled or exceeded for 95% of the time | |
| $Re$ | Reynold's number | |
| $R_f$ | factor relating cylinder aspect ratio *L*/*D* to drag | |
| $r^{px}$ | grid ride refinement ratio | |
| $\boldsymbol{R_{xy}}$ | Reynolds stress tensor | |
| $S_f$ | sheltering factor | |
| $t$ | time | (s) |
| $u$ | streamwise velocity | (m/s) |
| $U$ | average streamwise velocity | (m/s) |
| $\bar{u}_i$ | time-averaged velocity | (m/s) |
| $u_i'$ | fluctuating component of velocity in the $x_i$ direction | (m/s) |
| $\overline{u_i'u_j'}$ | time-averaged turbulent Reynolds stress | |
| $U_{friction}$ | friction velocity | (m/s) |
| $U_{plane1}$ | velocity at a point on the first plane above the bottom | (m/s) |
| $U_{shear}$ | shear velocity | (m/s) |
| $U_v$ | average velocity in the y-direction (lateral) | (m/s) |
| $u_x$ | velocity in the x-direction (streamwise) | (m/s) |
| $U_x$ | average velocity in the x-direction (streamwise) | (m/s) |

| | | |
|---|---|---|
| $u_{xy}$ | velocity $u_x$ in the y-direction perpendicular to the x-direction | (m/s) |
| $u_y$ | velocity in the y-direction (lateral) | (m/s) |
| $u_z$ | velocity in the z-direction (vertical) | (m/s) |
| $u_{zx}$ | velocity $u_x$ in the x-direction perpendicular to the z-direction | (m/s) |
| $u_*$ | shear velocity | (m/s) |
| $\vec{u}$ | velocity vector whose 3D components are $u$, $v$, and $w$ | |
| $\vec{U}$ | vector of average velocity | |
| $V$ | average lateral velocity | (m/s) |
| $\vec{x}$ | spatial vector whose 3D components are $x$, $y$, and $z$ | |
| $Y_i$ | measured value for a given flow quantity | |
| $\overline{Y_i}$ | average mean of the measured flow quantity $Y_i$ | |
| $\hat{Y}$ | predicted value for a given flow quantity | |
| $z^*$ | finite element mesh co-ordinate independent of time | |
| $Z_f$ | elevation of the numerical bottom | (m) |
| $Z_p$ | elevation of the prescribed mesh layer | (m) |
| $Z_s$ | elevation of the numerical bottom | (m) |
| $\Delta S$ | average distance between cylinders ($nt/A$) | |
| $\Delta_z$ | altitude of the numerical plane | (m) |
| $\delta$ | the distance from the wall at which *k* and ***ε*** is calculated | (m) |

| | | |
|---|---|---|
| $\boldsymbol{\delta}$ | identity tensor | |
| $\varepsilon$ | dissipation of turbulent kinetic energy | |
| $\varepsilon$ | error estimator for grid resolution fractional error | |
| $\theta$ | angle | (degrees) |
| $\mu$ | coefficient of dynamic viscosity | |
| $\rho$ | fluid density | ($kg/m^3$) |
| $\boldsymbol{\sigma}$ | stress tensor | |
| $\sigma_k$ | Prandtl's turbulent number for turbulent kinetic energy | |
| $v$ | coefficient of kinematic viscosity | |
| $v_t$ | turbulent eddy viscosity | |
| $\Phi$ | porosity | |
| $\Omega$ | the numerical domain | |

# Chapter 1 | Introduction

Globally, flood-related disasters impact more people per year than all other disasters combined (Berz et al., 2001; Field et al., 2012) with river flooding being the most common type (Kummu et al., 2011). Climate change is expected to intensify the hydrological cycle to alter river flow (Huntington, 2006; Schneider et al., 2013) with the outcome of an increased risk of river flooding in Europe (IPCC, 2013). In the UK, climate change is predicted to increase the frequency and intensity of extreme weather events during the colder months, resulting in higher flood levels (Watts et al., 2015). Observations have described how changes in the climate has resulted greater autumnal flows in UK rivers (Hannaford & Buys, 2012) following a trend of increased mean annual flood discharges across Northern Europe from 1960-2010 (Blöschl et al., 2019). Whilst flood risk within the UK has decreased throughout the last century due to improved flood management (Stevens et al., 2016) a growing population combined with floodplain construction has increased the number of people and assets potentially exposed to flooding. For example, in England and Wales over £200 billion worth of properties are at risk (Evans et al., 2004). The last National Flood Risk Assessment (EA, 2009) highlighted that 2.3 million people in England are at risk to river or coastal flooding. Aquatic vegetation, frequently referred to as macrophytes, which are an important flow control within river systems are also sensitive to climate change: the IPCC (2007) highlighted that an increase in global mean temperatures and dissolved CO2 is expected to increase photosynthetic rates for in-stream vegetation. This has been linked to a possible increase in the abundance of in-stream vegetation. Additionally, a warmer climate is also expected to delay the occurrence of peak biomass for in-stream river vegetation to coincide with the stormier autumn season in the UK (Franklin et al., 2008). In-stream river vegetation controls flow by decreasing local velocities and increasing flow depth. As such, in-stream vegetation has been associated with an increase in flood levels and slower recession of flood inundation for historical flood events in the UK (Pitt, 2008). Therefore, the role of in-stream vegetation as major flow control and how this is altered by climate change is key for understanding future changes to flood magnitudes.

Aquatic vegetation influences flow by absorbing flow momentum and dissipating kinetic energy through turbulence generation. An increase in the abundance of aquatic vegetation consequentially increases total channel resistance and results in a reduction to mean local flow velocities. Higher levels of hydraulic resistance exhibited in vegetated channels, in addition to a reduction channel capacity, can contribute to increases in local flow depths. In-stream aquatic vegetation is therefore a key control on river levels which may directly impact the magnitudes of flood events.

The considerable effect vegetation has on flow conveyance has established macrophytes as an important factor for river management (Järvelä, J., 2002). However, recommendations have historically been limited by a lack of knowledge which limits the effective assessment of geomorphic and hydraulic processes associated with vegetation change; less than two decades ago Wilson et al., (2003) described the discipline of fluvial vegetative ecohydraulics as still 'in its infancy'. To account for flooding historic river management strategies considered vegetation as obstructions. Vegetation was, and in some cases still is, frequently removed to improve conveyance (Kouwen & Unny, 1973; López, & García, 2001; Järvelä, J., 2002; Liu et al., 2008) to regulate water levels and reduce damages from flood events and storms (Augustin et al., 2009). However, researchers have noted that the removal of in-stream vegetation to reduce local total channel resistance can result in higher flood frequencies downstream, effectively shifting the burden of risk rather than ameliorating the problem (Trepel et al., 2003). More recently, in-stream vegetation have be considered as favourable assets due to their multi-functional role within river management strategies, resulting from their ecological benefits (Carpenter and Lodge 1986, Thiemer et al., 2021) and their status as a bioengineer in channel stabilisation (López & García, 2001; Braudrick et al., 2009; Yamasaki et al., 2021). The popularisation of strategies favouring river re-naturalisation has resulted in an increased interest the role of in-stream vegetation for their potential to be used as management mechanisms (López, & García, 2001; Järvelä, J., 2002; Peralta et al. 2008). Effective flood risk mitigation and climate change adaption can work with natural flood mechanisms in rivers by selectively increasing macrophyte abundance in river reaches where the adjoining floodplains have been delegated as floodwater detention zones. However, uncertainties remain regarding the impact of

different vegetation species and flow rates on flood mitigation efforts (Bal et al., 2011). Effective decision-making by flood managers requires an understanding of available flood controls (Downton & Pielke, 2001) as changes to management strategies can considerably alter flood risk; to account for the information requirements of decision-makers data must address regional level changes (Stevens et al., 2016). For management objectives utilising nature-based solutions a better knowledge of vegetation-flow hydraulics in needed (Järvelä, J., 2002). Management strategies are frequently informed by mathematical models through which the impacts of flooding are determined by testing the potential for overbank flow using different river flow scenarios. Quantifying the effect of in-stream vegetation on different flow scenarios can help inform flood risk management strategists of flow behaviour for a range of possible futures. Liu et al. (2008) reviewed the state of research in flow-vegetation hydrodynamics and found that research in the field was still emergent, but that future studies quantifying flow-vegetation hydrodynamics could improve knowledge on detailed flow structure needed for appropriate management.

Research using physical and numerical models have identified numerous vegetation-induced flow phenomena and complex flow characteristics. Ecohydraulic models have typically investigated vegetation-flow interactions using artificial environments and often employ two dimensional models (Sun et al., 2010). As such, ecohydraulic models show promise for simulating the impact of climate change on vegetation-flow interactions and their impact on river flooding. However, flow phenomena manifests across three-dimensional space and so the degree to which two-dimensional predictive models can effectively simulate tangible flow behaviour is limited. Additionally, natural river channels exhibit complex geometries across multiple scales which in turn considerably affect multi-scalar flow structures, information which is lost when simulating vegetation-flow interactions artificial environments. Key to understanding the impact of future vegetation change on flood events is the use of three-dimensional models which model interactions within an environment which effectively replicates natural channels. Previous research has identified how naturally occurring controls which may influence vegetation-flow interactions and flood events may be integrated into 3D models, including the representation of the vegetation patch geometries (Tinoco et al., 2020) and how double-averaging approaches to the

Navier-Stokes equations can represent the effect of form drag in both space and time (Nikora et al., 2007).

This study investigated flow-vegetation interactions in a natural channel using a three-dimensional numerical model. The aim of the study was to use a scenario-based approach to simulate changes to flow structures and flood magnitudes that result from how climate change influences the vegetative contribution to increases in channel resistance. The research questions were developed to consider the impact of vegetation in two key areas: the uniform change in vegetation cover at reach-scale, and the change in vegetation cover of patches with canopy geometry specific to a given species. Uniform changes to vegetation cover reflected real-world observations of in-stream vegetation growth due to increases in climate average temperatures. This allowed for the scenario-based approach to use parameters based on predictions of real-world changes, including in-stream vegetation and seasonal flow rate. Changing vegetation cover per species geometry, or morphotype, allows for the exploration how vegetation-flow interactions differs between plant geometry. A focus on plant geometry allows for the identification of key plant species have a higher flow control compared to other in-stream vegetation.

The model was calibrated using field data of in-stream vegetation-flow interactions and the scenarios were devised to represent different interactions between in-stream vegetation and river flood flow by integrating changes to peak flow under climate change, seasonal flow variation, different vegetation morphotypes, and vegetation patch abundances. This study provides an insight into the future impact of climate change, changes to in-stream vegetation abundance, and seasonal flow on peak. The results characterise the effects of vegetation on flood events under climate change which may be used to better inform river management strategies.

The thesis is structured thus: Chapter 2 presents a review of the current research on vegetation-flow interaction within the context of UK rivers and the predicted effects of climate change, the effects of in-stream vegetation on local river hydraulics, and how vegetation-flow interaction has been represented in numerical models. Chapter 3 details the field data and data collection methodology used in this study, whilst introducing the study reach on the River Blackwater. Chapter 4 introduces the methodological approach and the numerical parameters used when constructing the

hydraulic model. Chapter 5 addresses the construction of the model itself, including the definition of the finite element approach. Chapter 6-7 details the calibration of the model for both gravel-bed drag and vegetative drag for different seasons and different species' morphotypes. Chapter 8 discusses the design and the results of the scenario-based approach used to simulate the effects of changing vegetation-flow interaction on flood magnitudes. Chapter 9 provides the study's research outcomes alongside its implications for future research.

# Chapter 2 | Literature review

This chapter discusses the state of scientific knowledge and understanding regarding aquatic vegetation (macrophytes) and their impact on flow conveyance. Vegetation-flow interactions will be discussed in the context of fluvial systems, and how these interactions alter flood events and are in turn altered by future climate change. First, the aims of this study and the research questions are then summarised to provide context for the literature review. Second, macrophytes are discussed in terms of their morphology, as well as the current management practices and current understanding of the effect of climate change on macrophyte ecology. Third, the relationship between macrophytes and river channel hydraulics is explored, focusing on the alterations made to flow quantities within the three-dimensional (3D) flow. Following this, the chapter reflects on the integration of vegetation within one-dimensional (1D), two-dimensional (2D), and 3D models as well as current approaches to simulating the impact of climate change on flood risk.

Accurately representing vegetation-flow interactions within 3D numerical models is crucial for understanding how future climate change may influence river flooding and may provide a route for better informing vegetative roughness parameters in flood risk models. The scope of this study will be to address a key knowledge gap pertaining to the 3D effects of vegetation-flow interaction, its impact of floodplain inundation events, and how such flood events may change as in-stream vegetation patches and local flow regimes alter under future climate change. The research questions to be addressed are:

1. How might changes to in-stream vegetation patches and river flow effect floodplain flow under future climate change?

2. What is the impact of different vegetation morphologies on floodplain inundation under climate change?

## 2.1. Describing macrophytes within the fluvial environment.

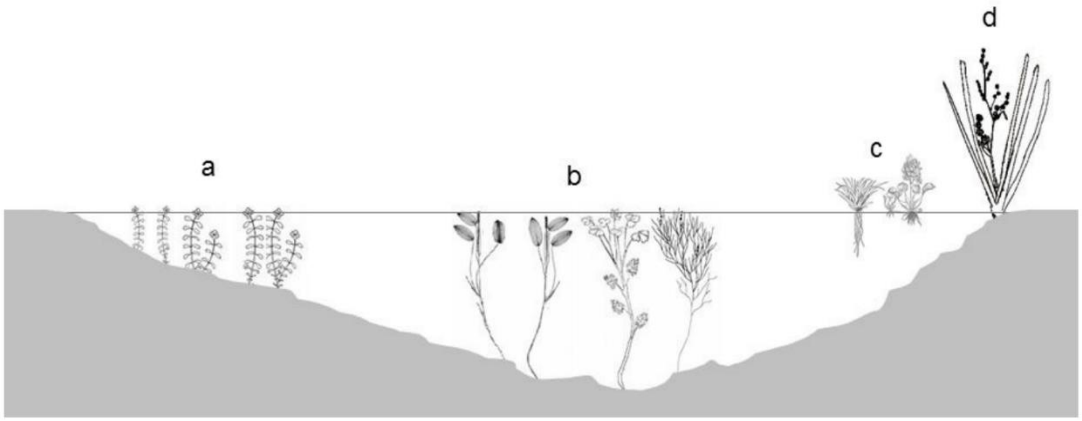


Figure 2.1. Types of riverine macrophytes including: a) floating-leafed, b) submerged, c) free-floating, and d) emergent. Source: Berger & Wells (2008).

Macrophytes are aquatic vegetation visible to the naked eye (Chambers et al., 2007), and as such encompasses numerous and varied species. The categorisation of macrophytes is typically achieved by discriminating between various morphotypes: the spatial dimensions, or morphology, of a macrophyte. Berger & Wells (2008) divide macrophytes into four groups of morphotypes, illustrated in Fig 2.1: A) submersed, vegetation that grow beneath the water surface and can occur at all depths where there is enough light penetration; B) floating-leafed, where1 macrophytes are rooted within sediments but whose canopy rest on the surface; C) free-floating, macrophytes whose root systems aren't located in sediments but which are suspended below the water surface; D) emergent, vegetation whose canopy extends beyond the water surface and which frequently grow in shallow water. Examples of species native to the UK for each category are given in Figure 2.2.

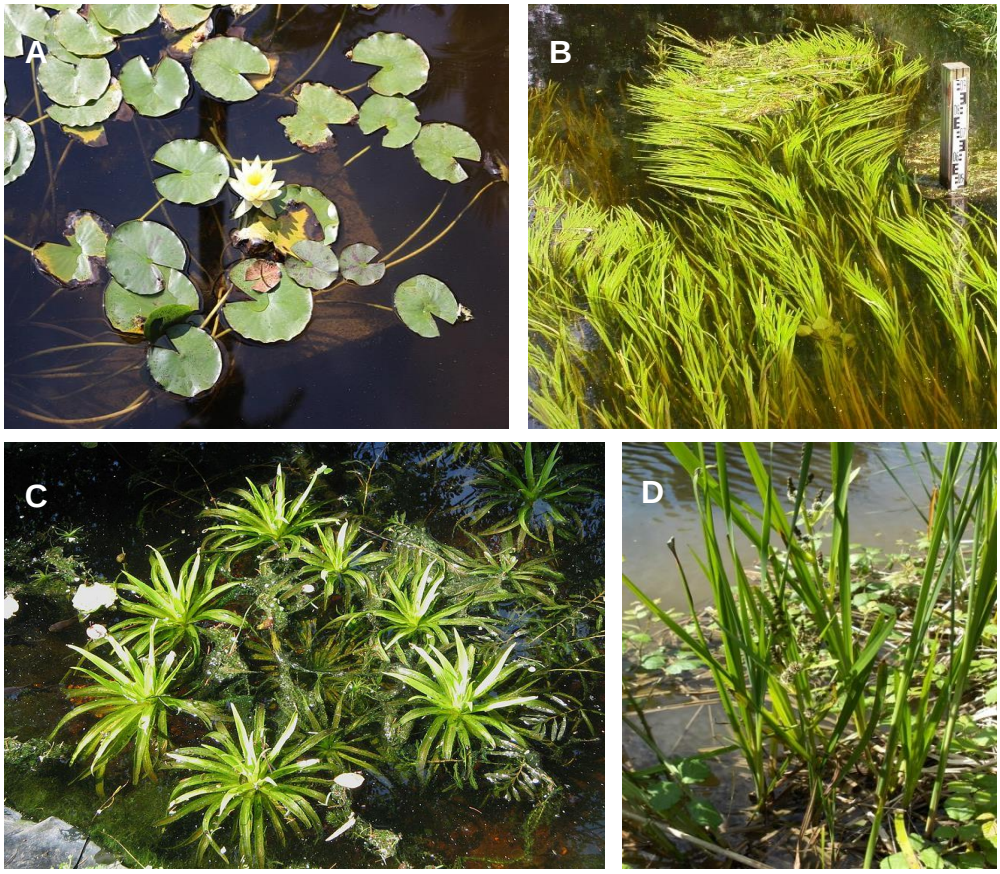


Figure 2.2. Examples of macrophyte morphotypes native to the UK: A) *Nymphaea Alba* (white water lily), floating-leafed; B) *Sparganium emersum* (unbranched bur-reed), submerged; C) *Stratiotes aloides* (water soldier), free-floating; D) *Sparganium erectum* (branched bur-reed), emergent.

*Images A & C downloaded from Wikimedia commons in January 2020. Image B downloaded from http://www.freenatureimages.eu/Plants/Flora%20S-Z/Sparganium%20emersum%2C%20Unbranched%20Bur-reed/index.html in March 2017. Image C downloaded from https://www.naturespot.org.uk/species/unbranched-bur-reed in March 2017.*

The natural composition of macrophytes in space and time is highly variable (Barrat-Segretain 1996, Feijoó et al. 1996) and is intimately related with the prevailing flow conditions. At larger scales spatial variation is exhibited through geographical trends: for example, in the UK emergent and submerged morphotypes have a greater diversity of species in lowland streams compared to upland systems (Baattrup-Pedersen et al., 2006). Here the degree a plant is classified as submerged or emergent is dependent on the ratio between water depth and submerged plant stem height (Augustin et al., 2009). Gurnell et al. (2010) builds upon this idea, describing that the sensitivity of macrophytes to flow conditions and the climate means that the geographical distribution of macrophyte communities somewhat reflects the unit

stream power: macrophytes are a more common feature in slower-moving, lowland streams (Boutellier & Venditti, 2015). At smaller reach-scales the presence of macrophyte communities is determined by prevailing flow conditions: Riis et al., (2008) observed that, in Danish lowland streams, macrophyte populations were at their lowest when streams had high flow variability or sustained low flow periods. Yamaskai et al. (2019) used a 2D model to simulate changes to the coverage of emergent patches under different flow conditions within a uniform channel and discovered that vegetation coverage depended more on flow velocity than the initial vegetation coverage or the pattern of patch distribution throughout the channel. However, channel flow is also considerably influenced by vegetation: as a patch develops flow conditions change, decreasing velocities downstream of the patch and increasing sedimentation which allows for colonization by other vegetation species.

Spatio-temporal descriptions of macrophyte communities are frequently articulated terms of abundance and distribution. Both concepts are dynamic and react to the channel capacity, flow conditions, and topography limit vegetation growth. Abundance, sometimes referred to as blockage (Yamasaki et al., 2019) or coverage (Grīnberga & Spriņge, 2008), refers to the amount of biomass within the channel, often expressed as a percentage of total channel area (Grīnberga & Spriņge 2008). Abundance directly relates to a channel's capacity for flow conveyance: areas with a high abundance of macrophytes are associated with a lower discharge and a higher local flow depth due to the increased surface area for moment absorption and reduced channel capacity (Bouteiller & Venditti, 2015). Distribution describes the location of macrophytes within a channel and is frequently characterised in terms of the pattern of vegetation patches, both across the channel bed and their expansion throughout the vertical flow column. Variations in patch distribution across the channel bed considerably influences the dominant flow regime by altering the main flow path through the channel and increasing or decreasing velocities respectively. This effect is due to the reduction of flow velocities within vegetation patches, with higher velocities at the patch boundary and surrounding non-vegetated flow. This is the result of flow being diverted around the head of the patch, known as bifurcation.

Zones with multiple patches further alter hydraulic phenomena resulting from flow-vegetation interaction: Vandenbruwaene et al. (2011) investigated how flow interacted with two patches of *Spartina anglica* (common cord-grass) and discovered

that decreases in the ratio between patch diameter and interpatch distance resulted in increases in flow velocity in the non-vegetated region between the patches. Multi-patch zones also result in wake mergers downstream when patches are very close (de Lima et al., 2015) whilst additional regions of low velocity farther downstream are generated along the centreline between two patches (Meire et al., 2014). Changes to patch distribution along the channel cross-section also alters the vertical distribution of patches, where more patches resulted in an increased vegetated wetted perimeter and contributes to increases in local flow resistance. Here, resistance is the hydraulic or flow resistance exerted by an element (e.g., vegetation) due to friction acting against the flow, and which may accelerate or decelerate flow (Bates et al., 2005). A greater volume of patches increases the area of the patch boundary, resulting in increased turbulence-inducing shear zones and vegetated surface area (Rameshwaran et al., 2011). Physically, changes in the cross-sectional distribution can describe how, for example, a fragmented distribution with a long effective wetted perimeter is representative of small, individual stands effecting variable flow patterns with high energy losses (Green, 2006).

Changes in dominant vegetation species due to seasonality, changing flow conditions, and river management therefore alters the dynamic characteristics of the hydraulic resistance exhibited by vegetation. For example, Bal & Meire (2009) discovered that increases in hydraulic resistance, measured using Manning's n, for three lowland rivers closely followed increases in vegetation biomass (Fig. 2.3.).

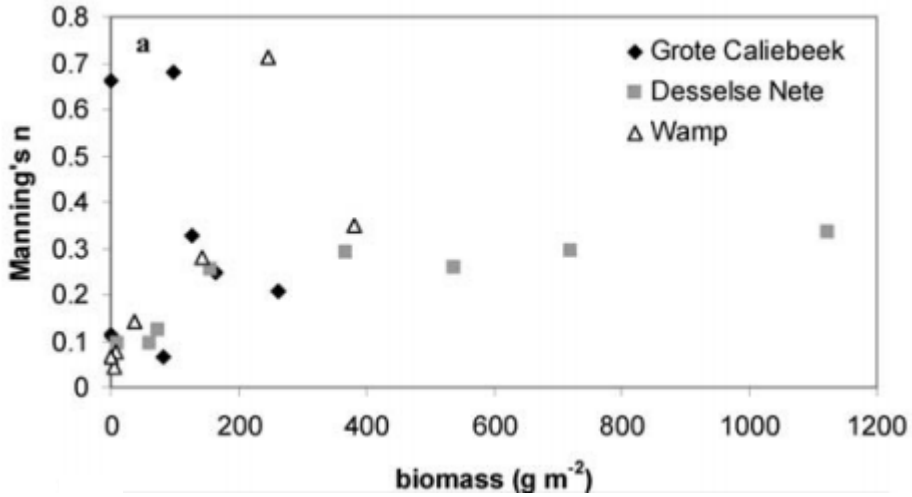


Figure 2.3. Bal & Meire (2009) reported significant linear relationships for lowland rivers Desselse Neter ($p < 0.01$) and Wamp ($p = 0.05$). No significance for Grote Caliebeek ($p=0.61$) was reported, which was attributed to cutting activities, natural senescence, and low discharge values in June and November.

Following vegetation cutting as a result of river management practices, hydraulic resistance decreased. Together with the growth of aquatic vegetation, the study also found a statistically significant linear relationship between increases in water depth and biomass on all three lowland rivers: all rivers had p values <0.03. This increase in depth has been associate macrophytes altering local flow processes by increasing momentum absorption and turbulence generation (Naden et al., 2006) whilst decreasing channel capacity (Green et al., 2006). Because of this, macrophytes have been identified as important flow controls within river channels, affecting sediment transport, water quality, geomorphology, and flooding (Darby, 1999). The ability of macrophytes to alter the physical environment through their structure has seen them termed “autogenic ecosystem-engineers” (Bouma et al., 2005), “biological engineers” (Byers et al, 2006) and “river system engineers” (Gurnell, 2014), and identifies as providing essential ecological services (Old et al., 2014). This study will investigate the role of macrophytes as a control for flood events at reach-scale channels.

Both the distribution and abundance of macrophytes are affected by seasonality. Continuing with Bal & Meire (2009), hydraulic resistance for three lowland rivers increased from May to a maximum in June during periods of macrophyte growth.

This phenomenon has been widely reported: Jeffres et al. (2008) described the growing season of a broad range of rooted macrophytes in the Shasta River California, USA, observing a seasonal low value of 26% coverage in March and a seasonal high of 73% in September. Seasonal changes in macrophyte coverage considerably affects flow. Champion & Tanner (2000) observe how higher vegetation biomass during the summer is an important control of river velocity patterns for a lowland river, whilst Cotton et al. (2006) investigated changes to the species *Ranunculus* at different months outside and within the growing season. They discovered that the dominant flow path throughout their study reach altered throughout the year depending on vegetation growth. In the UK, most plants reach their maximum growth potential in the late summer from the months of June to September (Haslam, 2006), however dead plant matter can persist into the autumn and winter months (Barret et al., 1999).

Vegetation distribution is also affected by the river flow: as patches grow the extend in the direction of flow (streamwise direction), elongating and becoming more streamlined as vegetation expands into zones of lower velocities in the wakes produced by the patch (Chen et al., 2012; Follett and Nepf, 2012). Whilst vegetation drag reduces local flow velocities, the plant must also withstand the opposing drag force imposed by the flow of water (Bouma et al. 2005). Where the flow drag overcomes the ability of the plant to withstand the vegetation can be damaged or uprooted, as in the case of extreme flood events. Uprooting immediately alters the local flow patterns, but also changes the species distribution as plants which have better recovery mechanics, such as higher uprooting resistance, faster growth, or benefit more from the seasonal period, may become more dominant and thus alters local flow-vegetation interaction. Seasonality is also an important consideration when representing vegetative characteristics. For example, the submerged *Ranunculus* species are highly flexible and deform to flow, however the presence of leaves along the entire its entire length means they exhibit a different response to flows during the summer compared to the winter where leaves are present only at the top of the stem (Nikora, 2012).

Representing macrophytes within model simulations is therefore a non-trivial problem: macrophytes are structurally complex, providing a heterogeneous environment at scales from leaf scale to patch distributions throughout a river reach

(Chambers et al., 2007). In order to accurately describe this complexity macrophytes are commonly defined using a combination of physical dimensions (e.g., stem length), characteristic area (e.g. frontal projected area – Fig. 2.4), and volume (e.g. foliage density). Computer models attempting to simulate the interaction between macrophytes and local flow conditions typically represent vegetation using hydraulic roughness and characteristic area (Derby, 1999) which are prescribed within a zone representing an idealised vegetated in the channel. The characteristics chosen also depends on the scale: at reach-scale patches are often described with a homogenous roughness, however at the leaf-scale the vegetation morphology is the more dominant factor.

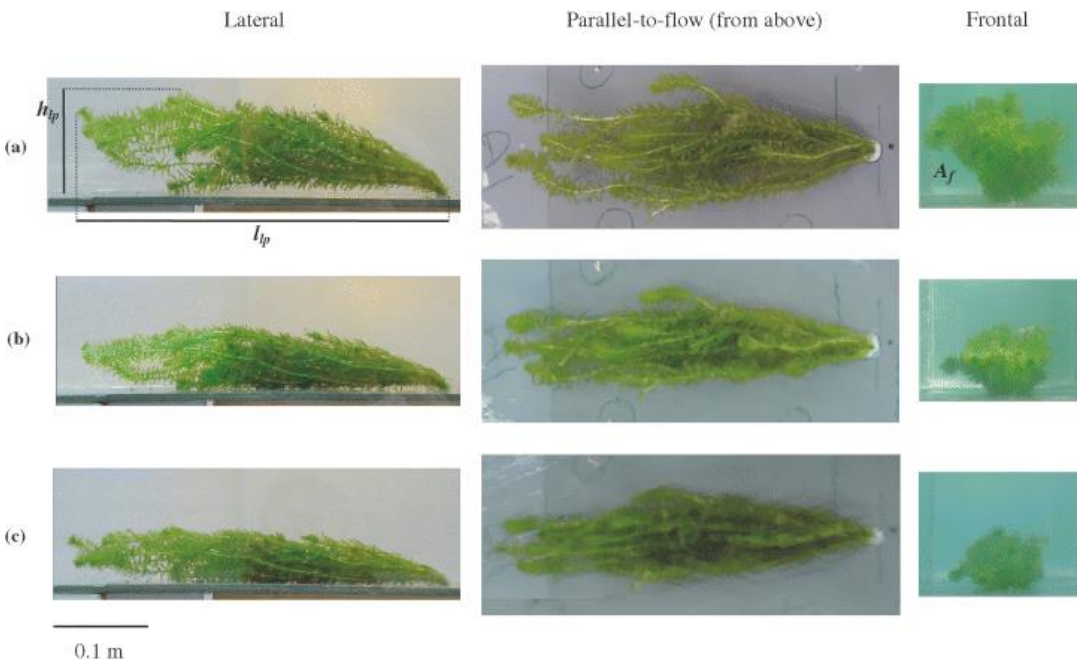


Figure 2.4. Characteristic areas for *Egeria densa* (large-flowered waterweed) deforming under increased velocities a) 0.2m/s, b) 0.5m/s, c) 0.8 m/s. From: Statzner et al., (2006).

Flow through the vegetated biomass, or 'canopy flow', is characterised by different length scales such as water depth, plant height, and stem diameter (King, Tinoco, & Cowen, 2012). For example, species with broad leaves will absorb comparatively more kinetic energy than species with narrow leaves or without foliage. However, an accurate description of macrophyte morphology is further complicated by the plant's response to flow: biomechanical properties like stem flexibility and flexural rigidity

determine their reaction to changing flow conditions. Many species can reconfigure their biomass to adapt to flow conditions, with many become more streamlined to minimise drag exerted on them by higher flow rates. Species with flexible stems are more likely to reduced local velocities as the greater movement afforded to the stems generates relatively higher levels of turbulence and thus dissipates more kinetic energy (Marjoribanks et al., 2014).

A considerable amount of research has been dedicated to elucidating the physical mechanics that govern flow-vegetation response, including stem flexural rigidity and patch density (Marjoribanks et al., 2014), in-channel location and distribution (Bal et al., 2011), growth seasons, and uproot resilience (O'Hare et al, 2011). In efforts to simplify the study of macrophytes, studies frequently categorise vegetation by discriminating between different physical characteristics such a stem flexibility, stem diameter, patch spacing (Darby, 1999) and whether the species is emergent or submerged (Vis et al., 2003). However, the utility of the above characteristics varies: for example, whilst stem diameter and patch spacing might be useful for rigid, inflexible vegetation both parameters may become inappropriate for describing heterogeneous and dynamic conditions where, for example, stem diameter changes with height and vegetation is susceptible to deformation. Further to his, individual species may exhibit numerous characteristics which are render them difficult to categorise (Darby, 1999).

Macrophytes are thought to affect local flood occurrence by decreasing channel capacity and reducing local velocities in proportion to vegetation abundance (Green, 2006; Spencer, 2013; Bouteiller & Venditti, 2015) with variation due to species and seasonality. However, this explanation belies the dynamic and heterogenic nature of macrophyte-flow interactions within complex river systems, which generates large degrees of uncertainty when trying to predict their interaction (Franklin et al., 2008) due to complex morphology and their position within the flow environment. Despite the understanding gained throughout the last few decades uncertainties still remain, such as the need for flow hydraulics models to build better physical representations inclusive of phenomena occurring at multiple scales and resulting from vegetation flexibility, whilst mass transfer dynamics involving interactions between unobstructed channel flow and vegetation patches and floodplain storage zones (Rowinski et al., 2018).

## 2.2 The effects of climate change on fluvial ecohydraulics

### 2.2.1 Observations of changes in catchment response.

Increases in global average temperatures throughout the next century is expected to intensify the hydrological cycle, altering precipitation patterns (Allan et al., 2011) and global river flow regimes (Huntington, 2006), and potentially increasing flood risk (Girogi et al., 2011). The IPCC (2013) has described increases in global precipitation with increases in the global mean temperature as 'virtually certain', with Europe expected to be at high risk from flooding as mean temperatures rise (IPCC, 2014). Allen et al., (2009) stated that even with restrictive greenhouse gas emission targets a warming of 2°C may still occur; globally, nations will contend with the adverse effects of climate change even if warming is restricted to 1.5°C.

Climate change initiates complex hydrometeorological responses in river systems, however climate signals are difficult to determine from monitored changes due to the non-linear reactions between temperature change, oscillations in natural meteorological variability, and catchment dynamics (Hannaford, 2015). Monitored flow data is sparse prior to the 1970s, and the lack of long-term data describing long-term climatic influences on river flow means the understanding of how future climate change will affect river systems is poor (Hannford, 2015). For example, the UK has experienced increases in rainfall totals during the winter which align with the modelled scenarios of climate change (Jones & Reid, 2001) however catchment response is heavily localised and deeply affected by natural variation in the local climate; in the UK short-term trends (40-50 years) are controlled by the North Atlantic Oscillation. Therefore, natural variability cannot be discounted as a factor influencing increasing recent precipitation intensities and river flow until long-term trends have been observed: Fowler & Wilby (2010) suggest that signals that would formally attribute changes in river flow trends to climate change might not emerge until the 2050s, although for some areas in south England this may happen sooner.

Precipitation data throughout the last century shows the UK has experienced little change to annual rainfall averages, however it has experienced an increase in the intensity – the average amount of precipitation during wet days - of winter precipitation uniformly across the whole country (Jones et al., 2012). For both the spring and autumn increases in rainfall intensity have occurred to a smaller degree

and less uniformly. From 1960-2006 the summer experienced uniform decreases in heavy rainfall across most of the UK except for the Northeast England and North Scotland (Maraun et al., 2008) however increases in rainfall intensity were observed during long-term rainfall events (5-10 days) for all seasons. Jones et al., (2012) also note there is some evidence for an increase in the clustering of extreme events.

Changes to river flow has been exhibited by high spatial variability in seasonal patterns are evident from monitoring river systems with limited human disturbance. Both Hannaford & Marsh (2008) and Marsh & Dixon (2012) describe an increase in winter flow in North-West of England and Scotland from the 1960s to the 2000s. This was complemented by Hannaford & Buys (2012) who discovered increases in high flows during the winter for the same regions. An increase in autumnal flows has occurred across much of the UK, with a weak decreasing trend in spring and no clear summer pattern. Higher annual variation in flood frequencies (MacDonald, 2010) and decadal variation (Stevens et al., 2006; Wilby & Quinn, 2013; Hannaford, 2015) have been reported. Blöschl et al., (2019) described increases in mean annual flood discharges in Northern Europe between 1960-2010; increases in flood discharge of +6.6% in the northern UK aligned with increases in precipitation (Fig. 2.5).

Increases in short-term (40-50 year) flow trends have been described for catchments relatively undisturbed by human interference (Kieldsen et al., 2012). Changes to river flow and rainfall haven't been formally attributed to climate change, however increases in the occurrence of extreme events are consistent with projections of climate change for flow (Kay et al., 2011; Pall et al., 2011; Hannaford, 2015) and rainfall (Ekstrom et al., 2005; Murphy et al., 2009; Prudhomme et al., 2012), respectively. For example, modelled simulations of future precipitation change show an increase in annual extreme precipitation events (for example: Kharin, Zwiers, & Zhang, 2005) where drier summers experience severe flash flooding (Christensen and Christensen, 2003).

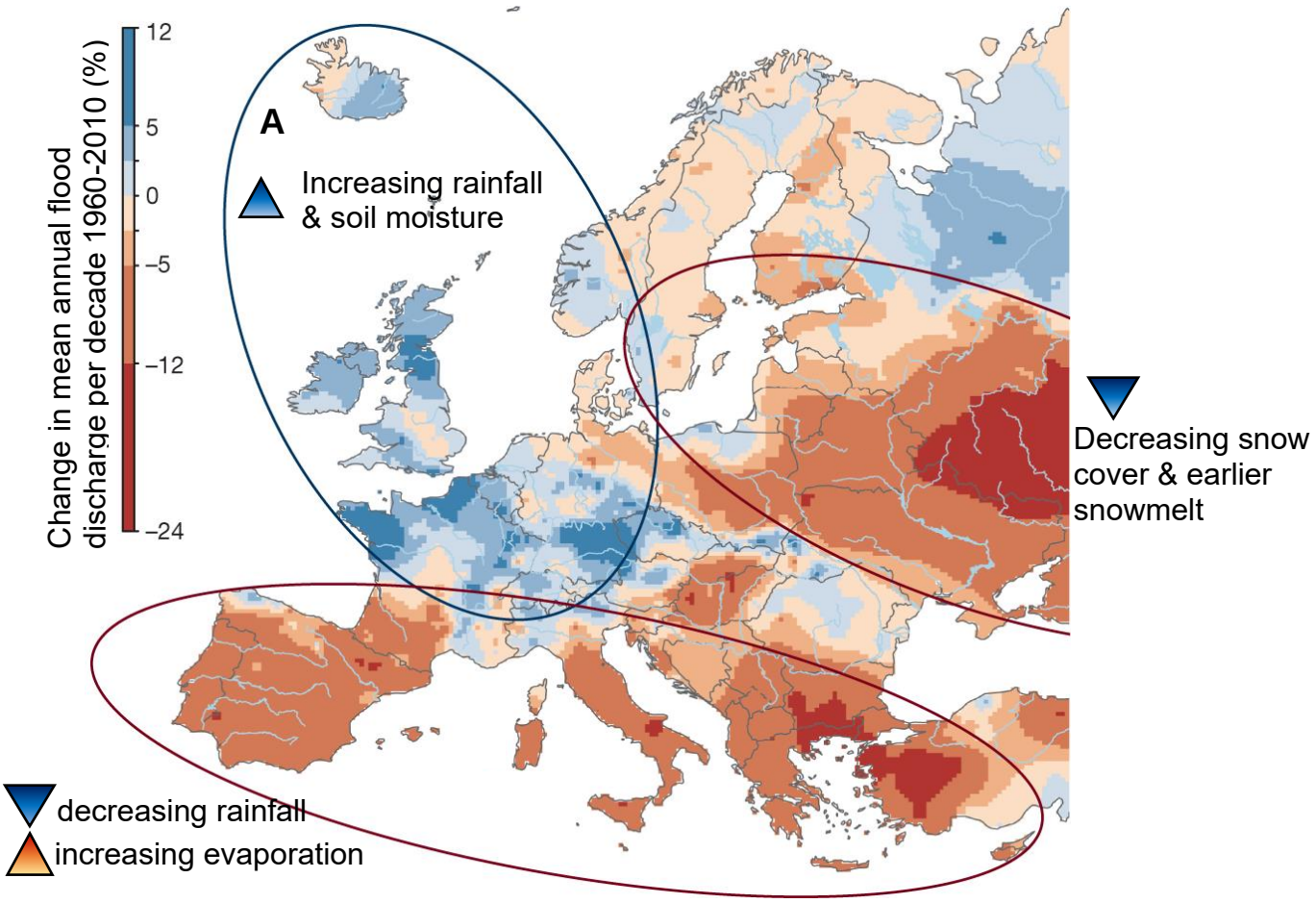


Figure 2.5. Historical changes (%) in annual flood discharge per decade from 1960-2010. North-west Europe (A) has been highlighted as a region of increasing flood discharge driven by greater soil moisture and precipitation. Adapted from Blöschl et al., (2019).

### 2.2.2. Macrophyte response to climate change

Temperature is the predominant factor governing macrophyte growth (Džigurski et al., 2015); long-term changes in average temperatures can impact vegetation abundance (Burnett *et al*., 2007). Previous research has identified how macrophyte growth is impacted by both changes in air temperature (Madsen & Brix, 1997) and how local temperature is moderated by water (Burnett *et al*., 2007). Previous research has already detailed a positive trend in river temperatures across Europe, increasing by up to 1°C per decade (Langan et al., 2001; Webb & Nobilis, 2007) with increases also observed in the UK (Hannah & Garner, 2015). However significantly more of the literature has focused on the impacts of changing water temperature on the abundances of river fauna rather than vegetation.

Research has elucidated how higher air temperatures result in longer periods with warmer water, eliciting more growth within macrophytes (Gessner, 1955) as temperature regulates the chemical control of photosynthesis and respiration (Bergen & Wells, 2008), especially during drought periods where low water and higher temperatures can result in overgrowing (Dhir, 2015). As such macrophytes can act as indicators of local, long-term environmental change (Melzer, 1999) through changes in species composition and abundance (Schneider & Melzer, 2003). Increases in global average temperatures will affect vegetation growth rates and growing seasons (IPCC, 2007). For example, Whitehead et al. (2008) simulated changes in macrophyte biomass under the long-term A2 warming scenario, and estimated a shift in biomass production to later in the year for the common submerged species *Ranunculus penicillatus* (water crowsfoot), however they note no major biomass increases were predicted (Fig. 2.6.).

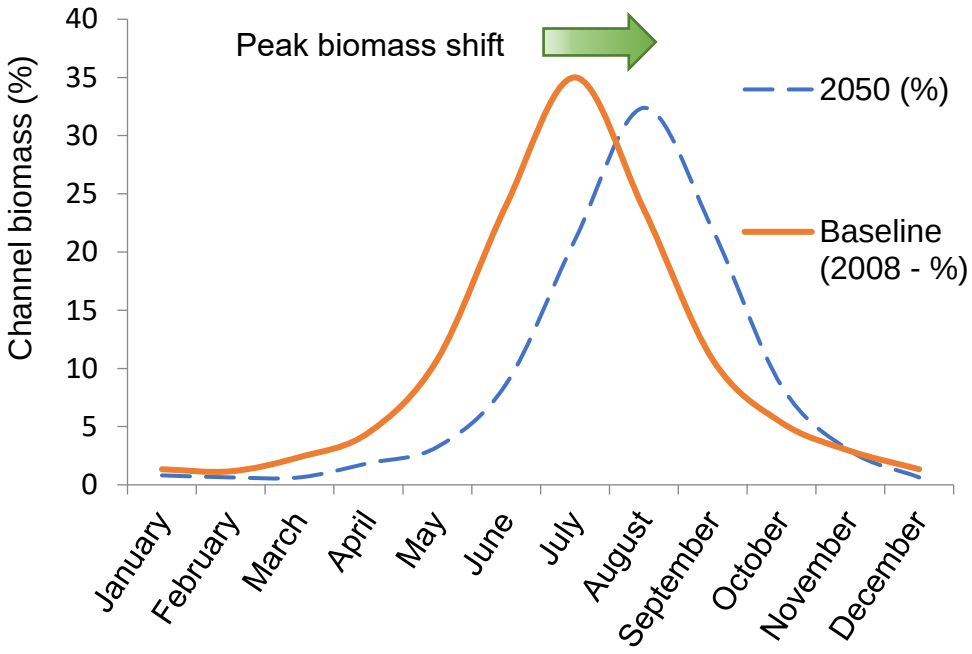


Figure 2.6 Monthly biomass change for *Ranunculus penicillatus* (water crowsfoot) for the River Lambourn, UK. Adapted from Whitehead et al. (2008).

However limited research has considered how a warming climate might influence macrophyte abundance: studies are limited by a lack of historical monitoring to establish baseline data with a wide geographic coverage (Wilby et al., 2010). The majority of research on in-stream vegetation has considered changes in distributions at regional (for example: Chappuis, Gacia, & Ballesteros, 2014), national (Alahuhta,

Heino & Luoto, 2011; Džigurski *et al.,* 2015), or supranational (Heikkinen et al., 2009) scales, often with a focus on ecosystem impacts rather than flooding.

Smaller scale studies, such as those investigating species distribution for specific individual, or sections of, water bodies, most commonly investigate changes within lacustrine or wetland distributions (for example: Wang et al., 2019). Studies considering changes to macrophyte abundances at reach-scale are rare, with few considering future changes to reach-scale macrophyte populations under climate change. However, research by Grīnberga & Spriņge (2008) monitored changes in the abundance of macrophytes within seven reaches for the River Salaca, Latvia over a period of 21 years. The river system was little affected by human activities, although changes in land use did occur between study periods. To investigate changes, they conducted surveys of vegetation coverage at the beginning of August in 1986, 2002, and 2007, where each reach which varied in length from 3.5km to 17km. They discovered that, for 40% of the surveyed reaches, the maximum cover of macrophytes increased by 50-60% for the 2002 and 2007 surveys since 1986 (Fig. 2.7).

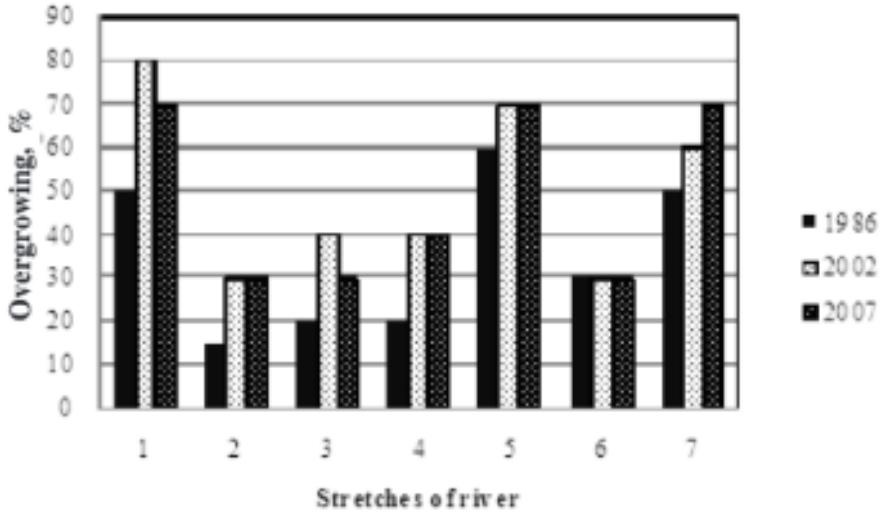


Figure 2.7. Percentage change in increased macrophyte coverage (“overgrowing”) across three decades for the River Salaca, Latvia. From: Grīnberga & Spriņge (2008).

They also discovered that overgrowing was more prominent in fast-flowing reaches, where macrophyte coverage was 70-90%. Increases in mean air temperature had been observed, with notable increases in spring air temperatures. In addition, an increase in water temperature was observed for April, as well as an increased length of vegetation season. Suspended nutrients had decreased between surveys due to

changing land use, and thus they assumed the overgrowing was not a result of agricultural runoff but due to increases in mean temperatures. However, whilst some studies have researched changes to reach-scale abundances there has been little research into future interactions between changing vegetation and future hydrological regimes; research into the impact of warming temperatures on macrophytes has largely focused on changes to species distribution. Macrophytes provide a key control of river flow which could alter under future climate change, affecting the frequency and magnitude of flood risk. The position of macrophytes as a changing flow control provides a challenge to managers attempting to mitigate future flood risk.

## 2.3. Description of key vegetation-flow phenomena

### 2.3.1 Introduction

This section will explore hydraulic phenomena associated with vegetation-flow interactions reported in the literature. The vast body of knowledge has been obtained through laboratory experiments, as such a general description of the historic characterisation of vegetation will be presented. The following sections introduces key concepts of fluid will frame the channel environment and define key concepts associated with the production of vegetation-flow phenomena. Following, the relationships between macrophytes, flow conditions, and resulting flow phenomena will be described.

### 2.3.2 Review of the characterisation of vegetation, flow, and vegetation-flow interactions in laboratory settings

Hydraulic characteristics are typically codified using numerous and complex parameters and include flow velocity, water depth, flow resistance, flow regime (Ye, Liu, & Wang, 2015), and turbulent energy. Key to understanding the vegetation-flow interactions is how changing flow phenomena around the vegetation patch in turn changes the drag exerted by the vegetation on the flow, which subsequently determines the vegetative resistance (Majoribanks et al., 2017); the magnitude of the hydrodynamic effects depends on the characteristics of the flow and vegetation (Irish & Lynett, 2009). In a broader sense, these characteristics are influenced by macrophytes through two key processes: the restriction of the conveyance volume

due to biomass abundance (Berger & Wells, 2008), and by reducing velocities due to momentum absorption by the vegetative surface area as well as the dissipation of kinetic energy from turbulence generation downstream of the patch. This interaction is further complicated by external factors, including the flow velocity and channel roughness, as well as the structural and hydrodynamic properties of the plants itself: the previously mentioned stem flexural rigidity (Berger and Wells, 2008)., patch density (Marjoribanks et al., 2014), in-channel location and distribution (Bal et al., 2011), growth seasons, and uproot resilience (O'Hare et al, 2011) and patch shape (Sonnenwald et al., 2017). In addition, characteristics pertaining to plant geometry and stem-scale surface area have been reported to considerably contribute to total channel resistance. For example: variation in morphological factors such as plant size, shape, patch geometry, submergence ratio and flexibility can result in differences in the contribution of vegetation to total channel resistance between different climates, spatial distributions, and species (Sandercock, 2007). The impact vegetation can have also depends on the scale used to frame the hydraulics. For example, at patch scale classifying species into functional plant groups (i.e., emergent, submergent, surface floating leaves, and free-floating leaves) is important because their flow resistance is informed both by the aerial extent (Green, 2005) as well as the density. However, at stem-scale smaller variations in plant morphology and biomechanics dominate, with more consideration needed to account for how flow interacts with geometric characteristics such as stem diameter, leaf shape, leaf area, distance between stems, as well as the flexibility of the stem and how that may differ from frond flexibility (Tinoco et al., 2012).

Developing useful parameterisations from natural vegetation is difficult due to complex morphologies, flexible elements, canopy reconfiguration, an unstable and changing volumetric area, and heterogeneity present in stem distribution, stem height, and patch distribution. Additionally, vegetation patches are exposed to variable and complex environmental conditions including heterogenic channel geometry, changing flow rates and depths, microclimates, biodiversity and suspended nutrients, sediment loads, and combinations of fluvial- and tidal-dominated flow regions with greater proximity to estuarine environment (Tinoco et al., 2020). Capturing these complex non-linear interactions is difficult within lab environments. Researchers reduce this complexity to focus on specific processes

which allow for practical study, using simplified geometric idealisations of vegetation within uniform, open channel flumes.  idealised vegetation is frequently substituted in lieu of real-life samples by using simplified mimics. Whilst the idealised vegetation allows for the development of useful parameterisations and may be appropriate for single-stem aquatic plants, differences between natural vegetations and synthetic mimics means that laboratory experiments utilising mimics will neglect complex flow phenomena otherwise generated at the vegetation-flow interface. Consequentially, studies are limited without representing the complex branching morphologies and heterogenic distribution of biomass and are unable to develop a comprehensive understanding of ecohydraulic dynamics. For example, natural vegetation patches exhibit a heterogenic cross-sectional shape; vegetation-flow processes occur at multiple relevant length scales including the stem, branch, and leaf-scale (Luhar and Nepf, 2011; Albayrak *et al.* 2012, 2014; Aberle and Järvelä, 2015; Boothroyd *et al.* 2016) whilst changes to the position and orientation of vegetative components affect the generation of flow structure; stem-scale shear and Reynolds stresses will vary with morphological changes (Yager & Schmeeckle, 2013); vegetative characteristics alter depending on the age of the plant, thus assuming a uniform simplification of plant geometry in long-term simulations is problematic (Bradley & House, 2009). Additionally, idealised patches are typically arranged as arrays with linear, staggered, or random distributions that result in preferential flow patches which are atypical for naturally occurring plant patches (Etminan *et al.* 2017; Zhang et al. 2018). Stem height heterogeneity affects different flow patterns (Bai *et al.* 2015; Hamed *et al.* 2017; Horstman *et al.* 2018*)* and studies typically idealised canopies as having uniform canopy height (for example: White and Nepf, 2007) however research by Hamed et al., (2017) and Horstman et al., (2018) have revealed heterogenous canopy height reduces shear at the canopy boundary whilst the location of the turbulence maximum was increased by around 1.5 times the mean canopy height (Tinoco et al., 2020).

Idealised vegetation in commonly used due to difficulties separating the influence of numerous phenomena in field data, substantial environmental variability, and practical limitations in obtaining such data. Research utilising idealised vegetation has been integral for numerous theoretical advancements, including the parameterisation of the drag coefficient in relation to cylinder diameter (for example:

Kothyari et al., 2009; Busari & Li, 2016), patch density (for example: Tanaka & Yagisawa, 2010), and Reynolds number (for example: Sonnenwald et al., 2019), and has since been applied to numerous computational model in both 2D (for example: Sun et al., 2010; Verschoren et al., 2016; Marcinkowski et al., 2018) and 3D (for example: Fischer-Antze et al., 2001; Stoesser et al., 2003; Zhang et al., 2010). How idealised vegetation is characterised is dependent on the processes being investigated and will vary with the event scale (for example, local production or reach-scale changes); sources of resistance (for example, the stem, the leaf, the whole canopy, or entire patch, and whether other channel roughness elements are included); the spatial characteristics (for example, within-patch processes or external processes); the environment being represented (for example, riverine, estuarine, or coastal zones); the study environment (for example, an indoor laboratory or outdoor field model); and the inclusion of additional systems (for example, erosive effects and sediment deposition) (Tinoco et al., 2020). To this end the vegetation mimic is typically characterised by considering the vegetation morphology, biomechanical properties, patch assembly and homogeneity, and submergence ratio. Studies attempt to address these characteristics by adjusting parameters for plant volumetric area (for example, the volumetric frontal area of a whole patch); rigid or flexible material; array density, frequently parametrised by the mean space between stems, the number of plants per unit areas, or the solid volume fraction of an array; and the emergent conditions.

The most common mimic are rigid cylinders which have been used in studies since the earliest experiments in vegetation-flow interactions (Fenzl, 1962; Li and Shen, 1973; Nepf, 1999; Lopez & Garcia, 2001; Stone and Shen, 2002). When organised as arrays cylinders are often parameterised using the same dimensions in terms of diameter, height, space between elements (Tinoco et al., 2020). Studies adopting cylinder mimics typically focus on measuring the isolated effect of vegetation on flow processes and for determining the bulk drag coefficient (Tanino & Nepf, 2008). Bulk drag coefficients are empirical parameters critical for quantifying the impact of entire drag forms on flow conveyance, such as that riverbed asperities or vegetation canopy occupying a river reach. Much of the literature concerned with vegetation-flow interactions seek to parameterise the bulk drag coefficient for this reason (Wang, Yin, & Liu, 2021). However, bulk drag coefficients are difficult to

parameterise as they include numerous biomechanical and geometric factors which influence flow-vegetation interactions. For this reason, bulk drag coefficients are often calculated using idealized representations of vegetation, such as rigid cylinders, in lieu of quantifying the hydrodynamic complexities of vegetation canopies.

Synthetic flexible material has also been adopted (for example: Ortiz et al., 2013; Huai et al., 2019; Tseng et al., 2020); the parametrisation of flexible vegetation from laboratory data is less common, however there has been progress (Boothroyd et al. 2017).

Real-life vegetation has also been used in laboratory studies: Järvelä (2003) investigated the effects of different grass, sedge, and willow species influenced energy losses at different levels of submergence and noted that vegetative friction increased with depth independent of velocity for leafless willows. Bal et al. (2011) used multiple species of common macrophytes to investigate the effect of differing patch patterns on hydraulic resistance, and reported that resistance varied significantly between patch pattern, species, and degree of submergence. Boothroyd et al. (2016) used the laurel species *Prunus laurocerasus* to quantify the contribution from biomechanical properties operating at sub-patch scales under foliated and de-foliated conditions. Tinoco et al., (2011) used quantitative imaging techniques to characterise the changing volumetric frontal area of Eurasian watermilfoil and noted that an accurate vertical profile requires the digitisation of multiple stems and account for spatial variation in the frontal area due to the bending and oscillation of the vegetation. Experimentalists have also used woody vegetation to investigate vegetation-flow interactions at the riparian zone and floodplain: Armanini et al., (2005) calculated the drag produced for single stems of the willow species *Salix alba*, whilst Righetti (2008) observed the impact of staggered *Salix pentandra.* Parameters for real-life vegetation have been proposed to account for plant flexibility and reconfiguration (Arberle and Jarvela, 2015), and for describing flow resistance using a bulk drag for multiple vegetative layers, vegetative friction factor, and Manning coefficients for 1D and 2D models (Vastila and Jarvela, 2018).

### 2.3.3. Key concepts in vegetation-flow interactions

Primary flow conveyance in natural river systems is situated within a main channel, with an adjacent floodplain which carries flow during flood events (Tand and Knight, 2009). Both floodplain and channel zones are frequently vegetated, which can considerably alter the hydraulic characteristics of the flow; additional vegetative resistance contributes to an increase in overall channel resistance. The effect of resistance on channel flow conveyance is described by the concept of continuity, which describes the transport of a fluidic quantity the energy of which cannot be destroyed, nor can new energy be created. In the case of river channels this can be summarised as the conservation of liquid mass as a fluidic quantity progresses and deforms spatially and temporally i.e., flow. The presence of vegetation within the channel disrupts the flow by absorbing momentum or dissipating energy, changing flow behaviour to satisfy continuity. For example, for a given vegetated channel cross-section the vegetated flow region will experience a reduction in velocities whilst the adjacent vegetation-free region will experience an increase in velocity to compensate. This separation between slower and quicker flow regions is named bifurcation. Continuity also determines changes to flow depth: a channel section exhibiting a higher mass flow rate, or discharge, at the channel inlet than at the outlet indicates an accumulation of mass within the channel. Physically speaking, this accumulation may occur when an abundance of vegetative biomass reduces local flow velocities, producing lower mass flow rates downstream and consequentially increasing local flow depths. This interaction has identified macrophytes as one of the main controls of channel flow (Kothyari et al., 2009), along with bathymetry, sedimentation, grain size, and other flow blockages (Augustin et al., 2009). This interaction is a two-way process: fluid interaction with the vegetative surface exerts drag on the flow (Tinoco & Coco, 2018), influencing water depth, velocities (Järvelä, 2002; Nepf et al., 2007), turbulence intensities (Nikora, 2010; Marjoribanks et al., 2017), turbulent Reynolds stresses, and their vertical and horizontal distributions (Nepf 1999, Garcia et al. 2004, Liu et al. 2008, 2010). The overall impact is a reduction in the volumetric flow rate, an increase in local flow depths (Tanino & Nepf, 2009) increasing the duration of flood water detention (Bergen and Wells, 2008) and therefore the possible exaggeration of local flood risk (Majoribanks et al., 2014).

For flood conditions, vegetation-flow dynamics also extend to the adjacent flood plain. Riparian vegetation, like trees or bushes, also considerably affect flow conditions by contributing to the total channel resistance and altering the stage-discharge curve compared to non-vegetated conditions (Terrier et al., 2010). How vegetation influences flow is dependent upon the vegetation characteristics and the type of flow, together determining the degree of flow vegetative resistance. The vegetative area exerts drag on the flow resulting in flow adjustments (Marjoribanks et al., 2017) exhibited in the reduction of local velocities within the patch canopy, the generation of turbulence at the boundary between vegetated and non-vegetated flow, and through an increase in water levels (Stephan & Gutknecht, 2002). Understanding this dynamic requires knowledge of interaction within the boundary layers, as well as the fundamental impact of roughness, resistance, and drag:

### 2.3.4. Boundary layer characteristics

The concept of the boundary layer was developed by Prandtl in 1904, and is used to differentiate the region near the channel edge affected by friction, i.e. the boundary, and the fluid region not in contact with the boundary where the influence of friction is a negligible (Powell, 2014). At the channel boundary this is also associated with the idea of the wall: the solid, rigid extremity of the channel, or flow region, within whose perimeter hydrodynamic flow occurs. The influence of friction at the wall, or the ‘law of the wall’, describes the influence of turbulent shear flow over the solid surface for the bottom 10% of boundary flow, or ‘inner flow’, assuming the boundary is positioned directly below the flow (Bradshaw & Huang, 1995). This is important for determining the distribution of flow phenomena within the boundary layer in turbulent flows, where flow close to the wall is controlled by walls hear stress and distance from the wall. For example, velocity is typically assumed to vary between the viscous sub-layer, the thin flow layer adjacent to the wall where viscous forces are considered important and where turbulent stress is negligible (Van Den Berg, 1975), and the turbulent, outer, or ‘free-stream’ region, where turbulence stress is large and viscous stress is negligible (Chanson, 2004). Velocity is considered zero at the wall (a ‘no-slip’ condition) and increases in a logarithmic fashion with height towards the ‘free-stream’ region. A schematic for a hydraulically smooth flow, where roughness elements are smaller than the viscous sublayer in Figure 2.8.

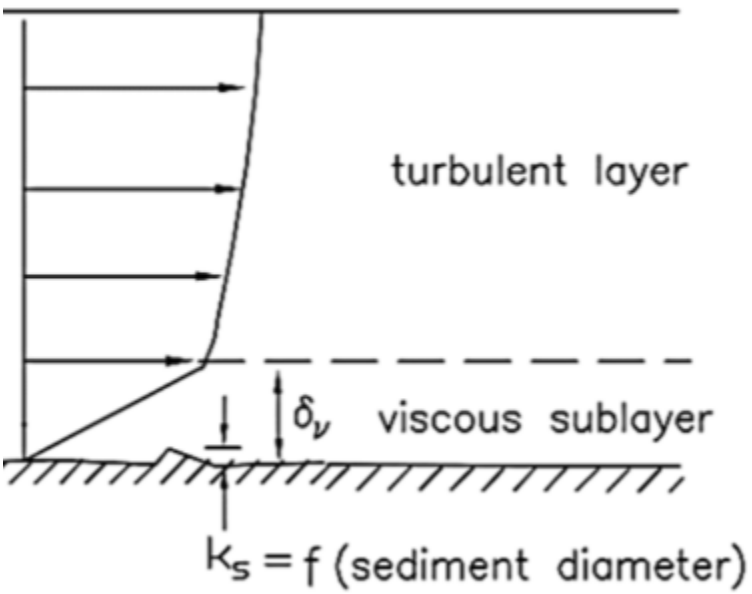


Figure 2.8. Typical logarithmic velocity profile at the boundary layer for a hydraulically smooth flow, where roughness elements are smaller than the viscous sublayer. Chirol et al. (2015), adapted from Liu, (2001).

In-stream vegetation introduces the influence of friction into the turbulent flow column, influencing river flow by exerting drag and can therefore be considered as introducing a vegetative boundary throughout the flow column. The effect of drag is three-dimensional and modifies the vertical flow column by altering vertical velocity and turbulence profiles (Bouteiller & Venditti, 2015). This results in flow partitioning (bifurcation) between fast-moving slow at the canopy boundary and slow-moving flow within the canopy, generating high levels of shear and thus producing turbulence patterns at the interface between the two flows (Bouteiller & Venditti, 2015).

### 2.3.5. Roughness

Roughness describes the projection of elements, such as rock or vegetation, into the liquid layers resulting in a disruption to the flow. Higher roughness values describe the greater effect the roughness element has on the flow. Physically this translates to smooth, compact soil having a lower roughness value compared to a gravel surface. Roughness values are frequently described by roughness heights, which describe the elevation to which roughness elements project into the flow layer. Roughness varies with vegetation density: highly dense vegetation canopies act as a single rough surface compared to a less dense, sparse canopy where drag and roughness are produced by multiple individual roughness elements. Within fluid

models, roughness is frequently included within empirical equations to quantify the interaction between roughness elements, often described in terms of flow resistance and drag. The majority of rivers can be classed as hydraulically rough-bed flows (Nikora et al., 2007) which provides numerous challenges in accurately representing the interaction between natural riverbed roughness and open-channel flow. For example, the 3D small-scale structures of average flow and turbulence at the near-bed region is highly spatially heterogeneous, which can be problematic when using time-averaged equations because they do not account for the additional shear stress contributed by these structures.

### 2.2.6 Resistance and drag.

Resistance describes the friction resulting from the interaction between a flow layer and either another fluid layer or element. The total resistance exhibited within a channel depends on the area, height, and length of the roughness element as well as the hydrodynamic characteristics of the flow. Hydraulic resistance typically reduces velocity, increasing velocity differentials to produce shear. Resistance occurs at the boundary between distinct flow layers, such as between vegetated flow and non-vegetated flow, or channel flow and floodplain flow. Vegetative resistance has been shown to considerably affect hydraulic phenomena. For example, Tang & Knight (2009) described strong lateral shear inducing mass and momentum exchanges at the channel and floodplain boundary whilst the inclusion of vegetation increases total channel resistance (Bennett et al., 2002). Rouse (1965) identified four sources of flow resistance within open channels: skin friction (for example, the roughness exhibited by variation in the texture of a rock or leaf), surface distortion (such as changes in channel topography), from drag (for example, the projection of roughness elements into the body of the flow, such as a vegetation canopy), and local acceleration. Hydraulic models often assume staticity for such elements: common roughness elements, such as rocks, rarely change in length and area in response to hydrodynamic changes. This is also assumed for vegetation within many models. This may practically capture the resistance exhibited by rigid vegetation, however realistically rigid vegetation will exhibit change when high flow overwhelms the plant's natural biomechanism resulting in damage or uprooting. In addition, many plants react to changing flow conditions by bending, and this of the vegetation results in changing resistance at different flow conditions. For example, flexible vegetation

will become more streamline in reaction to increased flow rates, changing the vegetative resistance as the canopy projected area is reduced. The introduction of additional hydraulic resistance by vegetation is considered one of the most important contributions as it can significantly reduce the volumetric flow rate: Tanino & Nepf (2009) state that the impact of vegetation if largely determined by the additional drag it provides; Green (2003) discusses the contribution of vegetation resistance can increase channel resistance an order of magnitude higher or more than the minimal channel resistance. Green (2006) expanded upon by this by characterising the cross-sectional distribution of macrophytes in terms of the effective wetted perimeter which describes the relative contribution of vegetated surface area to channel resistance and the additional turbulence generation produced through the increase in patch boundaries. Kothyaru et al. (2009) state that total channel resistance is considered to be largely composed of vegetative resistance, with bed sediment particles having previously been observed to have a negligible contribution (Stone and Shen, 2002). Key to emulating the impact of vegetative resistance on flow is drag: the force acting against an object as exerted by the flow, the magnitude of which is dependent on the velocity of the fluid. Drag reduces the flow velocity as a result of friction between flow and element: as an object experiences the force velocity decreases as energy is transferred from flow to object or dissipated through turbulence.

## 2.4. Impact of vegetation on flow depth

The obstruction provided by vegetation increases the total channel resistance, affecting local flow by reducing the cross-sectional area and increasing water depths (for example: Pitlo & Dawson, 1990; Kouwen & Fathi-Moghadam, 2000; Stephan & Gutknecht, 2002; Kothayari et al., 2009; Mulahasan & Stoesser, 2017; D'Ippolito et al., 2021). This flow blockage adds to channel resistance by providing additional roughness; Nezu et al., (1994) defined this as roughness which obstructs the wall region at 10 – 15% of the flow depth. The additional roughness exerts drag on the flow that contributes to a greater dissipation of velocity due to turbulence generation (Boutellier & Venditti, 2015). To satisfy momentum conservation and continuity the consequence is an increase depth (Stoesser, Kim, & Diplas, 2010), and thus resulting in greater river depths in vegetated channels compared to non-vegetated

channels. Nehal et al. (2012) observed flow resistance relationships for the emergent grass *Acrous calmus* using laboratory experiments, observing that increases in vegetation density (here, attributed to leaf density) resulted in increased local water depths with increasing discharge, linking a relationship between increases in vegetative roughness, characterised by vegetation morphology (Fig. 2.9.) Additionally, the importance of vegetation density was highlighted as the most considerable contribution to changes in flow depth, followed by changes in patch patterns. This work built upon on earlier work by Fathi-Moghadam and Kouwen (1997) who observed that, for emergent trees, density was consistently a dominant parameter despite other factors such as canopy geometry, distribution, and species. When investigating changes to depth at reach scale natural channels are frequently sloped and irregular, therefore reach-scale assessments consider changes to the gradient of the river surface. The flow conditions also affected the degree to which vegetation influences depth: Hamimed et al. (2013) observed that sensitivity to vegetation density was reduced for very shallow flows. Mulahasan & Stoesser (2017) observed that for a given flow rate the water depth increased with vegetation density. They noted that the relationship between flow rate and vegetation density and their impact on flow depth were similar between study cases of varying vegetation densities when flow rates were low. However, as flow rates increased differences between these relationships became apparent and increasingly dissimilar with denser arrays exhibiting steeper gradient for increases in flow depth. Bal et al., (2011) observed that the friction exhibited by vegetation patches increased at higher water levels, a result of greater pressure drag exerted by the increase surface area of submerged species presented perpendicular to the flow.

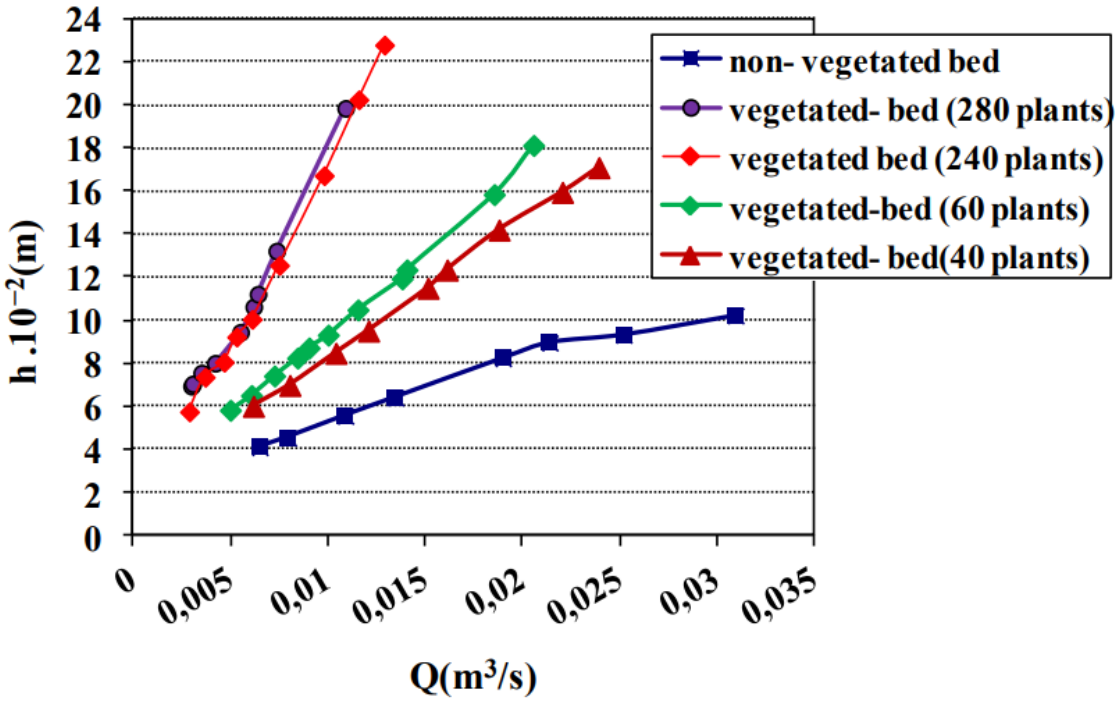


Figure 2.9 Changes to discharge Q($m^3$/s) and flow depth with changing plant density of *A. calmus*. Increases in vegetative density is associated with increases in flow depths with increasing discharge. Image from Nehal *et al.,* 2012.

## 2.5. Impact of vegetation biomechanics on flow conveyance

Biological traits influence how vegetation biomass is expressed; biological variation between changes the degree to which vegetation interact with flow. Simple flow resistance models parameterise this influence as vegetative flow resistance, however the interaction between flow and biomass can be described through characteristics such as the degree of submergence exhibited by the plant, the flexibility of the respective species, and the spacing of individual plants or stems (Lee et al., 2004), or stems, within the flow region, and the dimensions of the patch architecture (Bal and Meire, 2009).

### 2.5.1. Flexibility

Flexibility describes how plants assume more streamlined positions (Kouwen and Fathi-Moghadam, 2000) in response to drag exerted on them by channel flow, a phenomena common to most plants (Luhar & Nepf, 2011). Vegetative drag is

defined by the relative velocity i.e. the flow speed relative to the moving plant (Tinoco et al., 2020) and thus plant deformation is the result of the plant adapting to reduce drag by altering patch morphology by minimising the difference between the vegetated and non-vegetated relative velocity. Vegetation flexibility and how this manifest, for example through stem bending or canopy oscillation, and the to what degree a plant is flexible, can considerably affect local flow dynamics; the momentum absorbed by vegetation is directly affected by the flexibility of vegetation. For example, Fathi-Moghadam and Kouwen (1997) investigated flow interactions for cedar and pine trees and noted that, in additional to the frontal projected plant area, plant movement provided an additional area of foliage which also contributes to momentum absorption. The in-channel species *Sparganium emersum* (unbranched bur-reed – Fig. 2.10) is a flexible, submerged species which deforms to a streamline position in the flow direction. Bal et al., (2011) detail how canopy deformation reduces vegetative friction as the streamlining of plant geometry reduces the flow-facing frontal area, in turn reducing the available vegetative surface area at the flow-vegetation interface. Flexibility also influences the friction factor which has been observed to be largely dependent on the deflected height of flexible vegetation alongside mean velocity and depth (Jarvela, 2002). Further to this, Wilson (2007) investigated multiple resistance models and noted that, for flexible grasses, vegetative resistance was strongly dependant on plant height but weakly correlated to stem density. Righetti (2008) further observed that vegetation flexibility, alongside density, were key controls for the development of the turbulent mixing layer at the vegetation canopy. Ghisalberti and Nepf (2009) performed laboratory experiments using buoyant plastic and wooden dowels as the respective proxies for flexible and rigid vegetation. They observed that when the flexible vegetation exhibited monami, a coherent and periodic waving of the canopy exhibited by submerged flexible vegetation at high velocities caused by Kelvin-Helmhotltz instabilities (Ghisalberti & Nepf, 2002), a 40% reduction in canopy drag occurred. This, consequentially, allowed for an increase for in-canopy velocities by 65% alongside greater turbulent stresses. Compared to the mean velocity measured for the rigid canopy of identical height and frontal area (2.7cm/s), the velocity in the waving canopy was almost double (5.4cm/s). Physically, this was stated to occur because the monami allowed

for the greater canopy penetration by the channel flow and thus turbulent generation was similar to that expected of sparser canopies.

Figure 2.10. *Sparganium emersum* (unbranched bur-reed).

*Image downloaded from https://www.naturespot.org.uk/species/unbranched-bur-reed in March 2017.*

The characterisation of flexibility is complex as its expression is determined by plant biomechanics which is different between species, local environments, patches, plant element, and they relate to changing flow conditions. When idealising flexible vegetation researchers parameterise the plant depending on the processes-of-interest, and thus may solely consider the canopy distribution or, at smaller scales, consider plants at an individual basis or even by the different vegetative elements such as stem and leaf flexibility. Research has identified numerous methods to characterise plant flexibility and an overview is given below. At the canopy-scale flexibility is described by the overall deformation of vegetation canopy in relation to flow, whereby patches adopt streamlined postures as velocity and discharge increase (King et al., 2012) the position of which is also a function of buoyancy (Augustin et al., 2009). The overall impact of this reconfiguration is a reduction in resistance and drag (Luhar & Nepf, 2011) which changes depending on the hydrodynamic conditions of the channel flow (Augustin et al., 2009). Comparatively, less flexible, rigid vegetation exhibit a higher flow resistance (King et al., 2012). Various drag parameterisations have been proposed for patch configuration, and

one of the most common methods uses the ‘effective length’, which describes the length of a rigid element where the drag generated is the same as the drag produced by a curved vegetative element (Luhar & Nepf, 2011). The effective length is dependent on the canopy configuration and can thus be predicted using parameters for buoyancy and the Cauchy number, a term for the relative strength of drag force with respect to plant rigidity (Luhar & Nepf, 2013). The inclusion of the effective length within the calculation of frontal area density thus links canopy configuration to drag generation (Lei & Nepf, 2019). Mullarney and Henderson (2010) developed a dimensional stiffness parameter which considers the effects of both vegetation and wave characteristics, allowing them to predict the dissipation of wave energy resulting from stem movement.

Characterising the resistance exhibited by vegetation within models is dependent on how the vegetative characteristics are represented. For example, Fathi-Maghadam & Kouwen (1997) measured changes to drag forces and velocities as the flow interacted with flexible models of pine and cedar. They observed that changes in the flexibility of vegetation altered the momentum absorbed by vegetation, implying that an assumption of rigidity could lead to errors in estimating vegetative roughness from experimental work. Wilson, Hoyt, & Schnauder (2008) investigated the impact of flexible pine branches and ivy stipes on the drag force and noted that the flexibility of plant foliage can alter the contribution of the vegetation canopy to the total drag. Wilson and Schnauder (2008) mention that increases in vegetative drag is dependent on whether the plant is foliated and the degree to which plant foliage can deform to adopt a streamline position and thus reduce the canopy’s frontal projected area. Research considering plant flexibility introduces an additional element of uncertainty where changing canopy geometry, in relation to variant flow conditions within natural channels, incurs an unsteady flow-vegetation interaction (Mendez & Lousada, 2004). Accurately capturing the changing position of vegetation throughout the water column is difficult to approximate and is dependent on the scale required by the study: stem-scale research frequently attempts to approximate the mechanical change across the stem height, whilst reach-scale investigations often assume variation in plant flexibility to be captured in the approximated projected area. The former approach is suitable for single-patch or single-species studies where identifying the flow-plant interaction is crucial for capturing, for example,

small-scale changes to turbulence however is labour intensive and may be inapplicable for large-scale approximations of multi-patch environments. The latter approach addresses the multi-patch level, aiding in characterising vegetation-patch interaction at the cost of lower resolution by avoiding small-scale phenomena. At higher flow rates macrophyte reconfiguration can reduce the surface area exposed to the flow, and thus reduce the pressure drag and consequentially reduce the friction. The impact vegetation has at stem-scale is also considerably affected by the local hydraulic condition: James et al. (2004) observed that the influence of rigid stems on local drag coefficients was related to the average flow velocity, whilst Fathi-Moghadam and Kouwen (1997) measured an exponential decrease in the drag force for isolated pines with decreases in the square of flow velocity.

### 2.5.2. Submergence ratio

Research into macrophytes typically separate species into either submerged (i.e. free surface elevation exceeds vegetation height) or emergent (i.e. vegetation biomass exceeds free surface elevation) groups (Järvelä, J., 2002). The degree of submergence is generally expressed as the ratio $H/h$ between water depth $H$ and the height of the submerged plant stem $h$ (Irish & Lynett, 2009; Augustin et al., 2009). Characterising emergent $H/h \leq 1$ or submerged conditions $\geq H/h\ 1$ considerably impact local flow hydraulics (Tinoco et al., 2020). Similar to flexibility, interactions affected by emergent vegetation are determined by the characteristic scale, the stem, branches, or leaves, whose obstruction generates downstream flow structures. Submerged vegetation exhibit additional complexity by producing a mixing layer resulting from vertical flow separation between the low velocity vegetated region, and the high-velocity, non-vegetated, free flow region above the patch. The presence of this high velocity region strongly influences shearing and thus turbulence generation along the canopy top, and which is lost during emergent conditions (Nepf, 2004; Boutellier & Venditti, 2015; Tinoco & Coco, 2018 Increases in the relative flow depth eases flow constraint, expanding the free flow region between the free surface and the top of the vegetated canopy (Finnigan, 2000; Nepf & Vivoni, 2000), however variable unconstrained flow conditions are rarely represented within laboratory experiments where plant height is typically assumed to be uniform and static, disregarding the considerable impact heterogenic canopy height has on velocities within the above-canopy mixing layer (Hamed et al., 2017; Norris et al., 2019). The

presence of the mixing layer has motivated researchers characterise separate submerged vegetated flow into three interconnected regions: the free flow region above the submerged canopy, the upper canopy, and the lower canopy (Nepf 2012). Luhar et al., (2008) observed that canopy density and roughness height exhibit a non-monotonical relationship, where roughness height was found to increase as submerged arrays but which decreased with increasing density. The vertical velocity profile representative of this effect for a rigid cylinder is presented in Figure. 2.11.

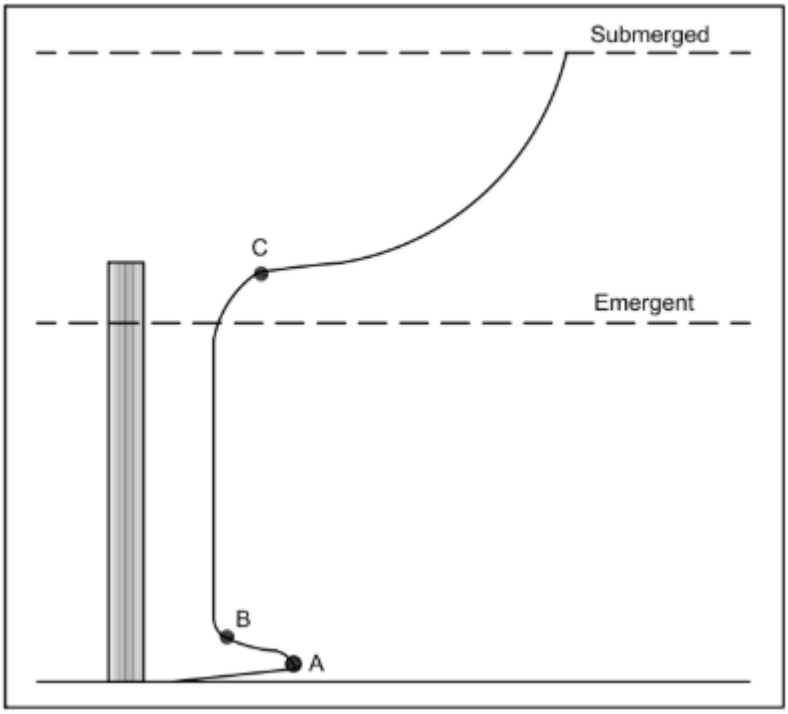


Figure 2.11. A typical velocity profile illustrating spikes (A) and inflection points (B, C) in velocity for emergent and submerged cases (Tinoco & Coco, 2018).

Nepf & Vivoni (2000) described how more research has focused on the flow-vegetation interaction for submerged vegetation rather than emergent, however over the last couple of decades studies have further investigated flow dynamics for broader canopy types (for example, see: Tanino & Nepf., 2008; Rominger & Nepf., 2011; de Lima et al., 2015; Maji et al., 2017). Research has generally noted that emergent species express lower friction values compared to submerged vegetation,

and thus exhibit less slow deceleration. Bal et al. (2011) observed that this effect was due to open canopies and the extension of leaves above the water surface during times of normal flow reducing the flow-facing frontal surface area (Bal et al., 2011). However, if an emergent species exhibits sufficient rigidity the friction values may increase during periods of high flow as the normally emergent leaves are submerged and remain upright. This is the case for *Sparganium erectum* (branched bur-reed – Fig. 2.12.), which has a high flow resistance to flow due to its rigid stems as well as being highly resistant to uprooting, allowing it to considerably affect flow conveyance during high flow conditions where the canopy is submerged (Liffen et al. 2011). In addition, *S. erectum* is also long-lived and highly prolific across the UK, highlighting the species as potentially significant controller of river hydraulics and flood risk in the UK. Differences in the friction have been assigned to differences in pressure drag. However, the overall resistance provided to flow is also informed other factors: *S. erectum* has rigid stems, is long-lived, and highly resistant to up-rooting allowing the species to exhibit control on the flow under periods of high flow which would cause more flexible species to deform. Its emergent nature also means that it is projected through more of the flow layer at high flows. These traits increase flow resistance, highlighting the species as a potentially significant controller of river hydraulics and flood risk in the UK: Bal et al. (2011) showed how higher water levels increases friction due to increases in surface area perpendicular to the flow.

Figure 2.12. Sparganium erectum (branched bur-reed).

*Image downloaded from http://www.makaques.com/gallery.php?sp=2789 in March 2017.*

### 2.5.3. Vegetation distribution

The degrees by which flow velocity and turbulence characteristics are modified by vegetation-flow interaction is considerably affected by both the distribution of patches within the channel reaches, and the different layouts - or patterns – of individual vegetative bodies (for example, stems) expressed within a patch (Armanini et al., 2005; Bal et al., 2011). Both patch layout and channel distribution characterise the spatial occupation of patches at different scales, dependent on whether experimentalists focus on patch-scale or channel-scale hydraulics, respectively.

Studies typically assumes patch layouts as squared or staggered, creating a consistent flow pattern and preferential pathways throughout the patch, and thus bias the sampling (Chang et al., 2017). Research by Shan et al., (2019) observed how preferential pathways incur differences in the spatial distribution of drag resulting from localised increases in velocity and shear stress. Etminan et al., (2018) detailed how differences in velocity was contingent on the proximity of stems, noting differences between the drag on individual stems when the array was staggered or

randomly distributed. Folkard (2011) and El-Allaoui (2015) noted variation in the gaps between elements was a considerable source of uncertainty; to accurately represent flow through vegetation patches researchers must adjust array spacing until flow conditions reflect flow within a vegetation patch.

Li and Shen (1973) discovered that total channel resistance changed with the channel distribution, depending on whether vegetation patches uniformly aligned, staggered, or scattered. Sonnenwald et al. (2017) noted that the accurate representation of vegetation distribution is more important that accurately characterising vegetation, their simulations of *Typha latifolia* in stormwater ponds and wetlands illustrated that including of stem-scale mixing effects within their model had little impact of resident time distributions of compared to simulations without. They observed that changes to vegetation distribution was fundamental the development of different flow fields and consequent resident times (Sonnenwald et al., 2017). Nehal et al. (2012) observed that staggered arrangement of patches of the plant *Acorus calmus* resulted in the largest decrease in flow rate. Whilst literature discussing the impact of patch species on flow have received attention, few consider the hydraulic impact of patches of mixed vegetation species: in natural channels the geometric characteristics and the patch distribution density varies however laboratory tests often use regular patterns (for example: Stone & Shen, 2002; Kothyari et al., 2009; Busari & Li, 2016). However, studies have observed that changes in vegetation distribution can considerably affect the local drag exhibited by a strong effect on the vegetation drag coefficient (for example: Freeman et al., 2000; Armanini et al., 2005).

Järvelä (2002) investigated changes to local flow hydraulics resulting from changes to cutting patterns in a catchment for a mixture of vegetation, including *Sparganium erectum* and *Potamogeton natans*, which covered approximately 19% of the reach. He observed that when two-thirds of the reach was vegetation, the increase in biomass resulted in bottleneck patterns where flow was constrained between patches and consequentially resulted in increases in friction values. This constraint also resulted in the acceleration of flow velocity in non-vegetated zones. However, friction values were found to reduce alongside decreases in vegetation density and increases in the degree of emergence. From these experiments, the channel stage was found to increase with increases in the vegetative surface area. Green (2005)

investigated cross-sectional blockage for a reach and discovered that the proportion of vegetated cross-section was weakly related to vegetative resistance due to high spatial variability in patches. He concluded that changes to the aerial extent of the vegetation throughout the channel was a more important contributor to total channel resistance compared to changes in patch density. Kothyari et al., (2009) similarly states that the vegetative control of flow is largely the result of distribution density as well as the plant characteristics. This was also confirmed by Bal et al., (2011) who altered patch patterns in a flume and observed that at the patch scale the interaction between stems and the aerial extent of the patch were both important factors which contributed to vegetative fiction. They also discovered that friction values were lower for emergent species with open canopies, like *S. erectum.*

The above section has considered the relationship between plant height and flow depth. It has been previously stated that both a plant's morphological characteristics and the local hydrodynamics play important factors which interact to alter flow conveyance, the literature has highlighted numerous other factors both which influence plant-flow interactions. For example, the degree to which a plant is emergent or submerged affects flow quantities such as velocity through differences in resistance, whilst turbulence is considerably influence by the species flexibility, buoyancy, surface area, spatial coverage, canopy density and stem geometry. The projection and interaction of vegetation within flow is usually parametrised by three key concepts: roughness, resistance, and drag. Roughness describes the vegetated region interacting with flow and which varies with plant characteristics, whilst resistance expresses the degree to which vegetation resists flow and is dependent upon the hydrodynamic conditions. The drag is the resultant change to flow due to the differential between the flow quantities and the friction provided by the plant characteristics.

The vegetative mechanisms above are frequently cited in the literature it is by no means comprehensive. For example, Leonard & Croft (2006) observed that variation in biomass density within natural vegetation relates the frontal area density to changes in depth, which increases drag, turbulence generation, and velocity reductions. The mean vegetation density of individual plants, or stems, has been used to determine the induced drag force (Stoesser et al., 2003; Wilson et al., 2006) or the density of the canopy: Neary et al. (2012) defined canopy density as the

volumetric frontal area calculated using $1/4MD$ where $M$ is the number of stems per planform and $D$ is the stem diameter (Ghisalberti and Nepf 2004). Nepf et al. (2008) noted that the relevant length scale is density dependant, with stem density exhibiting a stronger influence over stem diameter with increases in stem density. Spacing has been defined using the ratio of the stem diameter to the space between the stems (Stoesser et al. 2010), and by classifying the contribution of vegetative drag and turbulent stress within the momentum equation (Luhar et al., 2008). Righetti (2008) discovered a dependency of the drag coefficient on canopy density, with drag noticeably changing between the canopies of different species. The impact of changes to drag from biomechanical or morphological characteristics considerably affects flow quantities, such as velocity and turbulent energy.

## 2.6. Impact of vegetation on flow velocity

Velocity is reduced within vegetation due to drag in the canopy layer (Bennett et al., 2002; Tang et al., 2014; Bouteiller & Venditti, 2015) causing disparity in the spatial pattern of velocity throughout the flow column (Augustin et al., 2009). The magnitude to which vegetation affects flow velocity is dependent on two key factors; the flow properties and the vegetation characteristics, explored in the previous section (Bennett et al., 2002). Nepf (2004) used a steady flow condition to demonstrate how the hydrodynamic characteristics affect velocities: increases in depth, and thus the degree of a plant's submergence, considerably affects velocity. The effect vegetation has on flow velocity has been well substantiated through both field and experimental observations. For example, Sand-Jensen & Pedersen (1999) observed that velocities within patches can be reduced by 90% of the flow velocity measured in adjacent non-vegetated flow. It has been well substantiated that vegetation considerably affects vertical velocity through laboratory experiments (for example: Fonseca et al., 1982; Carollo et al., 2002; Jarvela, 2005; Bouma et al., 2007; Lefebvre et al., 2010). Nepf (2004) showed that submerged canopy can strongly influence the vertical velocity profile under steady flow conditions. Liu et al., (2008) described the changes to the vertical velocity profile around a cylinder for submerged and emergent conditions. Tinoco & Coco (2018) discuss how research has described how the dampening effect vegetation has on velocities and the generation of turbulence at stem and canopy scales are dependent on canopy

geometry and density. An example of using real vegetation to measure velocity profiles is presented in Zhang et al., (2016), where they observed adjustments to vertical velocity profiles for two different aquatic grasses. They noted an increase in the mean vertical velocity above the submerged canopy as well as below the height where branching begins due to vertical variation in the frontal facing area of the vegetation. This inverse variation in mean vertical velocity with frontal area, referred to as a counter-gradient (Zhang et al., 2016), has been reported in other studies with both emergent and submerged canopies (for example: Nepf & Vivoni, 2000; Leonard & Croft, 2006) and is shown in Figure. 2.13.

A

They discovered inflection points resulting from the mixing of flows with different velocities, the result of vortices generated from velocity differentials between the local fluid in the wake behind the cylinder with the bottom boundary roughness and higher velocities above the cylinder, respectively. For example, they found the velocity spike changed in intensity with changes to bottom roughness as local fluid behind the cylinder is forced upward and away from the bed due to increased shearing at the bottom. When submerged the additional inflection point above the cylinder as the fluid is forced downward due to mixing between the higher velocity zones above the lower velocity wake zone. Lacy & Wyllie-Echeverria (2011) investigated the interaction of submerged eelgrass canopies with channel flow and

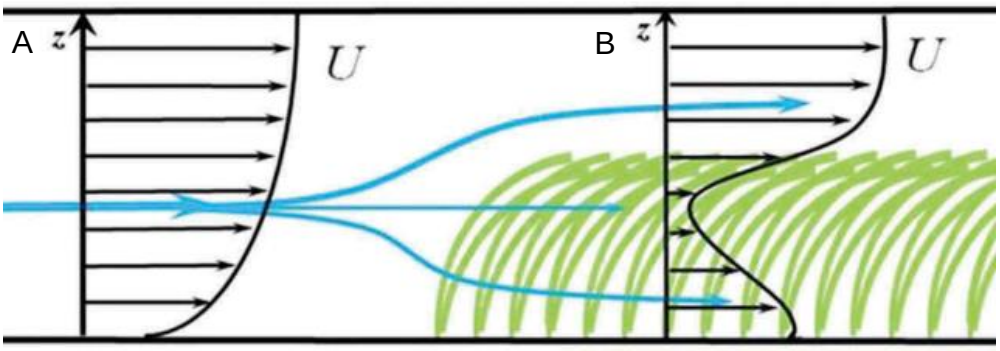


Figure 2.13. Vertical velocity profiles for a) non-vegetated flow and b) flow vegetated with plants featuring distinct basal stem regions below the canopy. Velocities have been shown to increase above the canopy and beneath the branch height (Zhang et al., 2016).

observed decreases in flow velocity between 40-70% depending on vegetation density. They also observed a thicker wake zone downstream of the site with increases in vegetation density. Velocity profiles in non-vegetated flow regions and above the canopy were logarithmic, however the submerged canopy profiles were

consistent with shear-layer profiles in contrast to the uniform profiles exhibited by emergent vegetation in other studies. Nepf (1999) observed near-uniform velocity profiles within an array of emergent rigid cylinders. Jiang et al. (2015) discovered similar uniform velocity profiles for a similar array, but additionally described a second near-bed stress layer the thickness of which is characterised as the minimum value between stem radius and unobstructed channel velocity value. The result of reduced velocities is a decrease in discharge i.e. the volumetric flow rate (Vereecken et al., 2006; Tanino & Nepf., 2009); Grīnberga & Spriņge (2008) observed decreases in discharge correlated with increases in vegetation coverage.

## 2.7. Impact of vegetation on turbulence

Turbulent length scales in unobstructed open channels are determined by the channel geometry and flow depth. The introduction of vegetation provides an additional source of turbulence determined by the length scale of vegetative elements and spacing between said elements (Tinoco et al., 2020). Previous research has showed that vegetation significantly alters the bulk, time-averaged, and instantaneous turbulence characteristics of channel flow (Neary et al., 2012). Within vegetated channels the turbulence intensity is lowest in non-vegetated regions (Liu et al., 2008); turbulent intensities increase for vegetated regions because of the interface between low-velocity canopy flow and high-velocity non-vegetated flow create zones of high shear (Bouteiller & Venditti, 2015). Total shear stress increases with vegetation density, however shear stress is also spatially heterogeneous: greater shearing is present at the patch boundaries due to the additional resistance provided by biomass (Tinoco & Coco, 2018), whilst shear stress is reduced within vegetated patch and at the bed (Neary et al., 2010).

Vegetation induces turbulence at multiple scales, with studies commonly referring to turbulence production at the stem- and canopy-scales where deceleration and turbulence generation have been successfully observed (for example: Nepf, 2012, La Bouteiller & Venditti, 2015). However, Tinoco & Coco (2018) state that a full characterisation of turbulence at all the appropriate length- and time-scales is still an experimental challenge. Turbulence generation is largely confined to the patch boundary because of flow bifurcation at the patch head: flow is deflected and accelerates around the patch, providing a source of additional resistance and

increasing local shear stress (Bennett et al., 2008). Turbulence production at the patch boundary is notably different compared to the non-vegetated channel due to a higher level of spatial heterogeneity present in horizontal and vertical fields (Liu et al., 2008; Stoesser et al., 2010). For example, Liu et al. (2008) noted higher longitudinal and vertical turbulence down-stream of a wooden dowel and lowest in free flow zones, with similar phenomena have also been reported by Nepf (1999) and Lopez & Garcia (2001). Within the canopy the additional drag reduces the mean flow, and turbulence is produced by the vertical transport of momentum from overlying flow. The dispersion of TKE within patches and immediately downstream in the form of longitudinal dispersion occurs as a result of secondary stem-scale wake dispersion, or differential shear, where fluid particles move between areas of low and high velocity as they navigate spaces between stems, and vortex trapping, where fluid particles are temporarily caught within vortices generated immediately downstream of stems (White & Nepf, 2003). Nepf (1999) described turbulence at the stem-scale showing transverse mixing including turbulent diffusion and mechanical dispersion.

The spatial complexity of vegetation-induced turbulence is also dependant on the submergence ratio: for submerged vegetation turbulence intensities increase near the canopy tops (Bennett et al., 2002) as flow is forced between the free surface and canopy and turbulence patterns propagate along the top of the canopy (Nepf & Vivoni, 2000), however this decreases as the hydraulic space between the canopy top and free surface increases. The regions above vegetation canopies typically dominate turbulence production: Nepf & Vivoni (2000) describe how turbulence generated above the canopy defines the scale of active turbulence both above and throughout the canopy, as the turbulence shear length is of the order of the canopy height. Similarly, Nezu & Onitsuka (2001) describe how the top of canopies is where Reynolds shear stress peaks and whilst they are at their lowest within the canopy. Shear is generated in the flow layer immediately above the vegetation canopy as velocities are reduced by a canopy resistance layer which has been equivocated to bed shear stress (Huthoff et al., 2007) and akin to the turbulent boundary layer flow (King et al., 2012). Luhar et al., (2008) state that the affect the canopy boundary has on turbulent production can be used to classify the canopy density, where greater canopy densities increases the shear stress at the vegetation layer but decreases

bottom shear stress (Tsujimoto, 1999): when turbulent shear dominates the canopy can be defined as sparse, and when drag forces dominate the canopy is regarded as dense and the mixing flow layers result in Kelvin-Helmholtz instabilities (King et al., 2012). These instabilities in turn increases local flow resistance and decelerates flow both within the canopy and downstream of the patch, whilst accelerating and deflecting flow at the vegetation-flow boundary (Neary et al. 2011). This has been replicated in experimental work where an increase in the density of cylinder arrays results in higher turbulence levels (King et al., 2012). For emergent vegetation, the lack of an additional shear boundary results in comparatively less TKE production, however as emergent vegetation penetrates the free surface turbulence is generated throughout the entire water column Nepf (2012) and turbulence intensity is relatively constant throughout the flow depth for emergent vegetation (Liu et al., 2008). The lack of, or lesser, canopy shearing during emergent conditions establishes wake shearing as an important factor influencing turbulence (Bal et al., 2011); wake turbulence is a smaller length-scale compared to canopy shearing and is largely considered an augmenting factor, however Nepf (1999) observed that its small scale reduced turbulent diffusivity compared to non-vegetated channel zones.

The above section has summarised the key physical mechanisms within in-stream vegetation responsible for turbulence generation, however multiple sources of turbulence are dependent on biomechanical characteristics. For example, turbulence is also generated by flexible vegetation due to monami: the periodic waving of canopy elements as they respond to and generate turbulence (Okamoto et al., 2012) Additionally, turbulence generation is also spatially dependant; the interface zone between channel flow and riparian vegetation has also been identified as a key source of turbulence induction (Bennett et al., 2002). Alongside the vegetative characteristics, the hydrodynamic characteristics also impact turbulence magnitudes: shallow depths inhibit the generation of large–scale 3D turbulent structures compared to increased depths (Stoesser et al., 2010).

## 2.8. Characterising vegetative resistance and drag for numerical modelling

Numerical models typically employ Reynolds-averaged Navier-Stokes (RANS) methods or Large Eddy Simulations (LES), and either represent the effect of

vegetation using a bulk resistance parameter or drag coefficient, or by explicitly modelling stem geometry. Three dimensional (3D) models simulate flow-vegetation interactions by treating channel hydrodynamics as interacting components of fluid flow, vegetation dynamics, and mass transport. The appropriate selection of RANS or LES approaches depends on the scale of the flow processes of interest, the availability of explicit data regarding plant location and functional characteristics, and the computational burden. LES-type simulations require both detailed knowledge and a large degree of computational resources, which is prohibitive when simulating hydrodynamics in domains greater than the stem-scale. As such, LES approaches are largely constrained to small-scale hydrodynamics and the explicit representation of stem geometry at a high resolution (for example: Stoesser et al., (2009), Okamoto & Nezu (2010), Gac (2014)) whilst RANS approaches are used to capture large-scale processes. A common approach to numerical simulations of vegetation-flow interactions is to define representative characteristics and then extrapolate these values throughout the environment of interest (Tinoco et al., 2020). These characteristics are usually informed by experimental studies and observed data, and often use vegetation height, canopy density, and vegetated area, amongst others (Baptist et al., 2007). Simulations are then calibrated using, or validated against, experimental laboratory or field data.

### 2.8.1. A brief history of numerical approaches

Early numerical models were one-dimensional (1D), which typically use known velocity profiles to simulate mean flow and the interaction between depth-average flow with vegetation, variably represented by considering the impact of viscous drag (Price et al., 1969), such as drag on an idealised rigid cylinder (Petryk & Bosmajian, 1975), or as a zone with high friction (Camfield, 1983). Pasche and Rouvé (1985) used a one-dimensional model to investigate flow over a floodplain, parameterising vegetation through practical experiments on rigid cylinders and developing empirical relationships for plant density. Mork (1996) later accounted for the effect of kelp by representing their impact as form drag within the vegetated zones. Representing the effect of vegetation as idealised cylinders as continued to be a common approach in vegetation modelling (for example: Wilson e t al., 2003; Lee et al., 2004; Takemura & Tanaka, 2007). Whilst commonly used due to their practicality, 1D approaches are a

poor analogue of river flow as they cannot effectively model the effect of either channel morphology or vegetation on flow.

Two dimensional (2D) models were built to overcome the limitations of 1D approaches by better representing the influence of channel shape on flow phenomena, and frequently models parametrise vegetation-flow interactions as an additional source of roughness in addition to bed roughness. Additionally, they are often favoured over 3D approaches due to their lower computational cost (Sun et al., 2010). Early 2D modelling by Tsujimoto (1999) analysed fluvial processes for depth-averaged flow, representing vegetation using the drag force approach. Hunter et al. (2008) used Manning's equations to represent vegetation within an urban environment; their coefficients varied between 0.015-0.075. Tusjimoto (1999) used a spatial averaging approach and employed a drag force approach to represent vegetation elements and account for the additional turbulence generation. This approach was chosen as it was deemed unnecessary to know detailed, local properties of flow near vegetation elements. He discovered that increases in vegetation density also increases shear stress, however the bottom shear stress decreased. He interpreted this as the vegetation layer increasing flow resistance whilst having a strong resistance for surface erosion. Lotsari et al., (2015) used 2D models to quantify vegetation-flow interactions. Verschoren et al. (2016) studied changes to spatial patterns for submerged macrophytes. This was later expanded upon to simulate vegetation growth for a single season (Verchosen, 2017). Yamasaki et al., (2019) modelled vertical evolution in emergent vegetation within uniform channel using a blockage factor, which define the fraction of the channel area containing vegetation (Green, 2005,2006).

Three dimensional (3D) hydraulic models solve flow quantities using vertically distributed characterisations alongside formulations for vertical mixing and momentum loss (Luo et al., 2018). Approaches differ but common methods include the Reynolds-averaged Navier-Stokes equations (RANS), where flow quantities are separated into time-averaged and fluctuating components through Reynolds decomposition; double-averaged Navier-Stokes equations (DANS), where an additional decomposition occurs across space often through the inclusion of drag terms (Nikora et al., 2007); and Large Eddy Simulation, which ignores information at small length scales using low-pass filtering on the Navier-Stokes equations. Three-

dimensional approaches are necessary to capture the interaction between macrophytes and flow; vegetation extends up and across the flow layer, affecting the 3D velocity field and producing complex turbulence patterns. This section will discuss the 3D modelling approaches have been used to represent vegetation. López and García (2001) state that flow fields associated with vegetated flows are distinctly non-homogenous, with different phenomena induced above and below the plants and as such necessitates a 3D approach to appreciate the effect on turbulence. Marjoribanks et al. (2014) used computational fluid dynamics …. Marjoribanks et al. (2017) further expanded on it using RANS with a k ε Re-Normalization Group (RNG) turbulence closure model. Submerged vegetation was represented using a mass-flux scaling algorithm, which account for the blockage factor of vegetation patches by altering cell porosity. In addition, drag terms were added to the momentum equations which were estimated using a drag force approach, where the drag effect of the vegetation was represented by the drag coefficient CD. They found that the model could predict complex flow profiles, reproducing patch-scale spatial patterns and velocity variability due to the presence of vegetation. However, they noted a dampening effect occurred for large regions of flow recirculation. Nicholas & McLelland (2004) also used a drag approach to represent floodplain vegetation. Tanino & Nepf (2004) represented vegetation using rigid cylinders. Resistance was parametrised using the drag force approach. They described the relationship between Reynolds number and the drag coefficient Cd, stating how the coefficient decreased with a greater Reynolds number and a high density of cylinders. Overall, this resulted in a decreased drag downstream of the cylinder patch. Stoesser, Kim, & Diplas (2010) stated the merits of 3D approaches, mentioning how a more complete representation of flow can be obtained from using RANS equations and time-averaged flow-fields. The discussed how RANS approaches are often the most practical due to their reasonable accuracy and computational efficiency, and portability to field-scale flows. They accounted for vegetation grid by inserting additional source terms into the momentum and turbulence transport equations, and additional drag-related sink terms in the turbulence equations can reasonably predict the turbulence generated by vegetation layers. As an alternative to RANS, they discussed LES methods as preferable for modelling turbulence-dominated flows due to their ability to resolve large-scale

unsteadiness and large eddy asymmetry. Neary et al. (2012) discussed how studies investigation vegetation-flow dynamics at the patch-scale were largely focused as the intertidal zone, with few focusing on alluvial rivers. A result of this was a limited number of descriptors for vegetation characteristics (typical stem densities, fractional areas, submergence ratio, etc.) and a need to describe a wider variety of plant species. Whilst they accepted that variations within species mean that descriptors are not universal, they stated that future research needed to focus on flow interaction with isolated vegetation patches with a focus on changes to turbulence structure throughout the vegetation canopy, different configurations in patch extent, and the examination of isolated patches. Sonnenwald et al., (2017) modelled the impact of uniform, emergent vegetation on flow within stormwater ponds using a drag-force approach and introduced an additional anisotropic dispersion component to model stem-scale mixing effects within vegetation patches. They found that the additional mixing within vegetation resulted in little differences between residence time distributions, with the greatest differences resulting from spatial variation in vegetation. As such the accurate characterisation of vegetation within the model may be less important than representing the geometry and distribution. Anjum et al. (2018) investigated the impact of double-layered (i.e. emergent and submergent) and discontinuous patches. Lera et al., (2019) represented vegetation using hydraulic roughness derived from vegetation morphology (height and density) to analyse the impact of submerged macrophytes on river estuarine geomorphology.

### 2.8.2. Bulk-type numerical representations of the vegetative effects on flow

Previous research has built a vast background of knowledge detailing the effect of vegetation-flow interaction on exerted drag and the characterisation of bulk drag coefficients (D'ippolito et al., 2021). However, the result is an expansive range of parametrisations which may render the appropriate selection difficult (Mullarney and Henderson, 2018). Additionally, the relationship between vegetation and drag is complex: a summation of small-scale of drag forces through the use of bulk drag coefficients is not representative of total drag exerted by a vegetation patch (Albayrak et al., 2014).

Resistance relationships are typically used to describe the relationship between velocity and discharge with flow depth (Nehal et al., 2012). This relationship has

commonly been calculated using empirical approaches, such as the Manning-Strickler equation (Lee & Ferguson, 2002). Manning's *n* values increase with increases in vegetation patches and associated decreases in flow velocity (Bal et al., 2011). Wunder et al. (2011) discussed that resistance was controlled by the flow characteristics, including flow depth, velocity, and Reynolds number, as well as the characteristics of the vegetation patches. This was later discussed by Nehal et al. (2010) who found the impact of vegetation on flow depth was both dependent on vegetation density and the initial depth of the river. The resulting drag is dependent on stem geometry, flexibility (or displacement) stem density, and the hydraulic characteristics of the channel Sun & Shiono (2009). This consequentially influences turbulence production: the length-scale of turbulence generated due to shearing at the vegetation-flow boundary is of the order of the stem diameter, and turbulence intensities increases with decreases in vegetation density with the inverse true for increases in vegetation density (Nepf & Vivoni, 2000). However, Tusjimoto (1999) discovered that for a rectangular channel the velocity differentials between vegetation and non-vegetated zones increase as density increases, and thus results in higher turbulence intensities at high vegetation density. Whilst both findings seem initially contradictory, the effect described by Tusjimoto has be shown to be strongly affected by secondary flow currents which alter a shear layer adjacent to the vegetation-flow interface and has considerable impacts upon resistance, which itself is dependent on the adjacent shear layer (Pasche and Rouve, 1985). Drag forces impacting upon vegetation are commonly represented within numerical models by including a momentum sink term within the Reynolds-Averaged Navier-Stokes equations (RANS). Typically research simulating flow hydrodynamics use time-averages Navier-Stokes equations, however the three-dimensional small-scale characteristics of the mean flow and associated phenomena, such as turbulence, in addition to the highly spatially heterogeneous can reduced the efficacy of time-averaged equations where spatially-averaged roughness elements are not explicitly related with the point flow properties represented within the Reynolds equations. For example, the characteristics of uniform flow (i.e. flow properties do not change) can be difficult to channels with rough beds where the conditions for uniform flow aren't met near roughness elements due to the non-uniformity of time-averaged flow in the roughness layer. Similarly, the bed shear stress is defined for a point on the bed

surface, which is problematic for beds composed of heterogenic roughness elements (Nikora et al., 2007). The Manning's equation and Chézy-like predictors which predict bulk, depth-averaged quantities are useful for first-order approximation of flow resistance and vegetative shear stress, however Tinoco et al., (2020) noted they unable to predict hydrodynamics within a vegetation patch and neglect local effects within and around the vegetation. Indeed, historical assumptions of a uniform Manning's *n* are inappropriate for investigating vegetation-flow interactions during periods of low flow, where Manning's *n* increases considerably when the vegetation depth and flow depth are similar (Wilson & Horritt, 2002). Double-averaging approaches (DANS) have recently gained popularity within environmental hydraulics over the last decade, where the time-averaged equations include spatial-averaging by parameterising along the longitudinal, transverse, and vertical length scales of roughness elements (Nikora et al., 2007). Double-averaging approaches include additional terms for describing flow related to, for example, form-induced stresses and drag terms. To effectively represent drag, models are typically parametrised using values obtained from experimental work, either directly as an input or as guidance for calibrating models. Numerous studies have also considered the impact roughness on overland flow, where it is considered the most important factor determining flow after local topography (Straatsma, 2009).

The method used to represent drag dependent on the type of model: empirical relationships, such as the Manning's equations, Chezy formula, and Darcy-Weisbach equations, are commonly used by computing flow quantities resulting from the relationships between resistance and other factors, such as blockage factors (Green, 2005a) and biomass (Doncker et al., 2009). Flow resistance is often quantified using a bulk flow resistance parameter, such as Manning's *n*, and group a range of resistance effects into a single coefficient. Early research into vegetation-flow interactions frequently used bulk resistance parameters through either the Manning roughness coefficient, n, or the Darcy-Wesibach friction factor (for example: Petryk & Bosmajian, 1975; Chen, 1976). The Manning's *n* coefficient is an empirical approach which uses average flow velocity and channel morphology to calculate hydraulic resistance, and has been used since early attempts at numerically representing vegetation (Petryk and Bosmajian (1975)) and still dominates approaches to represent vegetation drag (Järvelä, J., 2002; Wu & He, 2009), along with the Darcy-

Wesibach friction factor (Chen, 1976; Augustin et al., 2009). However, both of the above approaches are unsuitable for environments with variable depths as the corresponding friction factors become variable (James et al., 2004): empirical relationships such as the Manning's approach assume a logarithmic velocity distribution (Neary et al.,2011) as they are often estimated from uniform pipes or flumes. For example, the Dary-Weisbach was both developed for steady flow within a pipe whilst being dependant on depth parametrisation, as well as Reynolds number and vegetation type. As such, empirical approaches can result in inaccurate estimates. Defining the coefficient and energy gradient can be problematic (Powell, 2014), especially for vegetated channels (Wilson et al., 2006), resulting in large levels of uncertainty and an error within flow estimations. Empirical estimations in particular can be inaccurate: the resistance forces are quantified and represent the form drag of roughness elements throughout the flow depth. These resistance coefficients typically represent bulk energy lost, however the large range of parameters for any given environment introduces additional uncertainties which question the meaning behind the parameter values, and thus potentially resulting in poorly characterised understanding of the impacts of plants of flow (Wilson et al., 2006). Difficulties arise when using Manning's *n* when vegetation is the dominant controlling factor; the value of Manning's *n* varies with hydraulic radius and velocity (Kadlec, 1990) despite the influence of the hydraulic radius on flow in vegetated channels is less significant compared to non-vegetated channels (Berger and Wells, 2008). This is despite that in-stream vegetation exhibit a significant degree of flow resistance: increases in channel resistance can be an order of magnitude greater than the minimal channel resistance (Green, 2005; Bal & Meire, 2009) and may be further exaggerated under extreme flow scenarios (Green, 2003). In addition, empirical approaches, such as the Manning's equation, represent resistance at the channel boundary however vegetation patches can vary with height, resulting in a heterogeneous distribution of drag throughout the flow depth not accurately represented by the Manning's coefficient (James et al., 2004). The Darcy-Wesibach friction factor has a similar short-coming as it was developed in reference to a pipe and may be inappropriate for representing complex, unsteady, and turbulent boundary layers (Augustin et al., 2008). Using the Manning's equation has other difficulties associated with accurately representing vegetation: gauging the correct

value for the coefficient can be problematic (Sun et al., 2010), with values often selected through qualitative descriptions (for example: Chow, 1959) and *a priori* knowledge (James et al., 2004) to select an estimation for calibration (Aberle & Järvelä, 2013). Both the Manning's equation and the Darcy-Wesibach friction factor are also strongly dependent on other factors such as depth and Reynolds, with the Manning's equation also dependant on vegetation density Darcy-Wesibach dependent on vegetation type (Augustin et al., 2008). Sun et al. (2010) mentioned how previously researchers employ uniform friction factor for the floodplain, however this can be problematic in terms of calibration. In addition, Stone and Shen (2002) stated that the resistance characteristics of large roughness elements on combatively smooth surfaces is not well understood. Alternatives to empirical relationships have thus been investigated to better represent these characteristics.

An alternative is the application of the drag force approach, which has been increasingly been adopted to model the influence of stem drag by using a drag term in the momentum equations (for example: Burke and Stolzenbach, 1983; Shimizu & Tsujimoto,1994; López & García, 2001; Stoesser et al. 2003; Choi and Kang, 2004; Wilson et al., 2006; Saggirori, 2010; Zhang et al., 2010; Rominger & Nepf, 2011; Tsavdaris et al., 2013) and has been used investigate the influence of vegetation on floodplain flow (Stoesser et al., 2003), woody riparian banks (Van De Wiel & Darby, 2004) and open channel flow (Li & Zeng, 2008). Previous research often has distributed a uniform drag force term across the vegetated areas by introducing the term into both the turbulence and momentum equations (Shimizu & Tsujimoto, 1994; Zhang et al., 2010) or just the momentum equations (Fischer-Antze et al., 2001). Sun et al. (2010) mention that an introduction of drag force terms in the turbulence equations necessitate the recalibration of turbulent constants. However, drag force approaches can be difficult to accurately estimate: the calculation of the drag force is dependent on how the projected area $A_p$ is defined, and arbitrarily selected values can significantly influence the calculated drag (Fischenich & Dudley, 2000). For example, Saggiori (2010) and Tsavdaris et al., (2013) suggested that the drag can be characterised using the stem diameter and solid volume fraction to represent porous zones. They confirmed that this approach could accurately capture large-scale hydrodynamics in ponds around vegetation patches. Whilst this is not difficult for inflexible, stable elements estimating the projected area for vegetation is

troublesome as it is limited by practical considerations. For example, it is impractical to measure the entire wetter area of vegetation across a large site. In addition, the projected area of vegetation is determined by its flexibility, where the degree to which vegetation bends within the flow, as well as its orientation to the flow direction, which is difficult to estimate as these characteristics will differ between plants of the same species (Wilson et al., 2006). Models simulating atmospheric flows through terrestrial canopies have heavily influenced many approaches for applying drag force to aquatic vegetation. A major outcome from this interdisciplinary collaboration is the usage of spatially averaged parameters, whereby characteristics of roughness elements are applied successively to mesh layers to represent the roughness region. Rameshwaran et al., (2011) used a double averaging approach to capture the spatially averaged flow field for pebble clusters. They used averaged frontal projected areas for computing drag force in the streamwise and lateral directions, and average surface area for drag force in the vertical. This study attempts to assess the feasibility to which a natural, vegetated gravel-bed river can be represented with a 3D free surface flow application by applying a spatially averaged flow field. Vegetative drag force is represented as the difference between the gradient of the turbulent stress in the overflying flow and the depth-specific gradient in Reynolds stress within the canopy (Lacy & Wyllie-Echeverria, 2011). Physically, drag describes the influence of the canopy on overlying flow and is analogous to the impact of roughness elements on the channel bottom on overlying flow layers (Järvelä, 2002). It is considerably influenced by both the canopy roughness and the shear at the near-roughness layer (Lacy & Wyllie-Echeverria, 2011). Drag is therefore highly related to vegetative characteristic area, with the canopy characteristic determining the drag exerted on the flow area reduces local velocities (Bouteiller & Venditti, 2015). For example, Nepf & Vivoni, (2000) observed that more drag is generated per unit of the frontal vegetated area for branched leaves than streamlined leaves. Therefore, the influence of macrophytes on stream flow is described by the momentum absorption area (blockage), often characterised by average leaf surface area. Vegetation drag is major contribution to total flow resistance (Tanino & Nepf, 2009; Wu & He, 2009) and as such determining the appropriate representation of drag is a key parameter for modelling approaches (Sun et al., 2010). Despite this, a universal description of drag induced by patch

reconfiguration and flexibility does not exist despite ongoing experimental work (Luhar & Nepf, 2011). Vegetation exhibits a complex boundary between vegetated and non-vegetated flow regions, however representing the local complexities of vegetation is not necessary at large-scale reach models and as such spatial-averaging if often used to represent biomass (Tsujimoto, 1999). The majority of research characterising vegetation uses bulk form approaches, including drag force estimation (Tinoco & Coco, 2018) implemented as drag coefficients at the bottom boundary (Medeiros et al., 2012). A common approach to modelling channel flow are finite element methods, which paramterise drag by applying head losses representative of roughness elements to layers of a finite-element mesh (Kim & Choi, 2009) alongside an appropriate turbulence closure scheme. The aforementioned vagaries surrounding the selection of appropriate resistance or drag coefficients frequently means that models require calibration: in order to improve model accuracy, drag coefficients, for example, are incrementally adjusted until the differences between modelled and observed data are at a minimum. In open channel flows a considerable amount of the total fluid force interacts with vegetation. The values for drag coefficients are thus frequently used as fitting parameters for numerical models (Kothayari et al., 2009; Mulahasan & Stoesser, 2017) and often obtained from simple empirical models developed from laboratory experiments of cylindrical arrays (for example: Tanino & Nepf (2008); Kothyari et al., (2009); Cheng (2013)). Generally, the resulting calibrated roughness coefficient is considered acceptable when its value is within a range reported in the literature (Medeiros et al., 2012) whereby the roughness coefficient is adjusted until the differences between modelled and observed water levels are minimum (Medeiros et al., 2012). However, the need for accurate representation of real-world phenomena often necessitates field observations, which can be limited by the sampling approach taken. For example, floodplain vegetation can be parameterised using remote sensing technology given that the biomass is short: Mason et al., (2003) mention that vegetative height can be estimated given that vegetative height is below 1.2m and attempted to use vegetation height data taken using LiDAR to estimate nodal friction factors for finite element approaches. However, considerable uncertainty exists over whether their approach was appropriate for distinguishing between submergent and emergent vegetation under different flow conditions. Studies have also attempted to

directly measure coefficients *in situ*, such as measuring the soil grain size distribution and the density of floodplain trees (Petryk & Bosmajian, 1975), microtopographic variation (Strelkoff et al., 2000), and channel biomass per square meter of a channel (Doncker et al., 2009). However, a high resolution parametrisation of local roughness factors are resource-expensive and not necessary for representing larger-scale processes, and thus roughness is frequently represented using coarse characterisation through spatial averaging (Järvelä, 2002; Tanino & Nepf, 2009): individual roughness elements are idealised, with the average specifications applied to the local region. The result is a reduction in the model complexity that represents roughness characteristics by using the same resistance factor. Drag forces are commonly quantified by including an additional drag force sink term into the Navier-Stokes momentum equations (Wilson et al., 2006). This method seeks to capture the effect of both form drag and the effect of surface resistances, and has been successfully applied to represent vegetation-flow interactions (for example: Lopez and Garcia, 2001; Choi and Kang, 2004; Rameshwaran et al., 2006).

## 2.9. Summary

Spatially distributed patches of vegetation are common within lowland river systems, exhibiting complex 3D morphology which exert a seasonally dependant control of local flow (Section 2.1). Climate change is expected to alter the occurrence of peak vegetative biomass in rivers to occur later within the year, whilst potentially intensifying extreme precipitation events during autumnal and winter months, consequentially creating an overlap between greater vegetative flow control and higher river flows (Section 2.2). Previous research has typically assumed vegetation as idealised simplifications in laboratory and numerical studies (Section 2.3) and has illustrated how changes to patch layout, channel distribution, and vegetation morphology throughout the water column depth considerably affects local flow depth (Section 2.4) by altering the path of flow conveyance within the channel (Section 2.5), the 3D velocity profile (Section 2.6), and the turbulence profile (Section 2.7). Numerical models have attempted to incorporate these effects by parameterising vegetation using roughness parameters and additional drag terms, and recent progress has highlighted double-averaging procedures as an effective method for representing vegetation ecohydraulics (Section 2.8).

# Chapter 3 | Description of the data and field site.

## 3.1. Introduction

This chapter considers the research site chosen for this study including a description of the site proper and its geographical context, and the data measured in-situ used to generate the 3D mesh, validate the model, and parameterise vegetation. The physical characteristics of the research site are described along with the available data collected by the UK Centre for Ecology and Hydrology (UKCEH) between 2001 and 2003. The data described in this chapter, provided by UKCEH and otherwise, are described in Table 3.1.

Table 3.2. Summary of the data used in this study, including literature sources for further reading.

| Data description | Data type | Date taken | Source | Relevant literature |
|---|---|---|---|---|
| Channel topography | Quantitative, continuous | February 2003 | UKCEH | Naden et al., (2006) |
| Spatially averaged gravel-bed samples | Quantitative, continuous | February 2003 | UKCEH | Rameshwaran & Naden (2012) |
| Vegetation patch distribution | Quantitative, continuous | May 2001; September 2001 | UKCEH | Naden et al., (2006) |
| Flow profiles for streamwise velocity, vertical velocity, and turbulent kinetic energy | Quantitative, continuous | May 2001; September 2001; February 2003 | UKCEH | Naden et al., (2006) |
| Water surface profiles | Quantitative, continuous | | UKCEH | Naden et al., (2006) |

| | | | | |
|---|---|---|---|---|
| Outlet/Inlet parameters | Quantitative, continuous | January, 2017 | NRFA | |
| River Blackwater Hydrometrics | Quantitative, continuous | January, 2017 | NRFA | |

## 3.2. Field site: River Blackwater, Hampshire, UK

The River Blackwater was chosen as the study site for this project, and was considered a suitable reach due to three reasons: firstly, previous research has provided historical data describing the local channel flow hydraulics and seasonal macrophyte distribution. The River Blackwater has been engineered as a two-staged channel, allowing for the study of overland flow behaviour during berm inundation. Secondly, the Blackwater has a known history of flooding with a flow regime described as “flashy” (Gunawan et al., 2008). Such a regime is useful for investigating the behavior of vegetation-flow interaction during peak flow events; it is necessary to consider flow behavior whilst the berm is inundated and how the flow is consequently influenced by changes to in-stream vegetation. Third, the river exhibits characteristics typical for many chalk rivers and is inhabited by aquatic vegetation common throughout the UK, as such the Blackwater can be considered as broadly representative of vegetated, natural chalk rivers. This section will expand on the three points above, detailing the Blackwater in relation to its topographic and hydrological context as well as its vegetation populations.

The River Blackwater is a small chalk river with a catchment area of 35.5km$^2$, the location and catchment topography of which is shown in Figure 3.1. The reach is presented within the broader context of its catchment area in Figure 3.2. The research site constitutes a 140 meter reach with an average width of 7.22m (Figure 4.3). The reach is located near Farnborough, Hampshire, UK and is immediately upstream of the Farnborough river gauge.

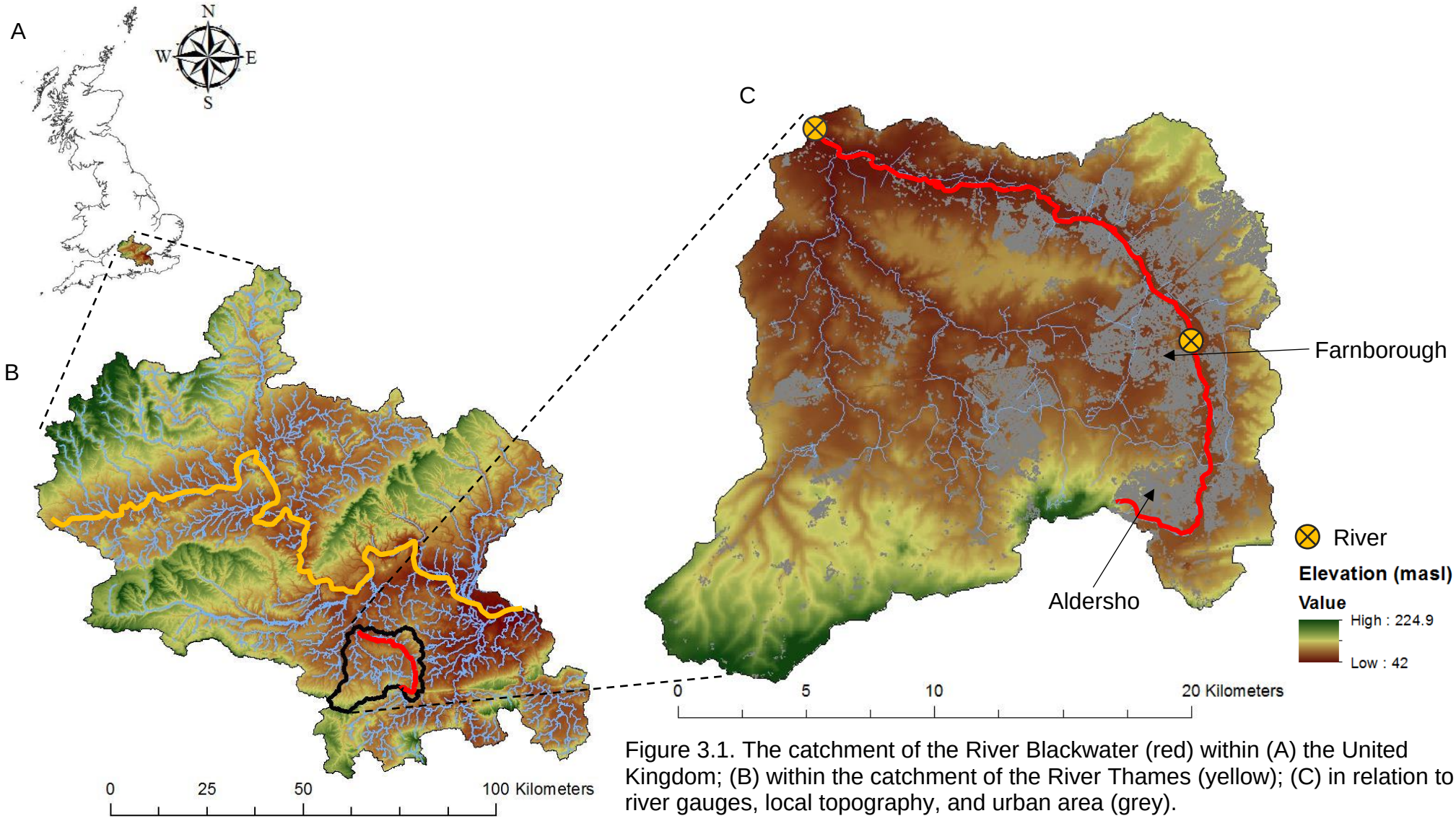


Figure 3.1. The catchment of the River Blackwater (red) within (A) the United Kingdom; (B) within the catchment of the River Thames (yellow); (C) in relation to river gauges, local topography, and urban area (grey).

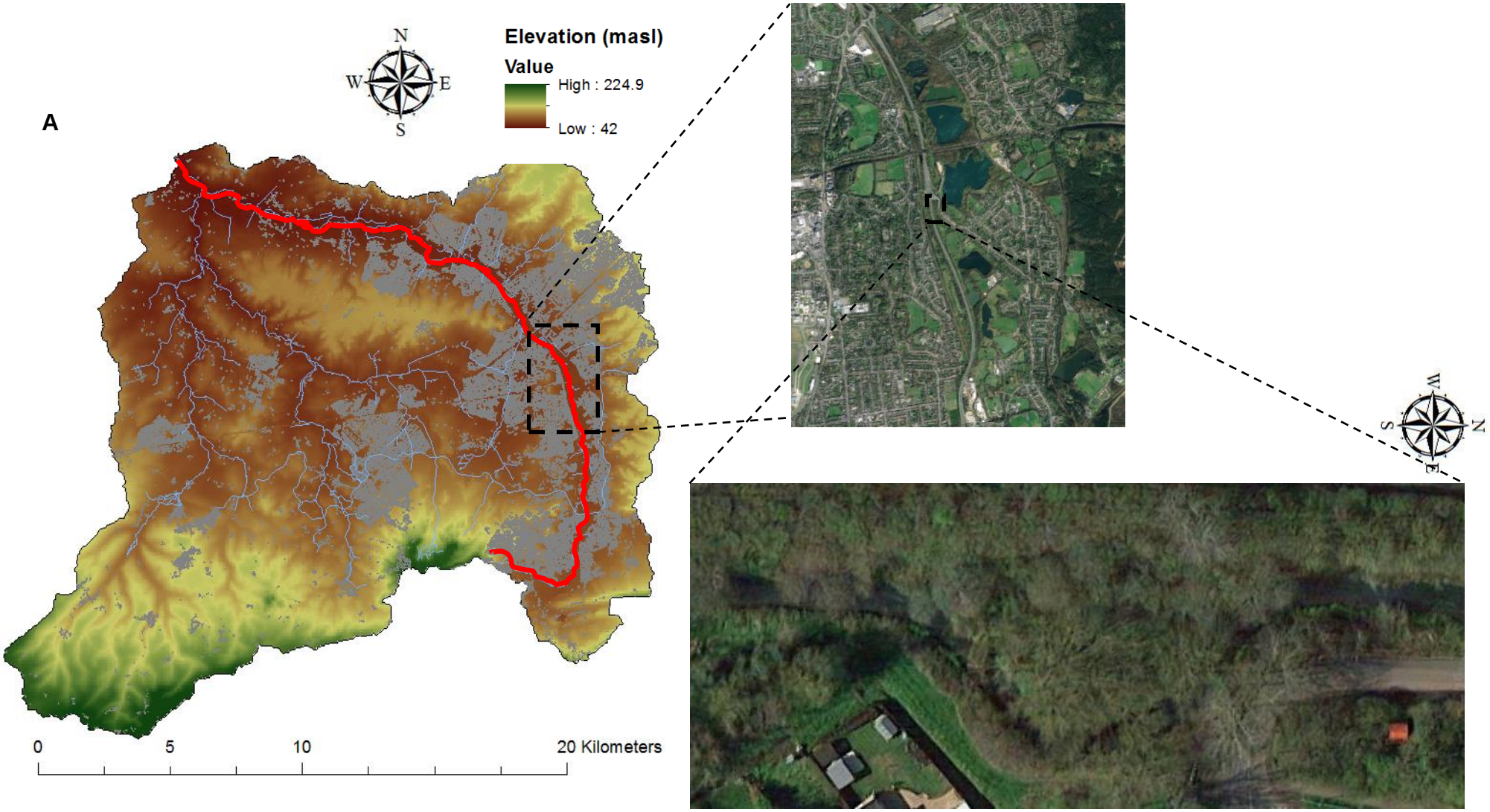


Figure 3.2. The location of the study's reach within (A) catchment of the River Blackwater (red); (B) within the town of Farnborough; (C) the reach itself (C).

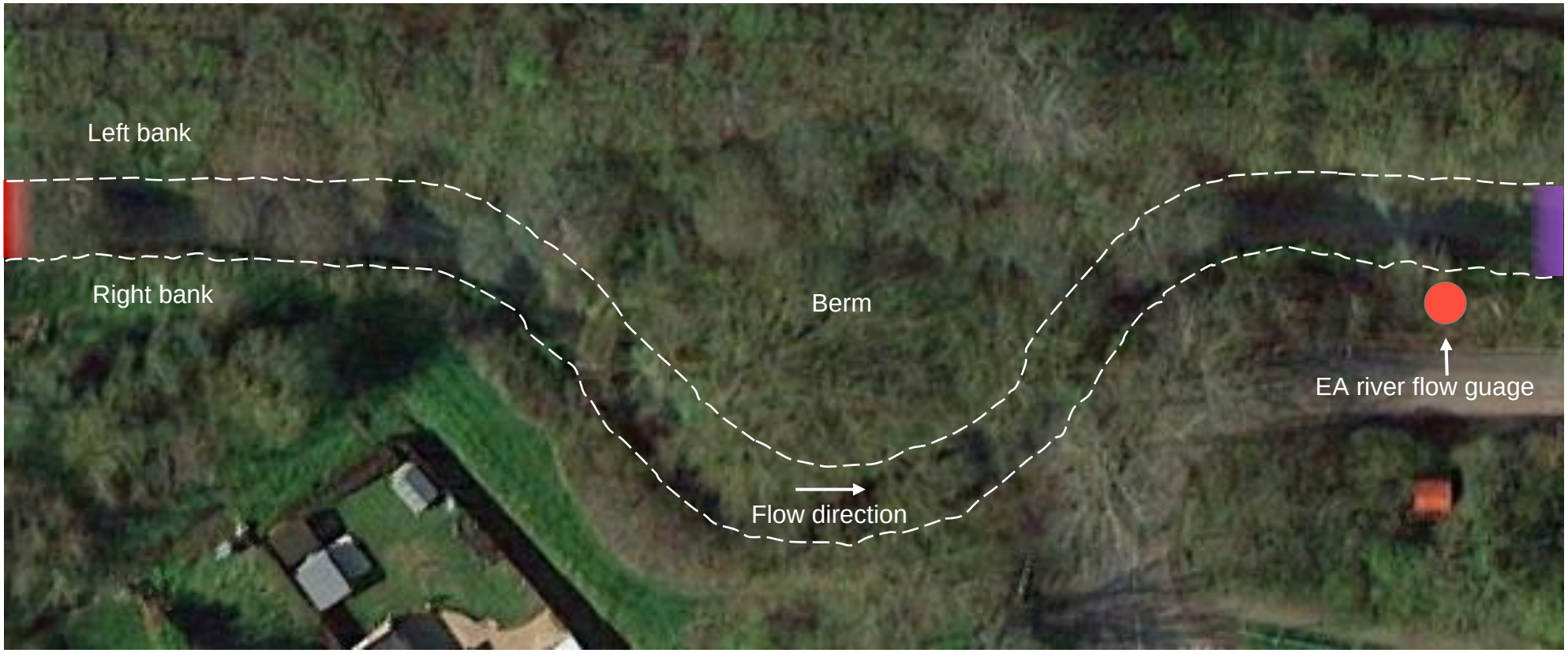


Figure 3.3. The River Blackwater: the dashed line describes the main channel banks otherwise obscured by riparian vegetation. The red zone indicates the flow inlet and the purple zone indicates the outlet. The location of the Environment Agency river guage is identified by the red circle.

### 3.2.1. Catchment Hydrology

The River Blackwater is a typical of lowland eutrophic chalk rivers found in the South-West of England. The Blackwater rises in Rowhill Nature Reserve, near Farnham Hampshire and is a tributary of the River Loddon which it joins near Swallowfield, Berkshire. The River Loddon is itself a tributary of the River Thames. The river is known to be influenced by a high phosphorus content stemming from treated sewage effluent and urban runoff (Rameshwaran and Naden, 2006). The resulting high nutrient levels encourage significant vegetation growth which has been shown to cause small diurnal changes in baseflow of less than $0.1m^3/s$ at another reach downstream (Sellin & Van Beesten, 2004). Upstream of the reach the Blackwater is heavily urbanized which contributes to increased overland flow, resulting in a hydrological response described as 'flashy'; historical records indicate that on average two flood events occur per year (Gunawan et al., 2008). An ultrasonic gauging station operated by the Environment Agency (EA) is located at the end of the reach, providing daily values for flow depth and discharge from 1996. Flow statistics for the period 1996-2016 are given in Table 3.2. The base flow index (BFI) is a ratio of long-term mean base flow to total discharge (Smakhtin, 2001) and, conceptually, can be thought as the proportion of rivet flow derived from stored water, where a higher value indicates a greater contribution from groundwater (Beck et al., 2013). The River Blackwater has a BFI of 0.69, which is relatively low compared to the mean BFI value of 0.83 for chalk-based river systems in the UK (Sear, Armitage, & Dawson, 1999). A lower BFI indicates some contribution from groundwater storage in the river's discharge. However, the Blackwater's BFI is similar to the mean BFI value of 0.65 reported for the Thames catchment area (Bloomfield & Griffiths, 2009). The mean annual rainfall for the region is 717mm (NRFA, 2012) which is below the UK national average of 1132.6mm for the period 1981-2010 (Met Office, 2017).

Table 3.2. Flow statistics for the River Blackwater, taken from the Farnborough gauging station (station number: 39123) provided by the National River Flow Archive (NRFA, 2017) for the period 1996-2016

| Mean flow ($m^3/s$) | $Q_{10}$ Discharge ($m^3/s$) | $Q_{95}$ Discharge ($m^3/s$) | Base Flow Index |
|---|---|---|---|
| 0.53 | 0.95 | 0.185 | 0.69 |

The flow rating curve for the river is presented in Figure 3.4. Higher discharges were common in the winter months between December - March compared to the summer months from June-September. This is illustrated in Table 3.3, which describes the seasonal flow percentiles for the flow duration curve. Flow percentiles are described by the $Q_{10}$ percentile, also known as the 90% percentile flow, where the flow rate equaled or exceeded 10% the flow rate recorded within the given time period, and the $Q_{95}$ percentile, also known as the 5% percentile flow, where the flow rate equaled or exceeded 95% for the time period. The $Q_{10}$ percentile is noticeably higher in the winter by 0.12 $m^3/s$, with discharge exceeding 0.42 $m^3/s$ for 10% of the time compared to 0.29 $m^3/s$ in the summer. The $Q_{10}$ percentile provides insight into the occurrence of high flow conditions, whilst the $Q_{95}$ percentile describes low flow conditions. The catchment has a higher variability in the winter, with a difference 0.91 $m^3/s$ between $Q_{10}$ and $Q_{95}$ compared to a difference of 0.09$m^3/s$ between the same percentiles in the summer suggesting that the Blackwater is flashier in the winter.

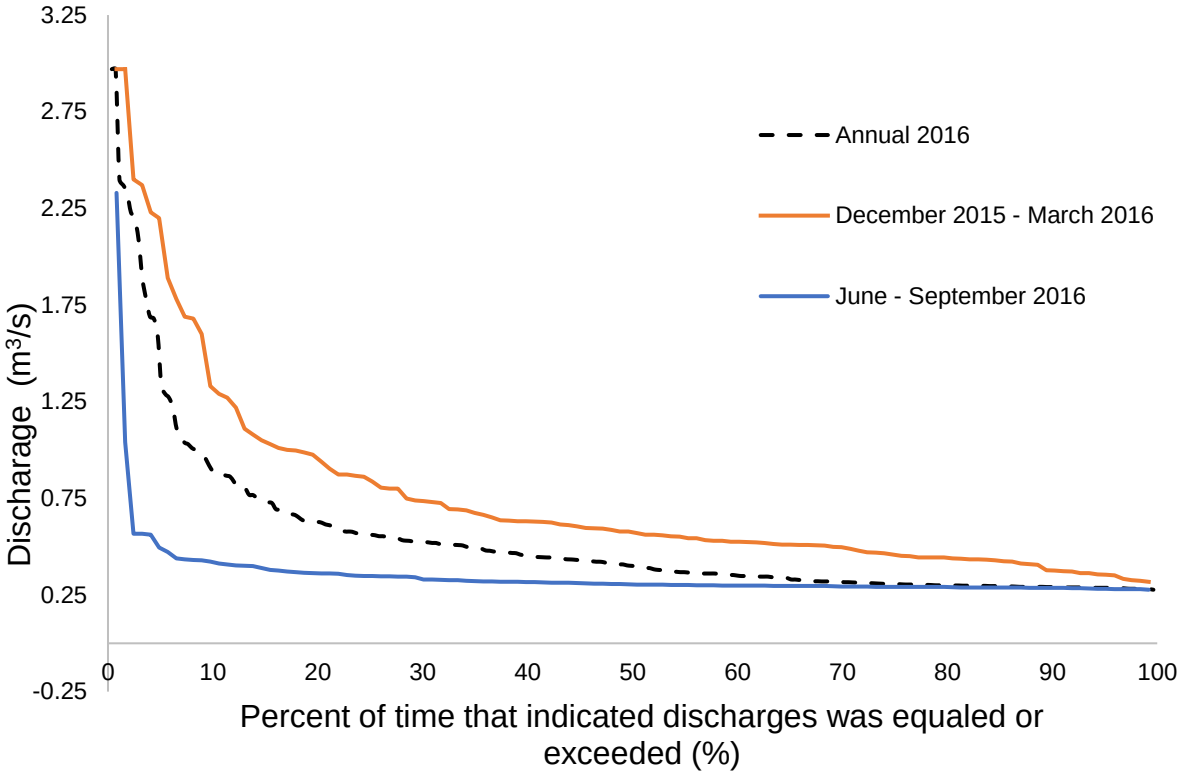


Figure 3.4. Flow duration curve for the River Blackwater at Farnborough

Table 3.3. Mean daily discharge values for the Q10 (90th percentile) and Q95 (5th percentile) flows.

| | $Q_{10}$ Discharge ($m^3/s$) | $Q_{95}$ Discharge ($m^3/s$) |
|---|---|---|
| Summer | 0.287 | 0.377 |
| Winter | 0.422 | 1.33 |

River stage and discharge data were provided by the National River Flow Archive (NRFA) by the ultrasonic river gauge at Farnborough, and was the same dataset used to calculate the above flow statistics. The river gauge is located immediately downstream of the reach. The river gauge monitors daily river flow for a catchment area of 35.5 $km^2$, with a maximum altitude of 186.6mAOD and a minimum altitude of 63.5mAOD. The flow data covers the period from the gauge's inception to the latest available data at the time of writing: October 1996 – September 2016. The data is considered as largely reliable however the NRFA indicates that flows can be overestimated when in the low and medium range, and earlier data between 1996 –

1998 could potentially be confounded (NRFA, 2017). Some gaps exist in the data however most are small and cover: one day in September 2005, one day in April 2012, and six days from 29/11/2007 to 04/12/2007. A considerable gap in the flow data is present for both 2008 and 2009. A flow duration curve was fitted to identify the peak and lowest discharge for 2016, the latest full year to be recorded. The duration curve is seen in Figure 3.5. The peak discharge was found to be 2.97$m^3$/s at 1.62% of the recorded flow.

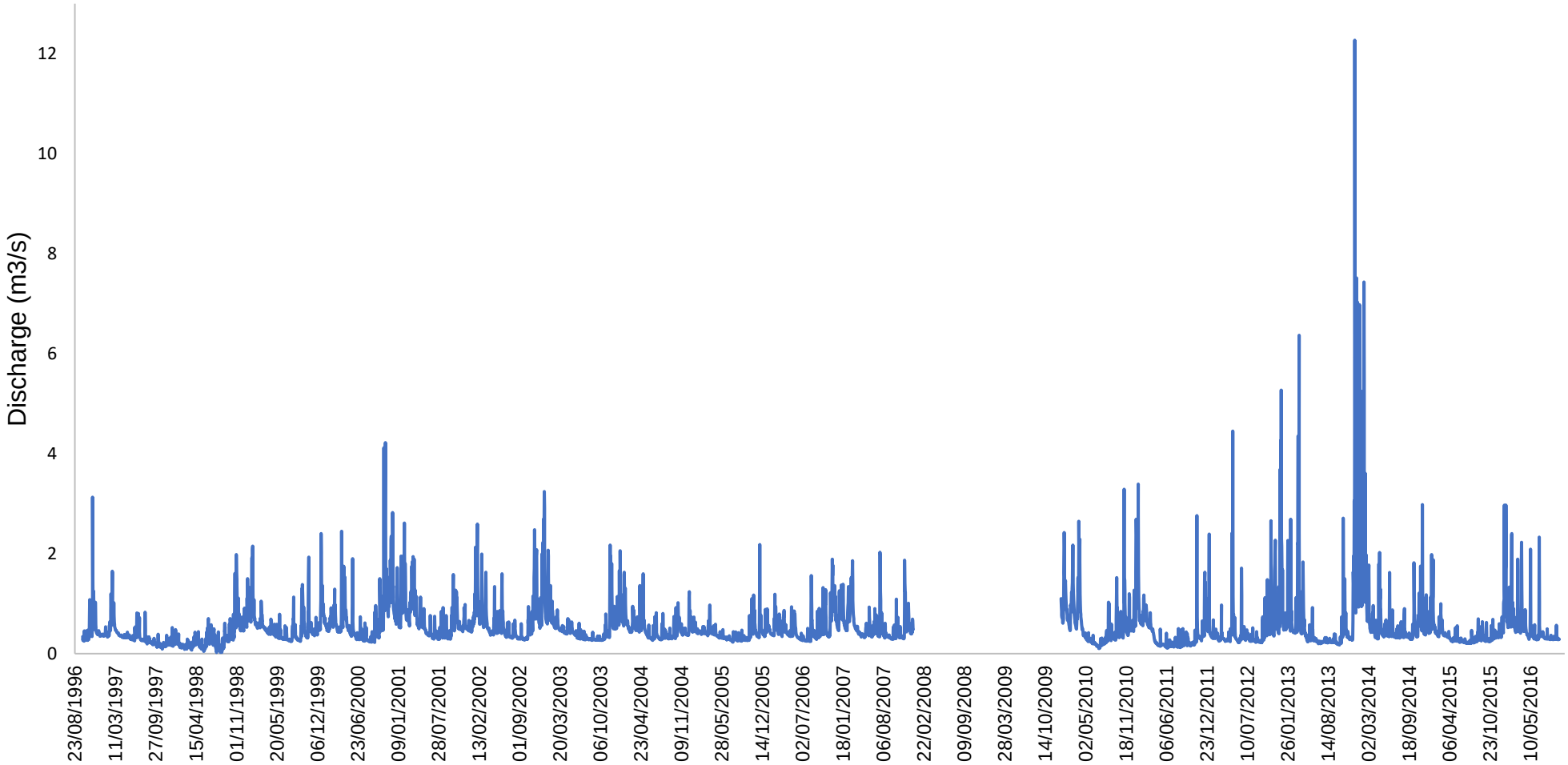


Figure 3.5. Daily discharge for the River Blackwater at Farnborough, 1996 - 2016

Previous research has identified macrophytes as significantly influencing local hydraulics, for example Sellin and Van Beesten (2004) used continuous flow data between 1998-2002 to model flow processes for another reach upstream of this studies' field site. They found that the estimated resistance coefficients, computed using Manning's law, varied annually and seasonally as a result of changes to vegetation growth. For a bankfull scenario with a depth of 0.75m, the summer months of May to September exhibited high coefficient values within a range of $n$ = 0.15-0.25, whilst the winter months of September to January had a low, less variable range of $n$ = 0.05 ±0.02. Results suggested that both aquatic, emergent, and floodplain vegetation were dominant controls of the values of the channel resistance coefficient (Sellin and van Beesten, 2004).

Naden et al. (2006) investigated the same reach used in this study, measuring flow variables at five different cross-sections for different periods of vegetation growth throughout 2001. They found that resistance varied monthly, calculating values of $n = 0.053 – 0.121$ for May 2001, and $n = 0.124 – 0.295$ for September 2001 across all channel cross-sections. This correlated with a lower vegetation count in May at the beginning of the summer growth period, and a higher vegetation count in September at the end of the summer growth period. They discovered that the largest influence affecting the Manning's $n$ value were vegetation patches situated in the centre of the channel during the summer. Monthly variations were also noted for other flow descriptors, with surface slope changing from 0.00084m in May to 0.00089 in September, and decreasing to 0.00083m in February 2003. In-stream vegetation was found to influence local velocities: in September high velocities were measured near the bed, thought to be a result of flow being accelerated around individual plant stems, whilst velocity decreased in the water column above the bed as flow interacted with plant matter. Low depth-mean velocities were measured behind plant patches, suggesting the formation of wake zones behind the patches as flow was redirected and accelerated between patches. Higher turbulence intensities were calculated for vegetated zones in September than in May, indicating an increase in the production of eddies associated with an increase in macrophytes (Naden et al., 2006).

This historical background allows for the model to be parameterized based on the distributions and abundances of natural-occurring vegetation. In addition, the River Blackwater is a focus for research by UKCEH and the EA, with the latter able to provide daily depth and discharge data from a Sarasota electromagnetic flow gauge just downstream of the reach (PEER, 2015).

### 3.2.2. Geology and soil characteristics

The geology of the catchment area is mostly composed of Bracklesham Beds Sandstone with patches of Barton Sands (Clarke et al, 2007). The dominant soil type is a loamy alluvium with naturally high groundwater identified as type 841b (Hampshire County Council, 2010) described by the National Soil Resource Institute (NSRI) as “coarse and fine loamy permeable soils mainly over gravel variably affected by groundwater” (NSRI, 2007).

### 3.2.3. Description of reach vegetation

The reach is heavily populated by macrophytes, with vegetation pronounced in the channel during the summer months (Gunawan et al., 2008). Macrophyte abundance varies seasonally, with previous research estimating macrophytes occupied 18% of the channel area in May 2001, and 27% of the channel in September 2001 (Rameshwaran and Naden, 2006). Predominant species are the *Sparganium* species *S. erectum* and *S. emersum*, as depicted in Figures 3.6 and 3.7, respectively. *S. erectum* is a linear emergent macrophyte and is the most populous species of this type in the UK (O’Hare et al., 2010) and is notable for its stem rigidity which provides high resistance to uprooting and maintains a high flow resistance (Liffen et al., 2011). Both species are typical of eutrophic rivers. Previous research in the Blackwater identified seasonal changes in *S. erectum* and *S. emersum* from May to September, with little changes apparent to *S. erectum* patches but a clear dominant change in the areal extent of *S. emersum* patches (Rameshwaran and Naden, 2006).

Figure 3.6: *Sparganium erectum* (branched bur-reed). Source: IUCN Red List. Photographer: Richard Lansdown.

Figure 3.7: *Sparganium emersum* (branched bur-reed), image foreground. Source: IUCN Red List. Photographer: Richard Lansdown.

## 3.3. Data description

### 3.3.1 Introduction

Channel measurements of topography, flow, and vegetation distributions were provided by UKCEH. Measurements were taken in May and September 2001, and February 2003. The topographic data consists of two datasets: profiles of the cross-sectional topography of the channel and the channel-bed topography, and the measured surface area of the gravel-bed. The flow data consists of measured water surface profiles at the banks, and profiles of flow variables for one cross-section for the non-vegetated February measurement period, and for five cross-sections for both the vegetated May and September periods.

### 3.3.2 Topographic data

Data describing the projected area and surface area of the riverbed gravel was used to parameterise the model bed roughness. The gravel-area data was collected using a physical bed profiler composed of 26 pointed 2.5mm diameter rods and used to measure the local bed elevation. The rods were separate by 10mm within a 0.25mx0.25m frame. The rod separation determines the resolution of the data, therefore the physical profiler had a 10mm resolution over a 0.0625m$^2$ footprint. The bed topography was measured using randomised sampling at five locations within the reach, and which measured vertically at a layer-by-layer basis for four layers separated by 10mm from the riverbed. A detailed report of the above approach is detailed in Rameshwaran & Naden (2012). The physical parameters for the reach bed, such as projected area and surface area, were then statistically derived from the sampled bed data. The averaged properties of the sampled data are presented in Table 3.4.

Table 3.4. Average properties of sampled areas of gravel bed data

| Layer | Height (mm) | Porosity $\phi$ | Frontal projected area $A_p$ ($m^2/m^3$) | Frontal projected area $A_{py}$ ($m^2/m^3$) | Surface area $A_s$ ($m^2/m^3$) |
|---|---|---|---|---|---|
| 1 | 0 -10 | 0.1338 | 1.6546 | 1.9889 | 13.824 |
| 2 | 10 - 20 | 0.5982 | 12.0348 | 15.0484 | 77.5191 |
| 3 | 20 - 30 | 0.9221 | 12.3361 | 14.8194 | 76.6161 |
| 4 | 30 - 40 | 0.9922 | 2.133 | 2.4954 | 15.333 |

At reach-scale the topographic data was used to represent the 3D channel geometry within a finite-element mesh. A topographic survey at the banks was undertaken using a Zeiss Elta R55 Total Station. The channel was surveyed by measuring the local elevation at 146 cross-sectional profiles along the 140m reach (Figure 3.8). The channel was found to have an average width of 5.9m, with the narrowest section located at the meander apex at 4.57m and the widest section located downstream of the apex in the straight portion of the channel at 7.95m. Facing downstream, the left bank including the berm had an average bank height of 1.80m. The berm itself had an average bank height of 1.08m. The right bank had an average bank height of 2.02m**.** The cross-sectional profile of the reach can be seen in Figure 3.8. The reach is composed of a single meander with a thalweg slope of -0.00063m and a sinuosity ratio of 1.24. Numerous asperities are found in the reach which can be observed in the irregular, staccato changes in channel elevation. Large concentrations of asperities can be seen in the straight upstream of the meander (Fig 3.8).

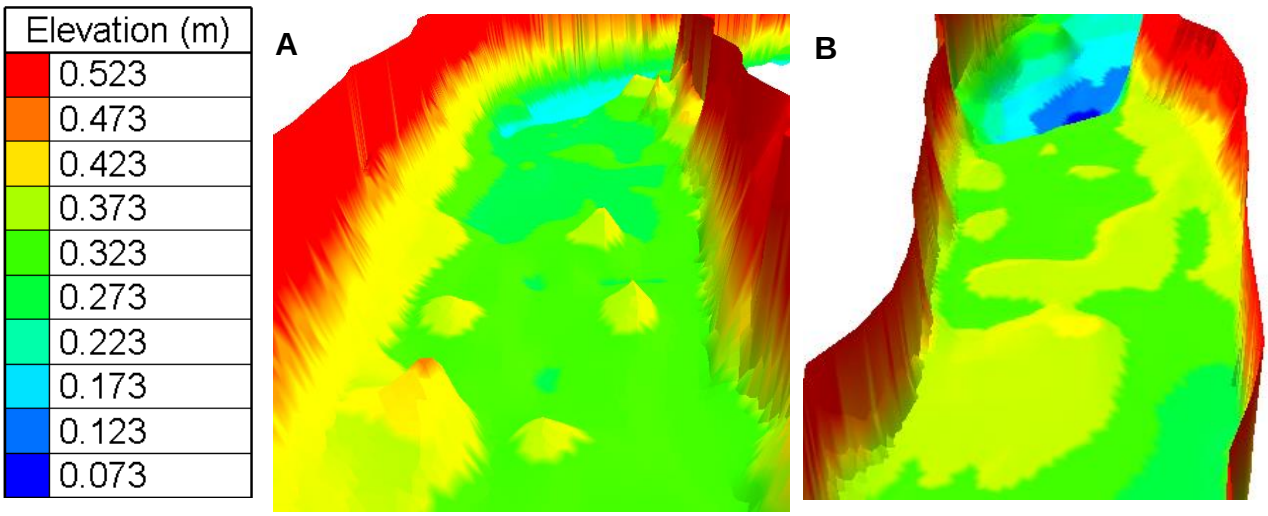


Figure 3.9. Asperities at: A) the section preceding the initial meander bend, facing downstream; B) the meander bend downstream of the apex, facing upstream. In both images the pools previously identified in Fig. 3.6 can be seen in the background. An interpolated surface was used for illustrative purposes.

Figure. 3.8 also shows large depressions in the channel bed, or pools, which increase in size with distance downstream. The largest pool is situated downstream of the meander and has the lowest bed elevation at 0.068m. The pools are responsible for sudden changes in bed elevation with the steepest slope located between the meander apex and the halfway point of the second meander limb (Fig. 3.9; inset D) with a mean difference in elevation of 0.055m.

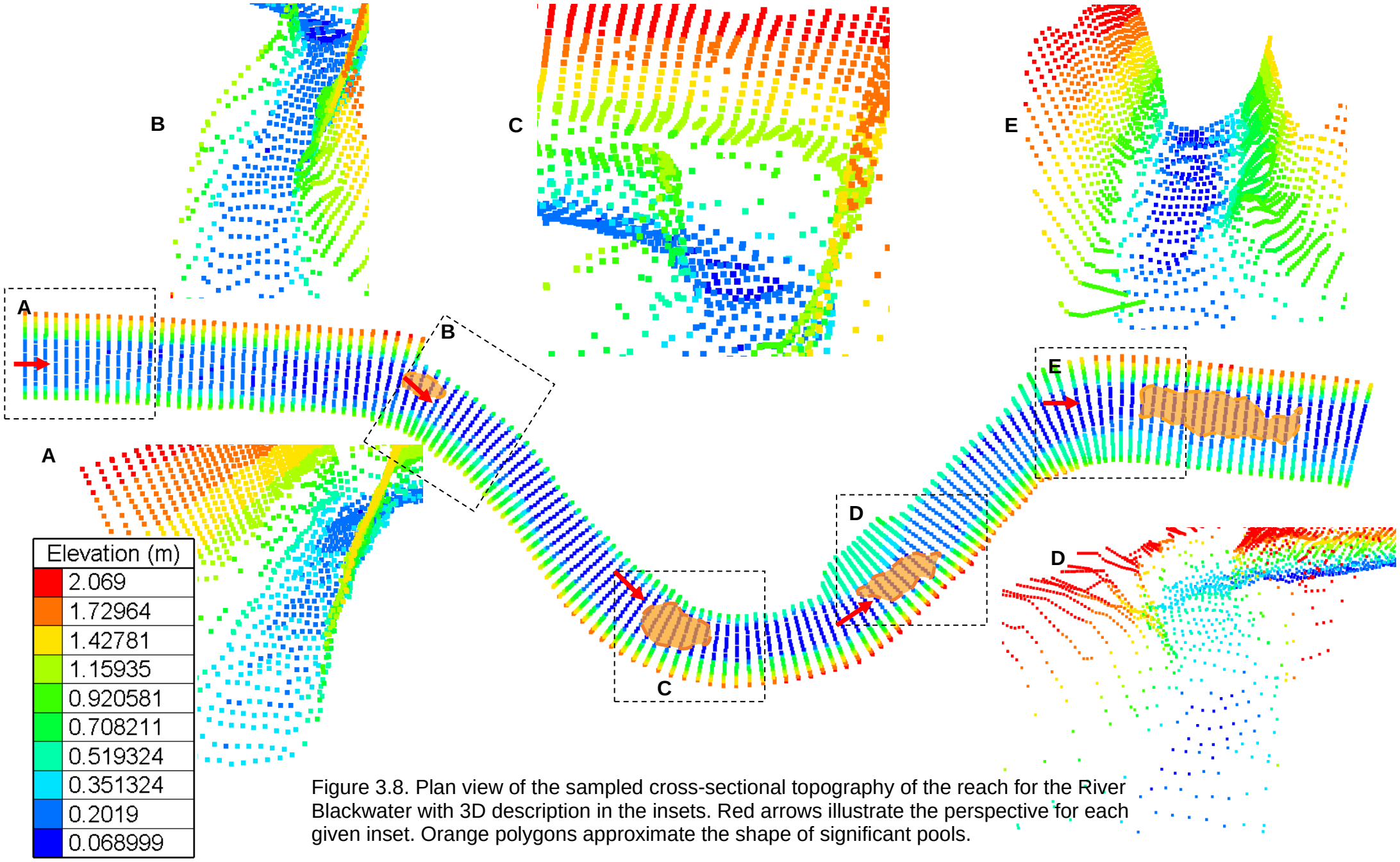


Figure 3.8. Plan view of the sampled cross-sectional topography of the reach for the River Blackwater with 3D description in the insets. Red arrows illustrate the perspective for each given inset. Orange polygons approximate the shape of significant pools.

### 3.3.3 Vegetation data

A vegetation survey was conducted in May and early September 2001 to capture the changing distribution of macrophyte patches and biomass abundance at the beginning and end of the growing season. The survey used the aforementioned Total Station to record patch location, size, and shape. The in May 2001 was achieved by measuring points around each patch's perimeter. The increased abundance of vegetation for September introduced difficulties in measuring the patches without creating disturbance, therefore a minimum of the upstream, downstream, and lateral extent of each patch was measured. The distribution of vegetation patches of the dominant species for May and September can be seen in Figure 3.10.

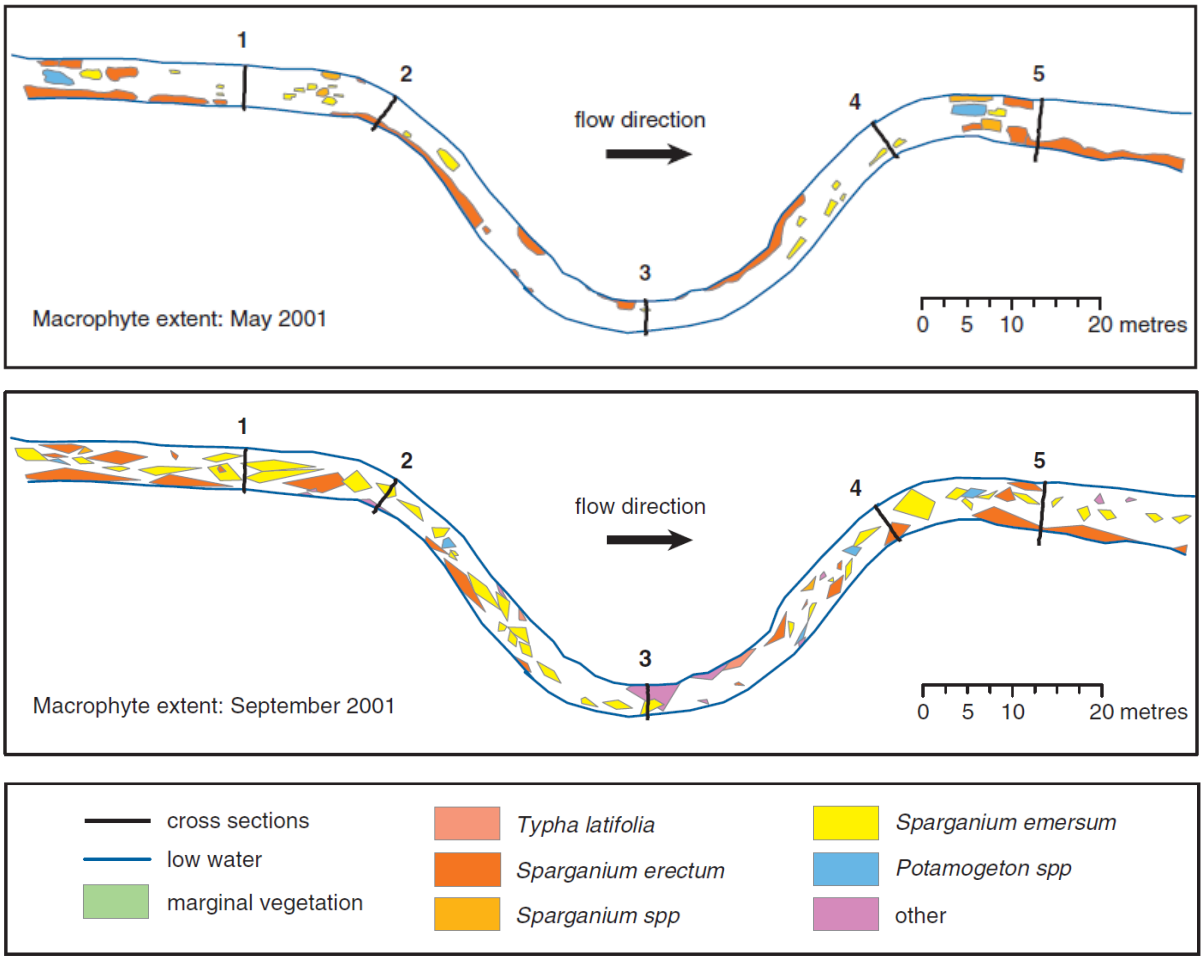


Figure 3.10. Plan view of the distribution of vegetation patches by species for the River Blackwater during the May and September 2001 sampling periods. The five cross-sections used to measure flow data are noted on both, including the apex cross-section noted by number three. Source: Naden et al., 2006.

The channel is dominated by *Sparganium* species, with *S. erectum* shown to colonise much of the near-bank area and the inside of the meander bend, whilst *S. emersum* has colonised the central area of the channel during both measurement periods. A photographic assessment of the site in May 2016 reveals that the channel still exhibits a similar distribution of patches (Fig 3.11). Patches of *S. erectum* are shown to heavily colonise the first and second inflections of the meander, whilst the apex remains relatively sparse in comparison. A greater variety of species was evident in September: a greater abundance of *Potamogeton natans* in the channel centre at the first inflection of the meander bend. In addition, a large patch of *Urtica dioica* (stinging nettles) was extant at the inner bank of the meander apex.

The average surface area was recorded for the dominant *S. emersum* and *S. erectum* species, shown in Table 3.5. The average surface area is an important for parametrisation of the drag term for vegetation patches (see: Chapter 4.4).

Table 3.5. Averaged surface area of dominant vegetation within the reach

| Vegetation | Surface area ($m^2/m^2$) |
|---|---|
| *Sparganium erectum* | 24.3816 |
| *Sparganium emersum* | 77.6668 |
| *Potamogeton natans* | 27 |


Figure 3.11. Plan view. Site description of the River Blackwater: *S. erectum* are clearly seen colonising the channel centre at the initial and latter stages of the reach. Photos taken: 05/05/2016.

### 3.3.4 Flow data

Data describing the Blackwater's free surface was obtained by measuring the surface elevation at multiple points along the right and left banks. Here the bank position is defined by the observer facing the streamwise direction e.g. the "right bank" is the bank to the right of the observer if they were looking downstream. Measurements of the water surface profiles were taken using the Zeiss Elta R55 Total Station mentioned previously in section 3.4.2. The free surface was measured for both the February 2003 non-vegetated and May 2001 vegetated cases. For the February case 32 points on the right bank and 26 locations on the left bank were used to measure the free surface, whilst the May case used 51 locations on the right banks and 60 locations on the left bank. The locations of the measurements for both cases are shown in Figure 3.12. The free surface profiles both for the September 2003 non-vegetated case and the May 2001 vegetated case are shown in Figure 3.13.

The free surface is notably higher during the February period with a difference at the right bank of 0.82m between the maximum elevations of 0.82 (February) and of 0.746 (May), and at the left bank with a difference of 0.76m between 0.825m (February) and 0.745m (May). The may surface profile also had a shallower slope, with 0.64m and 0.61m found for the left and right banks respectively, compared to 0.73m found for both banks in the February case over a similar distance.

The method used for measuring the flow velocity and turbulence is described in Naden et al. (2006) and summarised here. The profiles were measured at a series of vertical profiles using a 3D Nortek Acoustic Doppler Velocimeter (ADV) which reported velocities at 25Hz. A sampling volume of 0.346cm$^3$ was used using a velocimeter positioned 5.8cm below the instrument which was deployed in the downward-facing mode and held in place using a wading rod. The instrument was positioned horizontally with the aid of a spirit level. A graduating scale was used to position the monitor at heights or 1, 2, 3, 5, 7, 10, 15, and 20cm above the riverbed. Measurements were taken throughout a 3-minute period. Disturbance to the mount was minimised by positioning the wading rod and user downstream of the measured cross-section and no disturbance due to bed instability was reported, however there

was some interference by dead leaves on the surface. In post-processing data with a signal-to-noise ratio (SNR) of less than 15 or a correlation less than 0.5 were removed and replaced using nearest neighbour interpolation. Due to the very little spiking evident data and so a sophisticated de-spiking method was not used. Instead, data points with values greater than the values expected in a Gaussian distribution of the same sample size were removed and replaced using interpolation. For nearly all cases changes in the mean downstream velocity and root mean square were less than 0.0013m/s and 0.006m/s, respectively. The data was deemed to be within values recommended by the literature with the average mean correlation in the data reported as 95.3±3.4% and a mean SNR of 26.3±2.3.

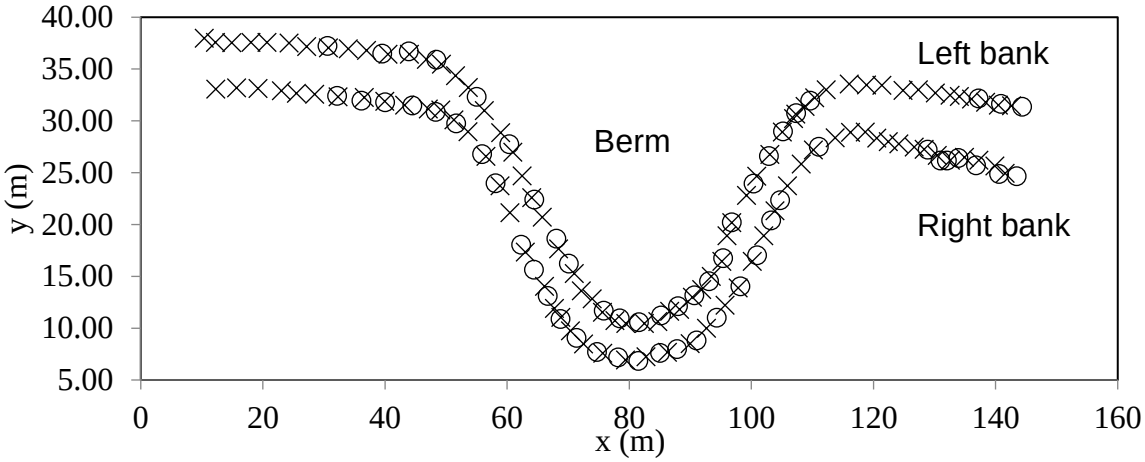


Figure 3.12. Plan ("bird's eye") view of the measurement locations for the free surface data for the February (circles) and May (crosses) periods for the right banks and left banks, respectively.

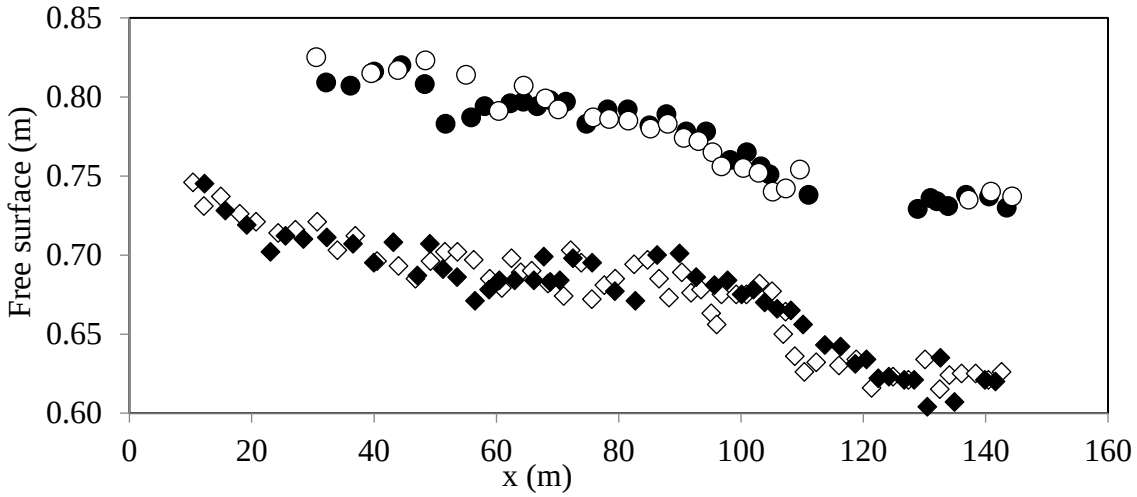


Figure 3.13. Water surface (free surface) data for the February (circles) and May (diamonds) periods, for the right banks (filled) and left banks (clear), respectively.

Measurements were taken at five cross-sections during May 2001, and at a single cross-section at the apex of the channel in February 2003. Flow profiles measured during the May sampling stage were taken at non-vegetated sections of the channel to describe the flow around the plant patches. The flow profiles taken during the February sampling stage represent non-vegetated flow. The apex cross-section was used for flow profile calibration, the measurements of which can be seen in Figure 3.9 at five locations for non-vegetated flow calibration, and in Figure 3.10 at six locations for the May vegetated flow. Flow profiles appear the most well developed in the channel centre, likely due to reduced variation in topographic gradients compared to at the banks. The TKE profiles capture the inflection point at the boundary between the roughness layer and main channel flow within each profile but is most prominent in the channel centre, and less clear at the right bank. The top of the TKE profile at the left bank has been attributed to flow interference by obstacles, such as dead vegetation at the surface (Rameshwaran & Nadan, 2012).

## 3.4. Summary:

This chapter has described the field site which is the focus of this study: the River Blackwater, Hampshire, UK. The river reach represented within the numerical model was introduced alongside its context within the broader local catchment, historical descriptions of river flow, and previous research detailing the distribution and composition of in-stream vegetation. The sampling strategy used to parameterise the model was outlined which provided an overview of the data used for flow profiles and the slope, the gravel-bed and vegetation drag forms, and the seasonal changes to vegetation abundance.

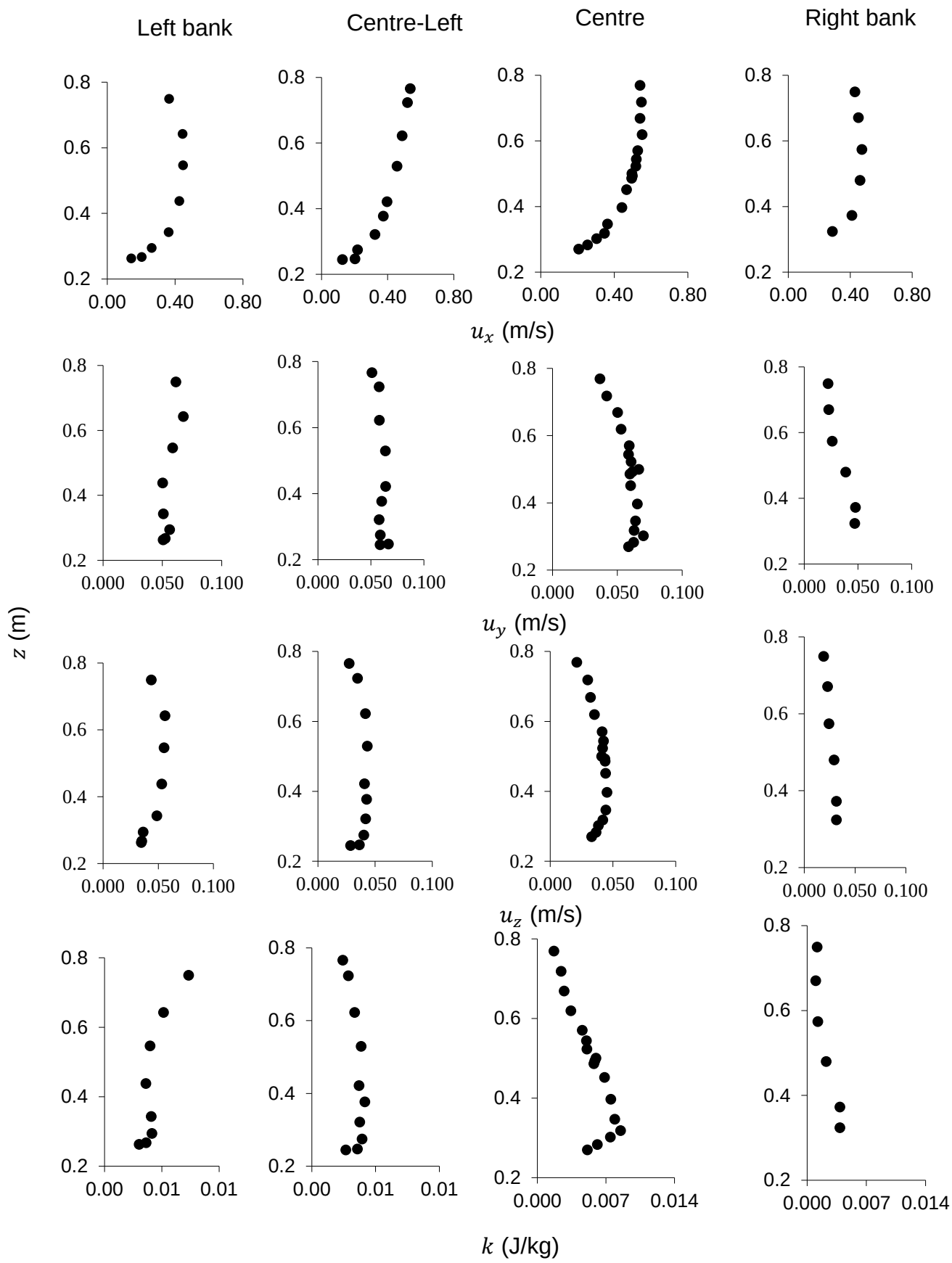


Figure 3.14. Flow profiles taken at four positions across the apex cross-section for the February 2003, non-vegetated case.

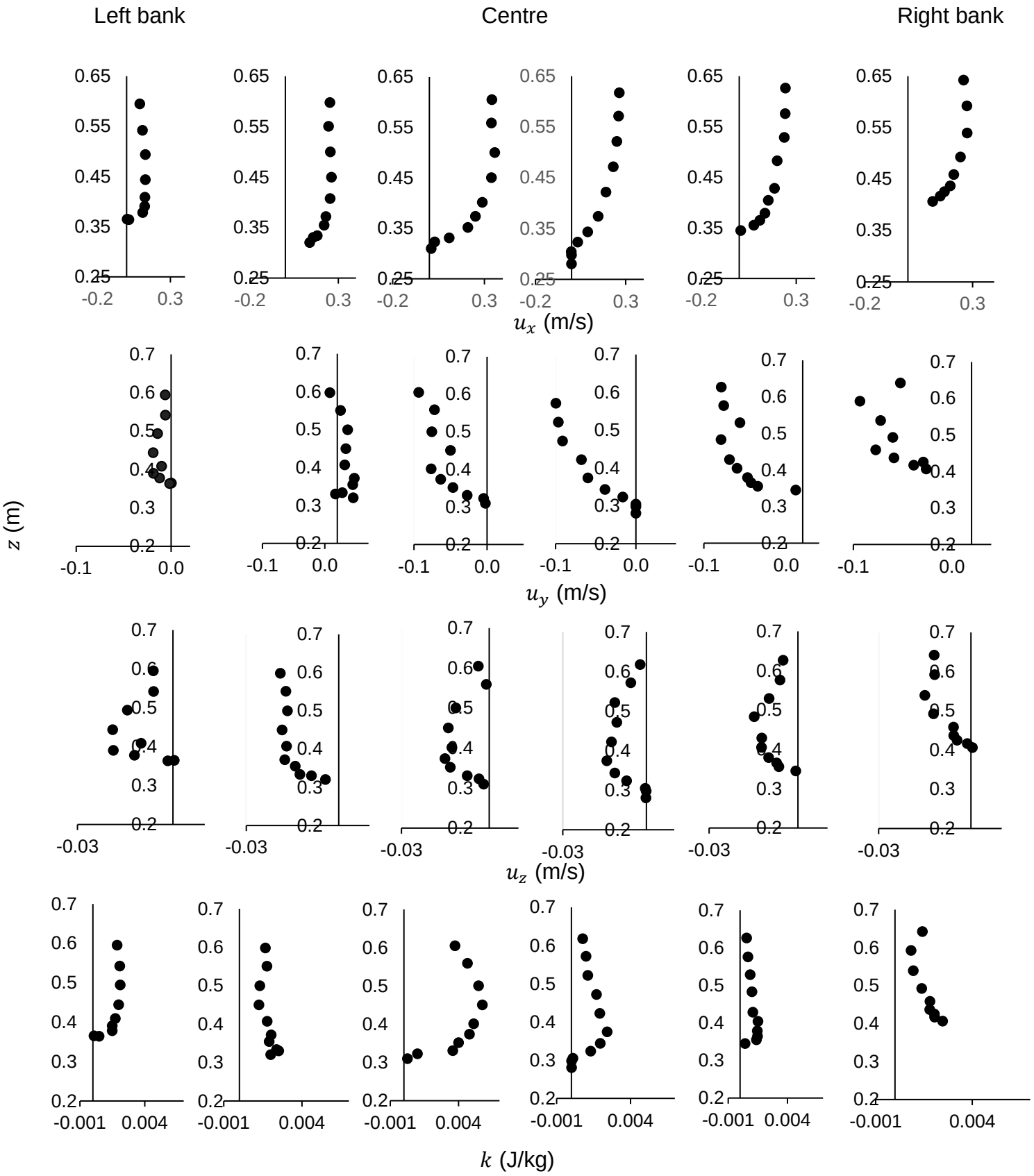


Figure 3.15. Flow profiles taken at four positions across the apex cross-section for the May 2001, vegetated case.

# Chapter 4 | Numerical approach

This chapter introduces the three-dimensional finite element modelling suite used within this study: TELEMAC-3D (Galland, Goutal & Hervouet, 1991; Hervouet, 2007). TELEMAC is an open source tool used for computational fluid dynamics (CFD) within industry and research. The three-dimensional continuity equations and the Reynolds-averaged Navier-Stokes equations (RANS) are solved in combination with a k-ε turbulence closure model. In this chapter the governing hydrodynamic equations are introduced: the RANS equations are outlined in reference to their application within TELEMAC-3D, along with a description of the roughness equations. The principle guiding documentation for TELEMAC-3D can be found in Hervouet (2007).

## 4.1. The TELEMAC-3D Model

### 4.1.1 Flow governing equations

For this study, a 3D hydraulic model is implemented using the CFD solver suite TELEMAC-3D (version 7.0) to solve the RANS and continuity equations. The non-hydrostatic version of the code was used. TELEMAC is a suite of solvers used to simulate free-surface flows, developed by the Laboratoire National d'Hydraulique, Electricitede France (EDF). TELEMAC was chosen for four reasons: firstly, it can effectively model river flow, solving full 3D non-hydrostatic RANS equations with a free surface. Secondly, as a popular tool for modelling flow it is ubiquitous in research and industry, ensuring the project's relevancy within the field. Thirdly, the model has been found to perform efficiently on parallel architectures (Moulinec et al., 2011). Fourthly, as an open-source model it freely allows for the addition of subroutines to specify complex flow phenomena which is required for the integration of vegetation in the flood prediction model.

TELEMAC supports cross-compatibility between its 2D and 3D models. As such, by using the same 2D mesh as a base the equations used within the 2D model are later translated to 3D during different computational steps outlined below (see: 4.3 Solution Algorithm). For further information on TELEMAC's cross-compatibility please refer to the Hervouet (2007). Many of the equations below used by TELEMAC-3D are therefore presented in their 2D form. TELEMAC-3D uses the non-conservative form

of the Navier-Stokes equations for incompressible fluids which are discretised using a finite element algorithm. In their basic form 3D, the continuity and momentum equations are written as:

Conservation of mass:

$$\frac{\partial \rho}{\partial t} + \nabla \cdot (\rho \vec{u}) = 0$$

4.1

Conservation of momentum:

$$\frac{\partial \vec{u}}{\partial t} + \frac{\partial \vec{u}}{\partial x_j} = g_i \frac{1}{\rho} \frac{\partial p}{\partial \vec{x}} + \frac{\partial \rho}{\partial \vec{x}} v \left( \frac{\partial \vec{u}}{\partial \vec{x}} \right)$$

4.2

where $\nabla$ is the del operator for a vector, $\vec{u}$ is the velocity vector whose 3D components are $u$, $v$, and $w$, $\vec{x}$ is the spatial vector in the $x$, $y$, and $z$ directions, t is time, $\rho$ is density of the fluid, $v$ is the fluid kinematic viscosity, $g$ is acceleration due to gravity, and $p$ is the pressure.

Spatial variation in elevation is described by Cartesian coordinates $(x, y, z)$. The numerical domain is limited at the bottom, as described by the equation $z = Z_f(x, y)$, and by the free surface, as described by $z = Z_s(x, y)$. The height of the water column $h$ is equal to $Z_s - Z_f$, as illustrated in Figure. 4.1.

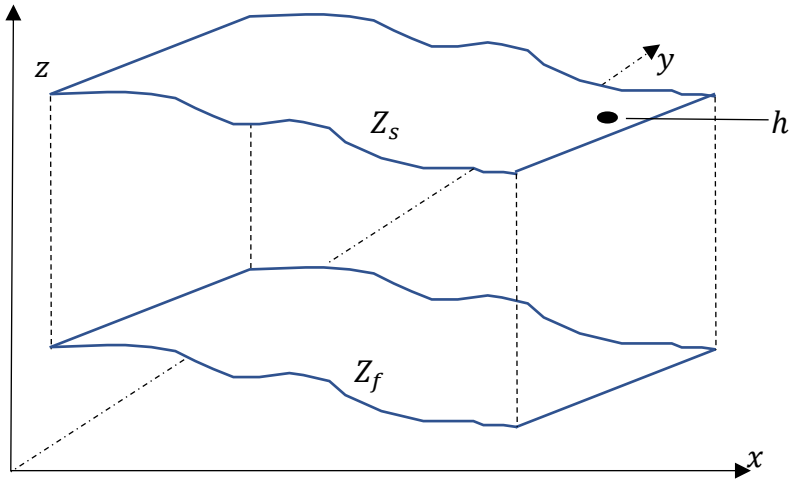


Figure 4.1. Schematic of the numerical domain.

The free surface elevation, or water surface, is updated each time-step at each node. Physically, the free surface can be conceptualised as a particle of water which remains at the surface as time progresses. The particle's placement in 3D space then adjusts in response to the flow solution. The free surface is updated using a fractional step method, in which the flow solution is composed of three steps solving for advection, diffusion, and pressure-continuity. During the third step the water depth is computed by vertically integration using the momentum and continuity equations (Hervouet, 2007). A depth-average continuity equation is then used to compute the final computed depth-averaged velocity, $\vec{U}^{n+1}$. With the depth-averaged velocity and depth computed the position of each node and, finally, the free surface are updated. The depth-averaged velocity is computed using the equation:

$$\frac{\vec{U}^{n+1} - \vec{\tilde{U}}}{\Delta t} = -\frac{1}{p}\overrightarrow{grad}(p_d)$$

4.3

Where $\vec{\tilde{U}}$ is the vector of components $(\tilde{u}, \tilde{v}, \tilde{w})$ and is $p_d$ is the dynamic pressure.

Depth and free surface elevation are related, as shown in $D = Z_s - Z_f$. As such, with the depth known the mesh is updated and the next time-step is initiated (Hervouet & Jankowski, 2000).

At each time-step the finite-element mesh is frozen to prevent changes to the flow variables. This is achieved by using a sigma transformation where the mesh is stopped from varying in the z-direction with free surface evolution by changing the z (x,y,t) co-ordinates to z*(x,y) co-ordinates which are independent of time. The generalised approach using classical sigma transformation for distributing layers throughout the mesh but above the prescribed bottom can be written as:

$$z^* = \frac{z - Z_p}{Z_s - Z_p}$$

4.4

where $Z_p$ is the prescribed layer and $Z_s$ is the free surface layer.

To investigate flows of practical interest, TELEMAC-3D makes further approximations and assumptions (Hervouet, 2007). TELEMAC-3D expresses flux through the domain boundaries by a volume integral in the mass equation with $\int_{\Omega} div(\rho\vec{u})\, d\Omega$ where Ω is the domain containing the fluid:

Conservation of mass:

$$\frac{\partial \rho}{\partial t} + div(\rho\vec{u}) = 0$$

4.5

When simulating a fluid with a rigid boundary the fluid density is considered variable and derived with respect to time for the fluid momentum within the domain i.e. $\frac{\mathrm{d}}{\mathrm{dt}} \left(\int_{\Omega} \rho\, \vec{u}\, d\Omega\right)$. The forces applied to the domain are also considered: external forces denoted are $\vec{g} + \vec{F}$ and the contact force is expressed using the stress tensor $\boldsymbol{\sigma}$ as applied to the surface element of the domain. The momentum equation is therefore written:

Conservation of momentum:

$$\frac{\partial(\rho\vec{u})}{\partial t} + \vec{u}\nabla\vec{u} = \frac{1}{\rho} div\,(\boldsymbol{\sigma}) + \vec{g} + \vec{F}$$

4.6

where $\vec{F}$ is the sum of external forces applied directly to the fluid body. The conservation of momentum is shown here in its non-conservative form. The mass conservation equation is retained in its compressible form. However, in the present study the density of the water is independent of the pressure and the flow can be considered incompressible. The stress tensor is therefore expressed as:

$$\boldsymbol{\sigma} = -p\,\boldsymbol{\delta} + 2\mu\,\boldsymbol{D}$$

4.7

here $\boldsymbol{\delta}$ is the identity tensor, $\mu$ is the coefficient of dynamic viscosity, which is constant depending on the fluid properties, and $\boldsymbol{D}$ is the strain rate tensor. For river water any variations in fluid density are considered sufficiently minor and so the mass conservation equation was used in an incompressible form. These

assumptions underlay the non-hydrostatic code for TELEMAC-3D which is expressed in Cartesian coordinates:

Conservation of mass:

$$\frac{\partial(u)}{\partial x}+\frac{\partial(v)}{\partial y}+\frac{\partial(w)}{\partial z}=0$$

4.8

Conservation of momentum:

$$\frac{\partial u}{\partial t}+u\frac{\partial u}{\partial x}+v\frac{\partial u}{\partial y}+w\frac{\partial u}{\partial z}=-\frac{1}{p}\frac{\partial p}{\partial x}+v\Delta(u)+F_x$$

$$\frac{\partial v}{\partial t}+u\frac{\partial v}{\partial x}+v\frac{\partial v}{\partial y}+w\frac{\partial v}{\partial z}=-\frac{1}{p}\frac{\partial p}{\partial y}+v\Delta(v)+F_y$$

$$\frac{\partial w}{\partial t}+u\frac{\partial w}{\partial x}+v\frac{\partial w}{\partial y}+w\frac{\partial w}{\partial z}=-\frac{1}{p}\frac{\partial p}{\partial z}-g+v\Delta(w)+F_z$$

4.9

where $p$ is the pressure in pascals, and $v$ is the coefficient for kinematic viscosity ($m^2/s$). The equations are non-hydrostatic as there is no hypothesis on hydrostatic pressure distribution.

It is unfeasible and unnecessary to consider all the small-scale fluctuations within the flow. As such, time-averaging or smoothing operators are used. CFD approaches commonly use an estimate of the time-averaged variables when approaching hydraulic engineering problems, as such the instantaneous Navier-Stokes equations are time averaged. The averaging of instantaneous quantities into time-averaged and fluctuating quantities is known as Reynolds averaging. The resulting equations are called Reynolds-averaged Navier-Stokes (RANS) equations and are primarily used to describe turbulent flow. In TELEMAC 3D the RANS equations for steady state flow are expressed as:

$$\bar{u}_j\frac{\partial\bar{u}_i}{\vec{x}}=g_i-\frac{1}{\rho}\frac{\partial\bar{p}}{\partial\vec{x}}+\frac{\partial}{\partial\vec{x}}\left(v\frac{\partial\bar{u}_i}{\partial\vec{x}}-\overline{u_i'u_j'}\right)$$

4.10

where $\bar{u}_i$ is the time-averaged velocity component in the $\vec{x}$ directions, $u_i'$ is the fluctuating part of the velocity where velocity is decomposed as $u_i = \bar{u}_i + u_i'$, $\rho$ is the fluid density, $v$ is the kinematic viscosity, and $\overline{u_i' u_j'}$ is the turbulent Reynolds stress based on time-averaged variables.

### 4.1.2 Boundary Conditions

The computational domain is limited by the impermeable bottom written as $Z_f(x, y, t)$, and the free surface of the water which changes over with time, $Z_s(x, y, t)$. Other boundaries include open boundaries, which represent non-physical structures, and closed boundaries, which can be either impermeable or permeable. In this study the open boundaries represent the upstream and the downstream of the river channel, respectively the inlet and the outlet, whilst the closed boundaries represent the riverbanks and are considered impermeable. Flow at the model inlet is prescribed using the mean flow rate determined from the data provided by UKCEH. The depth of the water flow is prescribed at the model outlet using data provided from the same source. As an initial condition the water surface profile was set as constant and parallel to the channel bed. A Dirichlet boundary condition, or fixed boundary condition, is prescribed at the inlet which assumes no gradient in the velocity profile and that the discharge is constant. For the free surface boundary TELEMAC-3D assumes any particle of water remains at the surface over time, and that the velocity of any particle adjacent to a point the surface is the same value as the velocity of the point on the surface. The free surface boundary can be written as:

$$\frac{\partial Z_s}{\partial t} - \vec{u}_{surface} . \vec{n}_s = 0$$

4.11

TELEMAC-3D applies a similar equation at the bottom:

$$\frac{\partial Z_f}{\partial t} - \vec{u}_{bottom} . \vec{n}_f = 0$$

4.12

where $\vec{n}_s$ is the vector normal to the free surface directed towards increasing $z$, and $\vec{n}_f$ is the normal to the bottom pointing downwards.

The boundary condition for velocity on a solid wall has a no-slip condition. However, the influence of turbulence at the boundary layer quickly established no-zero velocities in the near-wall region. The no-slip condition is the replaced by a weaker condition of impermeability (Hervouet, 2007) and is written as:

$$\vec{u}.\vec{n} = 0$$

4.13

When considering rigid boundaries, the turbulence computed using a $k$–$\varepsilon$ model (see: section 4.2) calculates both $k$ and $\varepsilon$ at distance $\delta$ from the wall. The distance $\delta$ is chosen as 1/10$^{th}$ of the local mesh size measured along the normal direction to the wall (Hervouet, 2007). As such, the numerical bottom sits just above the mesh bottom.

### 4.1.3 Source and sink terms

Estimating the effect of roughness on flow properties is necessary to accurately represent the processes controlling fluid dynamics within the natural environment. TELEMAC-3D supports cross-compatibility for friction terms, allowing the same terms to be used in 2D and 3D for formulae contingent upon depth-integrated velocity. The resolution required to resolve roughness geometry in three dimensions is difficult to apply due to the computational burden, practical limitations, and time-intensity needed to represent roughness elements with accurate detail. The RANS model provides a practical approach for estimating flow quantities whilst avoiding the computational expense of other approaches such as Large Eddy Simulation (Georgiadis *et al.*, 2010) or Direct Numerical Simulation. The Navier-Stokes equation obtains the Reynolds stress term from the averaged values of the turbulent solution. The Reynolds stress tensor is composed from the correlations of velocity fluctuations, and is expressed as:

$$\boldsymbol{R_{xy}} = -\overline{\rho u_x' \rho u_y'}$$

4.14

where $R_{xy}$ is the Reynolds stress tensor, $u'$ is the turbulent fluctuation of velocity, and the bar represents averaging. Turbulent stresses are unknown and to solve the Reynolds equations the tensor needs to be expressed on the basis of averaged

physical quantities using a turbulence model. This study adopts the most commonly used two-equation model: the *k-ε* model (see: section 4.2.)

Shear stresses act on the domain boundary in the opposite direction to the flow velocity. The friction at the bottom or sidewall is a continuity of the constraint at the fluid-wall interface. The bottom shear stress condition is represented using a friction coefficient and its associate velocity $\vec{U}$. The shear force can be also linked to the depth-mean flow velocity U and V together with the friction factor $C_f$. The general formula for shear forces can then be written as:

$$\vec{\tau} = -\frac{1}{2} C_f \sqrt{u^2 + v^2} \vec{u}$$

4.15

where $C_f$ is the dimensionless friction coefficient. In this study, the friction coefficient is provided by Manning's friction law which can be written as:

$$C_f = \frac{2g\, n^2}{h^{1/3}}$$

4.16

where $n$ is the Manning coefficient and $h$ is the depth of water. The computation of the turbulent constraint at the bottom depends on the velocity profile within the boundary layer, which itself depends on the ratio of the wall roughness size to the viscous sub-layer thickness. In cases where the roughness size exceeds the thickness of the viscous sub-layer a hydraulically rough condition is imposed. The method through which TELEMAC-3D computes the constraint varies depending on the friction law imposed. For example, when the Nikuradze law is chosen the shear velocity is computed from the velocity profile from within the logarithmic layer and the sand-equivalent roughness size $k_s$. When a local roughness factor is applied the friction velocity must be evaluated. For the Nikuradze law a logarithmic profile is assumed from the second plane from the bottom:

$$U_{shear} = \frac{kU_{plane1}}{\ln\left(\frac{33\Delta_z}{k_s}\right)}$$

4.17

where $U_{plane1}$ is the velocity at a point on the first plane above the bottom, and $\Delta_z$ is the altitude of the plane. Fig. 4.2. depicts direction of the shear velocity in the context of a gravel-bed river.

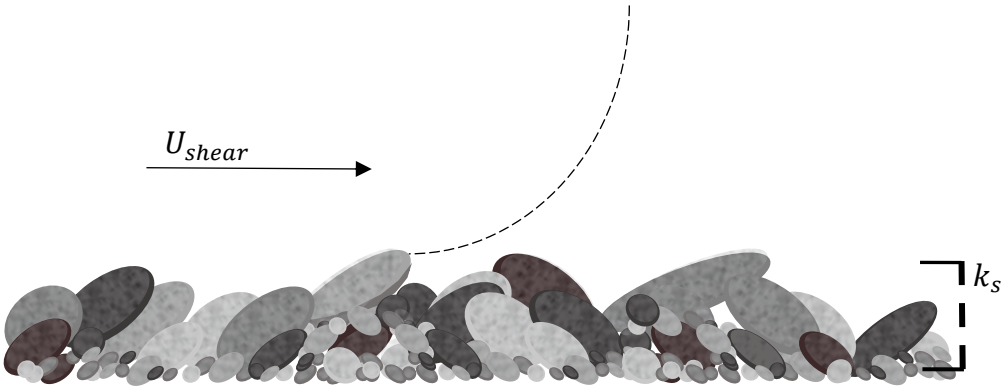


Figure 4.2. Velocity vectors are shown in physical context with reference to flow at the riverbed represented by an idealised velocity gradient (dashed line). The friction velocity is situated parallel to the shear velocity ($U_{shear}$). The grain size parameter ($k_s$) is also shown as a representation of bed gravel.

4.1.4 Turbulence modelling

TELEMAC-3D simulates turbulence using multiple models including a Smagorinsky model, a Large Eddy Simulation based on Smagorinsky (1963); a constant viscosity model; a mixing length model; and a *k*-*ε* two equation model. The Smagorinsky model computes the instantaneous velocity however it is computationally expensive. The constant viscosity model simulates turbulence for flows dominated by advection and pressure affects, whilst the mixing length model considers turbulence near the wall for computing the velocity profile. The *k*-*ε* turbulence closure model calculates time-average values for turbulent kinetic energy (*k*) and turbulent dissipation (*ε*). In this study the Smagorinsky model was considered inappropriate for the reach-scale used for the simulated domain, and the *k*-*ε* model is applied.

Derived from Launder and Spalding's standard model (1974), *k*-*ε* models are widely used, with the unmodified model frequently applied for modelling vegetated open

channel flow due to its capacity to capture shearing at vegetation boundaries (Fischer-Antze et al., 2001). The *k*-***ε*** model is suitable because it predicts a logarithmic velocity profile through the water column (Luek & Lu, 1997) which corresponds to a parabolic eddy viscosity profile (Winterwerp Walther & van Kesteren, 2004). Whilst the velocity profile deviates from the logarithmic profile in other flow types through the defect law in open channel flows this deviation is very small. Studies have implemented, with increasing computational expense, first-, second-, and third- order schemes to better capture processes within the flow field when vegetation geometry is well-defined. Other authors have sought to enhance *k*-***ε***-based turbulence closure models to better capture turbulence generation within complex canopy geometries, such as solute transport modelling in vegetation flows (Sonnenwald et al., 2019).

In TELEMC-3D the *k*-***ε*** model is calculated as:

$$k = \frac{1}{2}\,\overline{u_i' u_i'}$$

4.18

$$\varepsilon = v\overline{\frac{\partial u_i'}{\partial x_j'}\frac{\partial u_i'}{\partial x_j'}}$$

4.19

The 3D *k* and ***ε*** conservations are then written as the following equations respectively:

$$\frac{\partial k}{\partial t} + \bar{u}_i \frac{\partial k}{\partial \vec{x}} = \frac{\partial}{\partial \vec{x}}\left(\frac{v_t}{\boldsymbol{\sigma_k}}\frac{\partial k}{\partial \vec{x}}\right) + P - G - \varepsilon$$

4.20

$$\frac{\partial \varepsilon}{\partial t} + u_i \frac{\partial \varepsilon}{\partial \vec{x}} = \frac{\partial}{\partial \vec{x}}\left(\frac{v_t}{\boldsymbol{\sigma_k}}\frac{\partial \varepsilon}{\partial x_i}\right) + C_{1\varepsilon}\frac{\varepsilon}{k}[P + (1 - C_{3\varepsilon})G] - C_{2\varepsilon}\frac{\varepsilon^2}{k}$$

4.21

where $P$ is the production of turbulent energy, $G$ is the source term due to gravitational forces, and $v_t$ is the turbulent eddy viscosity.

The turbulent eddy viscosity can be defined as:

$$v_t = C_\mu \frac{k^2}{\varepsilon}$$

4.22

where $L_t$ is the characteristic size of vortices, and $D$ is the strain rate tensor of average motion. The constant $C_\mu$ was obtained from turbulent flow near a rigid wall (Hervouet, 2007). TELEMAC-3D uses the constants of the *k* – ***ε*** model as presented in Table 4.1.

Table 4.1. Constants of the k – ε model.

| $C_\mu$ | $C_{\mu T}$ | $Prt$ | $C_{1\varepsilon}$ | $C_{2\varepsilon}$ | $C_{3\varepsilon}$ | $\sigma_k$ | $\sigma_\varepsilon$ |
|---|---|---|---|---|---|---|---|
| 0.09 | 0.09 | 1.0 | 1.44 | 1.92 | 0 if $G$ > 0 and 1 if $G$ ≤ 0 | 1.0 | 1.3 |

where $C_{\mu T}$ is similar to $C_\mu$ with respect to temperature $T$; the constant $Prt$ is the Prandtl number; $C_{1\varepsilon}$ was obtained from turbulent flow near a rigid wall, similar to $C_\mu$; $C_{2\varepsilon}$ was obtained from experimental data for the free decay of grid turbulence; $C_{3\varepsilon}$ is equal to one during stable conditions and equal to zero during instability; both $\sigma_k$ , known as Prandtl's turbulent number for turbulent kinetic energy, and $\sigma_\varepsilon$ were optimised based on experiments mentioned in Hervouet (2007). The non-uniformity of the vertical velocity profile can be problematic because the integration of the Reynolds equation over the vertical produces dispersion terms. Therefore, in order to average the velocity over the vertical *k* and ***ε*** are integrated between the bottom $Z_f$ and the surface $Z_s$, and equations 4.17 and 4.18 become:

$$k = \frac{1}{h}\int_{Z_f}^{Z_s} \frac{1}{2}\,\overline{u_i' u_j'}\,dz$$

4.23

$$\varepsilon = \frac{1}{h}\int_{Z_f}^{Z_s} \frac{1}{2}\,\overline{u_i' u_j'}\,dz$$

4.24

The *k* and ***ε*** equations are then defined by:

$$\frac{\partial k}{\partial t} + \vec{u}\frac{\partial k}{\partial x_i} = \frac{1}{h} div\left(h\frac{v_t}{\boldsymbol{\sigma}_k}\overrightarrow{grad}\,(k)\right) + P - \varepsilon + P_{kv}$$

4.25

$$\frac{\partial \varepsilon}{\partial t} + \vec{u}\frac{\partial \varepsilon}{\partial x_i} = \frac{1}{h} div\left(h\frac{v_t}{\boldsymbol{\sigma}_k}\overrightarrow{grad}\,(\varepsilon)\right) + \frac{\varepsilon}{k}[C_{1\varepsilon}P - C_{3\varepsilon}] + P_{\varepsilon v}$$

4.26

The production term $P$ is calculated with the horizontal velocity gradients:

$$P = v_t\left(\frac{\partial \vec{u}}{\partial \vec{x}} + \frac{\partial \vec{u}}{\partial \vec{x}}\right)\frac{\partial \vec{u}}{\partial \vec{x}}$$

4.27

The terms $P_{kv}$ and $P_{\varepsilon v}$ are due to the shear force flow along the vertical and can be defined as:

$$P_{kv} = C_k\frac{u_*^3}{h}$$

4.28

$$P_{\varepsilon v} = C_\varepsilon\frac{u_*^4}{h}$$

4.29

where $u_*$ is the shear velocity on the bottom as defined at 4.16, and the $C_k$ and $C_\varepsilon$ terms are defined as:

$$C_k = \frac{1}{\sqrt{C_f}}$$

4.30

$$C_\varepsilon = 3.6\,\frac{C_{2\varepsilon}\sqrt{C_\mu}}{{C_f}^{3/4}}$$

4.31

where $C_f$ is the dimensionless friction coefficient as defined in equation 4.14.

## 4.2. Solution Algorithm

TELEMAC 3D uses the finite element method to discretise the computational domain into sets of non-overlapping triangle elements. The governing equations in 4.7-4.8 and 4.24-4.25 are linearized within each triangle element. The resultant linear algebra equations are then solved to give required values of velocities, turbulence quantities and water depth. For further information on TELEMAC-3D a greater in-depth exploration of the theory can be found in Hervouet (2007).

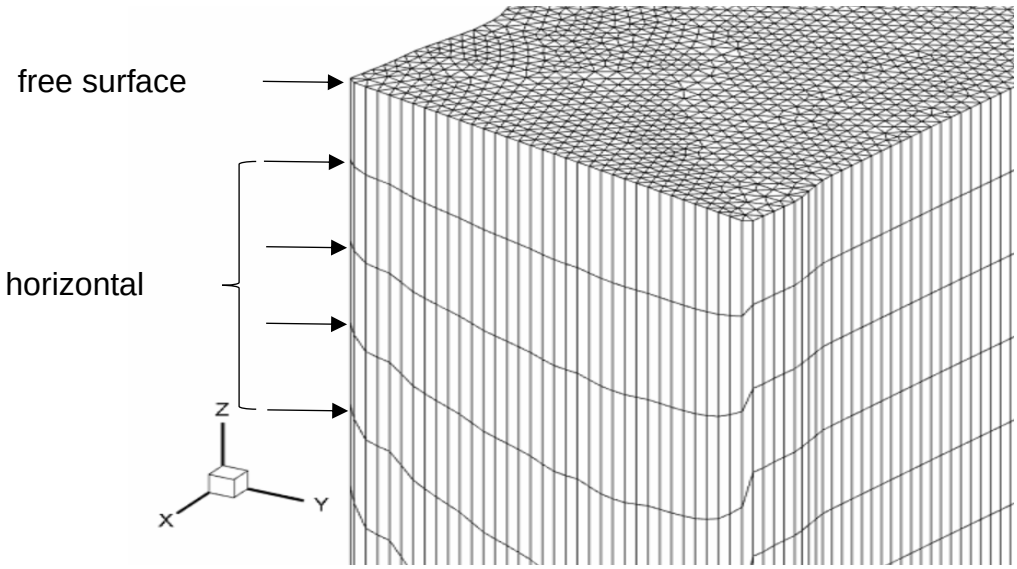


Figure 4.3. A 3D triangular mesh with horizontal planes identified.

TELEMAC-3D uses finite element unstructured triangular meshes to define the computational domain. A 3D prismatic mesh is generated from an initial two-dimensional 2D triangular base mesh produces using Delauney Triangulation. The 3D mesh is generated by duplicating the 2D mesh in their vertical direction over a prescribed number of horizontal planes (Fig. 4.3). Prisms are typically constructed from six nodes with three vertical quadrangular faces on the sides, and two triangular faces for the top and bottom. Prisms are commonly irregular as the mesh deforms to represent complex flow and topography, here meaning that the top and bottom faces are not necessarily horizontal.

The computational variables are defined at each point of the 3D mesh including both the bottom and the surface. The prisms of the new 3D mesh consist of 6 nodes, where the x and y coordinates of the prisms are the same as the 2D base mesh.

TELEMAC 3D is based on a decoupled algorithm using a fractional step technique, in which the governing equations are split into different modelling sections, or steps, and treated using appropriate numerical schemes. The basic algorithm considers three fractional steps: the advection step, solving the advected terms in the momentum equations; the diffusion step, where the resulting advected velocities is used by the algorithm to compute the velocity components with respect to the diffusion terms and source terms in the momentum equations; and the pressure-continuity step, where the water depth is computed by vertically integrating the continuity equations and momentum equation.

## 4.3 Advection schemes

TELEMAC-3D has multiple options for the choice of advection scheme (Table 4.2.). For this study the explicit advection scheme with MURD (multidimensional upwind residual distribution) PSI (positive streamwise invariant scheme) was adopted. This scheme, alongside the N scheme, is advantageous due to being conservative and monotonic and thus generate no numerical oscillation. Additionally, the PSI scheme is less diffusive if more computationally expensive than the N scheme, increasing its comparative accuracy. However, both have higher levels of diffusivity than the Streamline Upwind Petrov-Galerkin (SUPG) method. The other available scheme, the method of characteristics (MOC), or the Lagrangian approach, is the most diffusive and lacks exact mass conservation. Due to its lower accuracy the MOC approach was not adopted.

Table 4.2. Advection schemes for three-dimensional variables.

| Scheme | Velocity | Depth | $k-\varepsilon$ | Order of accuracy |
|---|---|---|---|---|
| MoC | Yes | No | Yes | First |
| SUPG | Yes | No | Yes | Second |
| Leo Postma | Yes | No | Yes | First |
| MURD scheme N | Yes | No | Yes | First |
| MURD scheme PSI | Yes | No | Yes | Second |

## 4.4 Convergence.

The convergence criteria for the numerical simulation was based on mass conservation and the residual error for each solved variable. The computations were assumed to converge when the mass balance was within 1%, and the residual error for each solved variable were below $10^{-4}$. Spot values for each flow variable was checked and were considered satisfactory when said values were almost constant.

## 4.5 Summary

This chapter has described the numerical approach adopted for this study, including the chosen software TELEMAC-3D and its governing equations. The modelling methodology was outlined including choice of turbulence closure scheme, chosen boundary conditions, and the use of the DANS equations to represent the effect of roughness elements. A study assessing the effects of DANS approach compared to a standard RANS approach was detailed, illustrating how the vertical velocity and turbulence profiles produced by the former method better represents the flow profiles described in physical experiments.

# Chapter 5 | Definition of the model domain

## 5.1. Introduction

The model equations described in Chapter 4, Section 4.1 are applied by using a boundary-fitted domain, within which finite elements form the base for the algebraic problems to be solved by local functions. This chapter describes the creation of these domains in the form of prismatic meshes. Overall, the study required four meshes for 16 flow conditions, 12 of which comprised the scenario-based investigation.

Spatial prediction was used to generate the mesh channel topography in Cartesian coordinates where *x* describes length along the channel in the streamwise direction, *y* describes the length across the channel, and *z* describes the channel elevation. This was required to refine the topographic data and better represent the channel in the mesh geometry. Following the linear interpolation of the topographic data an initial 2D mesh was constructed; TELEMAC 3D constructs the prismatic 3D mesh from an initial 2D triangular mesh by duplicating the mesh vertically. The initial 2D mesh contains the computational domain and was created using the boundary-fitted coordinates previously generated. The final model mesh had a cell resolution of 0.2m in the channel and 0.3m on the berm. The final mesh was composed of 34 horizontal layers, the first four of which were 10mm in height and represented the bottom roughness layer as described in the previous chapter.

## 5.2. Processing the topographic data

The model domain is determined by the extent of the sampled data. Due to the channel's trapezoidal shape the highest section of the bank provided the boundary limit for the channel. Velocity and surface errors have been found to increase with distance between cross-sections (Horrit et al., 2006), therefore spatial prediction was used to derive a suitable detailed description of the channel cross-sections and reduce error from sparse topographic data.

The resolution of topographic data has a significant impact on the accuracy of solutions for multidimensional flow, and increasing topographic resolution improves the ability of models to reliably solve and simulate the flow field perpendicular to the

channel (Legleiter et al., 2011.) Representing the influence of topography at smaller scales requires a progressively finer mesh in order to capture the necessary flow processes. Obtaining the high-resolution data required to accurately capture the heterogenic, spatially distributed topographies of river channels is difficult and is a limitation for CFD in environmental applications (Casa et al., 2010.) Uncertainties within topographic data can potentially reduce the accuracy of the model: one of the most influential parameters effecting model sensitivity is the resolution of the topographic data (Legleiter et al., 2011) where important flow processes are heavily influenced by complex variations in river topography (Biron et al., 2007.) This is pertinent for gravel-bed rivers where highly irregular topography at the channel bottom results in bed forms at different roughness scales (Lane et al., 2004.) Representing this high variability is a significant challenge for CFD approaches as fluid depth is closely related to bed form elevation (Hardy et al., 2009) thus to accurately simulate the free surface complex bed topographies must be sufficiently represented. The usage of poorly defined topography undermines the model accuracy, for example: velocity and surface errors have been found increase with distances between channel cross-sections for shallow river reaches (Horrit et al., 2006.)  Practical challenges preventing the acquisition of high-resolution topographic data from the field has incentivised alternative approaches to accurately representing river channels; using comprehensive high-resolution digital elevation models to represent highly detailed variations in channel topography is not feasible in terms of cost or time (Casas et al., 2010.) One successful technique for overcoming sparse topographic data involves interpolating channel surfaces between cross-sections (Conner & Tonina, 2013; Merwade et al., 2008; Casas et al., 2006) in order to produce a channel with a representative topography at a higher resolution (Schäppi, Perona, & Schneider, 2010.) In this study, the resolution of the topographic data for the River Blackwater is increased by adopting this type of approach by using linear interpolation to predict the topographic values between cross-sections. The method used to achieve this is detailed below.

### 5.2.1. Channel interpolation method

Spatial prediction was achieved by building an algorithm that used linear interpolation to estimate new point values for the cross-sectional data. The algorithm consisted of three steps: firstly, for the calibration case the topographic data was cut

below the observed free surface elevation; secondly, query points were generated along each cross-section on the *y*-coordinate; and thirdly, query points were generated between each pair of cross-sections on the *x*-coordinate. At each stage elevation data (*z*) was linearly interpolated across the query points. The number of query points between and across cross-sections were defined by respective density coefficients. The appropriate density coefficient was tested to find the optimum density of query points where errors from spatial prediction was reduced. Interpolation was performed using Matlab R2016a. A summary of the interpolation sequence can be seen in figure 5.1. The interpolation method for spatial prediction in the channel is described below:

*5.2.1.1. Cutting the channel below the free surface.*

To effectively test how well TELEMAC estimates the free surface and to aid model calibration the initial tests were completed using a mesh cut 10cm below the observed free surface. The equation describing the threshold for cutting was described by:

$$\mathrm{z} = -0.000825 * \mathrm{x} + 0.754422$$

The cutting plane determined the maximum elevation of the riverbanks, therefore complementary coordinates had to be produced to represent the bank top. This was completed using linear interpolation: the above equation was used to obtain the *x,z* coordinates for the bank height elevation at each cross-section, with the y coordinates for the maximum bank height interpolated between the highest data point at each end of the cross-section and the lowest data point in the removed data.

*5.2.1.2. Across channel interpolation.*

It was necessary to interpolate along the cross-sections first as the amount of data available for each cross-section varied: to ensure that the coordinate values are successfully linearly interpolated between each cross-section every cross-section must have an equal number of data points. As such, the across-channel *y*-values were first interpolated for each cross-section. The query points for interpolation were

Use plane to cut data below desired height.

Generate XYZ points for maximum bank height. Linear interpolation is used for Y.

Y-values are linearly interpolated between the maximum and minimum values for each cross-section (see diagram below.)

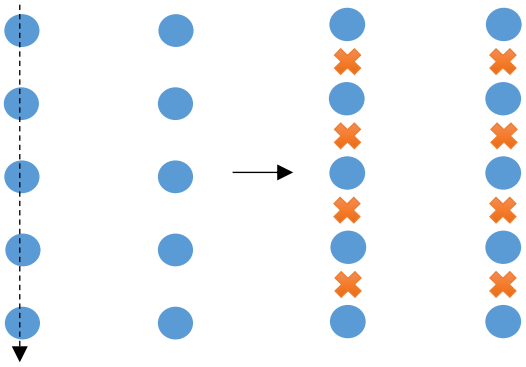

Interpolating across cross-sections. Circles are sampled data, crosses are interpolated data. Orange represents new data added at that step.

X- and Z- values are linearly interpolated over the Y-values previously generated.

X-values are linearly interpolated between complementary data points for each pair of cross-sections.

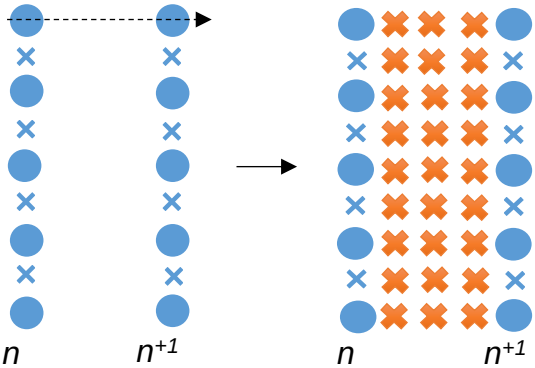


Interpolating between cross-sections n and n $^{+1}$ for corresponding pairs of data points. Blue crosses are data points interpolated in a previous step.

y- and Z- values are linearly interpolated over the X-values previously generated.

Figure 5.1 Channel interpolation method.

generated by linearly interpolating between the point with maximum and minimum *y* - value at each respective cross-section. This ensured that all the query points were within the same range as the sampled data for each cross-section. The same density coefficient was used to ensure that the same number of data points were generated for each cross-section. The *x*- and *z*-values were then linearly interpolated across the new query points to produce a new set of 3D Cartesian coordinates for each respective cross-section.

*5.2.1.3. Along channel interpolation.*

Interpolation between cross-sections was completed by generating query points for the *x*-values between each pair of cross-sections. This was done iteratively, for example: for the first pair of cross-sections *n* and $n^{+1}$ query points for the *x*-values would be generated between two complementary data points. The subsequent iteration would then repeat the procedure for the cross-sections $n^{+1}$ and $n^{+2}$. This would continue for each pair of cross-sections until the final pair. Because the previous step had ensured that all cross-sections had an equal number of data points, the query points for the *x*-values could be generated between complementary pairs of data points between a pair of cross-sections. For example, query points were generated between the data point $x^1$ in *n* and $x^1$ in $n^{+1}$. The *y*- and *z*-values were then linearly interpolated along the newly generated query points. This process was repeated for each pair fo cross-sections.

5.2.2. Quality assessment of the interpolated results.

Poorly performed interpolation can increases the topographic error within the mesh, resulting in inaccurate results (Bilskie & Hagen, 2013.) Errors and uncertainty can be produced by the interpolation process: errors in approximation derived from interpolation can result in unnatural artefacts, whilst issues relating to how well the modelled topography represents the physical terrain acts as a source of uncertainty (Fisher & Tate, 2008.) Artefacts can be problematic for CFD approaches where spurious terrain features generate complex flow mechanisms which can inhibit the model convergence. To avoid this the algorithm must be validated to ensure that the virtual channel accurately represents the physical terrain. This is achieved by comparing the interpolated output to the sampled data. The interpolated data was

checked using two methods: firstly, the topographic output was visually assessed to artefacts (identify terrain features not present in the original data); secondly, the interpolated output was compared to the original data by using RMSE method to check how well the predicted values matched the measured values. RSME has been sued successfully in other studies to determine the elevation error (Bilskie & Hagen, 2013.) The topographic output with the lowest RSME was used as the basis for mesh generation.

Different query point densities were selected to determine the number of data points to be interpolated across and between cross-sections, respectively. The results when visually checked for conscious differences between the interpolated data and the sampled data. Results containing conspicuous artefacts were disregarded and smaller densities were used. This process of identifying conspicuous artefacts and reducing densities was repeated until no obvious differences between the interpolated data and the measured data were apparent (Figure. 5.2).

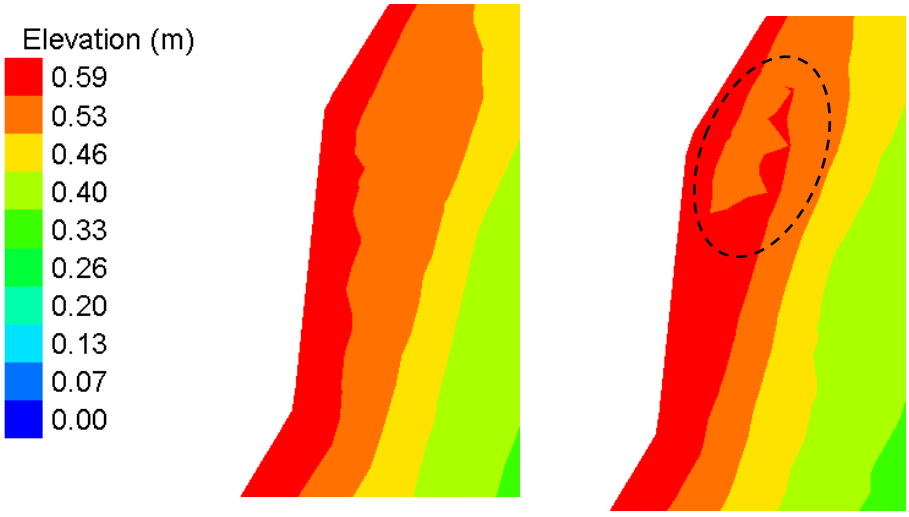


Figure 5.2. Comparison of the final interpolated topography (left) and an interpolated output with higher query point density exhibiting a conscious artefact (right.) The artefact is highlighted by dashed circle.

To avoid spurious changes in channel geometry at smaller scales and assess whether the interpolated elevation was within reasonable bounds the *z*-values for the interpolated data was checked against the measured data using root-mean-square error method (RMSE.) Data points with the same *x*,*y* values for both the measured data and the interpolated data were compared, with values for the river boundary ignored as the interpolated and measured data sets share the same points at the

banks, as explained above. The final density coefficients chosen were a value of 40 for across channel interpolation, and a value of 5 was chosen for interpolation between cross-sections. Physically speaking this allowed for the description of three additional cross-sections between each sampled cross-section, or an additional 441 cross-sections overall. Exceeding this number led to the generation of conspicuous artefacts (Figure 5.2.) The final densities chosen found an RMSE of 0.003873, suggesting that for the interpolated data the error contributed to 2.76% of the minimum elevation value of 0.14, and 0.54% of the maximum value of 0.7. This was deemed an acceptable margin of error, as such the chosen interpolated densities above were used. A visual representation of interpolated data for selected cross-sections can be seen in Figure 5.3.

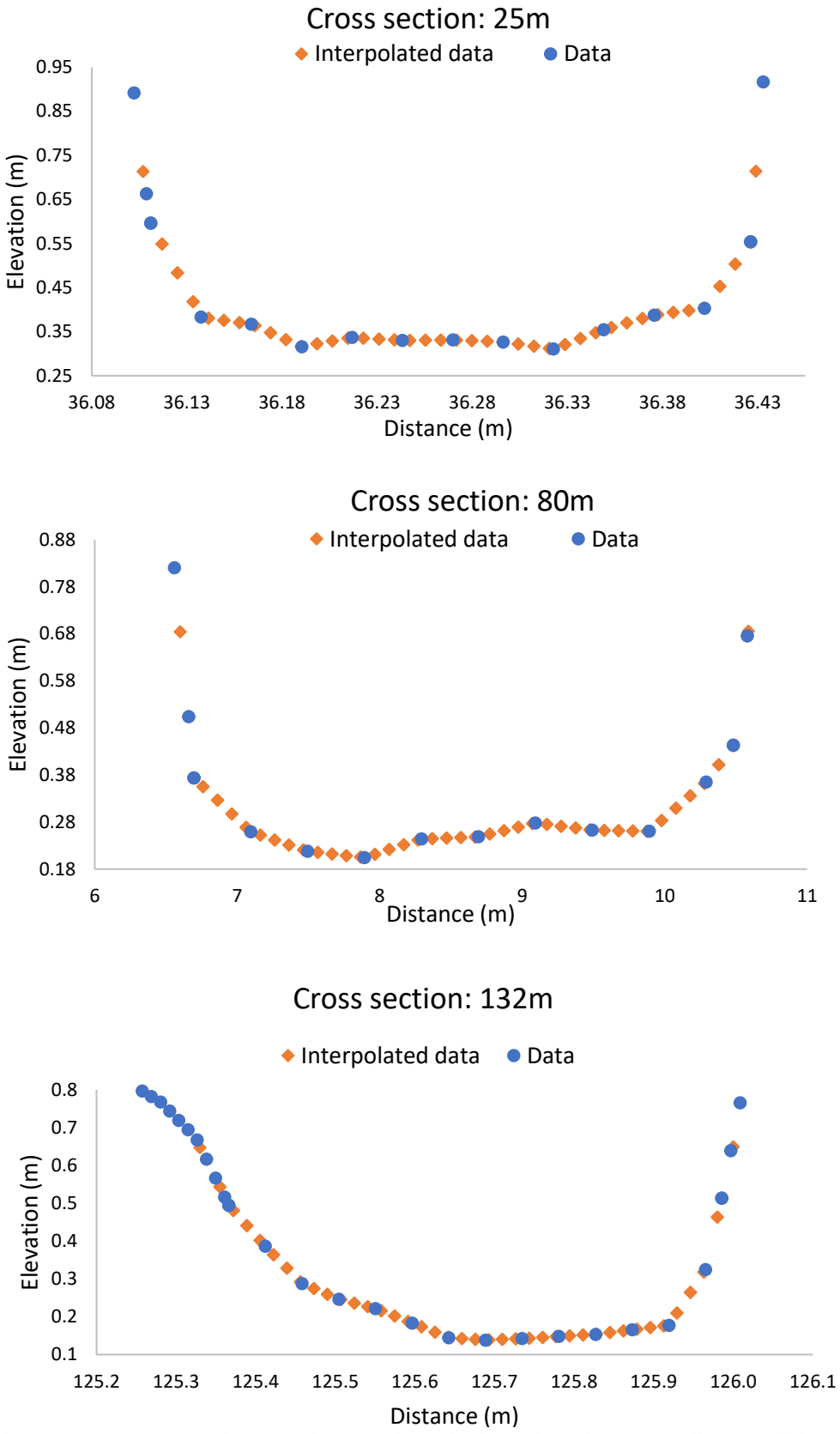


Figure 5.3. Comparison of interpolated elevation (orange diamonds) against measured data (blue circles) for three cross-sections at 25m, 80m, and 132m along the channel in the streamwise direction, respectively.

## 5.3. Mesh generation

### 5.3.1. Choice of mesh type:

The type of mesh used significantly impacts model accuracy, influencing how accurately channel geometry is represented, the computational expense, the rate of convergence, and the solution accuracy (Horrit, 2000). In fluvial this represents a fundamental problem in applying CFD schemes to natural channels, where the accurate spatial discretisation of complex topography and representation of the free surface present significant challenges (Hardy et al., 2005.) Differences between mesh approaches, including mesh quality and interpolation, alters the finite-element base on which the algebraic problems are solved and thus directly influences the accuracy of the end solution (Lane et al., 2005). Finite element approaches often use a triangular grid which is either structured or unstructured. Structured meshes are defined by regular connectivity between nodes which is used to identify neighbourhood relationships during computation, where the connectivity between meshes vertices is pre-determined and repeating (Castillo, 1991.) Unlike structured meshes, unstructured meshes are identified using a single index used to identify the neighbouring cells (Lo, 2017.) The costs and benefits of both approaches are discussed below. Visual comparison of both grid types can be seen in Figure 5.4.

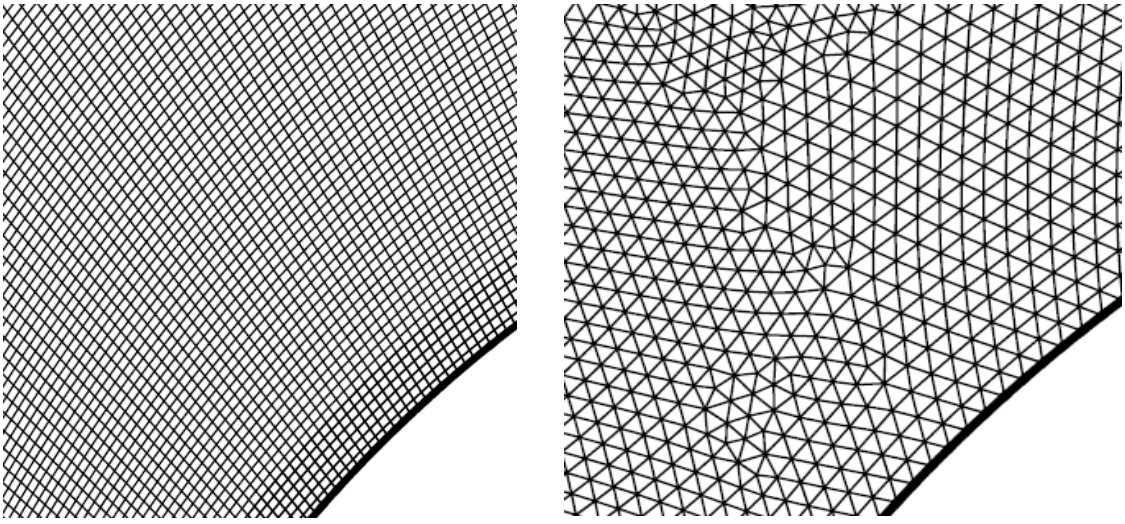

Figure 5.4. Comparison of regular structured (left) and irregular unstructured (right) mesh types for the same mesh section, as seen in Desai, Kulkarni, and Gadgil (2016.)

Unstructured grids consist of arbitrary polygons framed by irregular connectivity, which has contributed to their increasing popularity due to their ability to handle complex geometries (Lisiekin, 2017.) Unstructured grids are beneficial as the can be generated more easily within an arbitrary boundary. This allows for the generation of more irregular triangles, increasing element density and enhancing mesh resolution in regions that would otherwise be problematic for a regular mesh. By using an index to identify neighbourhood relationships during computation rather than local connectivity seen in structured meshes, the mesh has greater degree of flexibility for representing complex geometries and allowing, in principle, individual cells to be connected to an arbitrary number of other cells (Reider and Olsen, 2003.) This greater flexibility is advantageous for flow modelling at reach-scale (Fweziger and Peric, 1999), allowing for the modelling complex geometries (Stamou et al., 2012), higher resolutions for localised regions (Dietrich et al., 2011.) In terms of flood modelling, unstructured meshes can be better for describing the topofrpahical discontinuities influencing inundation (Baldassarre et al., 2010.)

Unstructured meshes for environmental applications were initially adopted in oceanographic modelling due to their aforementioned flexibility (Danilov, 2013.) This has led them to be adopted in flood modelling (Zhang et al., 2015) and for the representation of fluvial topography. Although fluvial domains were initially represented using 2D unstructured meshes (for example: : Lai, 2009; McGuigan, Webster, & Collins, 2015; Nguyen et al., 2016) unstructured meshes have increasingly been used for 3D river models (for example, see: Casulli & Walters, 2000; de Brye et al., 2010; Kang & Sotiropolous, 2012; Khosronejad et al., 2016) including estuaries (for example: Levasseur et al., 2007; Wang et al., 2009; Yang and Khangaonkar et al., 2009), and dam breaks (for example: Lai & Khan, 2016; Zhang, Peng, & Feng, 2018 ). However, the flexibility of the triangular elements can result in highly distorted elements with poor orthogonality which in turn reduces numerical accuracy. The distortion of mesh elements also significantly increases the complexity of the mathematical approximations and therefore increases the computational burden. This can be countered through numerous approaches, such as increasing local grid resolution or applying a Laplacian smoothing algorithm to re-adjust triangle nodes to better conform to Delaunay triangulation and increase element orthogonality. Applying a Delaunay criterion is a popular way to overcome

deformation issues as Delaunay triangles are nearly equilateral, minimising the maximum angle and maximising the minimum to improve the overall shape of the triangle (Liseikin, 2017.)

Structured grids are more uniform than unstructured grids and are defined by their regular connectivity. Structured grids have historically been popular in CFD approaches, in part due to their reduced computational burden: conserving memory and reducing computation time by occupying the same volume as unstructured meshes but with a lower cell count. Due to their regular connectivity structured grids generally have greater orthogonality than unstructured grid: cells with high aspect ratios are more easily generated using a structured mesh and may increase the accuracy of the solution compared to unstructured grids (Hardy et al., 2005.) Structured grids are also beneficial due to the alignment of the grid topology: convergence is easier to achieve when grid lines align with the flow direction. However, structured grids can be difficult to generate for complex geometries, as such complex surfaces are usually approximated leading to elements being blocked out and resulting in problematic effects such as flow loss.

For this study an unstructured mesh approach was chosen for 3D representation of the channel. This was deemed the most appropriate for two reasons: firstly, it was better suited for irregular channel boundaries, allowing the mesh to better conform to the complex geometry. The structured approach was found to poorly adhere to the channel boundary, requiring a higher resolution to ensure the boundary was accurately emulated compared to the unstructured mesh. In addition, complex geometries produced by irregular changes in the channel bottom and along the banks were better represented due to the unstructured mesh's ability to contort its triangles. Secondly, TELEMAC 3D was built to solve RANS equations using primarily unstructured meshes, including the modules developed for the system (Hervouet, 2007; Villaret et al., 2013) and the advection schemes, where TELEMAC favours the use of residual distributive advection schemes: a class of high-resolution methods developed for unstructured grids (Rossmanith, 2008.) As such, an unstructured grid approach was deemed the optimum method to use for flow modelling in TELEMAC 3D.

### 5.3.2. Constructing the mesh:

Mesh generation was done using BlueKenue, a data preparation, analysis, and visualisation software developed for hydraulic research by the National Research Council Canada. To produce a mesh with Cartesian coordinates in BlueKenue the mesh was first generated in 2D within the confines of the model domain. After the topographic data was linearly interpolated onto the nodes of the newly generated mesh. A summary of the mesh generation sequence is provided below in Figure. 5.5. A more detailed description of the mesh generation process in Blue Kenue is described below:

#### *5.3.2.1. Triangulation*

An unconstructed triangular mesh was generated by prescribing the domain boundary and edge length of triangles. The boundary was as described in Chapter 3, Section 3.2. Bluekenue's mesh generation produces 2D triangular meshes using a dynamic moving algorithm which places nodes within the domain boundary at a distance determined by a prescribed edge length. The edge length determines the greatest distance allowed between nodes and as such controls the node density. Due to the complex geometry associated with the river channel any resulting irregular connectivity means that a constant edge length is not always possible. This element distortion is limited by the edge length value, ensuring that any element distortion results in a node density with the prescribed edge length value or smaller. Consideration must be given to the mesh resolution so that it is sufficiently fine to capture flow features. The edge length is therefore the key component in controlling mesh refinement. Following node placement an unconstrained Delaunay Triangulation algorithm was used to implement node connectivity and complete generating the mesh. In the final step a Laplacian smoothing algorithm was used to adjust the mesh nodes and reduce angular deviation within the triangles.

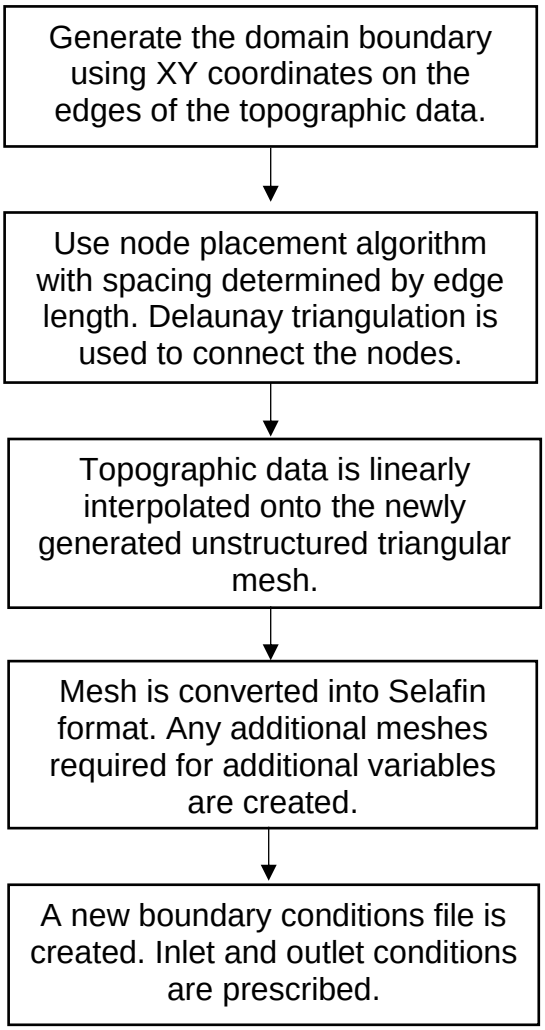


Figure 5.5. Process for integrating topographic data onto the mesh.

5.3.2.2. Topographic interpolation

The topographic values generated in section 5.2 are linearly interpolated onto the triangular mesh.

*5.3.2.3. Selafin file format*

The triangular mesh is then converted to the Selafin binary file format, which is the standard TELEMAC system format. In this section additional meshes with the same topography and structure can be generated. This is necessary for the addition of new variables (Chapter 4, Section 4.3.)

*5.3.2.4. Boundary conditions*

The boundary conditions for TELEMAC are specified via a CONLIM table of variables, where each variable corresponds to a boundary or edge node in the mesh. Boundary edge nodes at the inlet and outlet of the mesh are prescribed with their respective variables specified in (Chapter 4, Section 4.1.2)

5.3.3. Spatial discretisation of the 3D mesh:

TELEMAC constructs the 3D mesh by using the 2D mesh as a base and duplicating the vertices in the vertical direction. The number of times vertices are duplicated as a prescribed number of horizontal planes. The 3D mesh is constructed of prismatic elements made of six nodes, where their quadrangular sides are vertical. The *x* and *y* coordinates of the prisms match the coordinates of the original 2D mesh with the elevation of the vertices increasing from the bottom to the free surface. The 3D domain is built by applying sigma transformation and by default constructs the horizontal layers using the below equation:

$$z(x, y, ip) = Z_f(x, y) + \frac{ip - 1}{np - 1}(Z_s(x, y) - Z_f(x, y))$$

where $Z_f$ is the bottom elevation, $Z_s$ is the free surface elevation, $ip$ is the plane under consideration, and $np$ is the highest plane (i.e. the free surface.) The 3D mesh in this study was built using a similar method, using a double-sigma transformation-inspired approach to evenly distribute horizontal planes between the free surface and the new prescribed bottom as described in Chapter 4, Section 4.3. The results of the mesh construction in the x, y direction can be seen in Figure 5.6, and the result of horizontal distribution, including the fixed four bottom layers constituting the roughness layer, can be seen in Figure 5.7.

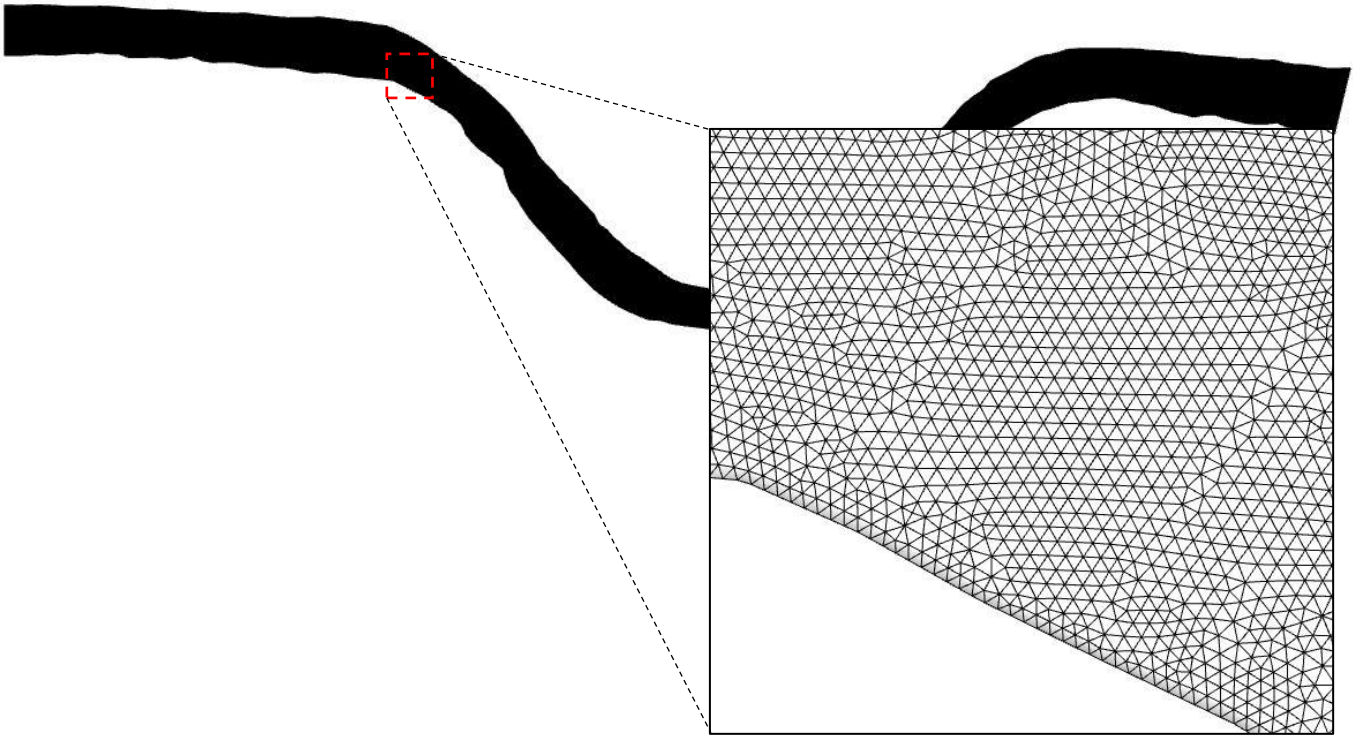

Figure 5.6. Visualisation of the unstructured channel mesh at its most refined with an edge length of 0.3m.

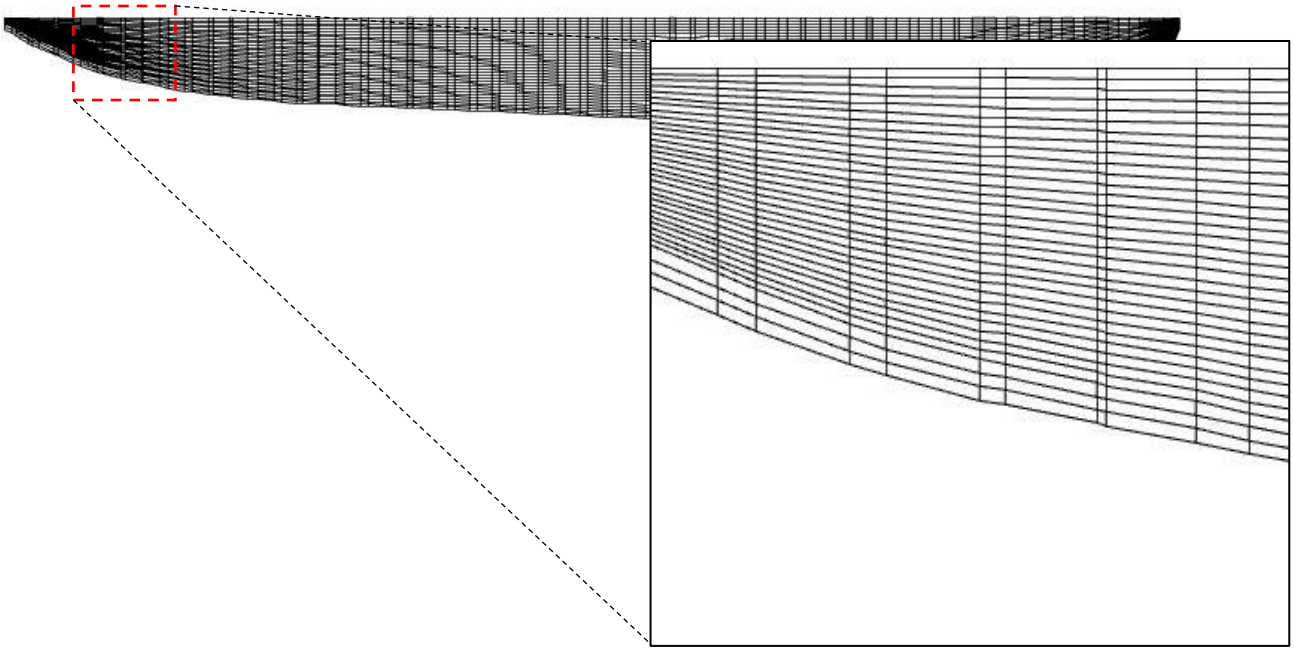

Figure 5.7. Cross-section of the unstructured channel mesh at its most refined with 34 horizontal layers, showing the irregular nature of the meshing approach. The inset displays how the first four layers have a prescribed elevation to form the artificial bottom.

## 5.4. Potential errors

Spatial prediction can introduce errors through the presence of artefacts in the flow and differences between the virtual and physical topography. The introduction of errors has previously been addressed in section 6.2 of this chapter. However, differences between virtual and physical topographies are difficult to totally remove. The interpolation methods used to increase mesh resolution does not increase the resolution of intrinsic topography: natural topography has heterogenic and fractal qualities (Bates, Lane, & Ferguson, 2005; Fisher & Tate, 2006) which are impossible to produce using interpolation to predict values between sampling locations. As such the topography produced through interpolation is artificial (Casas et al., 2010.) The overall effect is a smoothening of the channel topography due to the averaging of elevation values between measured data points, creating differences between the virtual and physical river channels at small scales. The differences between measured terrain and its virtual representation introduces uncertainties into the model and influence how well river processes are represented in the flow field (Fisher & Tate, 2006.) Very small-scale variability, as expected for the gravel bed, has already been discussed in context of the drag model in Chapter 4, Section 4.3. The largest impact stems from the use of averaged elevation values between cross-sections where natural topographies express heterogenic and fractal terrain. Due to the aforementioned costs financially and in time to attain sufficiently detailed topography data the mesh geometry was tested to confirm whether its representation of the channel was appropriate for the study. This was performed at two stages: firstly, the usage of RMSE to test the differences between measured and interpolated data discussed above; and secondly, through the calibration of the bulk drag coefficient to observe whether the model simulates the expected free surface within physically appropriate parameters, later discussed in Chapter 6.

The spatial discretisation approach used by TELEMAC can be problematic due to complex channel geometry: applying a uniform number of horizontal levels can result in over-discretisation in shallow areas, such as on floodplains, and an under-discretisation in deep-flow regions of the domain, such as the channel thalweg. This can be avoided by integrating separate meshes of different resolutions for the channel, and flood plains, respectively. By having a refined mesh for the main

channel and a coarse mesh for the flood plains both avoids the problem of under- or over-discretisation and increases the model economy by decreasing the computational burden associated with over-refined domains.

# Chapter 6 | Construction of the 3D model

## 6.1. Introduction

This chapter describes the 3D model, including its calibration, a discussion of the advection schemes available in TELEMAC 3D, and an assessment of numerical accuracy. The model was first calibrated for the non-vegetated case using the February flow data. Calibration was completed using the bulk drag coefficient defined at the first four layers of the model mesh as described in Chapter 5. In order to effectively analyse how well the free surface was reproduced, and the model was calibrated using the bulk roughness coefficient. Three meshes of different resolutions were used in order to assess the impact of refinement on the model results. The numerical accuracy of the model was then assessed to gauge whether a mesh-independent solution had been achieved.

## 6.2. Convergence criteria

Convergence is assessed by investigating the residuals between flow properties and mass balance produced as numerical solutions advance with each iteration. The solution is considered converged when the residuals between iterations have decreased beyond a threshold, also known as the convergence criteria (Tu, Yeoh, & Liu, 2018). The simulation is considered converged when residuals are at less than three orders of magnitude ($<10^{-3}$) between two time steps for the mass balance and the flow variable for velocities $u_x$, $u_y$, $u_z$ and turbulent kinetic energy (TKE) $k$. When no appreciable change in these properties is found for consecutive time-steps the solution can be deemed converged. The typical time step used in the present study is 0.4 seconds which amounts to 33.33 minutes of in-simulation time to ensure the stability of the simulation. The convergence criteria was chosen for being a standard for testing model convergence, below which the residuals between each iteration is small enough that the solution can be considered stable (for example, see: Tu, Yeoh, & Liu, (2018); Lane et al. (2005); Wilson et al. (2003); and Olsen (2002).

## 6.3. A spatially-averaged drag approach

Preliminary tests were conducted using the model configuration detailed in Chapter 5. The vertical profiles for turbulent kinetic energy (TKE) closely matched the observed values throughout the turbulent flow layer i.e. the region of the water column unaffected by roughness elements. However near to the channel bed region TKE values become unrealistically high as a result of unresolved near-bed boundary processes. To compensate for this a new approach was needed to accurately capture flow processes within the near-bed region. Accurately predicting 3D flow fields in natural rivers can be problematic due to difficulties acquiring data that sufficiently describes the heterogenic, multi-scalar distribution of roughness elements. In this study, small components contributing to boundary roughness are represented by spatially-averaged parameters applied at each layer in the roughness zone. Implementing double-averaged Navier-Stokes equations (DANS) allows for the representation of the effects of small-scale topography, such as gravel and vegetation structure, which otherwise cannot be captured by the mesh (i.e. sub-grid scale processes). In the model this can be done by introducing spatially-averaged parameters into the modelled source terms and new terms introduced into the Navier-Stokes equations. The section below discussed the parametrisation of the new terms which are introduced into DANS equations for this model.

### 6.3.1. Implementing DANS within TELEMAC-3D

The total drag force per unit volume was represented using a conventional drag force equation for each Cartesian direction and written as (Nikora et al., 2007):

$$F_x \approx \frac{1}{2} C_d S_f A_{px} |\langle \bar{u}_i \rangle| (\bar{u}_x)$$

$$F_y \approx \frac{1}{2} C_d S_f A_{py} |\langle \bar{u}_i \rangle| (\bar{u}_y)$$

$$F_z \approx \frac{1}{2} C_f A_s |\langle \bar{u}_i \rangle| (\bar{u}_z)$$

6.1

where $F_x$, $F_y$, and $F_z$ is the total drag force per unit volume in the three coordinate directions x, y, and z (m/s$^2$), $C_D$ is the drag coefficient, $S_f$ is the sheltering factor

generated by proximity to other roughness elements, $A_{px}$ and $A_{py}$ are the averaged frontal projected areas of the roughness elements per grid layer per unit volume in the x and y coordinate directions ($m^2/m^3$), $A_s$ is the averaged surface area of the roughness elements per grid layer per unit volume ($m^2/m^3$), and $|\langle \bar{u}_i \rangle|$ is the time-space averaged velocity. The sheltering factor $S_f$ is representative of the diminishing drag coefficient downstream of wakes. Nepf (1999) described how wakes from upstream rods reduces the drag coefficient on downstream rods, increasing in effect as the array spacing between rods decreases. Rameshwaran & Shiono (2007) discuss how using the model provided by Nepf (1999) the drag coefficient $C_D$ and $S_f$ are related through rod dimensionality: a rod array distribution with a ratio of 0.87 between the rows and a fractional volume of 0.0075 results in a bulk drag coefficient of 1.0. The bulk drag coefficient is a composite of $C_D * S_f$, thus where $S_f$ is equal to 1.0 then $C_D$ is also equal to 1.0 (Rameshwaran & Shiono, 2007). For a discussion on the usefulness of bulk of drag coefficients to represent the drag form interactions consult Chapter 2 (Section 2.8.2). It is noted that bulk drag coefficients are used in to represent numerous hydrodynamic processes, and that the bulk drag coefficient reported in this study does not represent the total drag expressed by a given drag form such as gravel-bed drag or vegetation canopy.

The skin friction for the riverbed surface was supplied by using the Nikuradse law and adopted a $k_s$ value of 0.01, which matches the value used for the roughness height in Rameshwaran, Naden, & Lawless (2011), a study for the same river reach which used a similar double-averaging method. The fluid flow and roughness layer interact at the surface of roughness elements. This point of interaction is represented using the frontal projected area which approximates the areal value of the gravel which interacts with the flow by representing the total are per unit volume of the bed roughness. These spatially-averaged roughness parameters were statistically derived from five random samples collected using the method described in Chapter 3, Section 3.3.2 but are repeated in Table 6.1 for convenience. The frontal projected areas were estimated for flow in the directions $u_x$ and $u_y$, and the surface area was used to parametrise the drag effect for $u_w$. The drag effect was applied layer-by-layer with the roughness region to represent the multi-scalar grain topography of the gravel-bed in the model. The parameters were applied at the first four layers of the mesh at 10mm intervals from the bottom. This data represented the sub-grid scale roughness which couldn't be

captured by the 3D mesh, and which formed the method for representing 3D drag force in combination with mesh topography.

Table 6.1. Average properties of the gravel riverbed

| Layer | Layer height (mm) | Frontal projected area $A_{px}$ (m²/m³) | Frontal projected area $A_{py}$(m²/m³) | Frontal projected area $A_s$(m²/m³) |
|---|---|---|---|---|
| 1 | 0 | 1.6546 | 1.9889 | 13.8340 |
| 2 | 10 | 12.0348 | 15.0840 | 77.5191 |
| 3 | 20 | 12.3361 | 14.8194 | 76.6161 |
| 4 | 30 | 2.1330 | 2.4954 | 15.3330 |

In TELEMAC 3D the user-defined source terms are considered implicit and are treated in the diffusion step, and are expressed as:

$$F_x = S1U \cdot u$$

$$F_y = S1V \cdot v$$

$$F_z = S1W \cdot w$$

6.2

where $S1U$, $S1V$, and $S1W$ are the intermediate terms defined by the user, and $u, v,$ and $w$ are the three velocity components (m/s). The intermediate drag terms can be computed directly using the below equations:

$$S1U = \frac{1}{2} C_d A_{px} |u|$$

$$S1V = \frac{1}{2} C_d A_{py} |u|$$

$$S1W = \frac{1}{2} C_d A_s |u|$$

6.3

where $|u|$ is the velocity norm $\sqrt{u^2 + v^2 + w^2}$, which resembles a typical drag force equation. The roughness coefficient $C_d$ is applied with a different projected area $A_{pi}$ for flow in the x and y direction, and the surface are $A_s$ in the z direction. In this manner the drag effect applied at each layer within the roughness boundary can simulate the impact of multi-scalar roughness on river flow.

To represent the bottom boundary and prescribe the drag effect at the bottom four mesh layers the elevation for the three layers above the mesh bottom needed to be prescribed. TELEMAC 3D is limited in its representation of vertical structures to three programmable options: the homogenous distribution of levels in the vertical direction using classical sigma transformation; the distribution of planes as a percentile of depth, using sigma transformation for given proportions; or at fixed altitudes relative to the lowest elevation values. As such a new subroutine describing the distribution of the horizontal layers was needed.

The new subroutine was based on the CALCOT subroutine; CALCOT is called by TELEMAC-3D to build the nodal arrays and prescribed elevations to individual mesh layers. TELEMAC-3D builds the 3D mesh by constructing prisms between each mesh layer where the vertices are the mesh nodes. The bottom and top face of each prism describe the shame shape, with the nodes for any given corner having the same *x*,*y* coordinates as the node in the mesh layer directly below or above. Physically, prisms can be described as composed of three tetrahedra formed by a set of four points, which is used for linear interpolation during the diffusion step (Fig. 6.1).

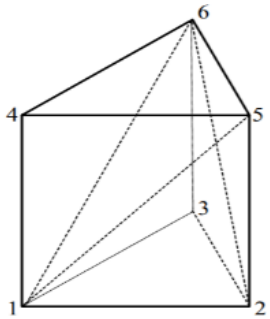


Figure 6.1. Example of a prism decomposed into three tetrahedra along with the associated points (Hervouet, 2007).

The node elevation in the first three planes above the bottom were equally distanced at 10mm, 20mm, or 30mm above the mesh bottom respectively. A routine for plane distance regulation was applied which considers the 30mm layer as an artificial bottom and applies a security distance which prevents inappropriate collision or tessellation with the layers above.

### 6.3.2. Results of the DANS subroutine

A comparison of the TKE profile for the channel centre comparing the TKE profiles for the converged runs using the Nikuradse law and the drag-force approach, respectively, is shown in Figure 6.2. The TKE profile produced from the Nikuradse run shows a clear divergence form the measured data below the inflection point at 0.3m where the TKE increases dramatically with decreasing elevation. Decreasing TKE values at this point is unexpected as turbulence is small within the roughness layer, and increases at the transitional zone with the main turbulent flow region. Running the model using solely the Nikuradse law clearly results in a poorly represented TKE profile as a result on unresolved boundary processes. The run using the drag-force approach exhibits a TKE profile more representative of the measured data, with the TKE below the inflection point decreasing in a similar fashion to the observed TKE.

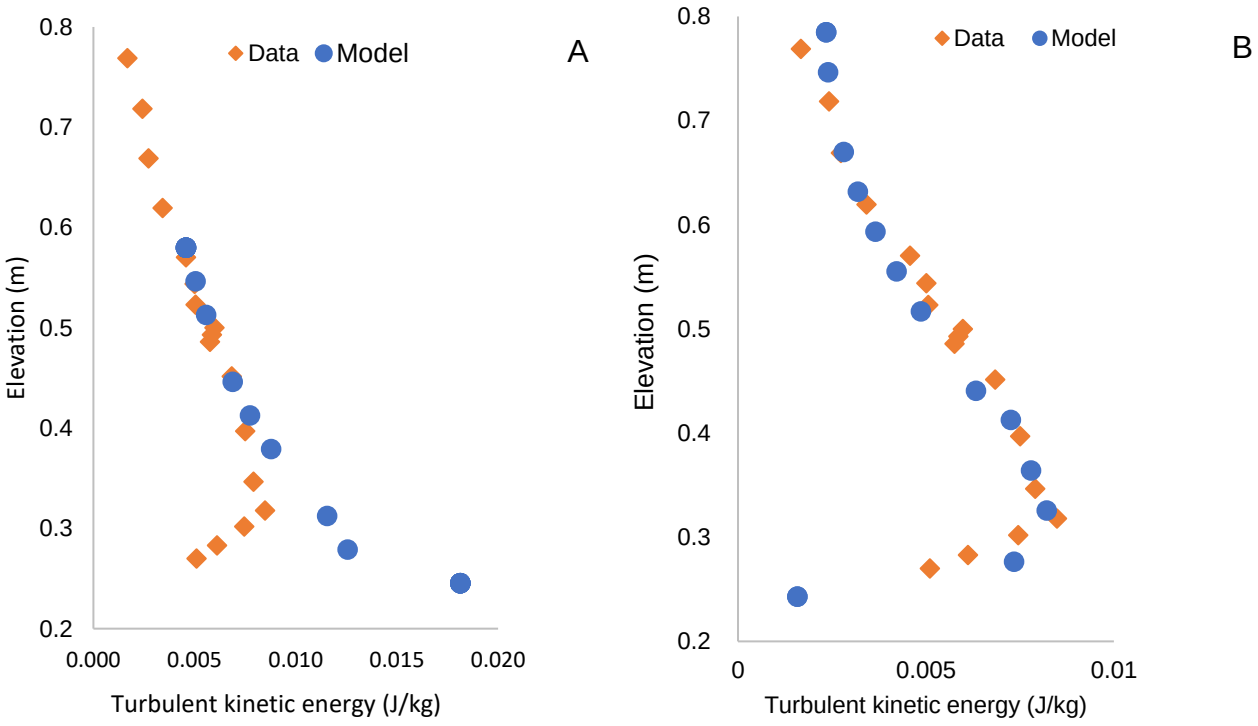


Figure 6.2. TKE profiles using solely the Nikuradse law (A) and using the DANS approach (B).

## 6.4. Calibration of the bulk drag coefficient

### 6.4.1. Calibration method

The drag force for the bottom roughness boundary was approximated by calibrating the bulk drag coefficient $C_D$ for the non-vegetated February case using the spatially-averaged drag model (Chapter 4, Section 4.3). The boundary conditions used the flow data are described in (Chapter 4, Section 4.1.2).

Calibration of the drag coefficient was completed by examining the differences between the slope for the observed and modelled free surface, and the flow variables for streamwise velocity and turbulent kinetic energy. The calibration methodology for the bulk drag coefficient can be summarised as:

1. An initial bulk drag coefficient was estimated at 0.69, based on Rameshwaran and Naden (2012) who researched a similar stretch of the same river.

2. The model was run until convergence. The free surface was then examined by comparing the modelled free surface against the measured data at both banks. Data for the free surface elevation was then extracted by finding the free surface data at comparative points between the *x, y* co-ordinates for sampling sites and the mesh nodes. This was achieved by using an algorithm which finds the minimum distance between the coordinates of the mesh points and the sampling sites along both banks, respectively. The maximum node elevation was then extracted from each mesh point to represent free surface elevation for the measured data and was compared against the modelled data. Figure 6.3 and Figure 6.4 show comparisons between the final calibrated free surface for the right and left bank, respectively. Figure 6.5. shows the data for both banks, the final calibrated surface, the simulated free surface using a drag coefficient reported for a physical model (Schmeekle et al., 2007), and the simulated surface where the drag coefficient as set to unity. Schmeekle et al. (2007) was selected due to its focus on gravel-bed drag, where the drag coefficient was calculated by measuring the effect of similar-sized gravel pebbles on near-bed flow conveyance by a force transducer in an artificial flume. The gravel-bed was 2.3cm deep with an average surface area

perpendicular to the flow of 1.97cm$^3$. The regressed results for all gravel-bed runs produced the drag coefficient $C_{DR} = 0.91$.

3. The accuracy of the free surface was determined by examining the difference between the gradient of the observed data for the free surface and modelled free surface. Linear regression was used to find the residuals which were in turn used to define the slope. The slope of the modelled data was then compared to the slope of the measured data using RMSE method. If the modelled free surface was too high compared to the observed free surface then the bulk drag coefficient was decreased, if the modelled free surface was too low then the coefficient was increased.

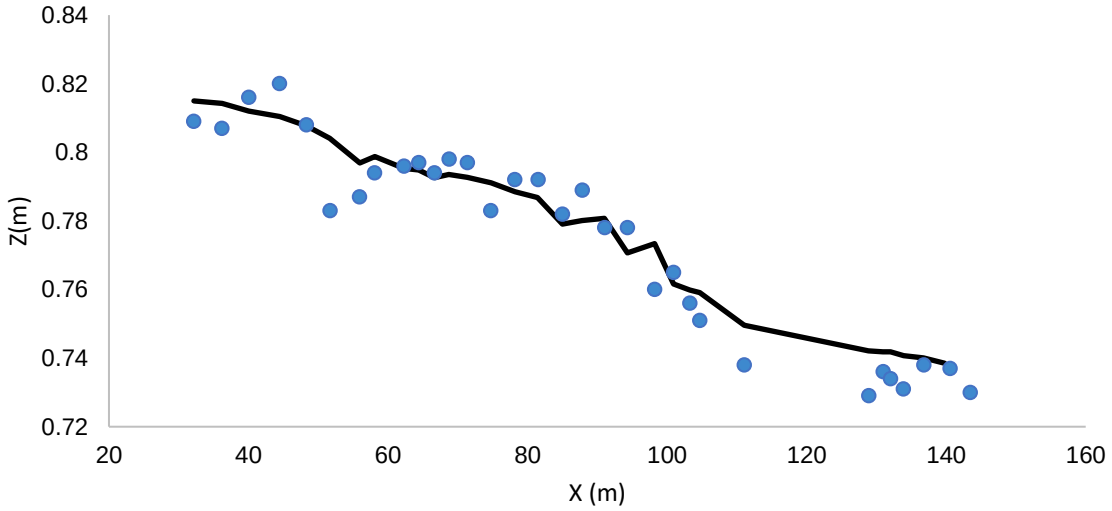


Figure 6.3. Comparison of observed free surface (blue circles) against calibrated free surface ($C_D = 0.52$, black line) for the right bank.

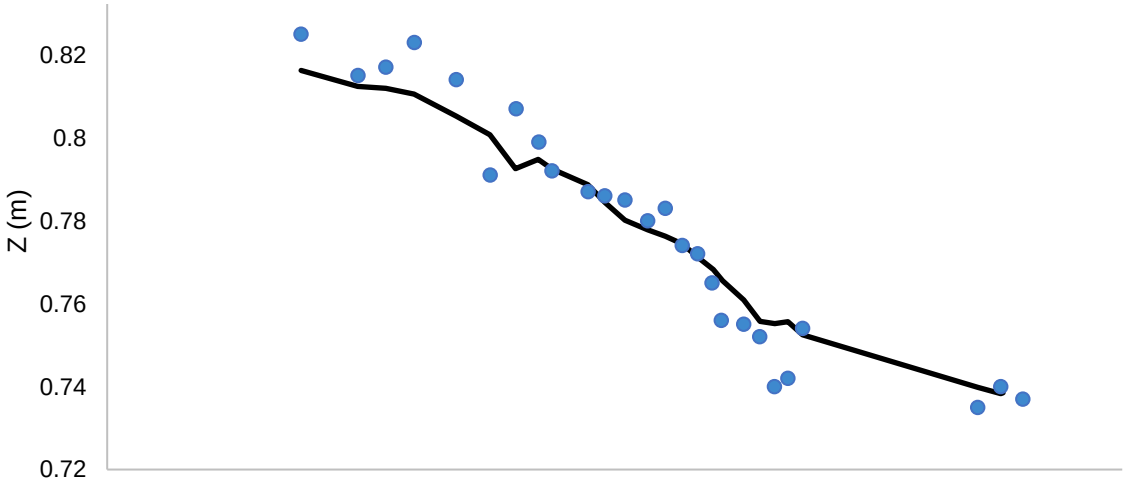


Figure 6.4. Comparison of observed free surface (blue circles) against calibrated free surface ($C_D = 0.52$, black line) for the left bank.

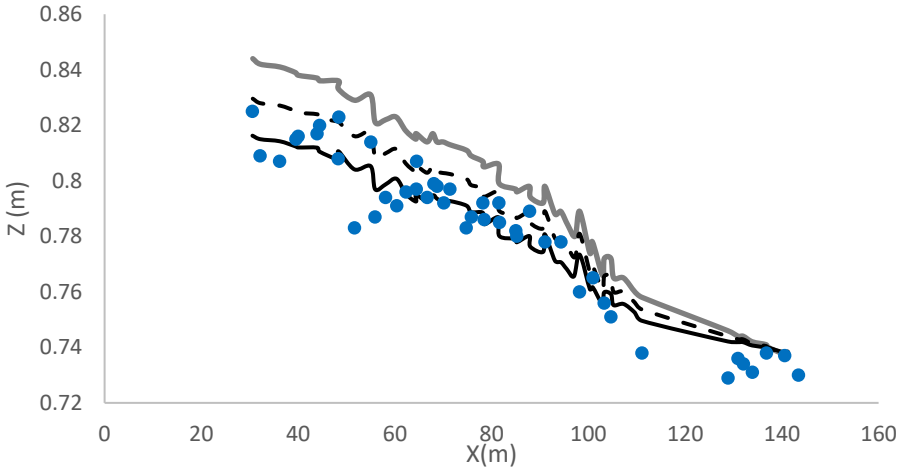


Figure 6.5. Comparison of observed free surface (blue circles) against calibrated free surface ($C_D = 0.52$, solid black line) for both banks, the simulated free surface using the drag coefficient taken from Schmeekle et al. (2007) ($C_D = 0.91$, dashed black line), and the simulated free surface where the drag coefficient was set at unity ($C_D = 1.0$, solid grey line).

### 6.4.2. Calibration results

The drag coefficient that produced the lowest RMSE was found to be $C_D$= 0.52 where the RMSE value was found to be 0.0029m, as shown in Figure 6.4. The RMSE was found to be 0.4% of the smallest modelled elevation of 0.73m, and 0.36% of the largest elevation of 0.82m. The calibrated free surface was also checked using the Nash-Sutcliffe efficiency index (Nash & Sutcliffe, 1971), a widely applied assessment of goodness of fit within hydrological models (McCuren, Knight, & Cutte, 2006). Therefore, it is perhaps helpful to quote index values of index results in order to effectively communicate the goodness of the calibration. The Nash-Sutcliffe Efficiency Index can be written as:

$$E_f = 1 - \frac{\sum(\hat{Y}_i - Y_i)}{\sum(Y_i - \overline{Y_i})} \quad (7.1)$$

Where $\hat{Y}$ and $Y_i$ are the predicted and measured values of the flow variable $Y$, and $\overline{Y_i}$ is the mean of the measured value. The efficiency index $E_f$ should be within the interval 0 to 1, where a value can be considered a good fit as it increases towards 1. The results for the roughness calibration can be seen in Table 6.2. The results show that a roughness coefficient of 0.52 results in the closest fit between the modelled

and the measured free surface (Figure 6.3) however a coefficient 0.51 also has a close fit and is comparable with $C_D$ 0.52 within three decimal places.

Table 6.2. The Index $E_f$ values for the calibrated bulk roughness coefficient.

| $C_D$ | $E_f$ |
|---|---|
| 0.51 | 0.9880 |
| 0.52 | 0.9881 |
| 0.53 | 0.9871 |

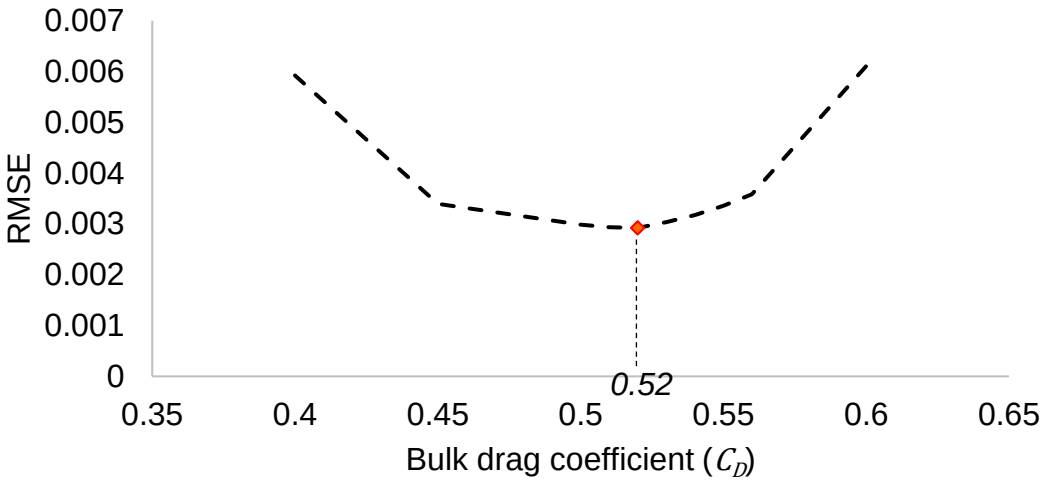


Figure 6.6. The calibrated bulk roughness coefficient (red) relative to the RMSE value.

All free surface simulations for the calibrated coefficient, the coefficient taken from Schmeekle et al. (2007), and the coefficient set to unity all described similar slopes. The similarity between the calibrated coefficient and the Schmeekle et al. (2007) coefficient suggests that the model simulates the effect of gravel-bed drag force in a manner similar to that reported in the literature. Differences between the free surface elevation reported here and Schmeekle et al. (2007) may be the result of numerous factors including differences in channel morphology, differences between the average surface area of gravel, and how the model's computational parameters determine the prediction of flow behaviour. The free surface elevation increased alongside increases in the drag coefficient, with the unity coefficient displaying the highest free surface elevation. This suggests that the model satisfies continuity, as greater gravel-bed drag results in surface elevation (see Chapter 2, Section 2.3 for more detail on continuity).

6.4.3. Comparison of the bulk drag coefficient against literature.

To determine that the calibrated bulk drag coefficient was appropriate, its value was compared to others reported in the literature. A summary can be shown in Table 6.3. The calibrated value was found to be of a similar magnitude as other bulk drag coefficients for gravel-bed rivers in the literature, which has been shown to vary from 0.45 (Wilberg & Smith, 1991) to 1.25 (Nicholas, 2005).

Table 6.3. Summary of some of the drag coefficients reported in literature.

| Author | Drag coefficient | Method | Parametrisation |
|---|---|---|---|
| Carney, S.K., Bledsoe, B.P. and Gessler, D., 2006. Representing the bed roughness of coarse-grained streams in computational fluid dynamics. *Earth Surface Processes and Landforms*, *31*(6), pp.736-749. | 0.45 | Same as Wilberg & Smith (1991) – double check! | $(F_D)_m = \frac{\rho}{2}(C_D)_m(A_D)_m\langle u^2\rangle$ Where $(A_D)_m$ is the grain cross-sectional area, and $\langle u^2\rangle$ is the average fo the squared velocity. |
| Gordon et al. 2004, based on White (1986) and Roberson & Crowe (1990) | Ellipsoid (0.08, 0.13, 0.2), 0.2 (sphere) ,0.5 (cone), 0.99-1.17 (flat-faced cylinder facing flow), 1.4 (cup, open towards the flow) | Drag coefficients based on frontal area of the object. | $F_s = C_f W L_\rho \frac{V^2}{2}$ Where $C_f$ is the skin friction, $W$ and $L$ are the width and length. |
| Kazemi, Tait, & Shao (2016). | 0.5 | Mesh-free particle method. Smoothed particle hydrodynamics method. Separate | $F_D = -\frac{1}{2}C_D\rho A_D u\|u\|$ |

| | | | |
|---|---|---|---|
| | | particles of 2mm spacing. | |
| Kean and Smith (2006) | 0.61, 1.10, 1.78 | Gaussian-shaped topographic features. The drag coefficient serves as a function of feature length divided by height. | $F = -\frac{1}{2}\rho C_D H B u^2{}_{ref}$ Where $H$ is the protrusion height of the element, $B$ is the length of the direction perpendicular to *x* and *z*, $u_{ref}$ is a reference velocity. |
| Nicholas, A.P., 2005. *Roughness parameterization in CFD modelling of gravel-bed rivers* (Vol. 540). p.340.John Wiley and Sons: Chichester. | 1, 1.25 | Drag coefficient was adjusted until appropriate water level was reached. | $F_i = \frac{\rho}{2D_{50}} N \hat{C}_D \, S_f u_i \lvert u \rvert$ Where $F_i$ is the drag force per unit volume, $N$ is the number of obstacles per unit length, $S_f$ is the shading factor, $u_i$ is the streamwise velocity, and $\lvert u \rvert$ is the velocity magnitude. |
| Rameshwaran, Naden, & Lawless (2011) | 0.27 – 0.85 | Laboratory experiment for plane bed, plane bed with clusters, and riffle-pool sequences with clusters. | $F_x \approx -\frac{1}{2} C_D S_f A_p \lvert \langle \bar{u} \rangle \rvert \langle \bar{u} \rangle$ Where $A_p$ is the average frontal projected area. |
| Rameshwaran, P. and Naden, P.S., 2012. Modelling the influence of macrophyte | 0.69 | DANs approach. Gravel-bed roughness; River Blackwater case site. | $F_i \approx -\frac{1}{2} C_d S_i A_p \lvert \overline{u_i} \rvert \langle \overline{u_i} \rangle_x$ |
| Rameshwaran, Naden, & Lawless (2011) | 0.27 – 0.85 | Laboratory experiment for plane bed, plane | $F_x \approx -\frac{1}{2} C_D S_f A_p \lvert \langle \bar{u} \rangle \rvert \langle \bar{u} \rangle$ |

| | | | |
|---|---|---|---|
| | | bed with clusters, and riffle-pool sequences with clusters. | Where $A_p$ is the average frontal projected area. |
| Schmeekle et al. (2007) | 0.76 (spheres), 1.36 (cubes), and 0.91 (pebbles) | Laboratory experiment for groups of spheres, cubes, and natural particles (pebbles) respectively. | $F = -\frac{1}{2}\rho_f C_D A_{\perp} u^2{}_x$ |
| Wiberg, P.L. and Smith, J.D., 1991. Velocity distribution and bed roughness in high-gradient streams. *Water Resources Research*, *27*(5), pp.825-838. | 0.45 (sphere), 1.2 (cylindrical rod) | Experimental relationship for spheres as a function of the particle Reynolds number. | $F_D = \frac{1}{2} C_D A_p U^2$ Where $A_p$ is the particle cross-sectional area |
| Zeng & Li (2012) | 0.23 – 0.87 | DANS method. | $F_x = -\frac{1}{2}\rho C_d C_s b_s N \langle \bar{u}_1 \rangle^2$ Where $C_s$ is the shielding factor, $b_s$ is the projected width of the roughness lement, and $N$ is the number of elements per $1^{m2}$ |

6.4.3. Comparison of different calibration results for three meshes with different levels of refinement.

Calibrating the bulk drag coefficient aids in determining the accuracy of the solution: meshes with increased resolution are expected to calibrate with a higher drag coefficient compared to that of relatively coarser meshes, as coarser meshes

compensate for the influence of diffusion. In other words, the more refined the mesh is the higher the drag coefficient should be, and therefore the solution is less influenced by numerical diffusion.

The bulk drag coefficient was calibrated for three different mesh resolutions to assess the impact of diffusion and therefore the relative accuracy of each mesh. Each mesh was generated using different grid dimensions which are defined as the specifications of which are shown in Table 6.4. For this study, the refinement ratio was chosen as 2. The ratio is further discussed below in Section 6.6.

Table 6.4. Specifications for the three meshes used to calibrate the bulk roughness coefficient.

| Mesh | Prescribed edge length (m) | No. of horizontal layers | No. of nodes |
|---|---|---|---|
| M1 | 0.4 | 14 | 5048 |
| M2 | 0.2 | 24 | 18839 |
| M3 | 0.1 | 34 | 78309 |

The calibration results are described in Figure 6.7. The coarsest mesh M1 is calibrated with the lowest drag coefficient, and the most refined mesh, M3, is calibrated with the highest coefficient. This suggests that the refined mesh has the least numerical diffusion.

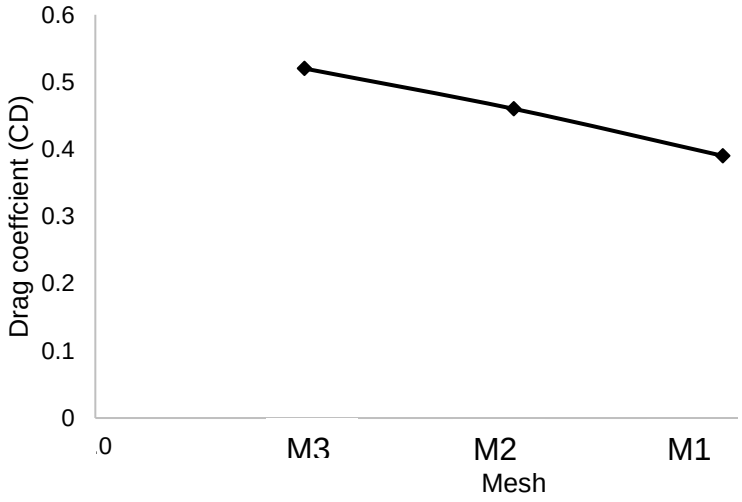


Figure 6.7. Calibrated values for the bulk drag coefficient for the three meshes.

### 6.4.4. Comparison of flow variables

The simulated flow data was then compared to the observed data for flow variables: $u_x$, $u_y$,$u_z$, and the turbulent kinetic energy (TKE) ($k$). The simulated data was taken from the converged solution for the most refined mesh, M3. Flow profiles were used to compare the simulated variables to the observed data measured at the four points across the apex cross-section, situated at 81.64m along the reach in the streamwise direction. Simulated results for the calibrated drag coefficient, the Schmeekle (2007) coefficient, and the coefficient set to unity. Disparity between the measurement coordinates and mesh node coordinates meant that the modelled flow quantities cannot be directly compared at the same location. The nodes nearest to each measurement location were therefore selected using a nearest neighbour search function. The small differences between the profiles at each node were assessed standard deviation. Differences between the flow variables for each node were minor, therefore the flow profiles only show the median profile for clarity and plots of standard deviation were absent as they did not allow for any meaning

comparison. For the standard deviation for the velocities and TKE at each cross-section please refer to the appendix. The median profile illustrates the median values for each flow variable where the profile represents the midway between the profiles with the maximum and minimum values. Bank locations are described as if facing downstream. The comparison between profiles for different flow variables can be seen in Figure 6.8 for streamwise velocity ($u_x$) and TKE ($k$), and in Figure 6.9 for the secondary flow circulation variables ($u_y$) and ($u_z$).

The results show that the streamwise velocity was predicted reasonably well in all profiles, with similar values observed for each of the simulated drag scenarios. The model was less accurate when simulating the vertical velocity, however the overall profile exhibited by the measured data was captured by the simulated results and shows that a fully 3D flow had been simulated. Notably, the accuracy to which vertical velocity profiles agree with the measured data increases towards the right bank on the outside of the apex, with the greatest differences reported at the left bank near mid-stream depth and extending to the riverbed. Vertical velocity increased with an increase in the value of the drag coefficient, identifying a particularly sensitive region for flow conveyance simulations. These changes be the result of increased circulation due to accelerated flow present at the meander's inner back interacting with an increased drag effect at both the riverbed and the walls. The TKE profiles were also predicted reasonably well across the channel, capturing the inflection point at the boundary between the roughness layer and main channel flow. However, TKE shows greater divergence from the measured data compared to the streamwise velocity. The TKE profiles conform the most to the measured data at the channel centre, with the flow profiles at the banks matching the measured data showing slightly less agreement. The largest differences between the measured and modelled data occur at the left bank, where the observed profile diverges from the modelled profile above 0.55m. This could be due to incidental vegetation disturbing the flow profile, such as dead vegetation resting on the channel surface. Another divergence is noted for the right bank where the observed $k$ is lower than that of the modelled. This may be a result of variations in bed topography at the bank not captured by the model. Figure 6.7 shows circulation at the meander apex for the simulation for the calibrated coefficient. The model has successfully captured the clockwise-rotating secondary circulation: the velocity vectors describe movement at

the bed in the direction of the right bank on the outer edge of the apex, and at the free surface towards the left bank at the inner edge of the apex. The presence of circulation in the upper half of the water column at the left bank may explain the increased velocities expressed near the riverbed as observed in the flow profiles.

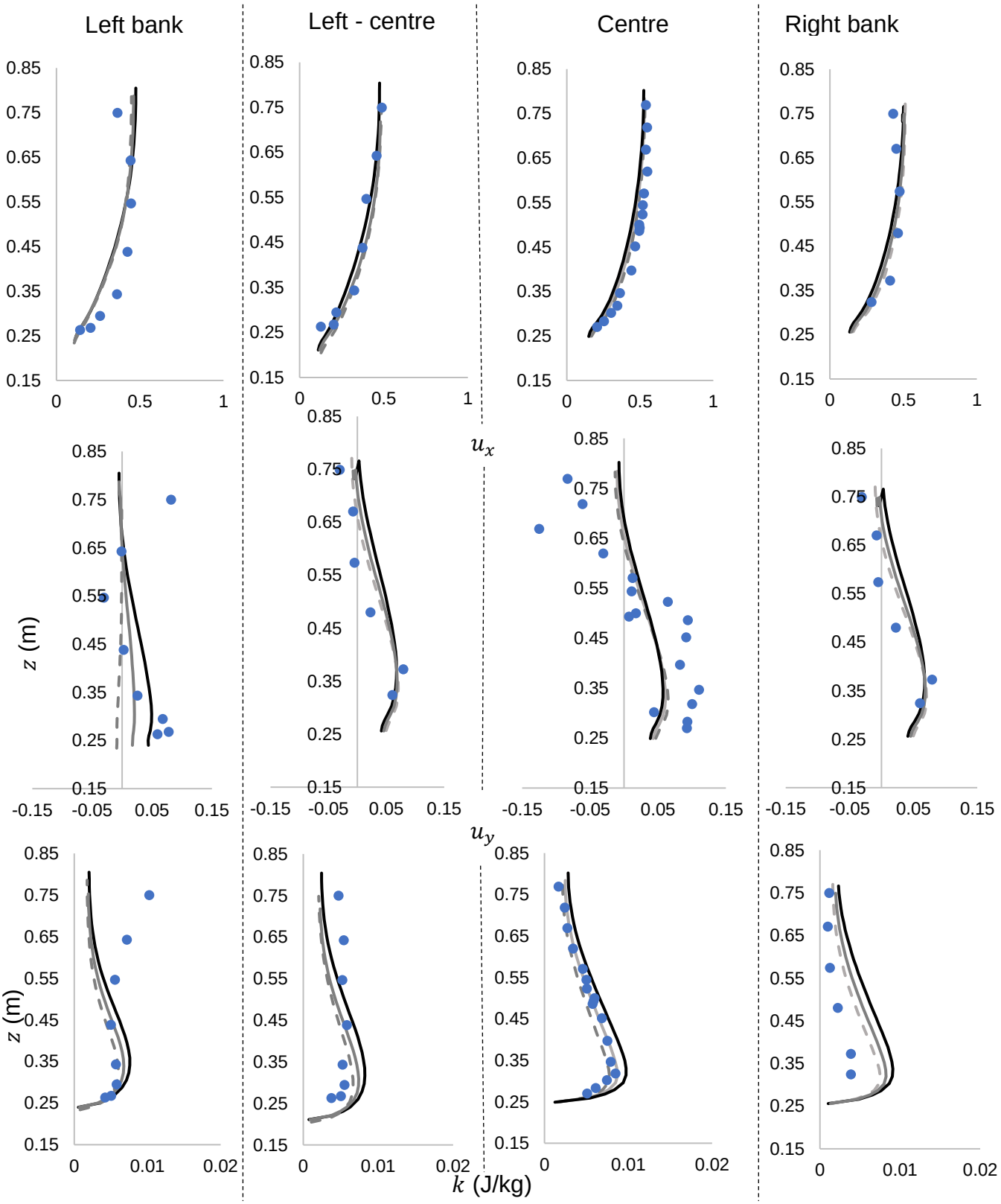


Figure 6.8. Comparison of observed data (blue circles) against results for the calibrated model ($C_D = 0.52$, dashed grey line), for the simulation where the drag coefficient was set to the value reported by Schmeekle et al., (2007) ($C_D = 0.91$, solid grey line), and where the drag coefficient was set to unity ($C_D = 1.0$, solid black line). Flow profiles describe the streamwise velocity ($u_x$), vertical velocity ($u_y$), and TKE (k) at four points along the apex cross-section.

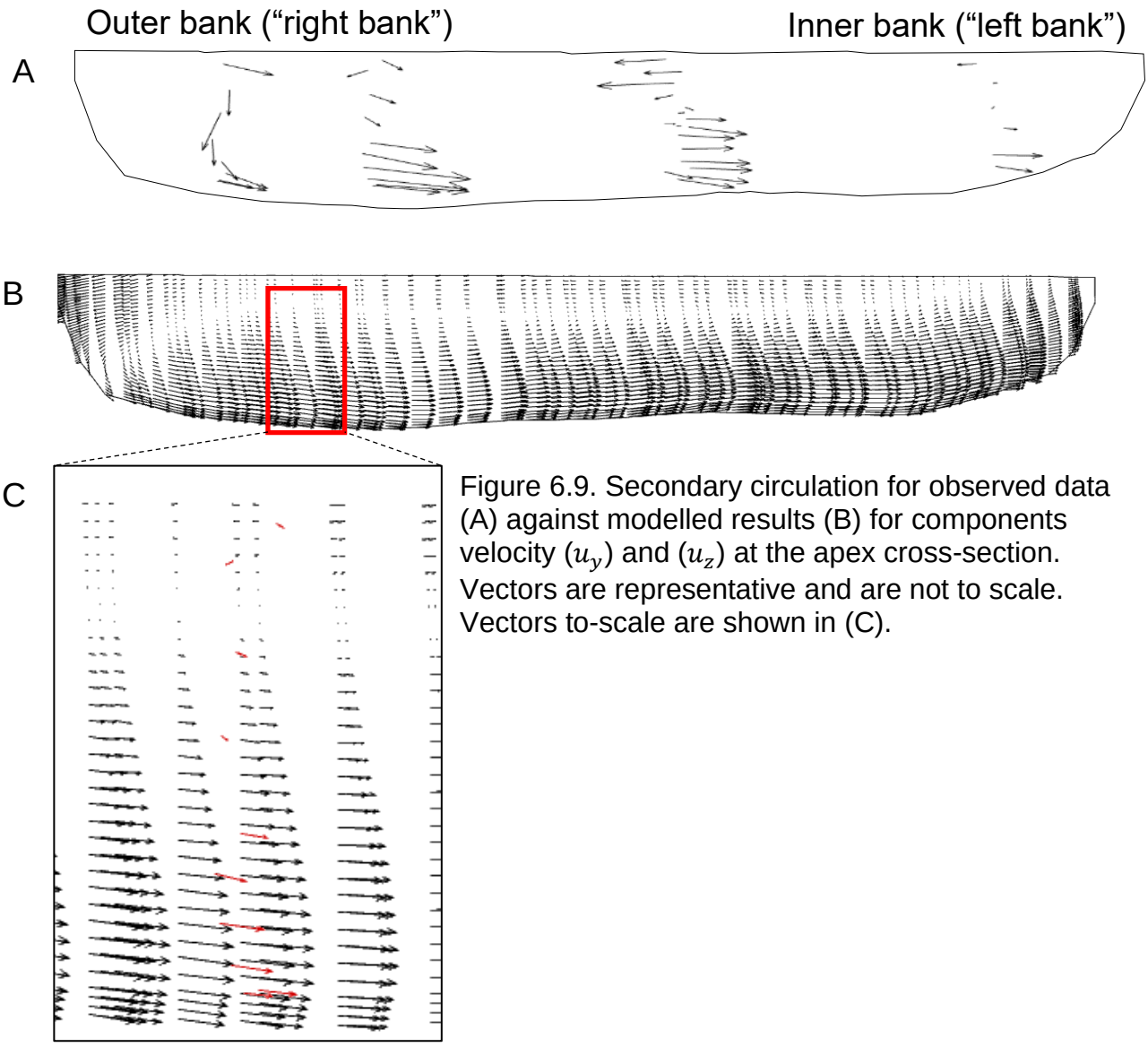


Figure 6.9. Secondary circulation for observed data (A) against modelled results (B) for components velocity ($u_y$) and ($u_z$) at the apex cross-section. Vectors are representative and are not to scale. Vectors to-scale are shown in (C).

Common descriptors for river flow are turbulence intensity (*I* ) and the Reynolds number (*Re* ) which may be useful for illustrating the characteristics of the calibrated flow. Values for *Re* and *I* were calculated for the central flow at the apex cross-section described above: *I* was found to be 0.136 and *Re* was had a value of 293904.87. The turbulence intensity is defined as the ratio of the root-mean-square of the velocity fluctuations $u'$ to the Reynolds averaged mean flow velocity $U$, described as $I = \frac{u'}{U}$ (Hickin, 2004). A turbulence intensity value of 0.136% is considered low and characterises a low level of turbulence. Reynolds numbers smaller than 500 described laminar flows dominated by viscous forces, where-as values exceeding 2000 indicate dominant turbulent forces. A high *Re* is expected for natural river flows (Bravard & Petit, 2009) and can vary between $10^5$ to $10^6$ (Birnir,

2008; Dingman, 2009). The Reynolds number for the modelled flow successfully falls within the above range, suggesting that the simulated turbulence is realistic.

## 6.5. Assessment of advection schemes

The ASME (1993) criteria for states that the numerical method, including the order of accuracy of the truncation error, must be reported. Additionally, the numerical method reported must be of a sufficient level of accuracy in order to overcome the disruptive effects of numerical diffusion. Numerical diffusion is known to affect simulation accuracy by masking the effects of physical processes on the flow. The choice of advection scheme is significant in reducing the effect of numerical diffusion and thus increasing the accuracy of the simulation.

TELEMAC-3D offers numerous advection schemes which are summarised in Table 6.6. An in-depth discussion of the advection schemes available in TELEMAC 3D are beyond the scope of this study, however further reading on advection schemes used in TELEMAC 3D is available: Hervouet, 2007; Hervouet, Pavan, & Ata, 2015; Pavan, Ata, & Hervouet, 2015.The majority of schemes available for TELEMAC 3D are residual distributive (RD) schemes, and are the most accurate schemes (i.e. least diffusive) developed for TELEMAC (Pavan, Ata, & Hervouet, 2015). RD schemes are akin to a hybrid between finite volume and finite element approaches, and have increasingly become an alternative to either approach (Deconinck, Ricchiuto, & Sermeus, 2003). The RD schemes used in TELEMAC are based on the positive streamwise invariant (PSI) scheme (Struijs, 1994) which is second order for steady cases, and is itself a limited version of the *N* scheme (Roe, 1987), both of which are also available. The accuracy of the available schemes are discussed in this section.

Table 6.6. Summary of advection schemes and their properties available for TELEMAC 3D.

| Advection scheme | Wetting/drying compatible? | Order of accuracy | Notes | Porosity treatment |
|---|---|---|---|---|
| Method of Characteristics | N | First order | Performs poorly; unstable. | - |
| SUPG | N | - | Unstable. | - |

| | | | | |
|---|---|---|---|---|
| Leo Postma | N | First-order | | Residual distributive (RD) scheme: computations are derived from fluxes leaving the triangle, discounting porosity after the initial fluxes. |
| N-Scheme | N | First-order | | RD scheme: computations are derived from fluxes leaving the triangle, discounting porosity after the initial fluxes. |
| NERD + N scheme (tidal flats compatible) | Y | First-order in time, second-order in space | | RD scheme: computations are derived from fluxes leaving the triangle, discounting porosity after the initial fluxes |
| NERD + PSI scheme (tidal flats compatible) | Y | First-order in time, second-order in space | | RD scheme: computations are derived from fluxes leaving the triangle, discounting porosity after the initial fluxes |
| PSI (classical) | N | First-order in time, second-order in space | | RD scheme: computations are derived from fluxes leaving the triangle, discounting porosity after the initial fluxes |
| First-order predictor corrector scheme | N | First-order | Performs poorly on shallow zones | RD scheme: computations are |

| | | | | |
|---|---|---|---|---|
| | | | (Hervouet, Pavan, & Ata, 2015). | derived from fluxes leaving the triangle, discounting porosity after the initial fluxes |
| Second-order predictor corrector scheme | N | Second-order | Performs poorly on shallow zones (Hervouet, Pavan, & Ata, 2015). | RD scheme: computations are derived from fluxes leaving the triangle, discounting porosity after the initial fluxes |
| Locally implicit predictor-corrector scheme (LIPS) | Y | First-order in time, second-order in space | The least diffusive scheme for shallow/ dry zones (, Hervouet, Pavan, & Ricchiuto et al., 2017) | RD scheme: computations are derived from fluxes leaving the triangle, discounting porosity after the initial fluxes |

The research requirements necessitated that the advection scheme was of low diffusivity and compatible with a wetting/drying regime. A review of the literature regarding advection schemes used by TELEMAC found that the most accurate schemes are the predictor-corrector (PC) schemes, which introduce the derivative in time in the upwinding process of the classical N and PSI schemes. The most accurate of these schemes is the second-order scheme. However, both the first- and second-order PC schemes are explicit and cannot work in dry zones (Pavan, Ata, & Hervouet, 2015). A semi-implicit scheme, the locally implicit predictor-corrector scheme (LIPS) has been developed for use with dry zones at the cost of increased numerical diffusion compared to the other predictor-corrector schemes. Despite the increased numerical diffusion associated with local implication on dry zones the LIPS method is less diffusive when compared to the other available schemes with wetting and drying options (Hervouet, Pavan, & Ricchiuto, 2017). After LIPS the next, least diffusive schemes are the classical PSI scheme, *N* scheme, and Leo Postma (Hervouet, Pavan, & Ata, 2015). The relative diffusivity of the RD schemes as based on the literature is illustrated in Figure 6.10.

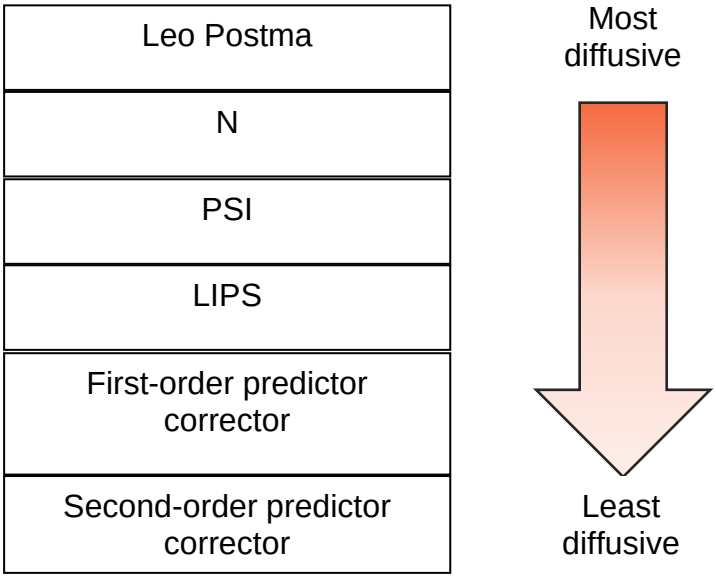


Figure 6.10. RD schemes available in TELEMAC 3D ordered in terms of diffusivity

In order to choose the most appropriate advection scheme the accuracy of each RD approach was tested using the model paradigm as described in the calibration section above. This was achieved by calibrating the bulk drag coefficient for each of the advection scheme on the refined M3 mesh, whereby the bulk drag coefficient was altered until the free surface and flow variables for streamwise velocity and turbulent kinetic energy closely matched those of the observed flow. The bulk drag coefficient was chosen as the calibration parameter to avoid altering the observed flow parameters. The initial conditions remained constant between model runs to ensure that any variation between the schemes could be attributed to numerical diffusion. The calibrated drag coefficients for each advection scheme tested can be found in Table 6.7.

Table 6.7. Calibration results for different advection schemes

| Advection scheme | $C_D$ |
|---|---|
| Leo Postma | 0.52 |
| *N* | 0.52 |
| NERD + PSI | 0.52 |
| NERD + PSI | 0.52 |
| PSI | 0.52 |
| LIPS | 0.52 |

All of the schemes tested calibrated with the same bulk drag coefficient. In order to better assess the impact of the different advection schemes different flow variables for velocities $u_x$ , $u_y$ , $u_z$ and TKE $k$ were compared to assess what differences manifested. The profiles for streamwise velocity and TKE can be seen in Figure 6.10. Visually only very small differences can be observed between the flow profiles for either velocity or TKE, with the overall shape of each profile consistent between advection schemes. The extent of the differences between the data and each advection scheme was tested by comparing the values on the node closest to the measured data at the same time-step. The differences between the results were assessed using RMSE method. Table 6.8 shows results of RMSE for the central channel location where the flow is the most stable. The LIPS and PSI scheme agreed with the measured profiles the best, having the lowest RMSE for streamwise velocity $u_x$ and TKE. However, both schemes displayed slightly lower accuracy for velocity $u_y$ compared to the other schemes. The differences between the measured and modelled profiles were small for all schemes, with differences increasing for velocity $u_y$ and $u_z$ respectively.

Table 6.8, Comparison of RMSE values for stream profiles in the channel centre for different advection schemes

| | $u_x\ (\mathrm{m/s})$ | $u_y(\mathrm{m/s})$ | $u_z(\mathrm{m/s})$ | $k(\mathrm{J/kg})$ |
|---|---|---|---|---|
| Leo Postma | 0.0436 | 0.0472 | 0.0125 | 0.0012 |
| N | 0.0435 | 0.0472 | 0.0125 | 0.0012 |
| PSI | 0.0427 | 0.0475 | 0.0125 | 0.0011 |
| LIPS | 0.0427 | 0.0475 | 0.0125 | 0.0011 |

Notably, both PSI and LIPS schemes had the same RMSE values for all variables suggesting a limited difference between either schemes for the calibration scenario. Both schemes are similar as LIPS is a PSI-variant which differs by, firstly, applying a locally semi-implicit scheme on dry regions therefore allowing for the dry-wet schemes otherwise disallowed by the PSI scheme and, secondly, by applying a predictor-corrector which introduces a derivative in time, replacing an implicit time

integrator by an element-by-element correction. Further information on the explicit predictor formulation is discussed in Ricchiuto & Abgrall (2010), which inspired the development of the LIPS scheme discussed in Pavan, Ata, & Hervouet (2014). The similarity may explain why the results are so similar, however a review of the literature suggests that the LIPS scheme is the least diffusive scheme of those tested above. Hervouet, Pavan & Ata (2015) tested the diffusivity of the *N*, PSI, and LIPS scheme by calibrating flow in reference to the height of a rotating cone, a common method for evaluating advection schemes consisting of a solid body rotating Gaussian cone with a steady velocity field (Pavan, Ata, & Hervouet, 2014). The height of the cone after one rotation is obtained and should be theoretically 1m, with the maximum values obtained for each advection scheme being an indicator of the performance of the advection scheme: the *N* scheme had a height of 0.18m, the classical PSI scheme had a height of 0.21m, and LIPS had a height of 0.79m. The LIPS scheme obtained the closest value to the cone height, suggesting that the LIPS scheme was the least diffusive compared to the others. For this reason the LIPS scheme was chosen as the advection scheme for the model.

However, the preference of TELEMAC 3D for RD schemes is problematic for the inclusion of porosity terms in the model. Porosity is the ratio of the volume of water to volume of blockage per model cell and is used to describe the spatial variations in blockage throughout the water column. The inclusion of porosity is problematic because of how RD schemes derive the solution form fluxes within the cell rather than at the points, or vertices. The solution derived from each cell ignores porosity values prescribed to each vertex after the initial computation, introducing a great level of uncertainty to the influence the porosity terms would have on simulated flow. The problematic aspect of including porosity in the model is further discussed in the next section.

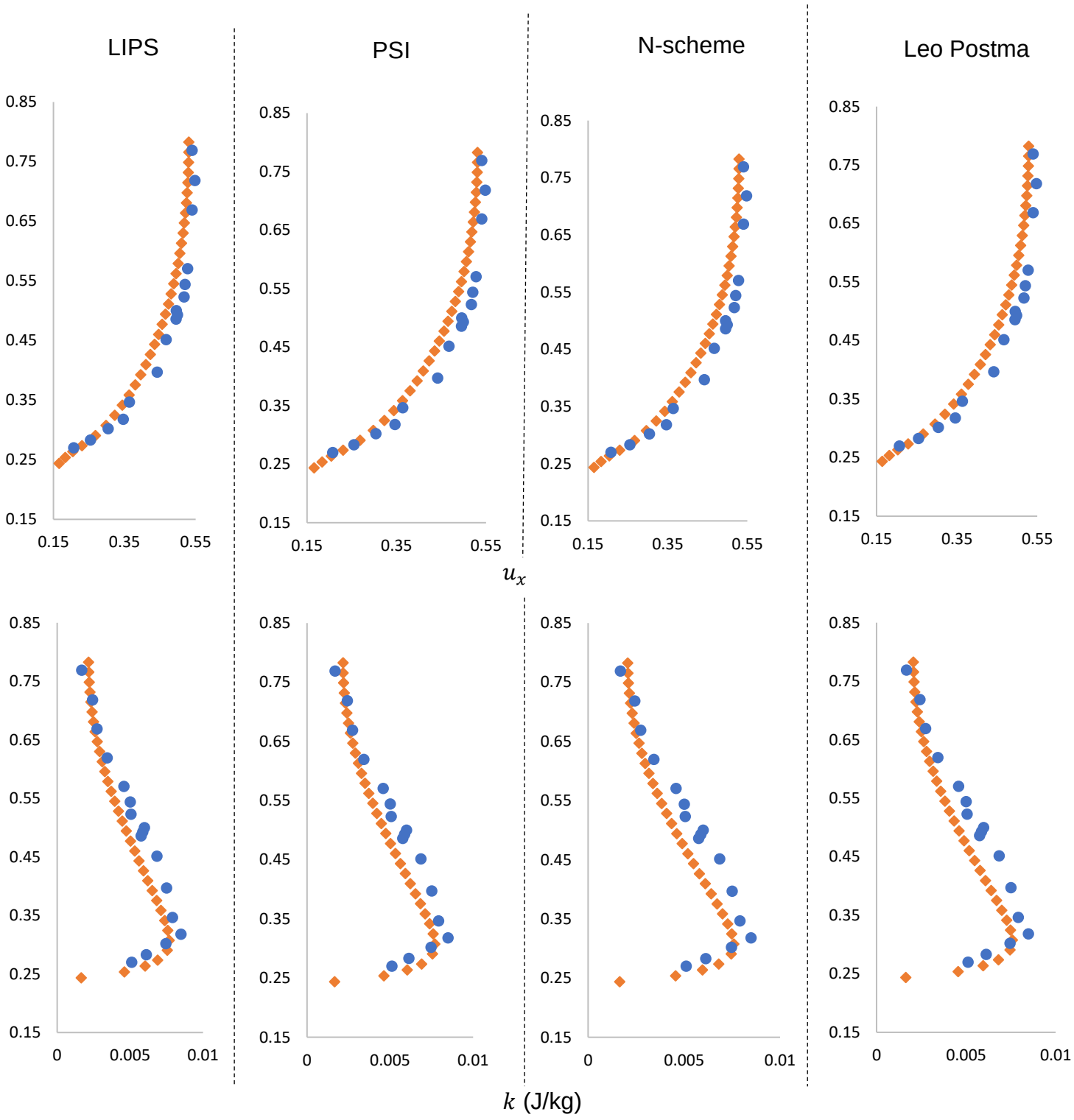


Figure 6.11. flow profiles for velocity $u_x$ and TKE $k$ for the RD schemes

### 6.5.1. Discussion of the exclusion of porosity from the model

Porosity is used to represent the blockage caused by roughness elements in the main flow. For example, in the DANS method porosity is one of the parameters considered when describing the effects of multi-scalar roughness elements, along with the frontal projected area, lateral projected area, and element surface area. In typical DANS methodology, the RANS equations are supplemented with porosity terms derived from roughness elements, with the porosity altered for each computational cell to represent porous media. However, a key methodological limitation of TELEMAC 3D is that porosity cannot be prescribed as a parameter, with no option available allowing the user to alter cell volume. This makes it difficult to implement porosity terms in TELEMAC 3D. Further to this, the usage of RD schemes is problematic due to two reasons: first, no tests for the coupling of porosity was completed during the development of TELEMAC's RD schemes and, second, RD schemes largely ignores the contribution of porosity during its treatment of fluxes within the cell domain. Both points are expanded below.

Considering the first point, during the development of RD schemes for TELEMAC 3D tests for the coupling of porosity with RD schemes were not performed. Therefore, no literature detailing the interaction of RD schemes coupled with porosity using TELEMAC 3D exist at the time of writing. This is significant as it is unknown how TELEMAC's RD schemes derives the solution with the inclusion of porosity terms and to what magnitude their inclusion might influence flow processes. The absence of any literature also makes it difficult to explore how porosity can be integrated within TELEMAC 3D. A thorough investigation into RD advection schemes and how they could be coupled with porosity would be time-intensive and beyond the parameters of this study.

The second point detailed how RD schemes may largely ignore porosity values at cell vertices. In classical finite-element approaches porosity is typically treated as a multiplication factor at the element level. For example, in classic Galerkin methods the porosity at each vertex is equal because the integral for the triangle is equal to the surface of the triangle divided by three (i.e. the number of vertices on the triangle). The solution is achieved by performing integrals at each element. However, RD approaches derive their solution from the fluctuations between each triangular

vertex. The fluctuations are defined by considering how the input from upstream and downstream points influence the triangular free surface and are used to evaluate the contributions of each vertex (Hervouet, 2007; Kozdon & Mallison, 2011). The input at each vertex is defined by the differences between the flow quantities at each vertex. These differences are then used to define the fluctuations from which the scheme derives the solution (Hervouet, 2007). RD schemes split the complete flux balance into its multidimensional flow components which are distributed over the cell and are used to update the cell vertices (Deconinck, Ricchiuto, & Sermeus, 2003). A suitable fraction of the fluctuation is assigned to each downstream vertex, rendering the cell domain dependant on a particular vertex (Morton and Baines, 1995). This differs from non-RD schemes, such as the Galerkin method, where the solution for the domain considers each contribution more generally by considering the equal contribution of the flow values at each vertex. In this way, after the initial computation, RD schemes derive the solution from the fluxes between the vertices rather than the values at each vertex. Because of this approach the porosity values are ignored after the initial computation. Including porosity terms in TELEMAC would therefore introduce a significant degree of uncertainty: it is unknown to what degree to which the initial porosity value influences the solution, especially considering that only the initial value is used before being ignored during the rest of the computation.

The difficulties presented above in the lack of option for including porosity as a parameter, the large unknowns present due to a lack of literature on the coupling of porosity with RD schemes, how RD largely ignore porosity values after the initial computation due to the treatment of fluxes, and the considerable time necessary to investigate the problem meant that porosity was not included as a parameter within this study. However, the influence porosity has on the flow can be replicated by applying head losses at specific nodes which represent the location of a roughness element. These head losses represent the form-induced stresses associated with the roughness effects associated with porous media. Appropriate head losses are applied through the parametrisation of the drag term, which uses the measured spatially averaged parameters previously mentioned above: the frontal projected area, the lateral projected area, and the element surface area. For a more detailed description of how the drag term was parametrised for the roughness elements at the bed see Chapter 4, Section 4.3. For a description of how the drag term was

parametrised for roughness elements obstructing the main flow (i.e. plant volume) see Chapter 7.

## 6.6. Grid Convergence Index

The ASME (1993) basic criteria for mesh independence testing states that solutions for a range of different grid resolutions must be reported to demonstrate the grid independence of the solution. One of the major components contributing to numerical error in CFD solutions stems from the approximations made using the finite element method in the transformation of the partial differential equations into algebraic equations (Eça & Hoekstra, 2014). This is known as discretisation error. The relative importance of discretisation error decreases with increasing grid refinement, making it necessary to identify the impact grid resolution has on the solution. The Grid Convergence Index (GCI) approach as described by Roache (1994) was used to analyse the numerical results of changing grid resolutions. The GCI method allows for the estimation of asymptotic solution and bounds of discretisation error, following the assumption that as the grid is successively refined the spatial and temporal discretisation errors asymptotically approach zero (Kwaśniewski, 2013). The GCI approach is ASME (1993) approved for the assessment of numerical accuracy through the impact of grid refinement. The GCI was estimated using:

$$GCI = \frac{F_s|\varepsilon|}{(r^{px} - 1)}$$

where $F_s$ is the factor of safety, $\varepsilon$ is the error estimator for fractional error for the fine grid solution, and $r^p$ is the grid refinement ratio, where $r = h_1/h_2$ and $h_i$ is the mesh resolution (edge length), and $px$ is the order of convergence. Using a comparison between the finest and intermediate meshes as an example, the error estimator is calculated as:

$$\varepsilon = \frac{(f_1 - f_2)}{f_1}$$

where $f_*$ is the quantity of interest (for example: streamwise velocity $u_x$). To effectively compare grid convergence between the meshes the grid refinement ratio must be constant i.e.

$$r = h_3/h_2 = h_2/h_1 = const.$$

where $h_1 < h_2 < h_3$. The order of convergence is calculated as:

$$p = \ln\left(\frac{(f_3 - f_2)}{(f_2 - f_1)}\right)/\ln(r)$$

As the order of convergence was estimated using three meshes the factor of safety used was 1.25, which is the factor of safety used for comparing more than two meshes as recommended by Roach (1994). The grid refinement ratio for this study is 2. This value was chosen because grid refinement ratios need to be greater that 1.3 to obtain acceptable results using the GCI method (Roache, 1998; Schwer, 2008), and refining a mesh by a factor of 2 is deemed a rigorous measure for grid convergence methods (Lockard, 2010).

GCI was conducted using the three meshes described previously in this chapter. Using three meshes is the typical approach to demonstrate a relationship between errors and resolution (Lockard, 2010). The solution accuracy was assessed by comparing the two coarsest meshes, M1 and M2, and comparing the intermediary mesh, M2, against the refined mesh, M3. The finest mesh, M3, was used to calibrate the bulk drag coefficient and to test the advection schemes in the previous sections. M3 was refined to a level that was deemed as practical as possible without causing the simulation to crash and converge within a reasonable time (i.e. less than three days). The accuracy of the numerical solution was determined using the calibration of the bulk drag coefficient and by comparing five quantities of interest: the three components of velocity $u_x$, $u_y$, and $u_z$, turbulent kinetic energy $k$, and the dissipation of turbulent energy ε. To compare the flow quantities between the meshes, the coarsest mesh was linearly interpolated onto the refined mesh. Linear interpolation was completed using the CFD visualisation and analysis software Tecplot 360 EX (version 2016 R1).

### 6.6.1. Results

The median values for each flow quantity is reported in Table 6.9. Mesh comparisons indicated that the model converged towards a mesh independent solution; the median GCI values for each quantity decreases as the mesh is refined. This suggests that the discretisation error is the smallest for the refined mesh M3.

Table 6.9. Median values of the Grid Convergence Index (GCI)

| GCI | $u_x$ (%) | $u_y$ (%) | $u_z$ (%) | $k$ (%) | $\varepsilon$ (%) |
|---|---|---|---|---|---|
| GCI M1 - M3 | 1.52 | 2.77 | 22.92 | 5.50 | 5.80 |
| GCI M2 - M3 | 0.97 | 2.01 | 18.36 | 4.31 | 3.90 |

Comparisons of the flow quantities of velocity $u_x$, $u_y$, and $u_z$, and turbulent kinetic energy $k$ between meshes are shown in Figure 6.12. Mesh comparisons were completed using the same mesh combinations used for the GCI analysis above. High scattering in the initial results were found to be a result of poorly developed flow at the inlet, within the new drag layer at the bed, and at the bank and free surface boundary. Greater scattering at shear zones has previously been reported and is not unexpected (Hardy et al., 2003). Data representative of these areas was removed, which reduced the scatter. The results showed a higher level of scattering for the M1-M3 comparison than the M2-M3 comparison. Linear regression was used to compare the differences between the values for flow variables at the same node between different meshes, the values of which can be seen in Table 6.10. When comparing M1-M3 linear regression showed a less agreement between the node values, with all variables exhibiting lower correlation values when compared to those of M2-M3. Higher degrees of scattering were found for TKE, with correlation values of 0.60 and 0.88 for M1-M3 and M2-M3, respectively.

Table 6.10. Regression coefficients for flow variables between meshes.

| $r$ | $u_x$ | $u_y$ | $u_z$ | $k$ |
|---|---|---|---|---|
| M1 - M3 | 0.98 | 0.99 | 0.857 | 0.60 |
| M2 - M3 | 0.99 | 0.99 | 0.94 | 0.88 |

Correlation values across all quantities increased with mesh refinement, which is reflected in the slope and the intercept values of the fitted linear regression tending towards one and zero, respectively, with greater refinement. This result suggests a good level of agreement between the intermediate and refined meshes, M2-M3.

The higher degree of scattering for the $u_z$–component and TKE are indicative of their higher sensitivity to mesh resolution. This sensitivity has been previously reported in other studies (see, for example: Hardy et al., 2003; Rameshwaran & Nadan, 2004).

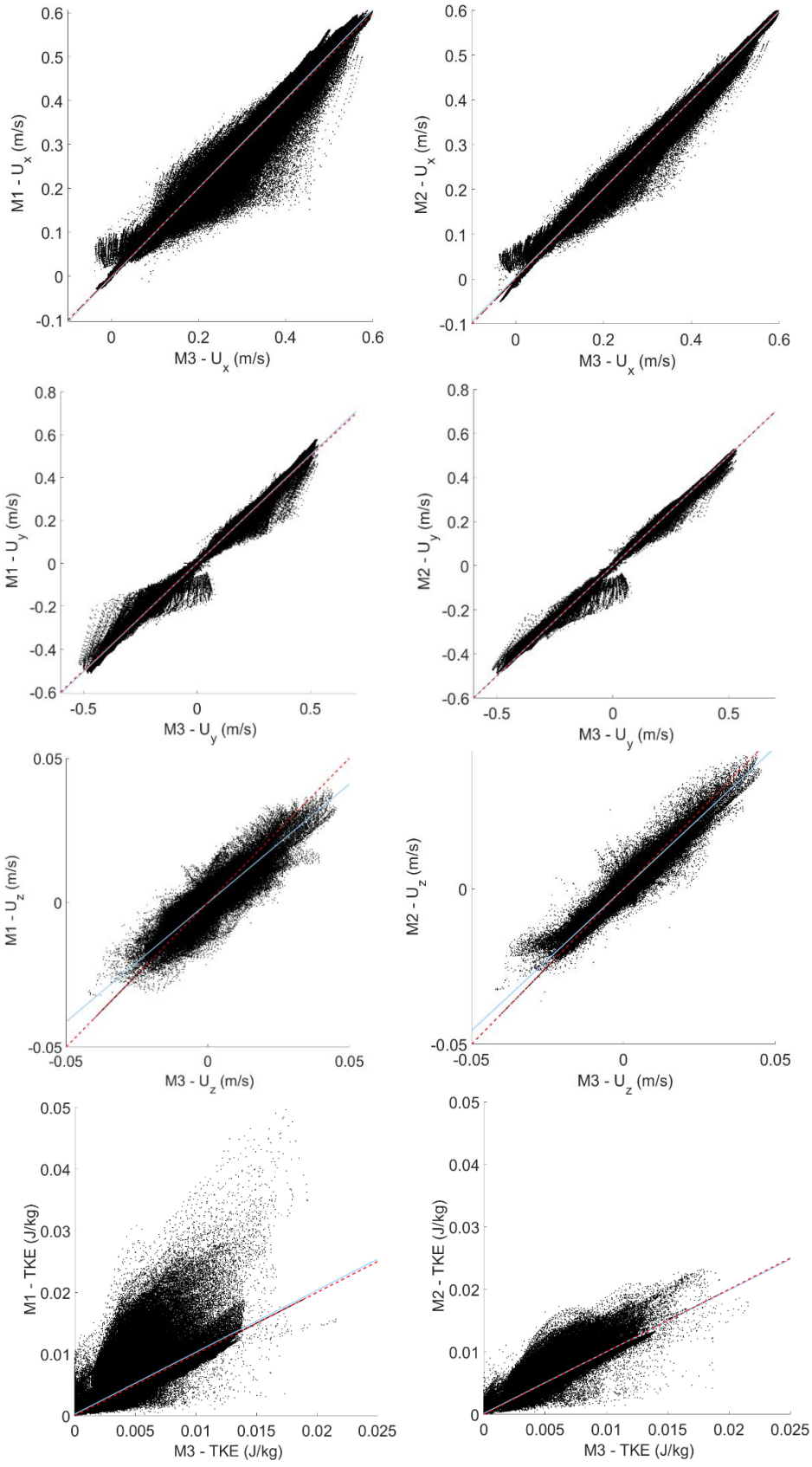


Figure 6.12. GCI results between coarse (M1), intermediate (M2) and fine meshes (M3). Also shown are 1:1 (red, dashed) and regression (blue) lines.

## 6.7 Summary

This chapter has considered the calibration of the bulk drag coefficient, the comparison of flow variables, assessment of advection schemes, and the analysis of numerical accuracy through successive grid refinement. The model was calibrated at a realistic bulk drag coefficient where the free surface at both banks effectively emulated the measure free surface slope. This suggested that the model can effectively reproduce the flow conditions represented in the February case, and is appropriate for scenario-based investigations. The model predictions also converged towards a grid-independent solution, indicating that discretisation error is reduced as the mesh resolution is increased. This indicates that the refined meshes are appropriate for the research requirements.

# Chapter 7 | Integrating vegetation within the 3D model

## 7.1. Introduction

This chapter discusses the integration of vegetation within the 3D model, including a discussion of the approach used to integrate patch planforms on the mesh, the programming for simulating the effects of vegetation flow resistance, and the calibration of the model using three vegetated cases: the May flow, September low flow, and September high flow conditions. Also discussed is the impact of drag exerted by overhanging vegetation on the free surface, and the parameterisation of the effect of floodplain vegetation flow resistance. The integration of the patch planforms used data which described the planform shape mentioned previously in Chapter 3. As previously discussed, TELEMAC builds a 3D mesh from a 2D base. As such, the patches were first defined on the 2D mesh using polygons which described planform geometry. The vertical profile for each patch was then related to the model mesh through a new subroutine. The model was calibrated using the vegetation distributions observed for both the May and September periods to represent low and high vegetation coverage, respectively. Two methods for approximating drag at the vegetation patches were assessed and the method with the best approximation of the observed flow was selected to represent the effects of vegetation-flow interaction. To better represent the influence of plant morphology on flow, a sub-routine was built which represented the two common patch profiles: the trailing geometry of *Sparganium emersum*, and the uniform, emergent shape of *Sparganium erectum.* The influence of overhanging vegetation on surface flow was also simulated to better capture the bulk effect of vegetation roughness on channel flow, and to realistically represent the impact of overhanging vegetation on the upper region of the velocity profile. Finally, the impact of vegetation occupying the berm, or the local floodplain, region was also implemented.

## 7.2. Describing the distribution of vegetation patches in the 2D mesh

Vegetation patches were integrated first onto the initial 2D mesh. The integration process involved generating a new mesh for May and September, respectively. The planforms for each patch were described by polygons, as discussed in Chapter 3, Section 3.2.3. An identifier for each species was prescribed to each polygon before being interpolated onto a 2D mesh variable which described the distribution of patches throughout the reach.

The method used for this process is summarised in Figure 7.1. A detailed description of the process is presented henceforth.

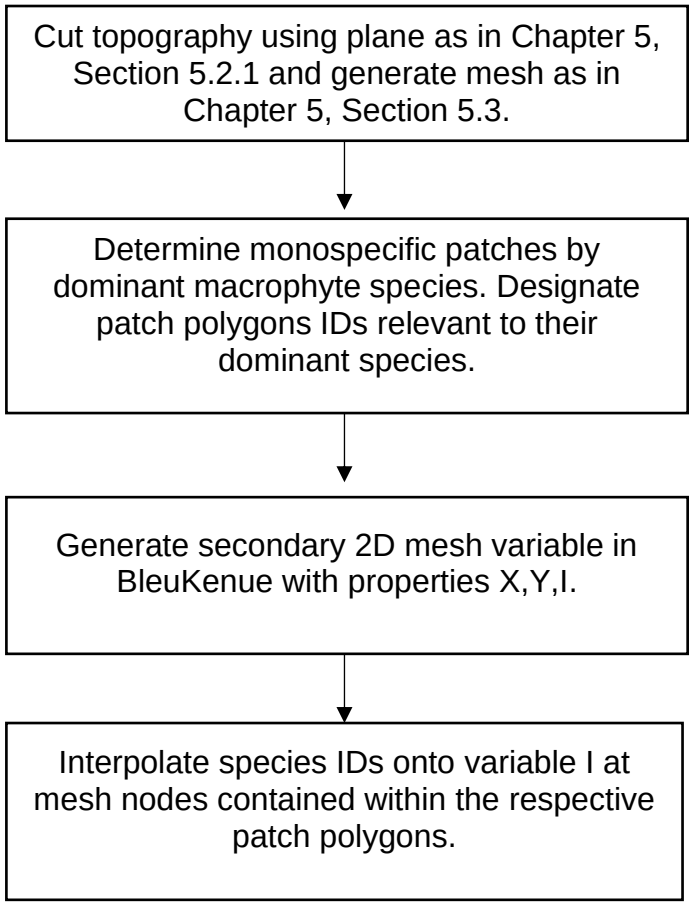


Figure 7.1. Method for integrating patch planforms on the initial 2D mesh.

The meshes were generated using the same method discussed in Chapter 5, Section 5.2 where the topography was cut by a plane describing the limit of the free surface measured for May and September, respectively. Once the topography was

cut to the appropriate elevation an unconstructed triangular mesh was generated for both periods using the same process used to generate the mesh in Chapter 5, Section 5.3. These meshes formed the basis for integrating, calibrating, and assessing vegetation described throughout the rest of this chapter.

The measured vegetation patches were originally organised into four groups: the first three groups were mono-species patches of *Sparnigum erectum*, *Sparganium emersum*, and *Potomogeton natans*, whilst the fourth group were patches composed of mixed vegetation. It is difficult to accurately represent the effects of patches composed of multiple vegetation species on the flow and, to the author's knowledge at the time of writing, no literature has attempted to elucidate the relationships between patches composed of two or more species and flow resistance. An exploration of the relationship between poly-species patches and flow resistance was beyond the scope of this study. Therefore, for patches containing multiple vegetation species, only the effects of the dominant species were considered. The final dataset was thus described three groups of patches. The species composition for the May case was dominated by patches of *S. erectum* and *S. emersum*, with *P. natans* present in two small patches. For the September case *S. erectum* and *S. emersum* were again the dominant species, however patches identified as other species were present in a greater variety and number compared to the May case. Of these, *P. natans* was the most common although still less frequent than *S. erectum* and *S. emersum.* The other species occupying the channel were largely terrestrial and included *Persicaria hydropiper, Urtica dioica,* and *Epilobium hirsutum,* as well as the aquatic species *Crassula helmsii* and *Callitriche* spp. Patch planforms measured for the September month are slightly underestimated due to measurement difficulties on account of high vegetation growth and fast flow. Figure 7.4. shows the distribution of overhanging bank vegetation, which was mainly composed of herbaceous and grass species, however the outside of bends also included osiers which had grown from willow spilings.

The planform patches were integrated into the refined 2D mesh described in chapter 6. BlueKenue was used to integrate the patch polygons. To integrate the vegetation, first a new mesh variable was generated; a mesh variable consists of a copy of the nodes which compose the 2D topographic mesh and to which a new variable can be prescribed. In this case, each node had properties denoting the position in *X,Y* coordinates and its patch identifier *i.* For each group, every polygon was assigned a species identification number, ID, which was shared by all polygons representing the same species. The polygons were then mounted onto the new 2D mesh variable by interpolating each polygon onto the mesh. Where the nodes were within the polygon, the property *i* was assigned the species ID (Figure.7.2). Where no nodes fell within a polygon *i = 0.*

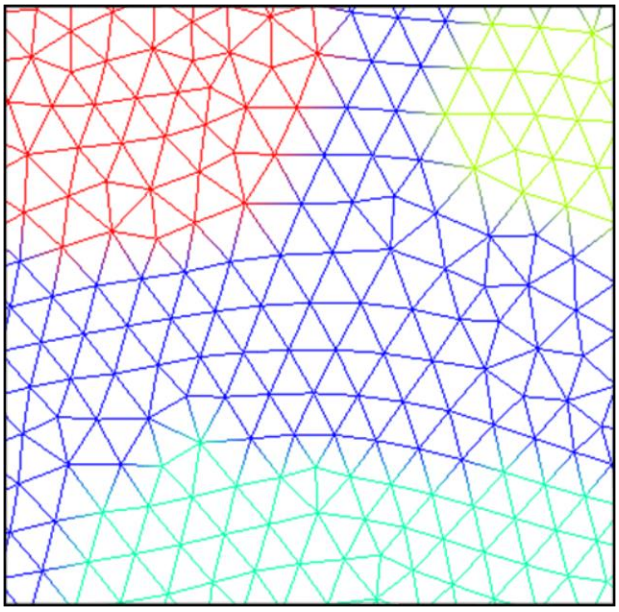

Figure 7.2 Example of interpolated patch IDs, comparing non-vegetated nodes (blue) against nodes assigned species IDs for S. erectum (cyan), S. emersum (lime), and P. natans (red).

This process was conducted for every polygon, resulting in the description of the distribution of patches for both the May (Figure 7.3.) and September (Figure 7.4.) periods, and for overhanging vegetation (Figure 7.5.)

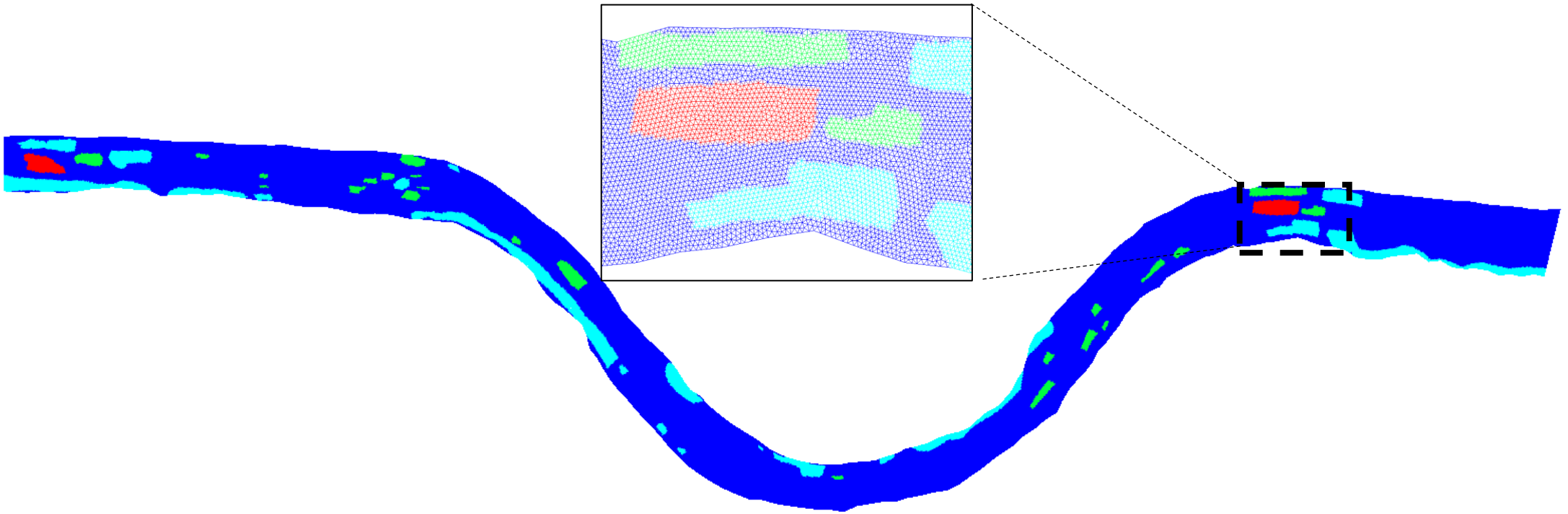

Figure 7.3. Distribution of the interpolated patch planforms for each group of species for the May, low abundance period for the entire reach. *S. erectum* (cyan), *S. emersum* (lime), and *P. natans* (red).

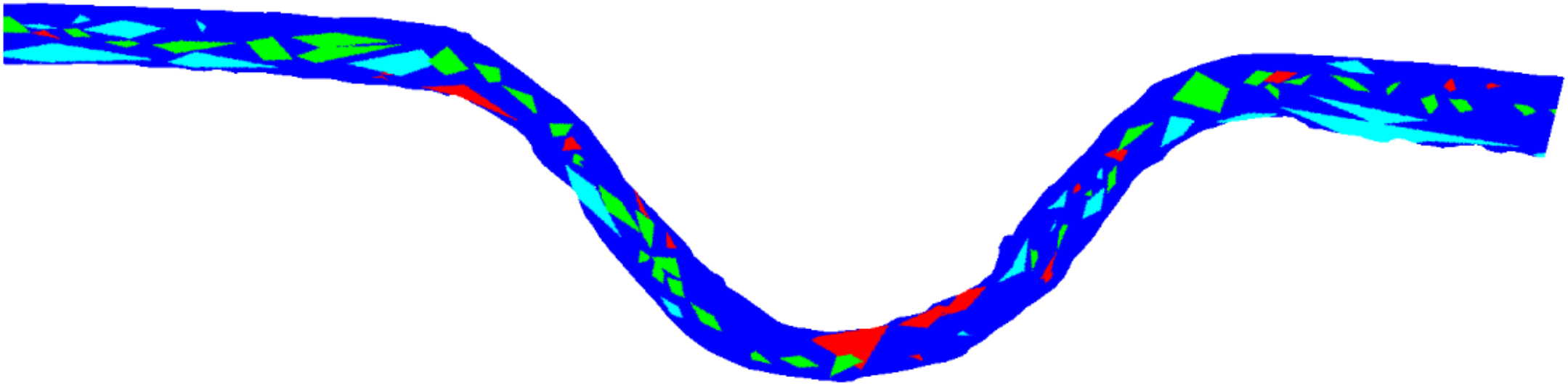

Figure 7.4. Distribution of the interpolated patch planforms for each group of species for the September, high abundance period for the entire reach. *S. erectum* (cyan), *S. emersum* (lime), and *P. natans* (red).

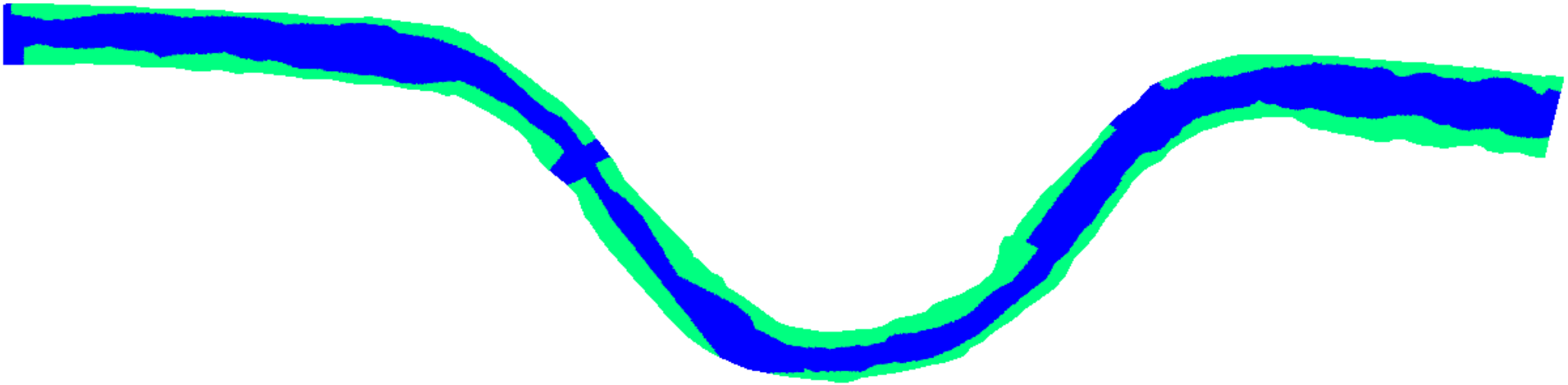

Figure 7.5. Distribution of the interpolated area for overhanging vegetation (green) measured during the September period.

## 7.3. Building the 3D vertical profiles of vegetation patches:

The second step related the vertical profile of each patch to the 3D mesh built at the beginning of TELEMAC's computation. The method involved building a new subroutine which accurately described the effects of vegetation through the 3D distribution of head losses.

### 7.3.1. Representing 3D vegetation using the DANS method

The key species, *S. erectum*, *S. emersum*, and *P. natans,* can be distinguished as discrete morphotypes: *S. erectum* is a linearly emergent species (Liffen et al., 2011) with high flexural rigidity and can be considered as extending uniformly throughout the water column. An analysis of the literature suggests that *S. erectum* is one of the most researched species, with many studies detailing its tall, rigid stems which exhibit high resistance and remain erect under relatively high flows (Liffen et al., 2011) and can be assumed to extend above the free surface. Where the river surface rises, resistance can be continued to apply at nodes at higher elevations as the free surface elevates. In this fashion the model simulates the flow encountering previously emerged sections of the plant. As such, *S. erectum* was represented by the uniform distribution of head losses at all nodes above the patch planform. Both *S. emersum* and *P. natans* are mechanically similar to rooted-floating macrophytes, meaning that their canopy largely remains at the river surface; their flaccid structures allow for the canopy to change elevation with changing surface elevation. As such, both species were represented using a trailing profile, with the influence of head losses maintained at each layer with increases in surface elevation until the peak of the profile reached a prescribed maximum elevation.

The influence of sub-grid scale vegetation roughness resulting from surface area was related to the 3D model mesh through the application of head losses at each mesh layer occupied by vegetation. Head losses were applied to nodes above the first four layers of the new bed described in Chapter 4, Section 4.3. This distribution is described by the schematic in Figure 7.6.

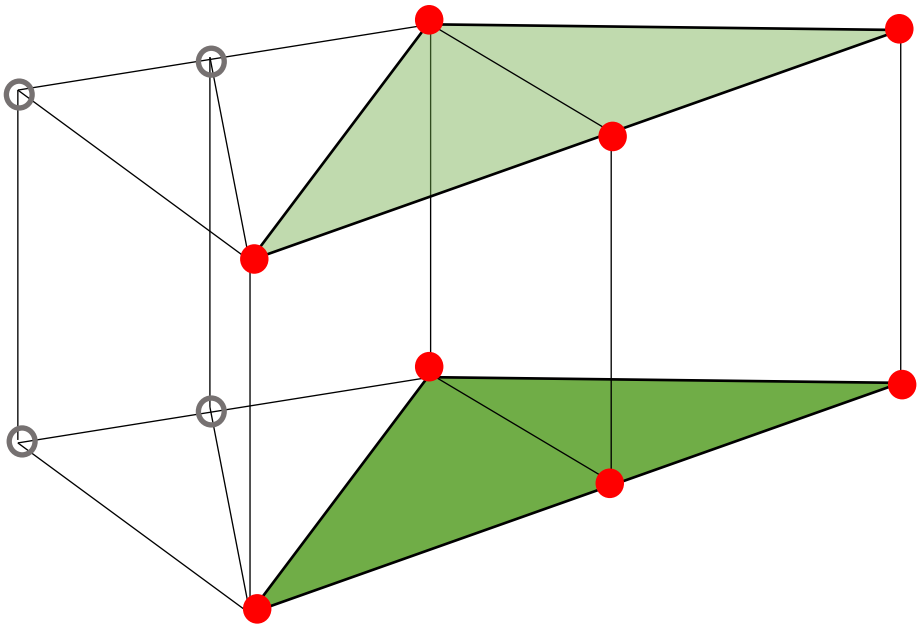

Figure 7.6 Nodes within an integrated vegetation patch (green) have head losses applied (red) in contrast to nodes in unvegetated zones of the mesh which remain untouched (grey circles).

Head losses were applied through a new subroutine which was composed of three sections: first, patch parameters were introduced along with the unique values for their respective patch ID and vegetated node ID. Each vegetated node ID was then sorted per patch ID, and then each respective vegetated node ID was matched with the node IDs belonging to the nodes in the 2D mesh. Subsequently, the matched 2D mesh nodes were used to compute their 3D counterparts at every layer at the same *x,y* coordinate. Following, for each vegetated node the areal value for the respective species and the local velocity norm were inserted into the drag equation. The local drag was then calculated at each node; the resulting head losses are the product of momentum transfer at the flow-vegetation interface and are modelled by estimating the flow resistance exhibited by vegetation (Helmiö, 2004). In this study, head losses were simulated by estimating the total drag force per unit volume, $F_i$, at each vegetated node. The equations used for modelling drag force are explored below.

The drag force at these nodes can be parameterised using the conventional drag force equation, previously discussed in Chapter 6. However, to the author's knowledge, no relationships between vegetation patches and drag coefficient have

yet been developed. Therefore, to ensure that the appropriate method was chosen two approaches were tested: the first method used the average frontal projected area for each species to estimate the velocity components $u_x$ and $u_y$ for head losses in their respective direction, whilst the average surface area was used to estimate $u_z$ components of the drag equation. The areal values were previously stated in Chapter 3, Section 3.3.3 but are reiterated in Table 7.1 for convenience.

Table 7.1. Averaged areal values for the three common in-stream vegetation species found in the River Blackwater.

| Species | Surface area $A_s$ ($m^2/m^3$) |
|---|---|
| *Spargnium erectum* | 24.3816 |
| *Spargium emersum* | 77.6668 |
| *Potamogeton natans* | 27.0000 |

The surface area was used for the $u_z$ velocity component; estimating the vertical projected area for vegetation is problematic because of canopy flexibility and deformation within the flow. High variability in vegetation positioning within the flow column introduces large levels of uncertainty when estimating an appropriate value for the vertical projected area. However, within patches drag largely results from frictional drag, which is itself proportional to the surface area of the plant. Therefore, the drag force exhibited within the patch is proportional to the surface area of the patch. As such, the averaged surface area for each species was used in to define the drag term: an approach which has been previously used in literature (see: Rameshwaran & Naden, 2012).

The second method further considers the relationship between drag and the shape of the vegetation patch: the magnitude of drag exhibited at any given patch is also proportional to the size and shape of the patch, represented by the surface area and the aspect ratio *L*/*D* (length *L* to width *D*). To represent this relationship within the model an additional term $R_f$ was introduced into the drag equation. The $R_f$ factor was determined from literature (Blevins, 2003) where solid, circular cylinders with different aspect ratios were positioned parallel to the flow. This geometry bears resemblance to the vegetation patches in regards to shape and ratio, and the use of cylinders to estimate the drag coefficient has been used in previous research (see:

Albertson et al., 1960; James et al., 2004; Rameshwaran & Naden, 2012). The relationship between the geometry and drag coefficient is described in Figure 7.7, which illustrates how the drag coefficient changes with aspect ratio for both the cylinder's surface area, defined as $\frac{\pi D^2}{2} + \pi DL$, for a turbulent flow with a Reynolds number of >$10^4$. Significant variation in the drag coefficient is evident: as the aspect ratio approaches zero the drag coefficient for the surface area reaches $C_{d0} \approx 0.575$, whilst the drag coefficient decreases as the aspect ratio increases. Physically, the drag coefficient can be said to be increasing when the aspect ratio approaches a flat circular disc, whilst the drag coefficient decreases as the cylinder lengthens and thins.

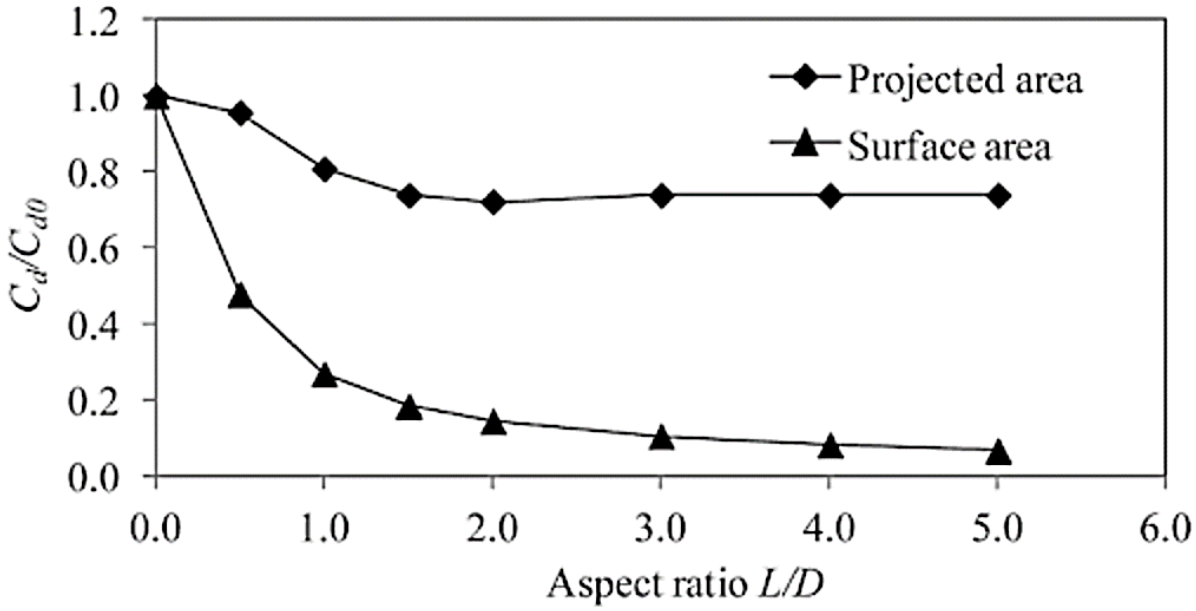


Figure 7.7. Drag coefficient variability with respect for aspect ratio for cylinders in turbulent flow (Blevins, 2003). The drag coefficients calculated using both the surface area and projected area are included.

With respect to the aspect ratio of the patch, the drag force term for the vegetation patches can be parametrised as:

$$F_i \approx \frac{1}{2} C_{d0} R_f A_s |\langle \overline{u_i} \rangle| \langle \overline{u_i} \rangle \qquad 7.1.1.$$

where $C_{d0}$ is the bulk drag coefficient applied at every patch; $A_s$ is the average surface area of the vegetation patch for the respective species; $|\langle\overline{u_i}\rangle|$ is the time-space averaged velocity' and the $R_f$ factor is defined as $R_f = C_{dn}/C_{d0}$, where $C_{d0}$ is the drag coefficient for a patch when the aspect ratio is nearly zero, and where $C_{dn}$ is the drag coefficient related to the cylindrical surface area taken from those presented by Blevins (2003) for different cylinders of varying length. The aspect ratio for each patch was calculated by dividing the maximum length and the maximum width (*L/D*). A curve was then fitted using the equation $y = 0.2651x^{-0.8506}$ which was used to estimate the coefficient $C_{d0}$ for each patch (Figure 7.8 – 7.9). This was then used to calculate the $R_f$ factor for each patch which was then inserted into equation 8.1.1 above.

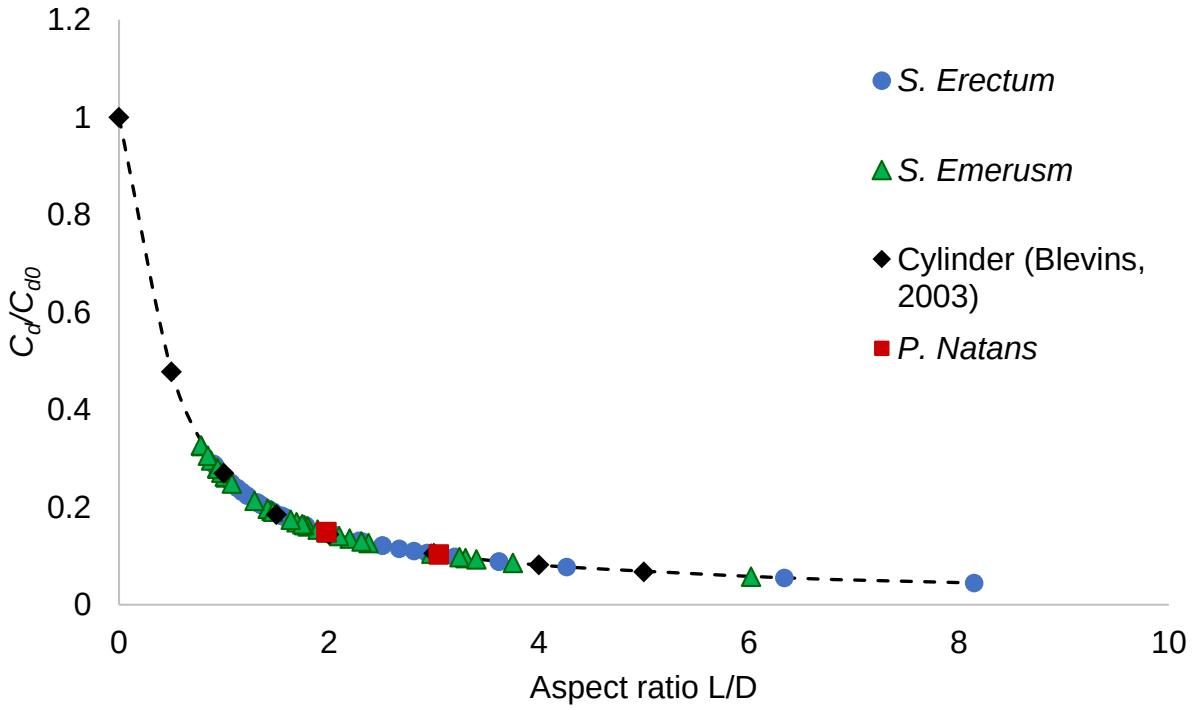


Figure 7.8. Drag coefficient variability with respect for aspect ratio for vegetation patches per species (May case), with the cylinder coefficients taken from Blevins (2003) for reference.

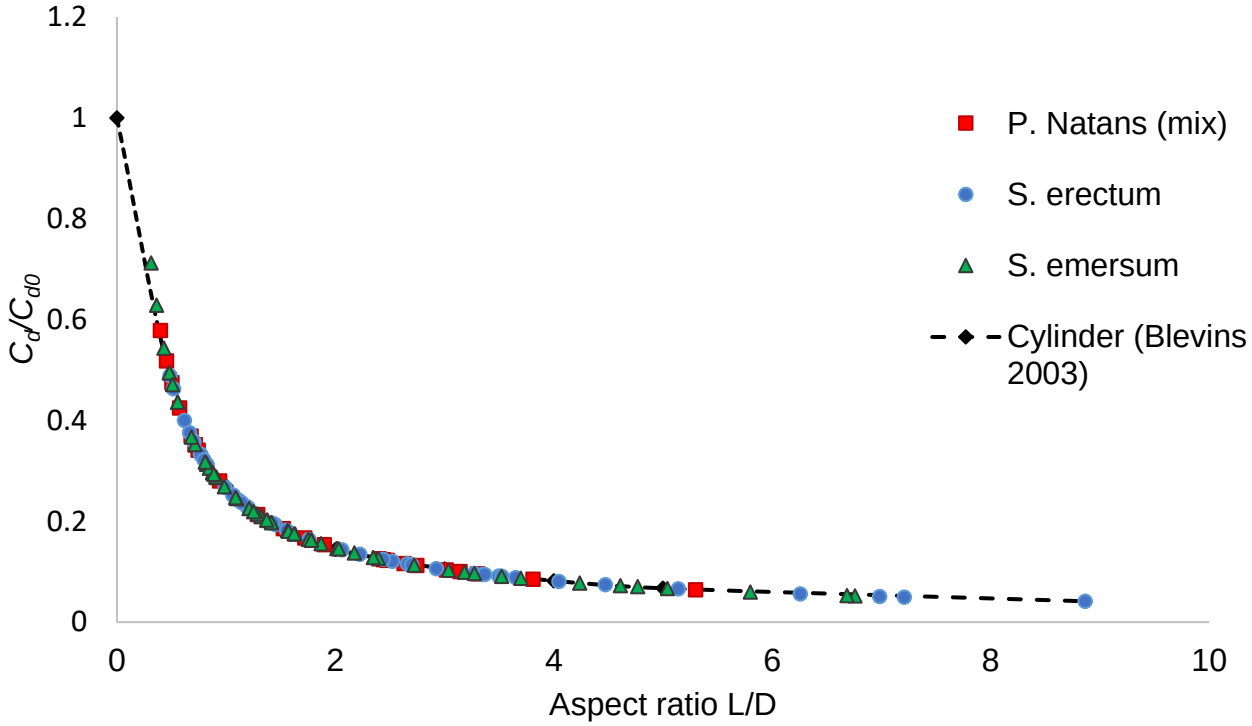


Figure 7.9. Drag coefficient variability with respect for aspect ratio for vegetation patches per species (September case), with the cylinder coefficients taken from Blevins (2003) for reference.

### 7.3.2. Representing trailing profiles

At high flows *S. emersum* deforms to more streamlined forms which results in a trailing profile. This vertical structure is more complex compared to the relatively uniform vertical structure of the May period; the patch can be described as having voids in the biomass containing only water. In general, a patch would have a void beneath the suspended canopy which begins after the root and which increases vertically in the downstream direction as the plant extends away from the bed. The trailing structure also means that the canopy would reach the free surface downstream of the patch head, resulting in a void above canopy at the beginning of the patch. To represent the complex dynamic between vegetation and flow more accurately complex canopy structures must be represented in the model. To achieve this, boundaries describing the upper and lower vertical extent of trailing canopy were derived from photographs of *S. emersum* patches taken during the measurement for the September flow period. To gauge canopy distribution along the

vertical and downstream in terms of x and y the chosen image needed to display a longitudinal canopy profile. The profiles were described by discretising the upper and lower vertical boundaries of the patch canopy using an image editor. The pixels were then converted to an x and y coordinates using Matlab R2016a.

To represent trailing profiles within the mesh four functions were fitted to the discretised coordinates mentioned above. In order to apply the profile to multiple patches the profile had to be able to be scaled with varying patch length: to keep the profile shape consistent between patches of different sizes the coordinates were converted into a relative metric. The relative distance, both longitudinally and vertically, was calculated in terms of percentage, where the maximum extent of the profile in both directions was 100%. Four functions were tested (Table 7.2):

Table 7.2. Functions tested for vegetation profiles.

| Function | Equation |
|---|---|
| Quadratic | $f(x) = ax^2 + bx + c$ |
| Cubic | $f(x) = ax^3 + bx^2 + cx + d$ |
| Quartic | $f(x) = ax^4 + bx^3 + cx^2 + dx + e$ |
| Quintic | $f(x) = ax^5 + bx^4 + cx^3 + dx^2 + ex + f$ |

where $x$ is the relative distance along the patch (%) and $a$, $b$, $c$, $d$, $e$, and $f$ are coefficients. The coefficients were determined by using the Matlab function polyval to evaluate the polynomial coefficient at for each point in $x$. The functions were fitted through the zero elevation at the lowest x value which represented the upstream limit of the profile, or the patch head, where the vegetation emerges from the riverbed. No field measurements were available to determined goodness of fit, as such the function was selected by calculating the RMSE between the estimated curve and the observed profile, and by visual assessment. Functions were tested for both the top and bottom profiles of *S. emersum.* To find the appropriate curve, polynomials of increasing complexity were used until the difference between them were deemed small enough to have negligible effect on describing the profile. For both profiles changes between the curves which were estimated using the quadratic and quantic

functions were considered appropriately small: for the lower profile, the RMSE between the quartic and quintic functions was 0.0008%, and for the upper profile the RMSE was 0.0012%. Comparing the quartic curves against the cubic showed that it was within a reasonable level of error with an RMSE OF 0.277% for the cubic, and 0.022% for the quartic. Differences were more noticeable for the upper boundary: the quartic and quintic functions both described the profile well and generally followed the same curvature throughout. However, the quantic profile curved upwards at the end of its trajectory in contrast to the downward curve present for the quadratic approach. The observed profile exhibits a downward trend, and as such the quadratic function was chosen to represent the upper boundary of the profile as it better represented the shape of the observed canopy. The quartic was again compared to the cubic function to assess its relative accuracy: the cubic function had an RMSE of 0.03%, and the quartic an RMSE of 0.022%. The cubic was of a higher accuracy compared to the functions fitted to the lower profile, but the quartic function exhibited the same RMSE value.

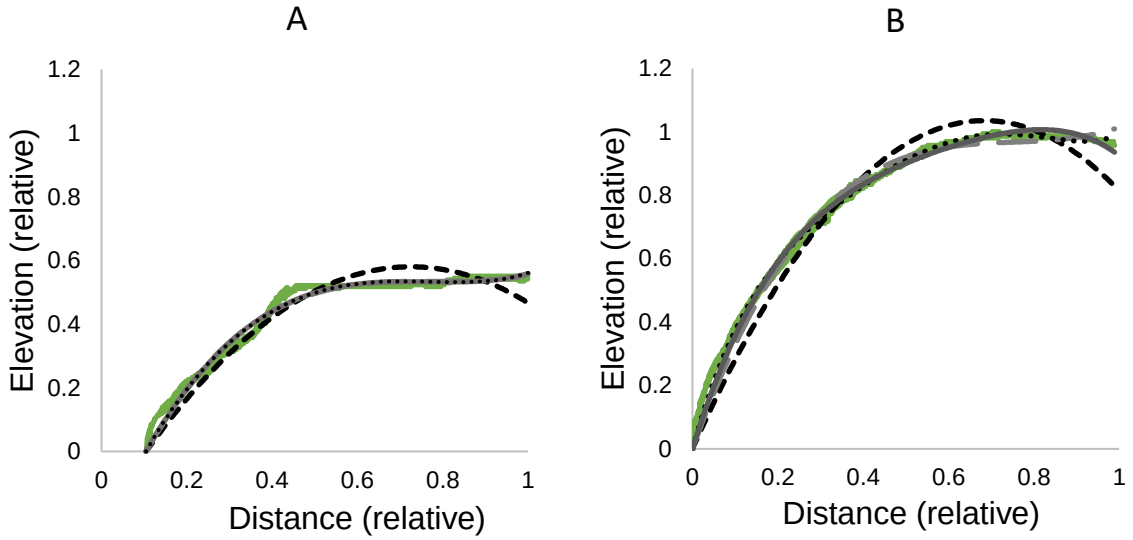


Figure 7.10. Profile boundaries for the bottom (A) and top (B) profiles for the quadratic (black dashed line), cubic (grey dashed), quartic (solid grey), quintic (black dots).

The above method idealises the vegetation as static, however in reality in-stream vegetation is dynamic and responsive to the local flow field, as well as turbulence produced at canopy shear layers and canopy movement (Nikora, 2010). The accurate parameterisation of vegetation patches is a known problem within

ecohydraulics however some progress has been made to capture dynamism using moving masks to represent the moving effect of the vegetative drag (Majoribanks et al., 2014). However, where the intensive collection of field data is not actionable within the study static vegetation patches are used (for example: Boothroyd et al., 2017). Practical restraints limiting the collection of such field data in this study means that vegetation patches are assumed to be static. Integrating the different morphotypes into the 3D mesh topography, in concert with the spatially heterogenous application of a bulk drag coefficient representing sub-grid scale roughness due to the vegetation surface area, forms the total approach for simulating 3D vegetation-flow interactions.

## 7.4. Calibration of the bulk drag coefficient for the vegetated channel for the May period

Calibration for both the May and September periods followed the same method used in the calibration of the gravel bed, discussed in Chapter 6, Section 6.3, and used the same boundary conditions described in Chapter 4, Section 4.1.2. The calibration for the May period used the mesh described in Section 7.2, the vegetation distribution described in Section 7.2 which was related onto the 3D mesh described in Section 7.3. The vegetation drag was parametrised as described in Section 7.3. The areal values for the spatially-averaged surface area for each species is specified in Table 7.1. The calibrated bulk drag coefficient for approaches with and without the $R_f$ factor are detailed in Table 7.3. The free surface results for both banks per each method are presented in Figure 7.7 alongside the field measurements at each bank, and shows that the model captures the slope of the free surface well.

Table 7.3. Model parameters, including the drag coefficients for all calibration cases (May and September) for both methods.

| Test case | Prescribed discharge Q (m3/s) | Prescribed outlet depth (m) | Calibrated drag coefficient CD (gravel) and CD0 (vegetation) | Vegetation cover (as percentage % occupied nodes of the total node count) |
|---|---|---|---|---|
| February | 0.775 | 0.739 | $C_{dg}$ 0.52 | n/a |
| Method one | | | | |
| May | 0.395 | 0.620 | $C_{dv}S_{fv}$ 0.04 | 15.59 |
| September (low flow) | 0.306 | 0.779 | $C_{dv}S_{fv}$ 0.07 | 24.03 |
| September (high flow) | 0.4333 | 0.888 | $C_{dv}S_{fv}$ 0.07 | 24.03 |
| Method two | | | | |
| May | 0.395 | 0.620 | $C_{d0}$ 0.32 | 15.59 |
| September (low flow) | 0.306 | 0.779 | $C_{d0}$ 0.34 | 24.03 |
| September (high flow) | 0.4333 | 0.888 | $C_{d0}$ 0.34 | 24.03 |

### 7.4.1. May calibration results

For the May case the modelled free surface slope was compared the slope of the observed free surface using the RMSE method for all banks (Fig 7.11), where the coefficient chosen was that which resulted in the lowest RMSE value (Table 7.3). For method one, the drag coefficient with the lowest RMSE was $C_{D0}$= 0.32, here the RMSE values was 0.002m. For method two, the drag coefficient the lowest RMSE was at $C_{D0}$= 0.32 where the RMSE value was found to be 0.003m, as shown in Figure 7.11 The RMSE was found to be 0.4% of the smallest modelled elevation of 0.7343m, and 0.36% of the largest elevation of 0.8207m.

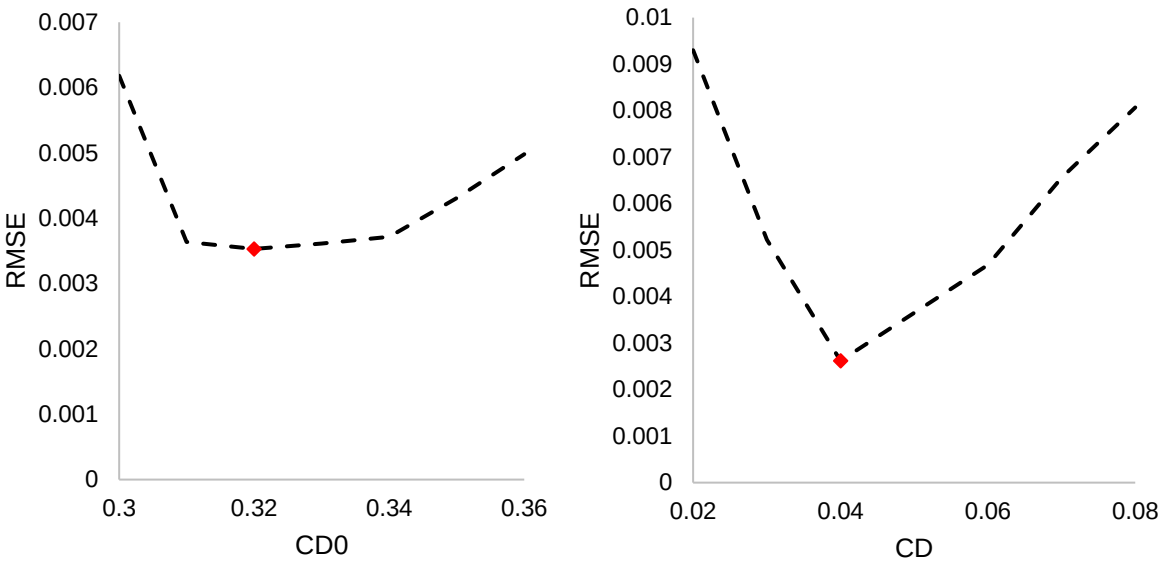


Figure 7.11. The calibrated bulk roughness coefficient (red) relative to the RMSE value for method one (left) and method two (right) for the May case.

The drag coefficient was also set to unity ($C_{d0}$ = 1.0), the results of which are compared against the free surface profiles for both method one and method two in Figure 7.12. The simulations using unity exhibited a higher free surface along both banks compared to the results for method two, whilst method one, which had the lowest drag coefficient values, exhibited a lower elevation. This is expected and is the result of the higher drag coefficient decreasing flow velocity, and thus increasing flow elevation to satisfy continuity. Consult Chapter 2, Section 2.3 for a more detailed discussion of continuity.

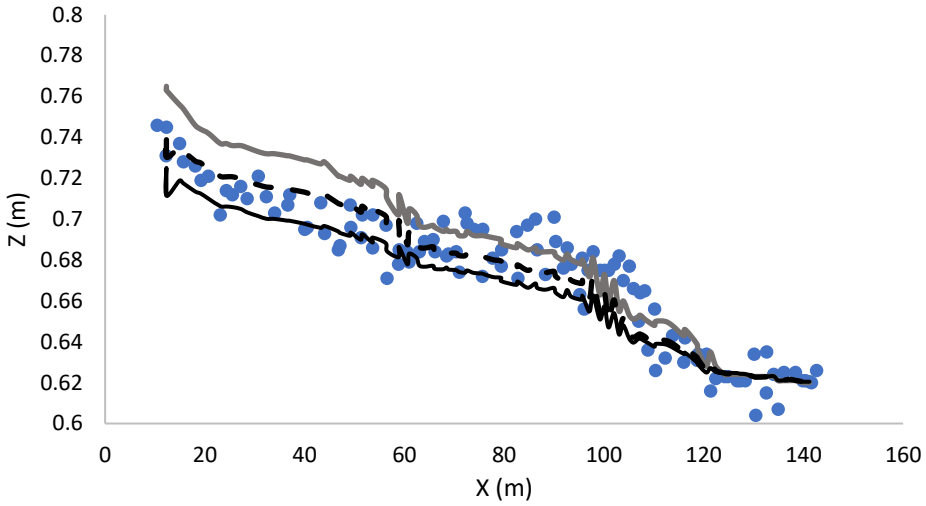


Figure 7.12. Calibrated free surface profiles for the May period for method one ($C_{d0}$ = 0.04; solid black line), method two ($C_{d0}$= 0.32; dashed black line), ($C_{d0}$= 1.0; grey black line) compared against the measured data for both rivers banks (circles).

Comparing the surface profiles on each bank for method one and method two revealed a very similar slope (Figure 7.13). The drag coefficients were compared with the calibrated values for vegetated channels found in literature. The values found in the literature, alongside their parameterisation and method, are detailed in Table 7.4. The method used to determine drag coefficients reported in the literature varied but can be summarised as: drag coefficients were selected through both the measurement of drag and calculating drag through empirical relationship in laboratory flume experiments either using real vegetation, plastic surrogates for vegetation, or by using independent or arrays of cylinders. In addition, drag coefficients were also reported based on the numerical modelling of vegetation based on such flume experiments mentioned above.

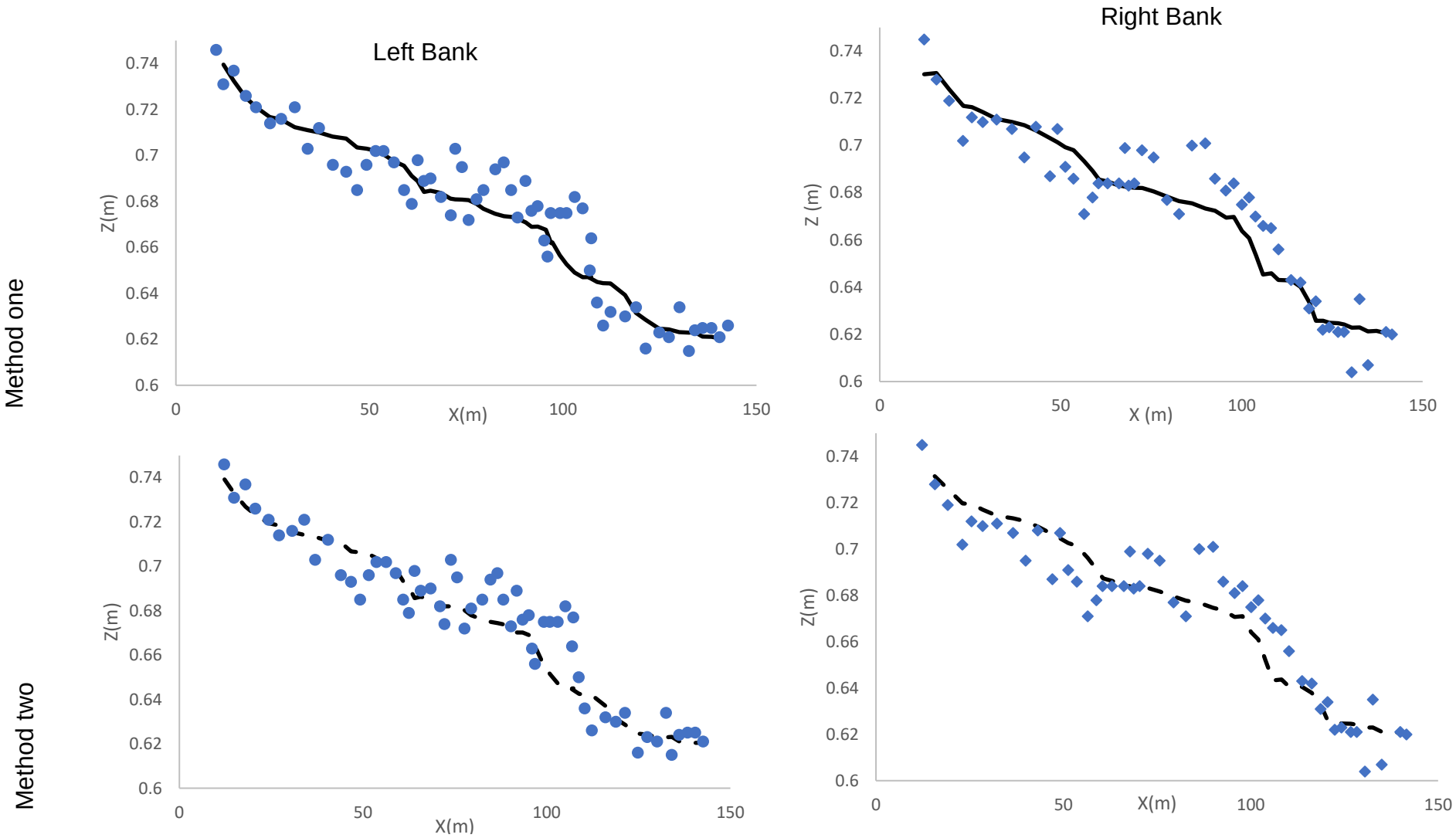


Figure 7.12. Calibrated free surface profiles for the May period for method one ($C_{d0}$ = 0.04; solid line) and method two ($C_{d0}$= 0.32; dashed line) compared against the measured data for the left bank (circles) and right bank (diamonds), respectively.

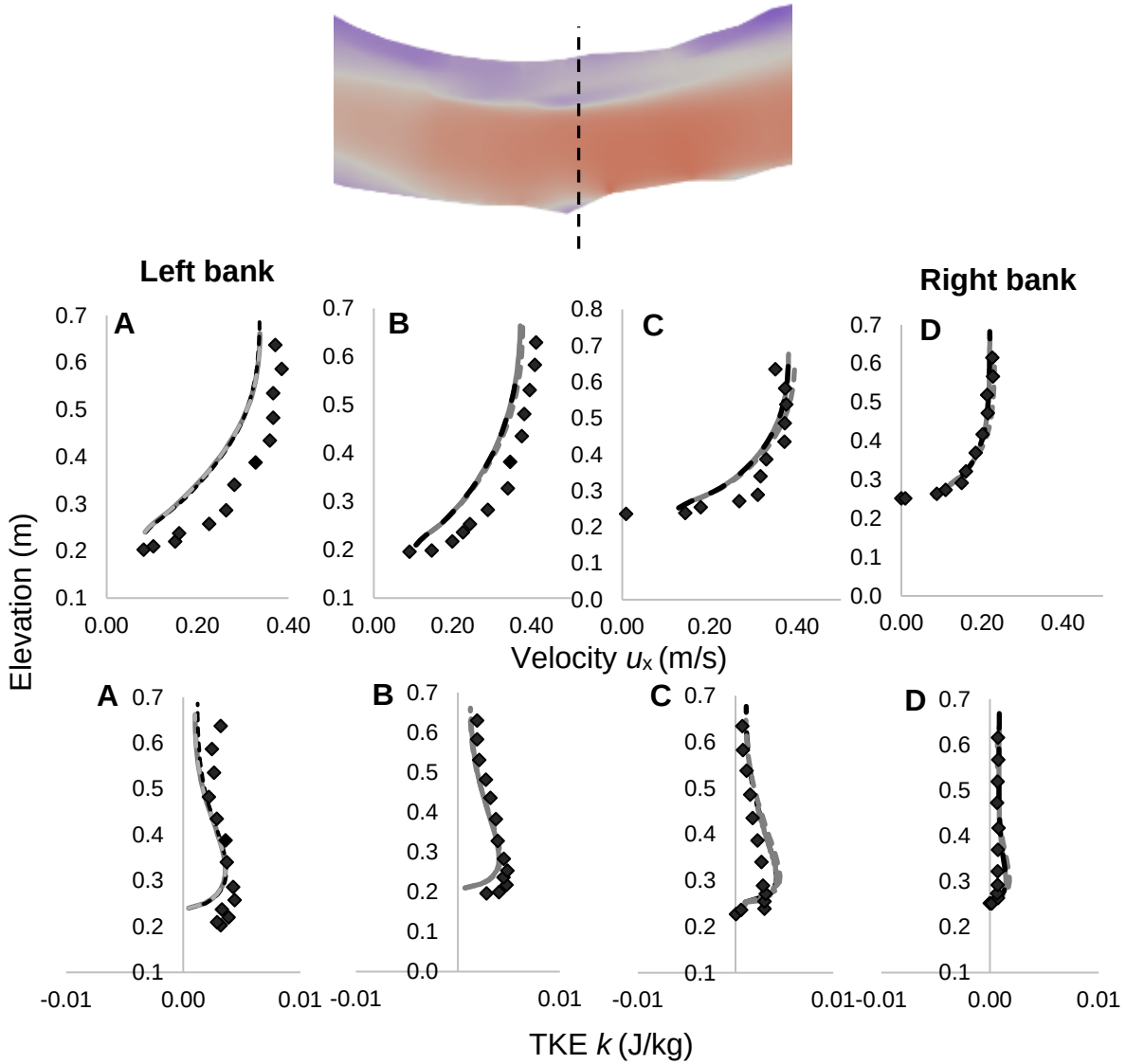


Figure 7.14. Cross-sectional velocity $u_x$ and TKE for the apex cross-section for calibrated Method One ($C_{d0}$ = 0.04; grey solid line), calibrated Method Two ($C_{d0}$ = 0.52; grey dashed line), drag coefficient set to unity for Method Two ($C_{d0}$ = 1.00; black dashed line), compared to the data (black diamonds).

The flow profiles (Figure 7.14) for the apex cross-section revelaed little deviation between both methods and the simulation where the drag coefficient was set to unity; profiles for streamwise velocity and TKE closely follow the vertical trends described by the observed data. All simulations slightly under-predict the streamwise velocity towards the left (outer) bank with the simulated trend matching the observed data more closely towards the right (inner) bank. The simulated TKE closely follows the observed data throughout the water column, with the only clear divergence from observed data appear towards the surface of the first profile (A). Rameshwaran et al., 2006) have previously noted that this deviation may be caused by the presence of dead vegetation suspended near the surface during measurement.

Table 7.4. Drag coefficients for vegetation as reported in the literature.

| Author | Drag coefficient | Method | Parameterisation |
|---|---|---|---|
| Cheng (2013) | 0.78 – 1.52 | Pseudofluid model of an array of emergent rigid circular cylinders in open-channel flow, where a generalised drag coefficient is related to a generalised Reynolds number. | $F_{Da} = \frac{1}{2} C_{Da} \rho d V_v^2$ Where $Da$ are parameters related to the cylinder array and $C_{Da}$tends to $C_D$ as the fraction of the stem-occupied bed area decreases. |
| Cheng & Nguyen (2011) | 0.78 – 1.92 | Emergent cylinders in open-channel flow, where the drag coefficient is related to a Reynolds number defined using a | $C_{Dv} = \frac{1}{4} f_v$ where $C_{Dv}$ is the vegetative drag coefficient with varies due with the vegetative Reynolds number due |

| | | | |
|---|---|---|---|
| | | vegetation-related hydraulic radius. | to the vegetation friction factor $f_v$defined as: $$f_v = f(R_v)$$ Where $R_v$ is: $$R_v = \frac{V_v r_v}{v}$$ and $r_v$ is the vegetation-related hydraulic radius. |
| Kothyari et al. (2009) | 0.84 – 1.31 | Single, emergent rigid vegetation in an open-channel flow. | $$C_D = \frac{F_x}{\frac{1}{2}\rho d h V_c^2}$$ Where $F_x$ is the drag force acting on the cylinder and $V_c$ is the depth-averaged velocity. |
| Liu & Zeng (2017) | 0.5 – 2.5 (1) 0.5 – 1.6 (2) 0.9 – 1.4 (3) | Channel experiment using rigid vegetation for subcritical flow, with a focus on $C_D$ variation with the Froude number, with $C_D$ values stated for (1) $0<Fr<0.12$, (2) $0.12<Fr<0.28$, (3) $0.28<Fr<0.48$. | $$F_p = \frac{1}{2} C_D A_0 \rho u^2$$ where $A_0$ is the vertical projected area of a single plant facing the current |
| Mendez | 0.01 – 0.52 | Empirical model estimating wave propagation for *L. hyperborean. Drag was paramterised as a* | $C_D = \exp(-0.0138Q)\, Q^{0.37}$ $\leq Q \leq 172$ |

| | | | |
|---|---|---|---|
| | | *function of a local Keulgan-Carpenter number.* | Where $Q$ is the Kuelegan-Carpenter parameter |
| Mulahasan & Stoesser (2017) | 0.65 -1.06 | Flume measurements of vertically orientated vegetation, represented as cylinders. | $C_D = 2\left\{\frac{\alpha_0}{Re_D} + \alpha_1\right\}$ Drag of rigid cylinders, where $Re_D$ is the cylinder Reynolds number, $\alpha_0$ and $\alpha_1$ are functions of vegetation volume fraction (overall volume occupied by vegetation). |
| Nepf (1999) | 0.2 – 1.2 | Emergent cylinders arrays in an open channel, where the bulk drag coefficient $\overline{C_D}$ is related to vegetation density and Reynolds numbers ≥ 200 | $F_T = \frac{1}{2}\overline{C_D}aU^2$ |
| Rameshwaran & Naden (2012) | 0.15 | Vegetation patch reach-scale model of the River Blackwater. Patches occupied the full depth. | $F_D = -\frac{\rho}{2}C_D S_f A_s \lvert\langle\bar{u}\rangle\rvert\langle\bar{u}\rangle$ |
| Sand-Jensen (2003) | 0.01 – 0.1 | Flume measurements for five species: *Egeria densa, Hydrophilia corymbosa, Limnophila aquatic, Myriophyllum tuberculatum,Vallisneria natans* | $F_d = 0.5C_d\rho A_c U^2$ |

| | | | |
|---|---|---|---|
| Plew (2011) | 0.6 - 1.35 | Flume measurements of suspended canopies represented by cylinders. | $F_D = -\frac{1}{2}\rho C_D(z) a \langle U(z) \rangle^2$ where $a$ is the unit volume of the canopy, |
| Puijalon, Bornette, & Sagnes (2005) | | | $\mathrm{Cd} = 2\mathrm{D}/(\rho \mathrm{SU}2)$ where D is drag in N,S is total leaf area ($m^2$) |
| Wang et al., (2015) | 1.31 | Flume measurements of shallow from through different densities of emergent vegetation, represented as cylinders. | $F_D = -\frac{1}{2} C_D m D H_\rho U^2$ where $m$ is the number of vegetation stems per unit ground area, $D$is the frontal width of the stem. |

A variety of drag coefficients have been reported in the literature, with differences in vegetation types, parametrisation approaches, and in approaches for modelling or measurements impeding direct comparisons between the coefficients calibrated in this study and those reported. Generally, the range of coefficient values reported tend to vary within the upper limit of the unit interval [0,1]. The calibrated May case, $C_{D0}$ 0.32, appears to be closer to the range of reported values; very few values in the literature were less than 0.1 with reported values being, for example, 0.2-1.1 (Nepf, 1999),0.01-0.1 (Sand-Jensen, 2003) 0.15 (Rameshwaran & Naden, 2012), 1.31 (Wang et al., 2015), 0.65-1.06 (Mulahasan & Stoesser, 2017). As such, the value of 0.04 may be considered less realistic. However, Rameshwaran and Naden (2012) have similarities in both the drag parametrisation and used the same method relating parametrisation to patch aspect ratio, and therefore their study was an appropriate comparison for method two. They reported a value of 0.15, lower than the calibrated value of 0.32 is notably higher than their reported value of 0.15, however differences between

modelling approaches, such as the inclusion of porosity terms, choice of advection scheme, choice of solvers, and other parameters, may explain such differences.

The modelled flow profiles are compared with measured data at each of the five measured cross-sections. The comparisons are detailed in Figures 7.15 – 7.19, with each figure comparing the data for $u_x$ and turbulent kinetic energy (TKE) for both methods against measured field data. TELEMAC calculates flow quantities using a Cartesian coordinate system, therefore the simulated data extracted from locations where the channel flow is unaligned with the x-direction cannot be truly streamwise i.e. representative of flow in the channel direction. To account for this, velocity values were adjusted from the Cartesian x-direction to the streamwise direction using the equation:

$$u = \rho(u_{zx} \cos\theta + u_{xy} \sin\theta)$$

where $\rho$ is the fluid density kgm$^{-3}$, $u_{zx}$ is the Cartesian velocities $u_x$ in the x-direction on planes perpendicular to the z-direction in m/s, and $u_{xy}$ is the velocity $u_x$ in the y-direction perpendicular to the x-direction, and $\theta$ is the angle between the x-direction and the streamwise direction as measured from the sampling location.

The flow profiles for the May case are shown in Figures 15-19. The profiles for the streamwise velocity appear to be predicted reasonably well, however the velocity profiles conform the most to the measured data at the channel centre with a greater divergence between the simulated and measured data towards the banks. Generally, the streamwise velocity profiles were slightly under predicted throughout the channel, with the degree of under-prediction varying along the reach: the velocity profiles match the measured data well in transect C at the apex of the channel, whilst diverged to a greater degree at transect E towards the end of the reach. The profiles for TKE exhibit similar trends, with greater consistency between the measured data and modelled occurring at the channel centre, however, similar to the calibrated results in the previous chapter, the turbulence profiles show greater divergence from the measured data compared to the streamwise velocity. Divergence between the measured turbulence and the modelled is mostly evident at the bottom of the profile where the turbulence

values at the inflection are exaggerated, suggesting that the model over-predicts the effects of shearing at the boundary layer. The degree to which the model exaggerates shearing varies along the reach, with the profiles at transect C at the apex appearing to conform to the measured data well, whilst the largest differences occur near the beginning of the domain at transect A. Both methods express similar profiles to the measured data with small differences present between the two methods. The most explicit difference is the turbulent profile at the right bank, where the lower half of the profile is overpredicted for method one. Generally, method one overpredicts the data more than method two however the differences are small enough to be negligible: using root-mean square error method the largest difference for the velocity profiles was 0.0071 m/s for the channel centre, and the greatest difference for TKE was 0.00018 Kg/J at the right bank. For both methods the streamwise velocity is approximated reasonably well, capturing the characteristic logarithmic curve. The velocity profiles match the measured data well at locations C and D, the right bank looking upstream, but is slightly underpredicted at the A, the left bank. The TKE profiles are generally underpredicted left of the channel centre, and overpredicted towards the right bank. The greatest deviation in TKE is at the banks where the turbulent energy is underpredicted for the near-free surface zone at location A, and underpredicted at the shear layer for D. Discrepancies are apparent in the description of secondary flow between the two methods, with method two presenting a similar flow pattern to the non-vegetated case. However, method one describes a less distinct circulation pattern across the channel, with rotation occurring at the near-surface region near the channel centre.

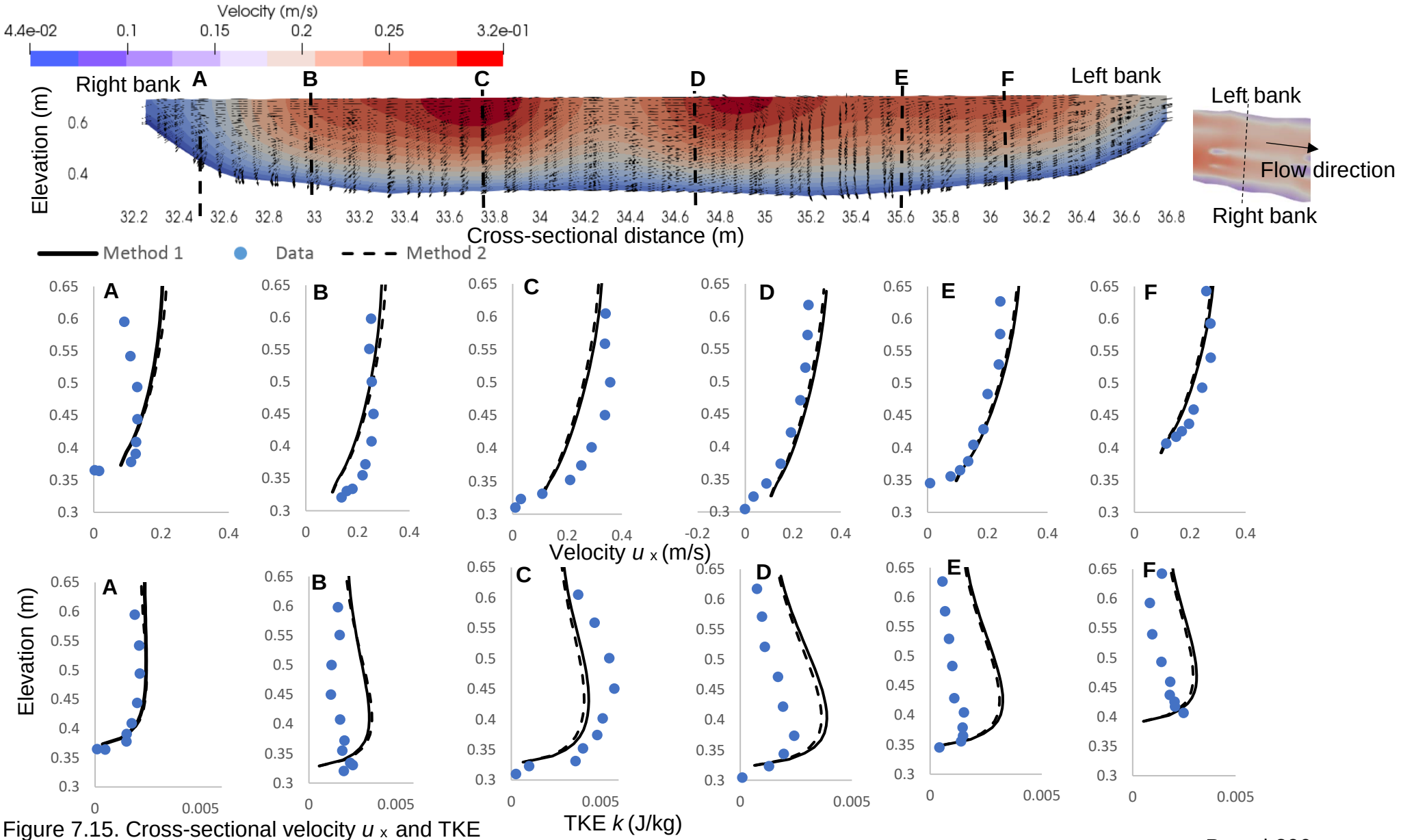


Figure 7.15. Cross-sectional velocity $u_x$ and TKE

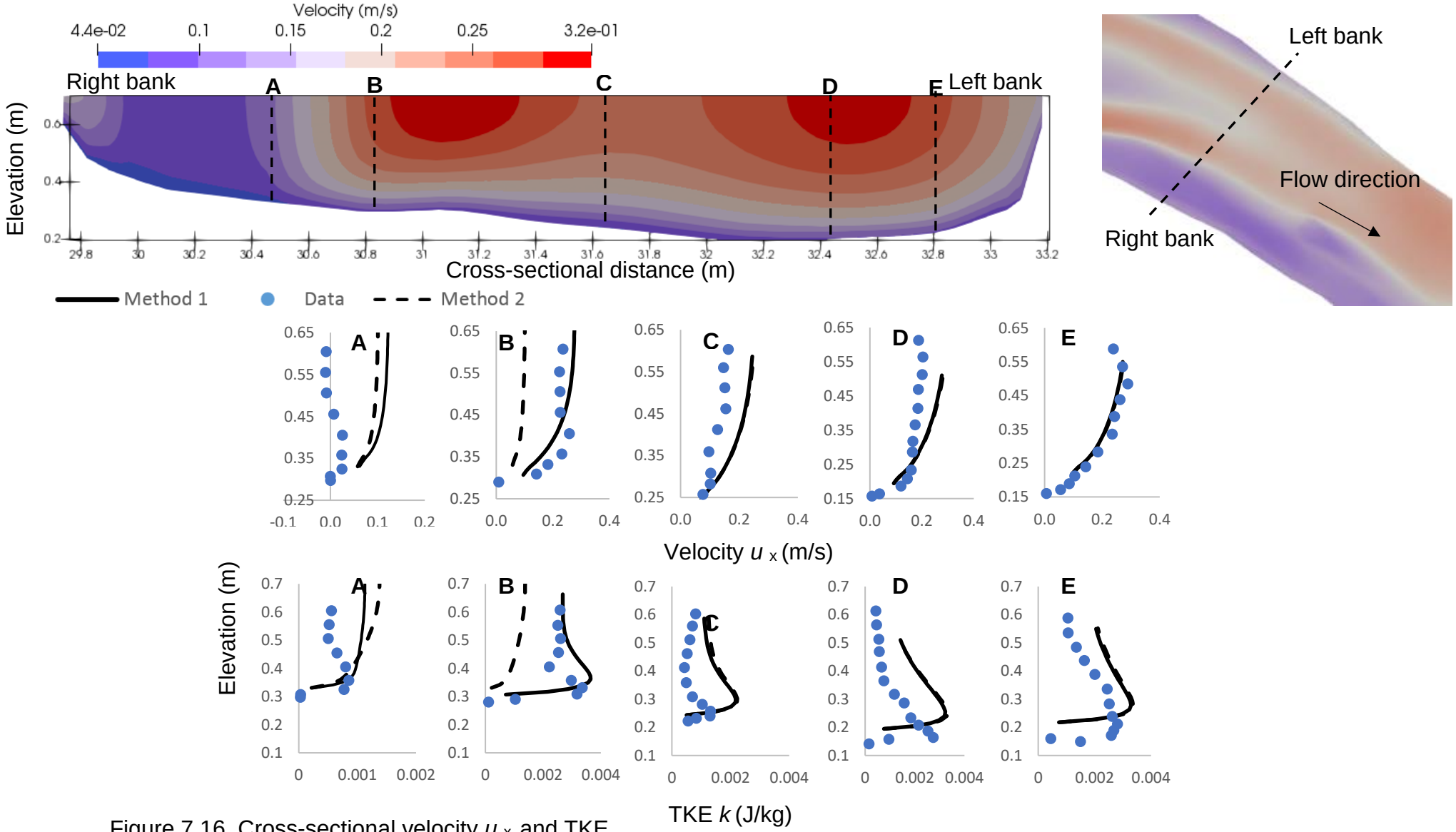


Figure 7.16. Cross-sectional velocity $u_x$ and TKE

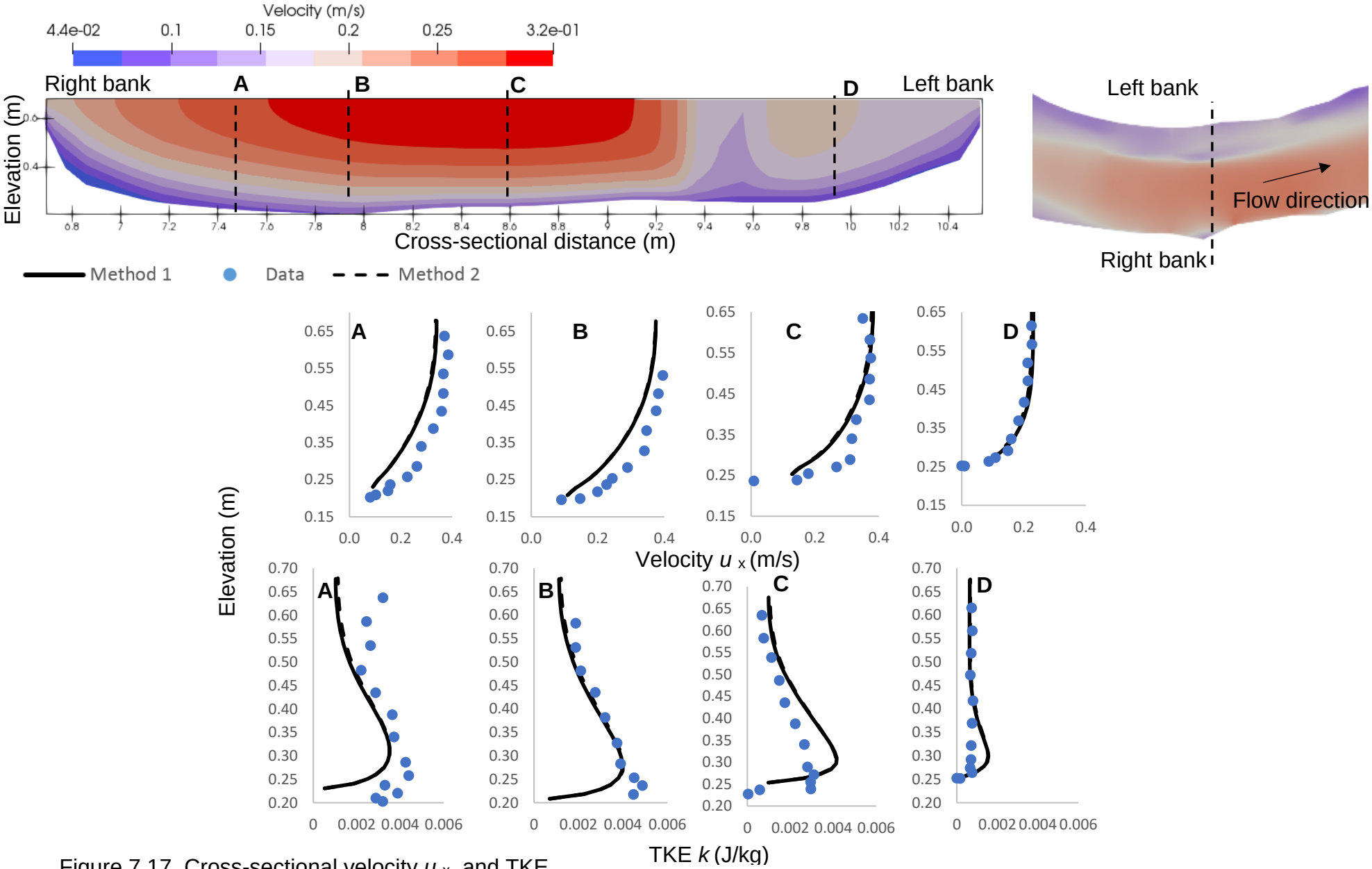


Figure 7.17. Cross-sectional velocity $u_x$ and TKE

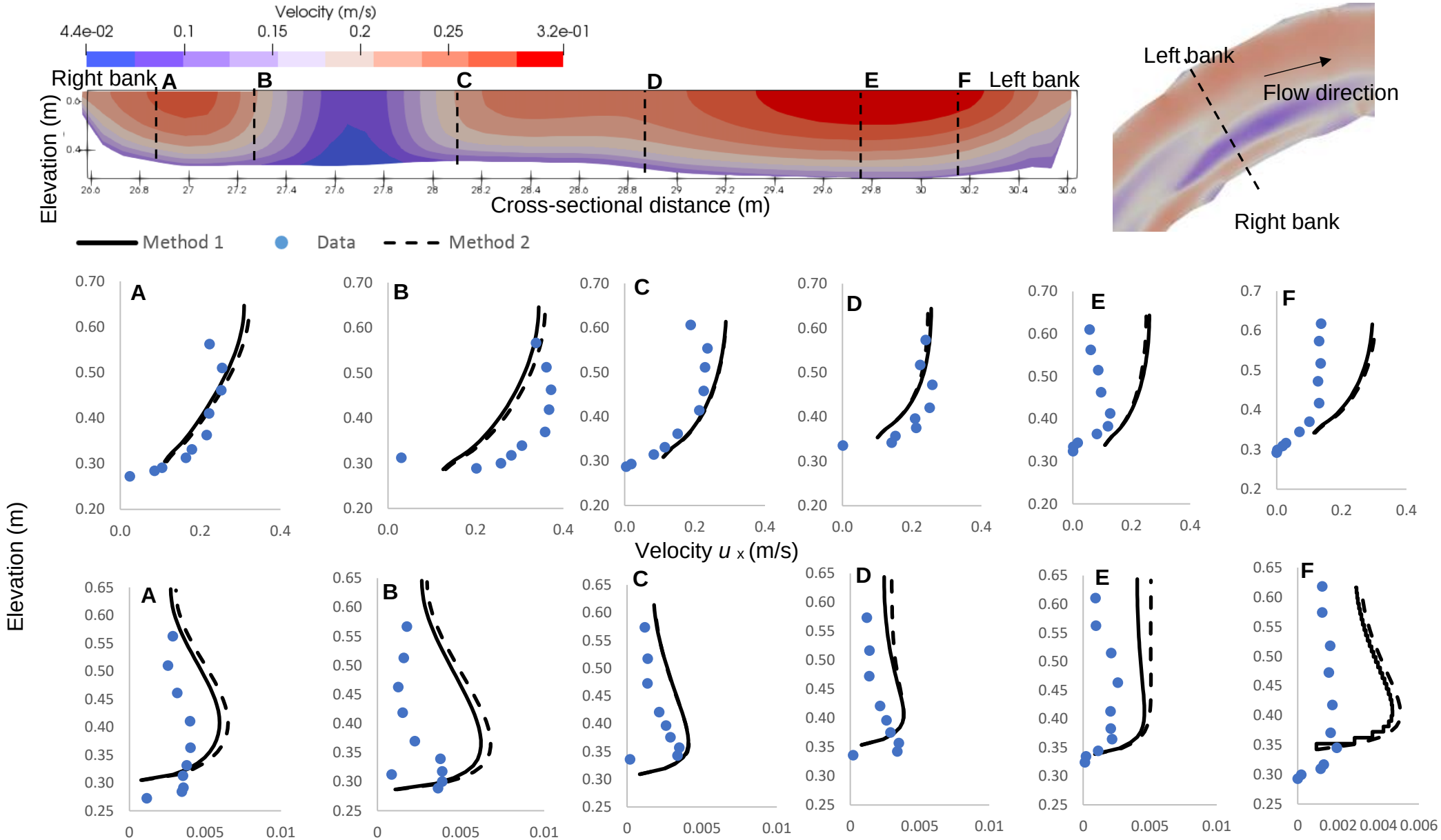


Figure 7.18. Cross-sectional velocity $u_x$ and TKE

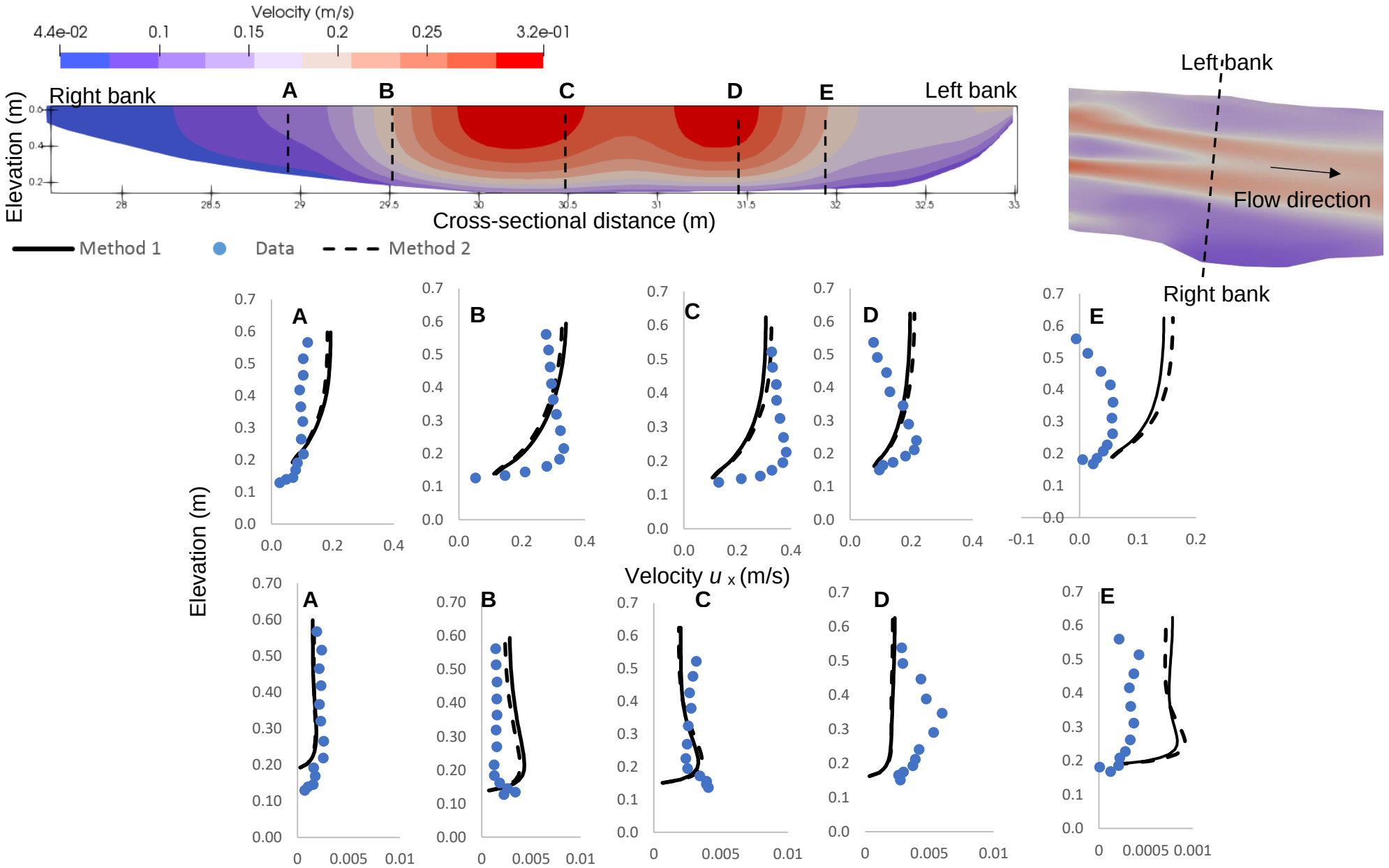


Figure 7.19. Cross-sectional velocity u x and TKE

Fig.20 illustrates the simulated streamwise velocity and TKE quantities affecting the free surface at the leading limb of the meander for the vegetated May case. The influence of the vegetation patches is obvious in the pattern of both the velocity and TKE fields (I). Velocity is clearly shown to lose momentum within the patch and immediately downstream, whilst accelerating around the patch boundary and in regions where the non-vegetated flow is channelled through restricted regions between patches. Increases in TKE is evident at the patch boundaries as the accelerated flow induces a strong shearing effect. A closer investigation of flow surrounding the patch is also presented (II) and describes the impact of the patch on vertical streamwise velocity in the streamwise direction. The streamwise velocity is considerably slowed within the patch followed by a slow recovery, seen in the wake downstream. Higher velocities are present immediately before the patch and as the wake is subsumed by non-vegetated flow downstream. The TKE values appear highest near the bottom preceding the patch, indicating the dominance of the riverbed roughness on turbulence generation. Downstream of the patch relatively

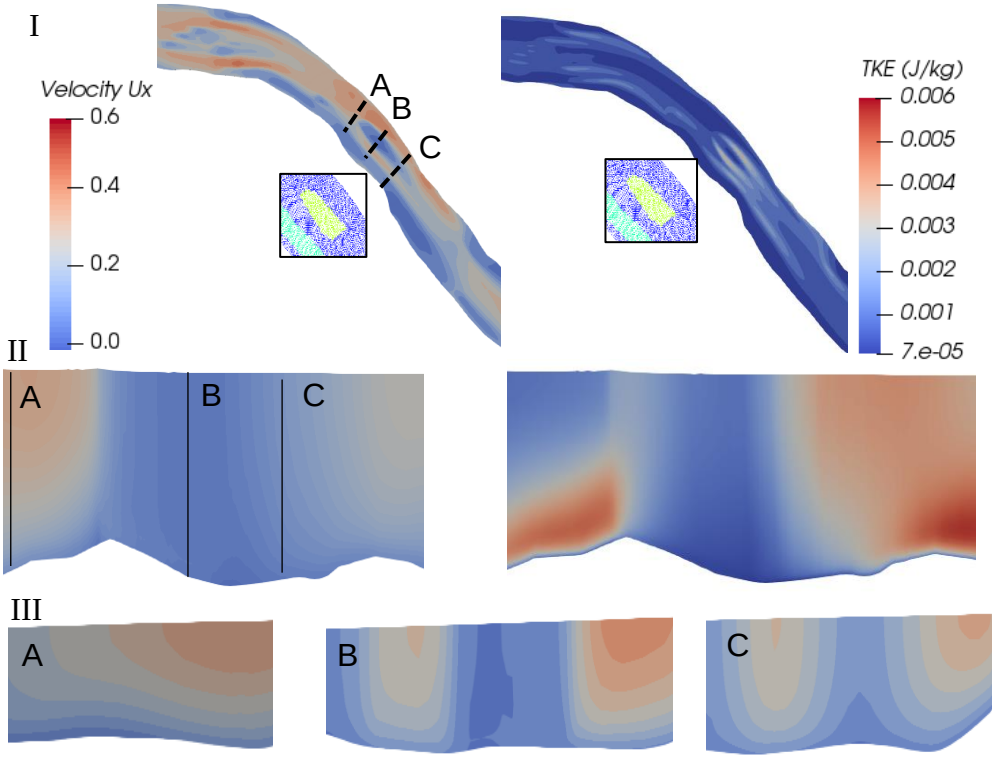


Figure 7.20. Spatial distribution of streamwise velocities and TKE for the initial limb of the meander (I), including cross-sections of in-stream vegetation patch in both the streamwise (II) and cross-channel (III) directions. Selected nodes are presented for comparison (inset).

high TKE values are present throughout the water column suggesting the patch is generating a large level of turbulence generated by shearing between the non-vegetated and vegetated flow. Low TKE values are found within the patch where velocities are reduced, and at the riverbed immediately downstream of the patch where a sheltering effect of the vegetation reduces shearing at the riverbed. This shearing subsequently recovers further downstream where TKE can be seen in increase above the bed. Considering the effect of the patch on cross-sectional velocity (III), preceding the patch (A) the velocity field is largely affected by roughness at the channel bottom and acceleration due to the meander bend. The flow is subsequently bisected by the patch (B), increasing the velocities either side whilst reducing the momentum throughout the water column. Additional slow-down is evident to the left of the patch facing upstream where the flow encounters near-bank vegetation. Downstream of the patch a wake is evident with continued reduction of velocity (C). Local variations in flow around and within vegetation patches can be attributed largely to the geometry of the patch profile and planform.

Figure 7.21 describes changes within the patch to the velocity and TKE profiles for both methods. Both methods exhibit a reduction in velocity as flow encounters the patch from location B onwards, resulting in a reduction in the gradient of the velocity profile, accounting for the momentum absorbed by the patch. A slight recovery occurs in location G, just downstream of the patch, but velocity remains reduced compared to the upstream location because of a wake induced by the patch. Method two exhibits a greater reduction in velocities than method one, with the respective velocity profiles diverging from initially similar shapes upstream at location A. This suggests that the effect of the drag force is stronger with the additional consideration of patch aspect ratio. The TKE profiles are reduced for both methods within the patch, as most of the turbulence generated by vegetation patches occur at the boundary due to shear created by differences in the flow between vegetated and non-vegetated channel. Method two again exhibits a greater reduction in TKE, however the differences are lesser compared to the streamwise velocity. The largest differences occur after location C, based approximately a quarter of the through way through patch in the streamwise direction, where the lower half of the TKE profiles shows divergent results.

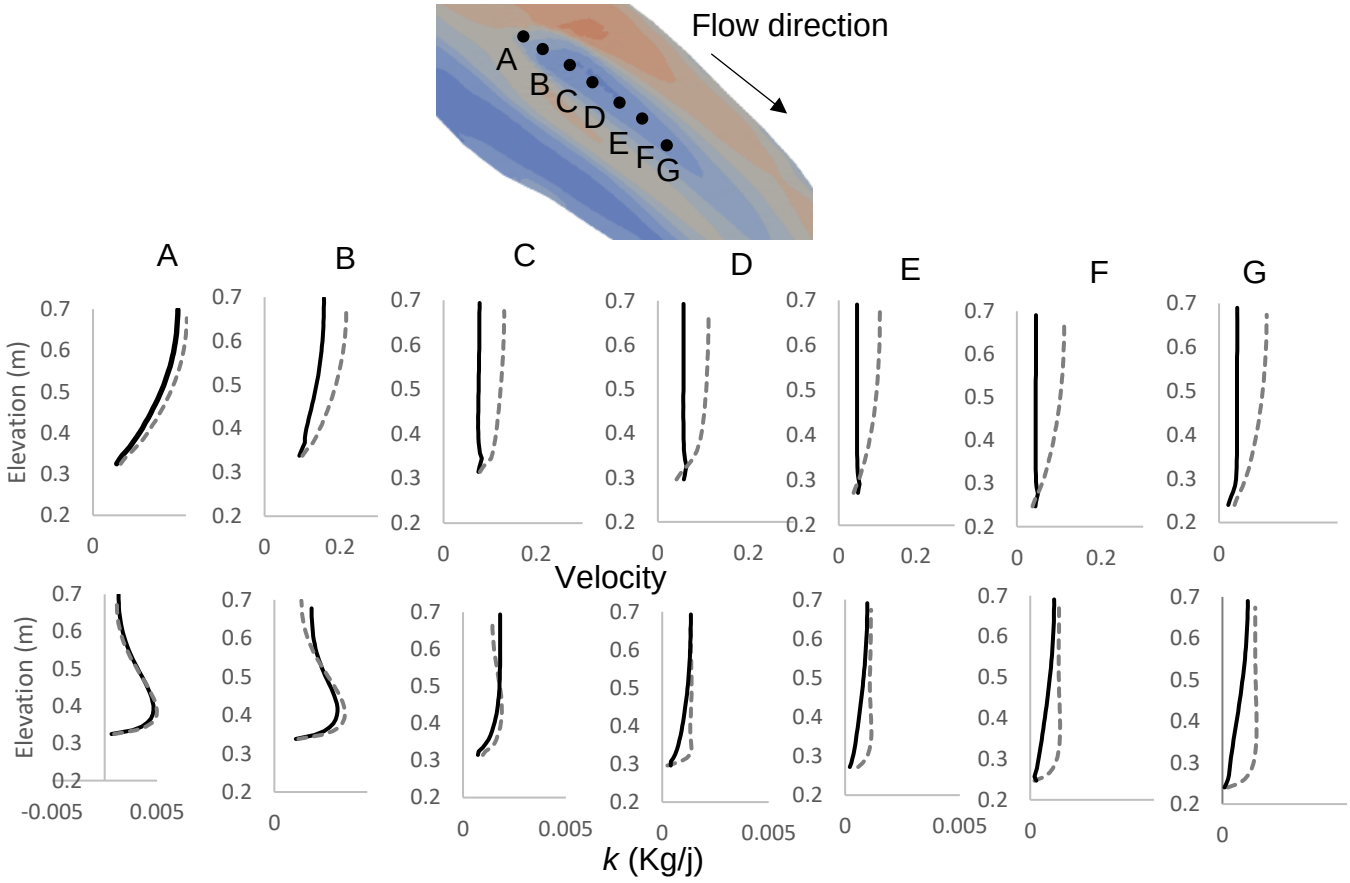


Figure 7.21. May: modification of streamwise velocity and TKE profiles upstream (A), throughout (B – F), and downstream (G) of a patch for method one (grey, dashed line) and method two (solid black line).

## 7.5. Calibration of the bulk drag coefficient for the vegetated channel for the September low flow and high flow periods:

High flow and high vegetation abundance during the September period resulted in fewer measurements to use when calibrating the simulated September free surface: May had 60 data points measuring free surface elevation, whilst September had 12 data points for the low flow period, and 16 for the high flow period. To calibrate the free surface flow for the September cases the mesh needed to be cut 0.1m below the free surface slope, as used in the method previously described in Chapter 5, Section 5.3. Two methods were used to estimate the free surface slope for each September periods: first, linear regression was used to predict the slope from the available data. However, this resulted in slopes with physically unrealistic steep gradients and thus poor free surface results. The second method used the free surface slope from the May period and adjusted the slope until it reasonably predicted the free surface for the September cases. In this case, the May slope was first adjusted in total elevation by adding or subtracting the respective difference between the average elevation for the May period with that of the respective September case. Secondly, the slope angle was adjusted until the free surface results reasonably reflected the estimated slope i.e. until the prescribed inlet depth matched the elevation of the predicted slope at the inlet. The free surface was then calibrated using the same method above, with the drag coefficient adjusted until the smallest difference between the estimated slope and the modelled free surface. The model was first calibrated for the September high flow period, and then validated by running the model using the September low flow case. In both cases the drag coefficient calibrated at $C_{D0}$= 0.34, as shown in Table 7.5:

Table 7.5. Calibrated values for the September low flow and high flow periods.

| September flow period | $C_{D0}$ | RMSE |
|---|---|---|
| High flow | 0.34 | 0.0007m |
| Low flow | 0.34 | 0.0018m |

The high flow condition was predicted with greater accuracy than the low flow condition: the RSME for the high flow condition was an order of magnitude less than the value found for the low flow period (Fig.7.22). However, both RMSE values were reasonably small (<0.01m) suggesting that the model can represent the free surface well; both calibrated flow periods can reasonably simulate the same vegetation scenario under different flow conditions (Fig.7.23). As such, the model can be said to have been successfully validated.

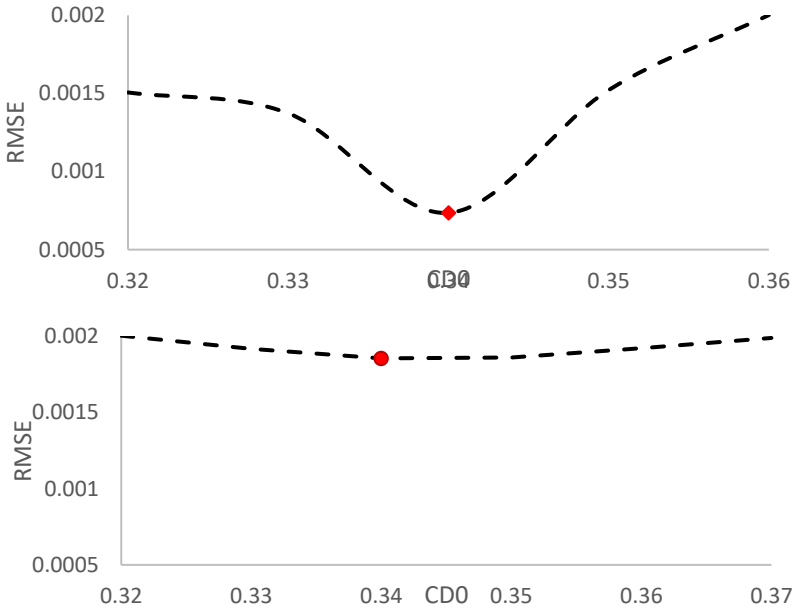


Figure 7.22. Calibrated bulk drag coefficient for the vegetated channel during the September high flow (top) and low flow (bottom) cases.

Figures for the September flow profiles are detailed below: first, the uncertainties for method one is assessed in Figures 7.24 – 7.26, and for method two Figures 7.27 – 7.29. Due to the large amount of data only the low flow case is presented. The uncertainties were generated using the same method in the previous chapter i.e. a cloud of data points was produced at the nodes closest to the mean of the measurement coordinates for each profile. Following both methods are compared for the low flow and high flow conditions and are presented in Figures 7.30 – 7.35.

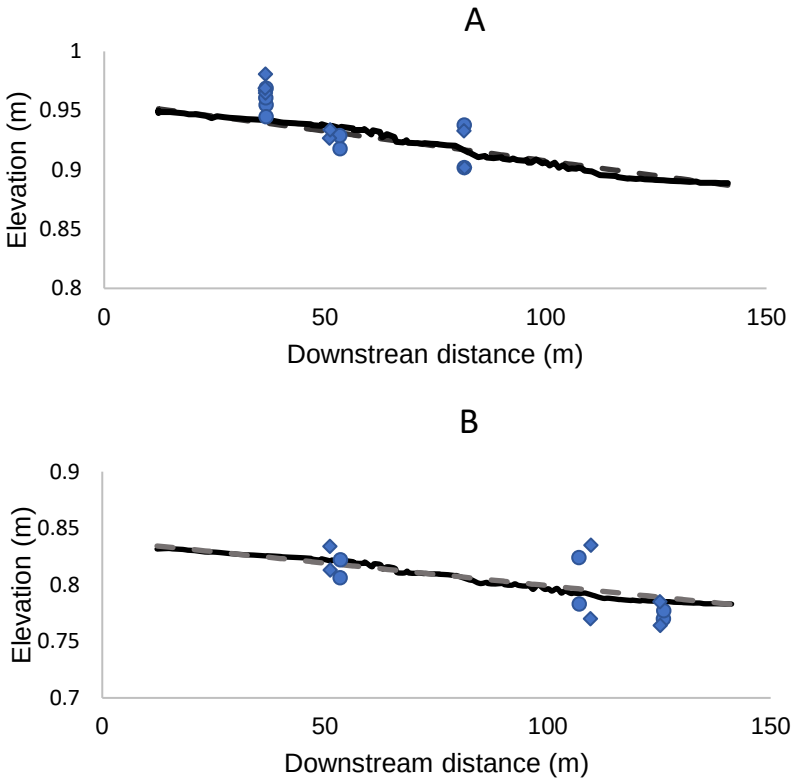


Figure 7.23. Calibrated free surface slope for the September high flow (A) and low flow (B) case: the modelled free surface (black line) is compared against the estimated slope (grey, dashed) and the measured data for both the left banks (blue circles) and right banks (blue diamonds).

Generally, there were little differences between both methods: trends in profile uncertainties across all three transects revealed that the greatest uncertainties were present at the near-bank regions. This was similar to the results for the February flow case (Chapter 6, Section 6.3) and may be a result of greater topographic variability resulting in greater variability in flow patterns at the bank. For method one, transect B exhibited the least variability in flow quantities throughout the flow column, whilst the greatest degree of variability is found in transect C. For most profiles greater variability appears to occur just above the roughness layer, suggesting that flow variation was a result of processes within the turbulent flow layer and not the result of processes at the riverbed boundary. These variations occur more dramatically at the patch boundaries: for example, the flow profiles I, II, and III at transect A exhibit the greatest degree of variation in velocity and TKE and all occur either at a patch

boundary or within a patch. The flow profiles broadly match those of the measured data; similar to the May case the overall trends are captured however the profiles are smoothened. The greatest divergence between the measured and simulated data occurred at transect C: larger differences between the measured and simulated data occur just above the roughness layer, complementing the observation that greater uncertainties occur at the turbulence layer.

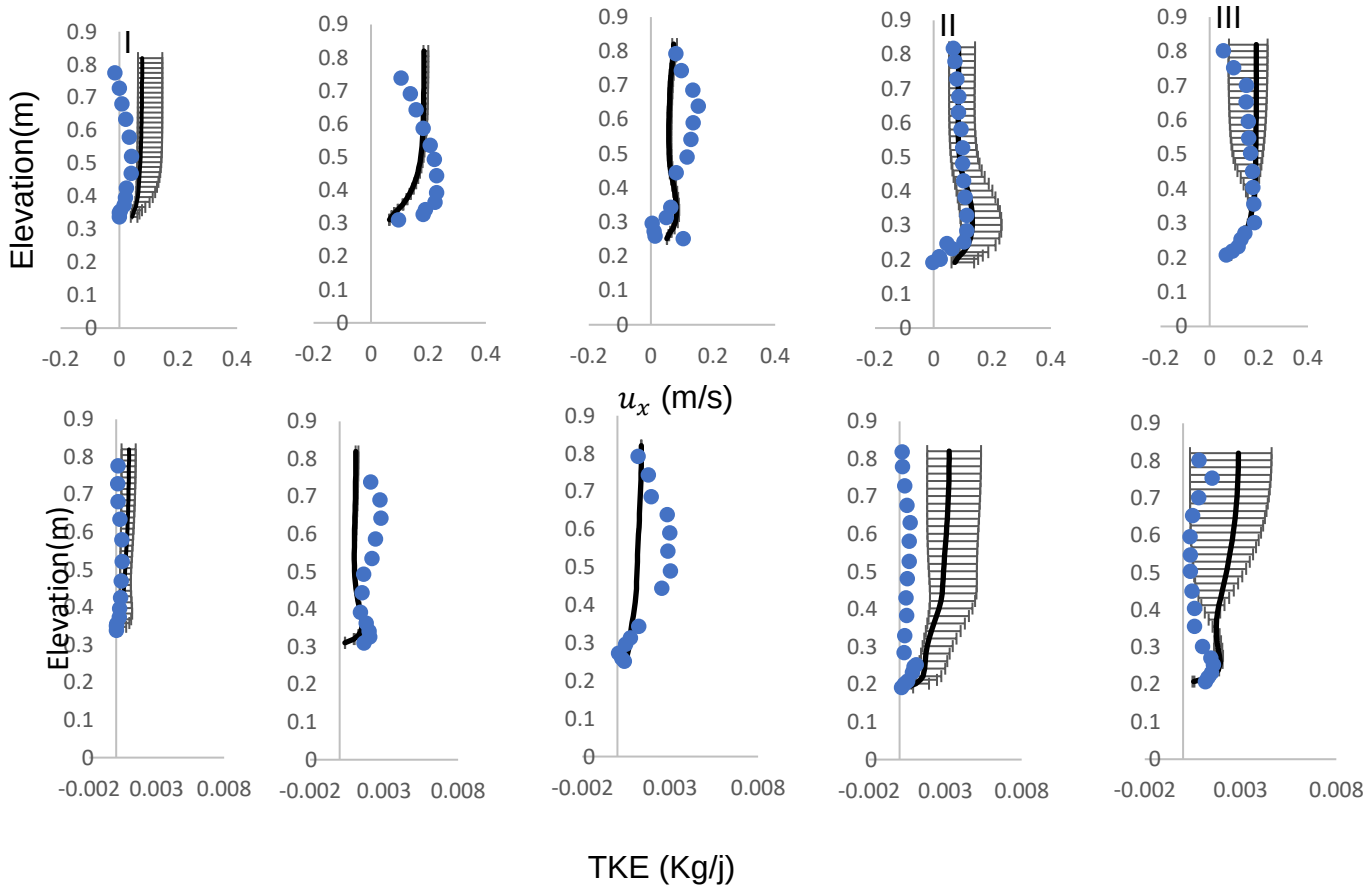


Figure 7.24. Method one: transect A (September low flow condition).

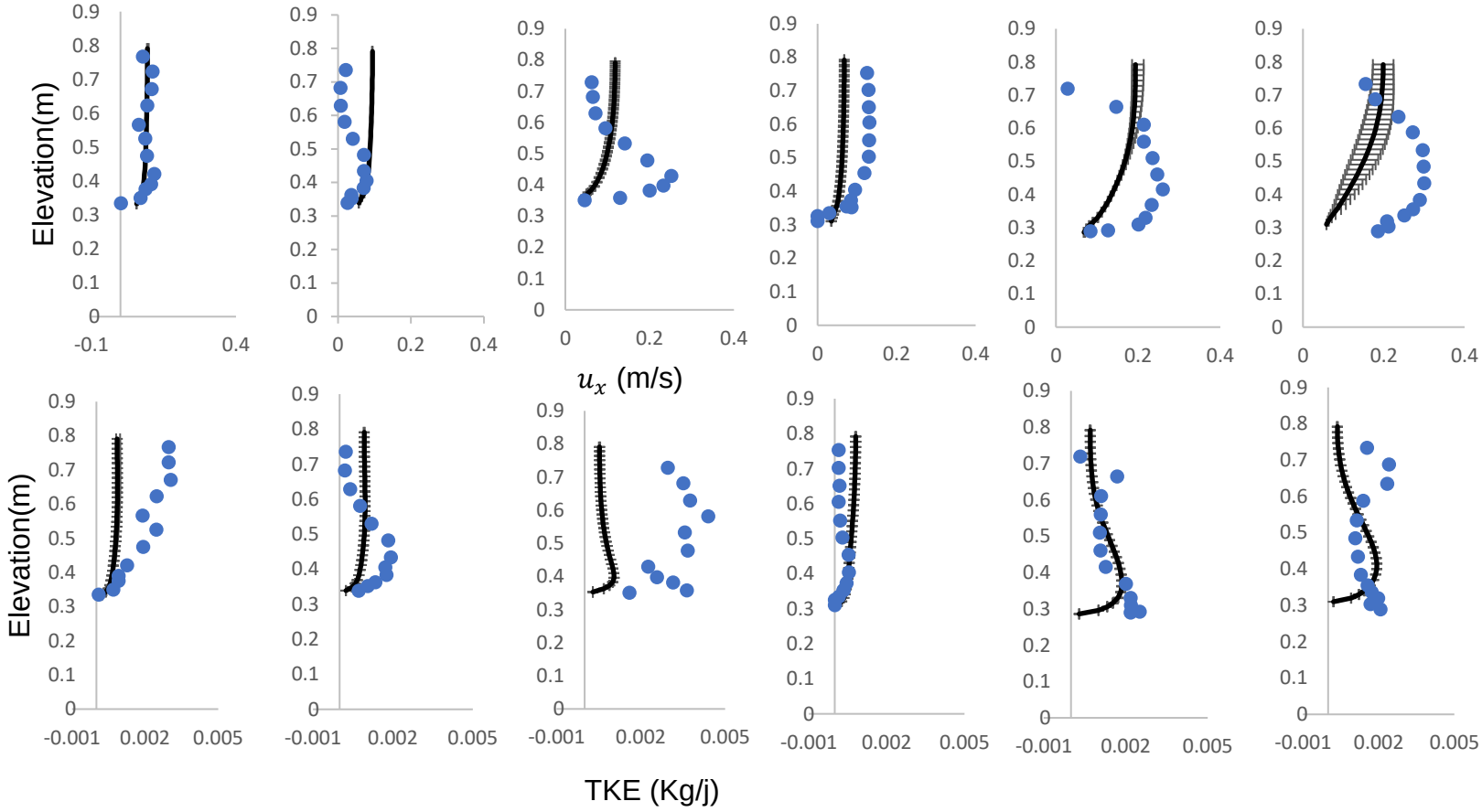


Figure 7.25. Method one: transect B (September low flow)

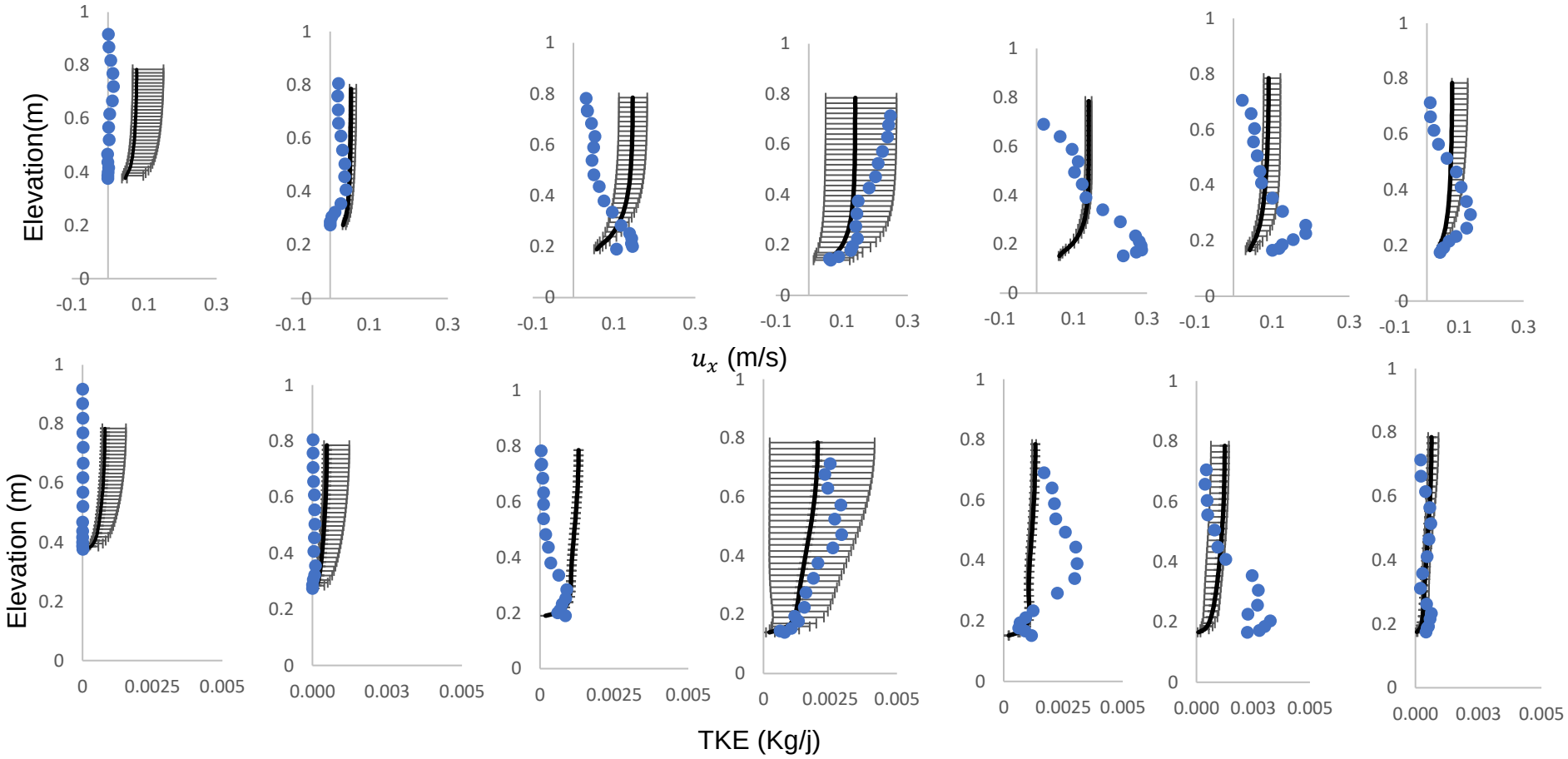


Figure 7.26. Method one: transect C (September low flow).

Figures 7.27 – 7.29 show the flow profile uncertainties for the September low flow conditions for method two. For method two, the uncertainties are comparatively a lot smaller whilst having a similar spatial distribution: again, the largest uncertainties occur at the banks. Transect A exhibits the most variability with the largest variations occurring just above the roughness layer. Transect C exhibits the least variability in flow quantities throughout the flow column, whilst the greatest degree of variability is found in transect A. Similar to method one, most profiles exhibit greater variability just above the roughness layer and the greatest variation between each profiles occurring in areas occupied by vegetation for all flow variables. Notably the TKE exhibits slightly more variation than the TKE profiles in method one, which again suggests that the second method has higher turbulence generation out of the two methods.

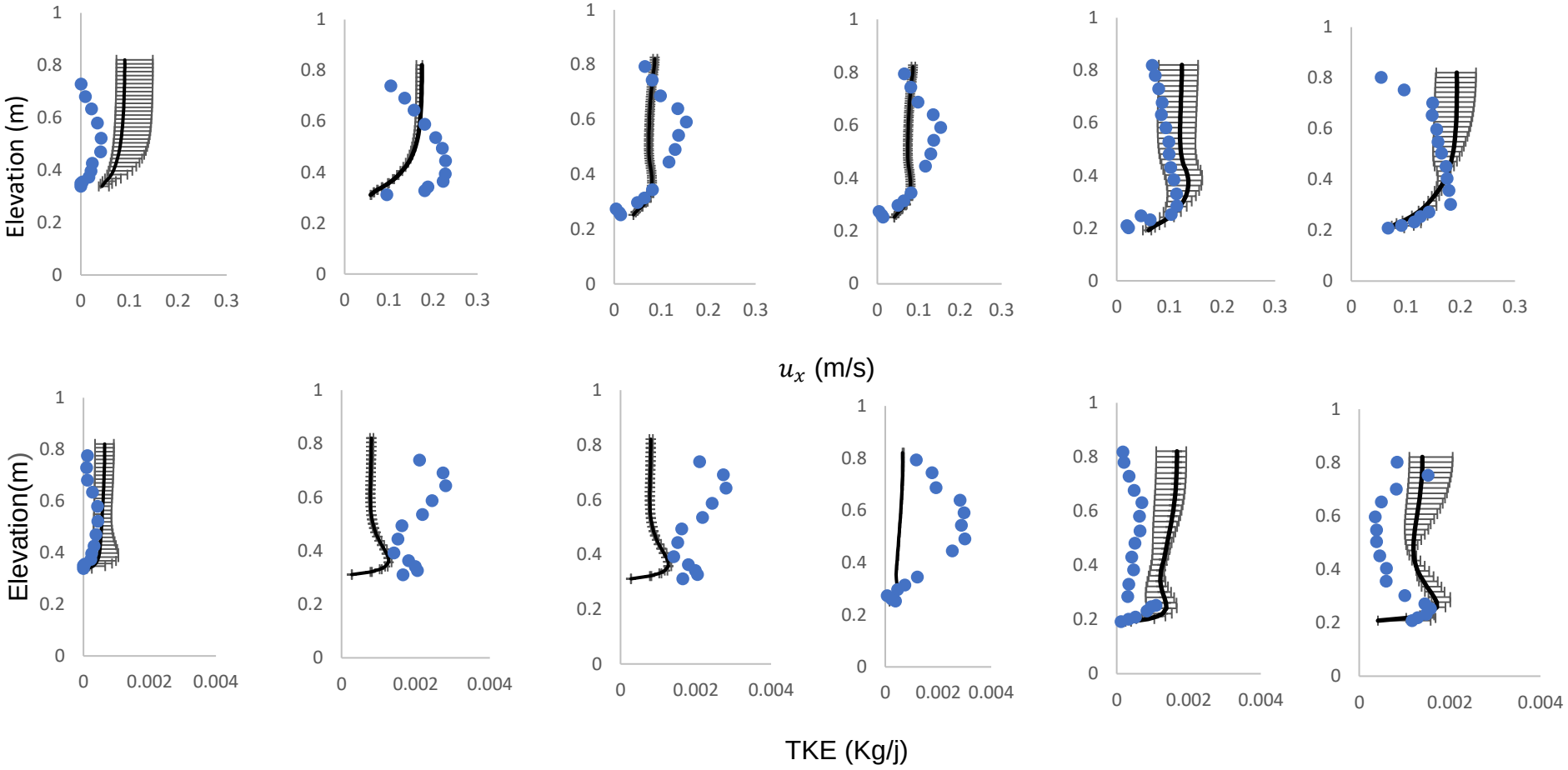


Figure. 7.27. Method two: transect A (September Low flow)

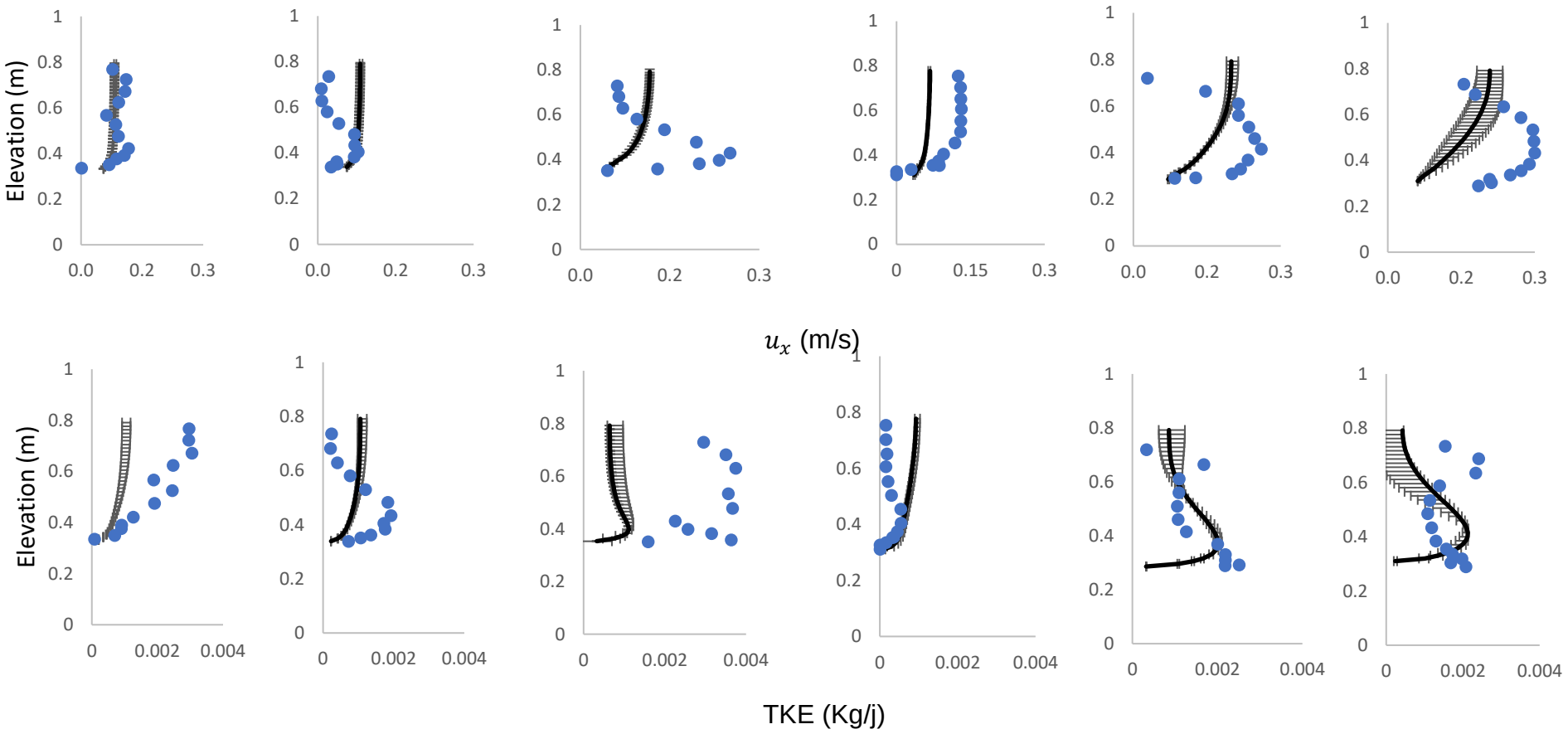


Figure 7.28. Method two: transect B (September low flow)

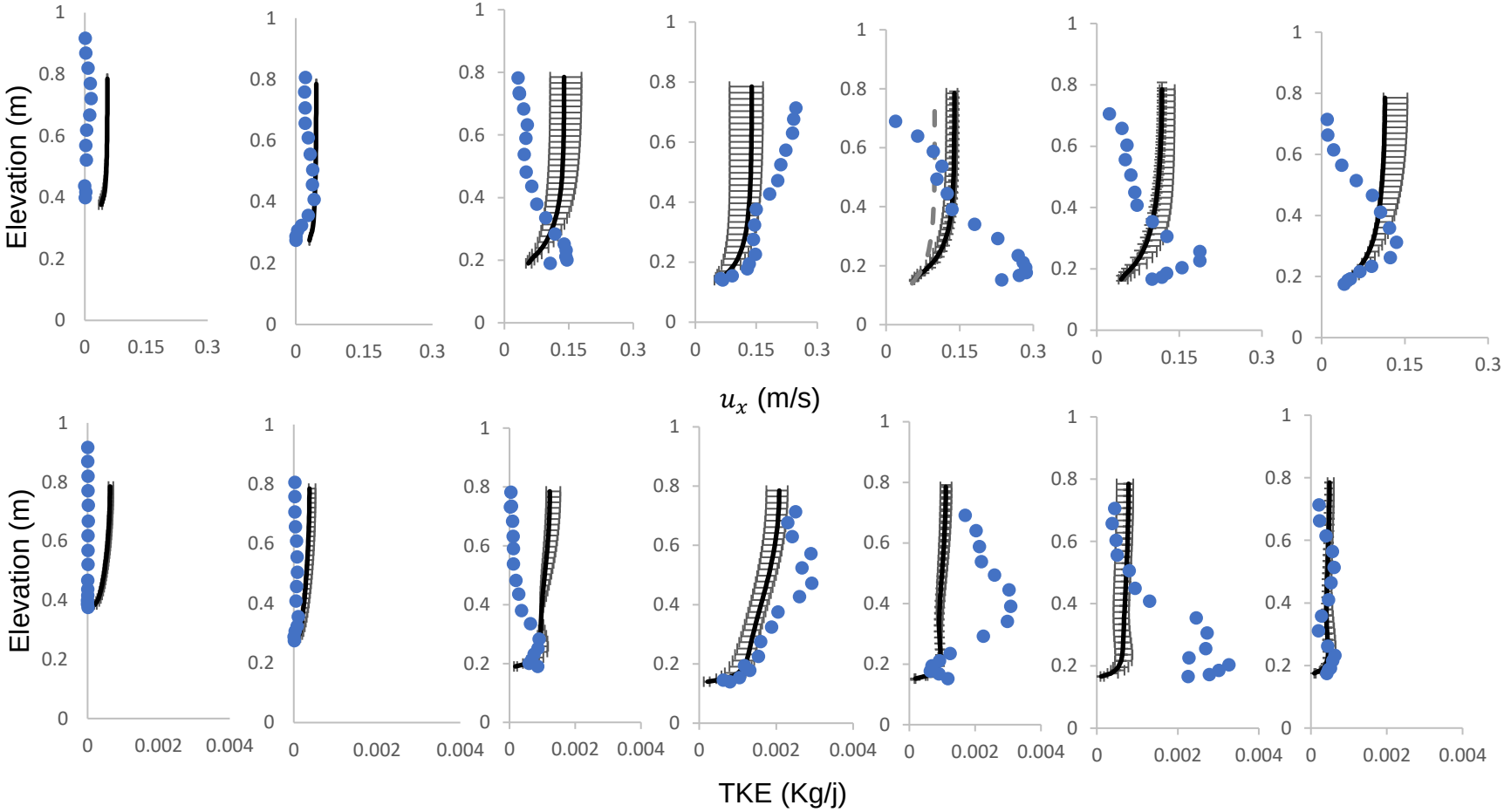


Figure 7.29. Transect C (September Low Flow)

Figures 7.30 – 7.35 compare the flow profiles for both methods for both low flow and high flow conditions. It should be noted that the transects for the high flow and low flow periods are not complementary with each cross-sections positioned at a unique location at the reach. As previously mentioned, profiles are broadly within the same region as the measured data, with the simulated data exhibiting a smoothened profile compared to the flow data. Broadly speaking both methods generally have similar shapes for their flow profiles suggesting that both methods capture similar processes. For the high flow case, differences between the methods are largely due to changes in the magnitude of flow quantities: transect A consistently shows method one as estimating higher velocities and TKE than method two. This is broadly consistent with transect B, however transect C shows method one as estimating higher flow quantities. The greatest divergence between measured and simulated data occurs in transect C at the right bank, where both methods overestimated both streamwise velocity and TKE near the roughness layer. For the low flow case, both methods exhibit flow profiles with a much greater similarity than those in the high flow case. The exception to this is transect C, where method two estimates higher flow quantities near the left bank, and method one estimated higher flow quantities towards the right bank. The greatest differences occur at the left bank, here both methods significantly overestimate both streamwise velocity and TKE throughout the water column.

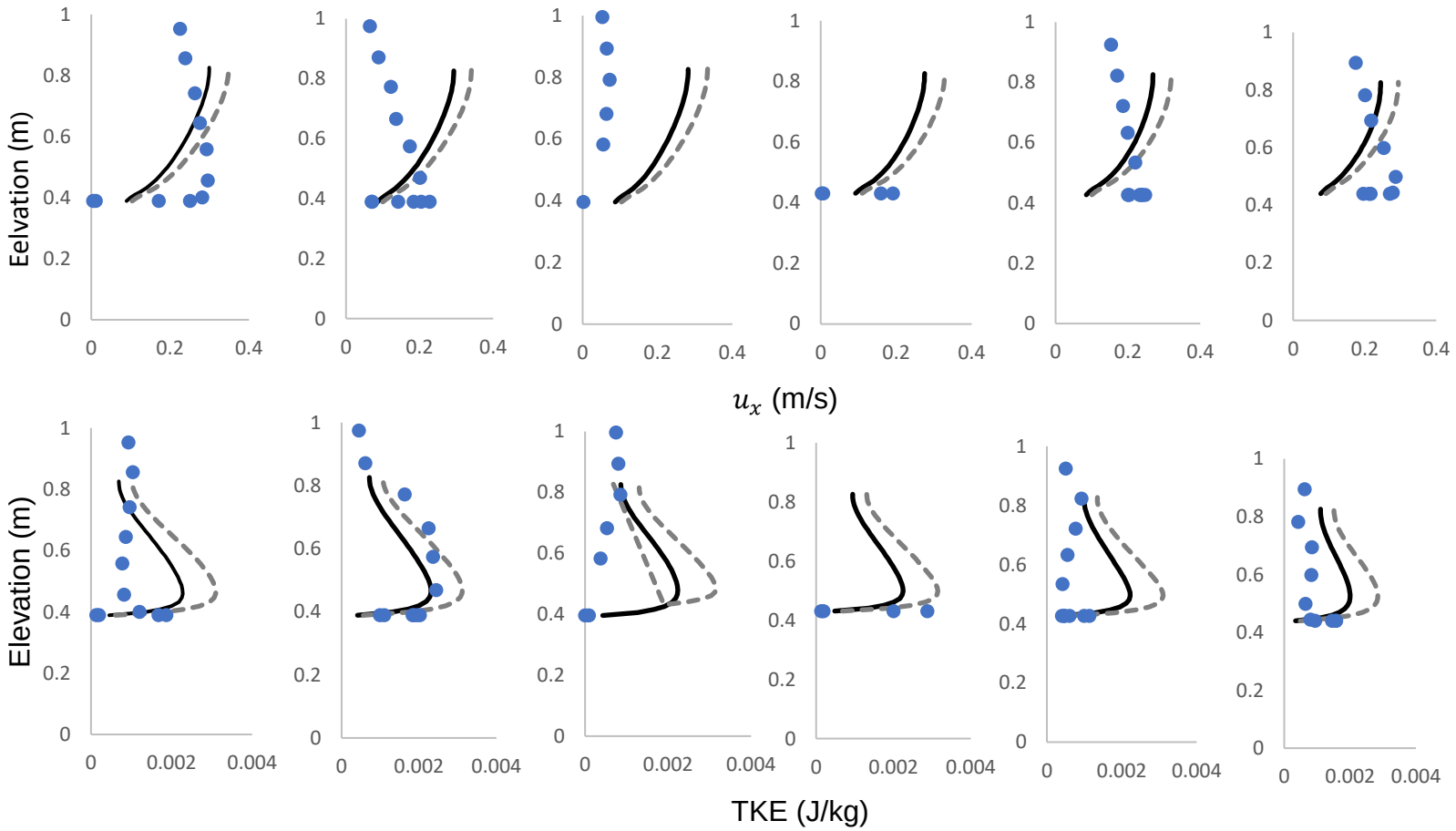


Figure 7.30. Transect A (September High Flow)

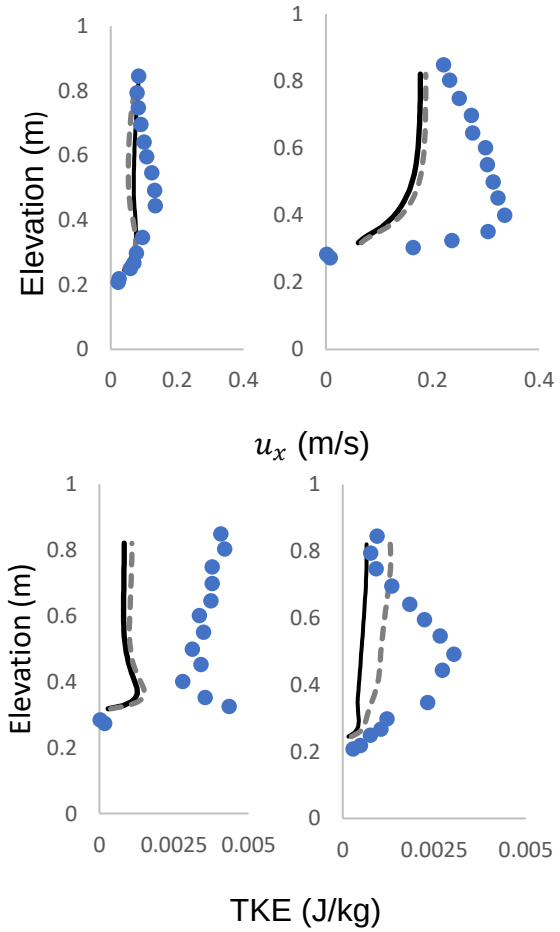


Figure 7.31. Transect B (September High Flow)

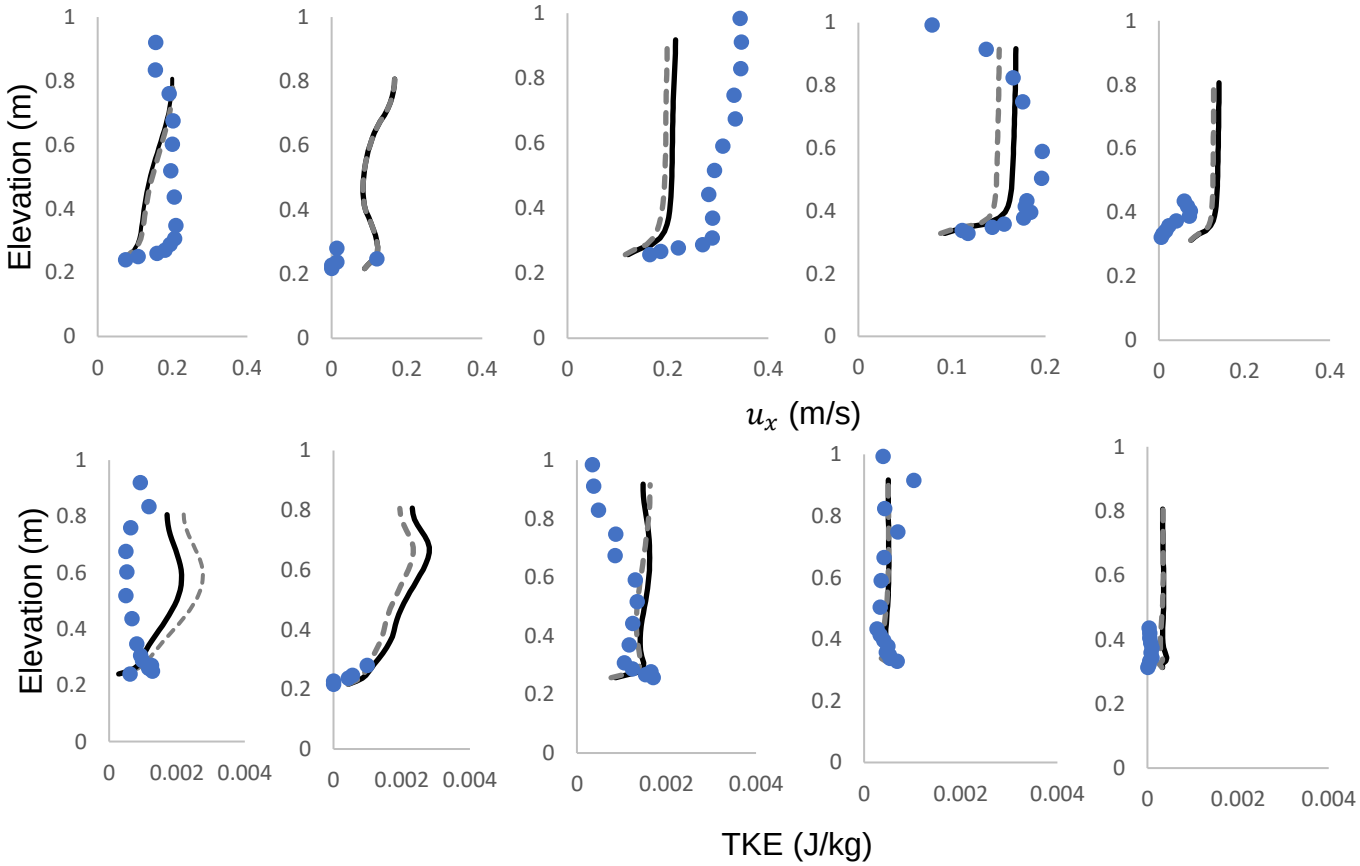


Figure 7.32. Transect C (September High Flow)

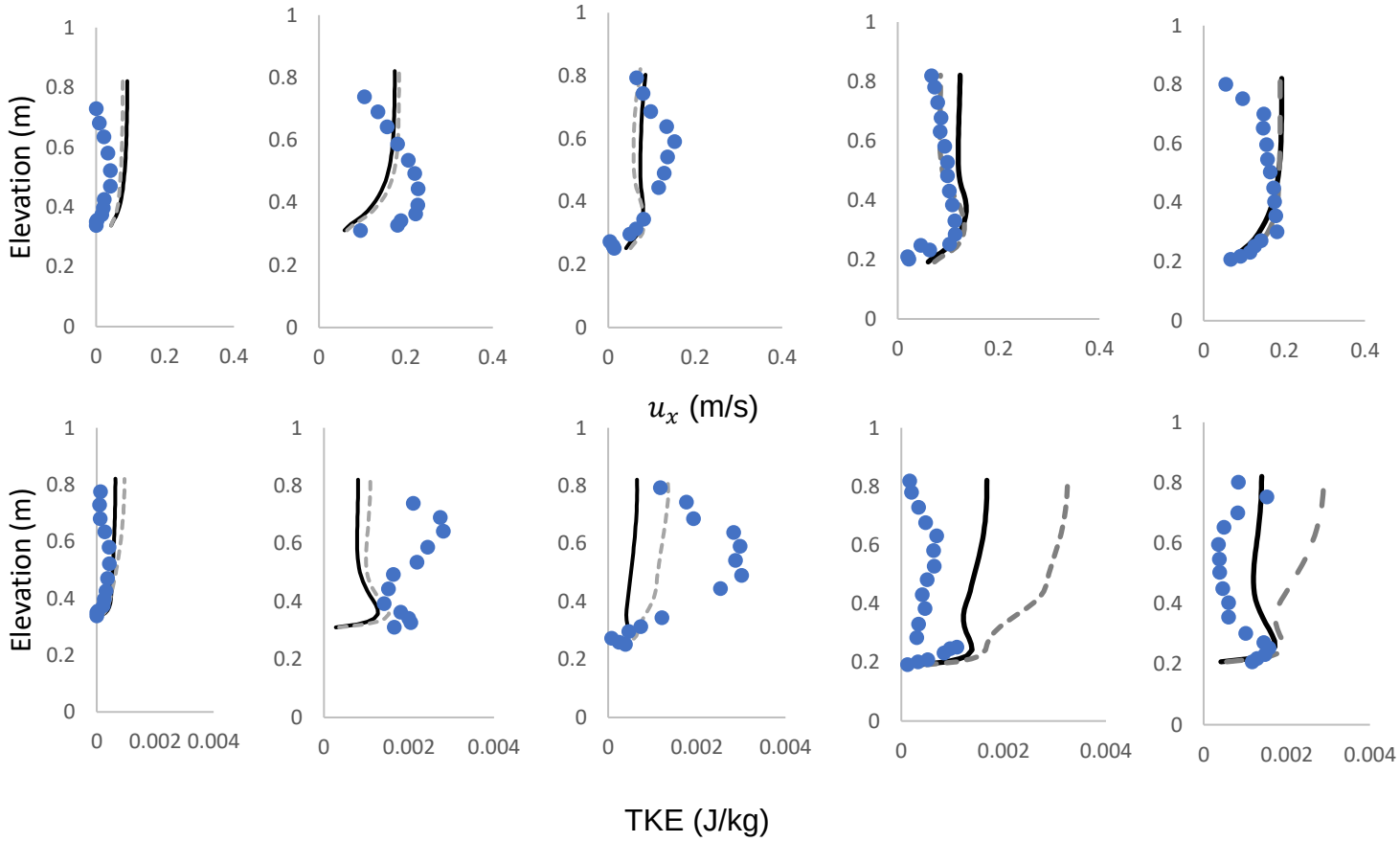


Figure 7.33. Transect A (September Low Flow)

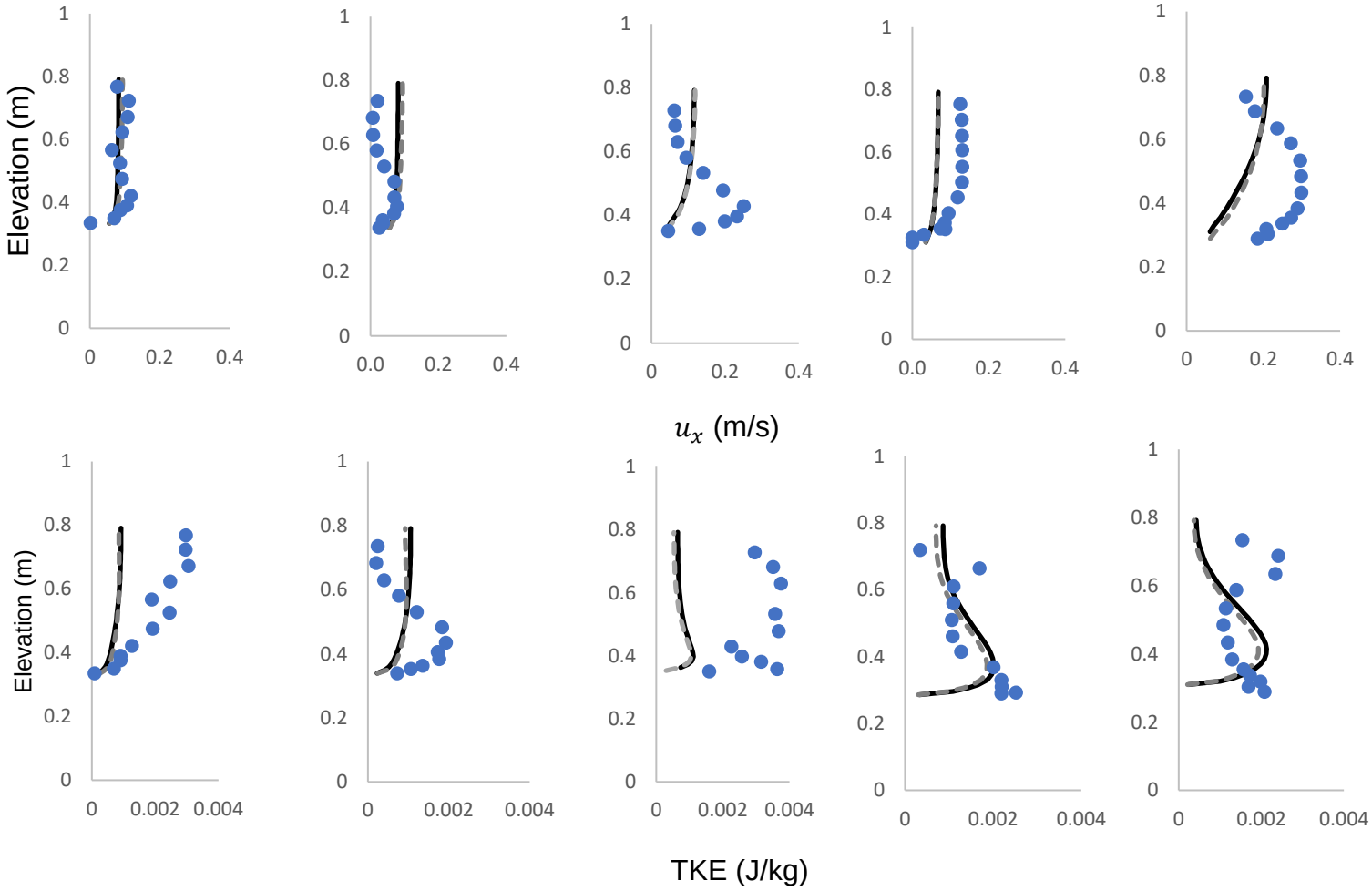


Figure 7.34. Transect B (September Low Flow)

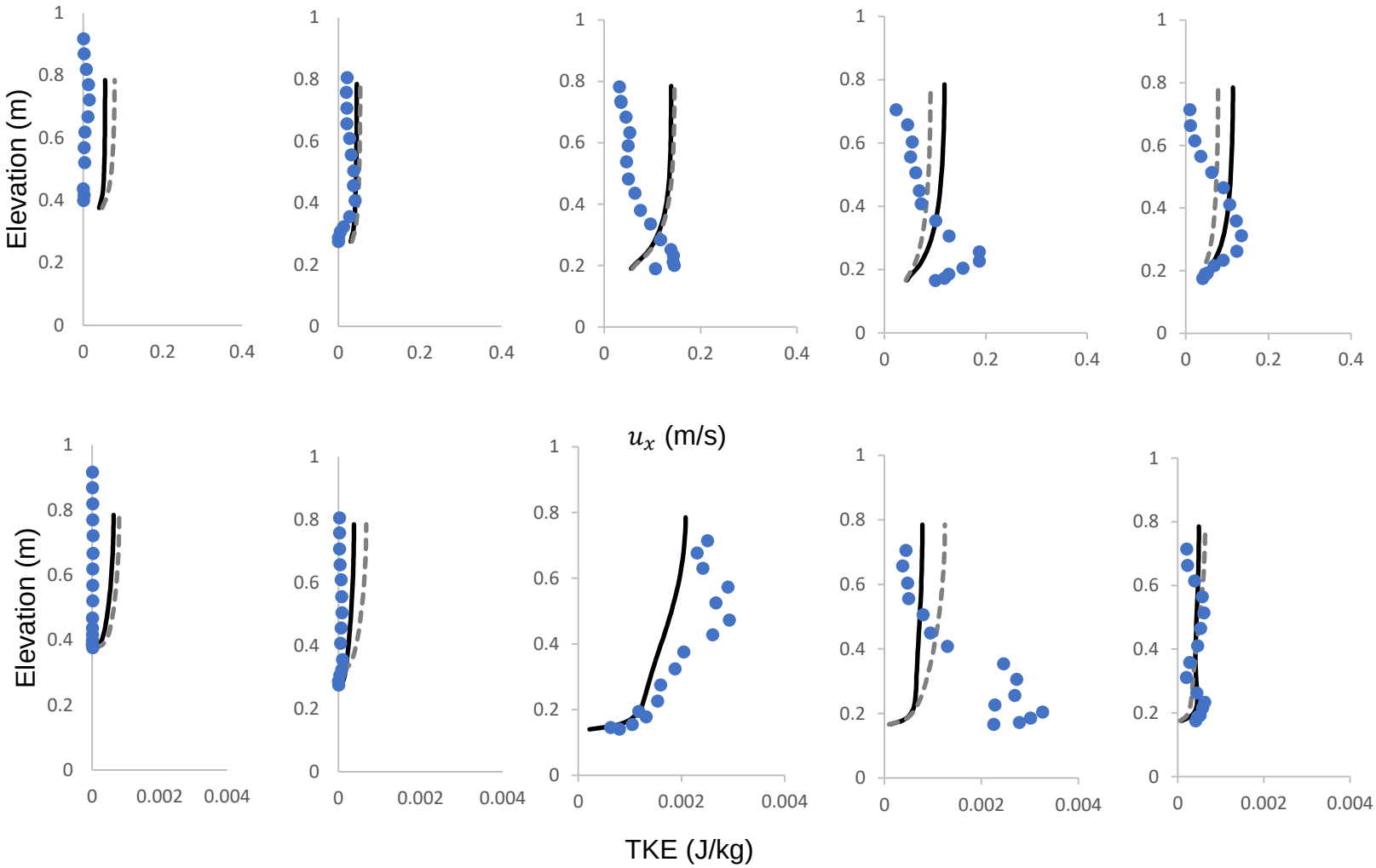


Figure 7.35. Transect C (September Low Flow)

The influence trailing vegetation has on flow is described by Fig.7.36: in section (I) the streamwise velocity component is shown to be increasingly reduced towards the tail of the patch, suggesting increased deceleration along the patch. Similar to the uniform nodal array used for *S. emersum* species shown in Fig.7.18, the flow is bisected by the patch with the highest velocities observed in the non-vegetated flow on either side. However, compared to the uniform arrays the patch is less discretised by the flow with high velocities continuing further past the patch head. This is a due to the curved patch geometry shown in section (II), where the flow interacts with the patch in two ways: firstly, the velocities are inhibited only near the patch base resulting in unimpeded velocities higher up in the water column; secondly velocities increase in the non-vegetated flow domain between the patch and free surface, which has previously been described in the literature (Sand-Jensen & Pedersen, 1999). Section (II) also shows where velocity is reduced within the whole patch but begins to increase once the flow encounters the non-vegetated channel in the void at the riverbed and downstream of the patch. The highest TKE values occur at the head of the patch close to the surface where the velocities are highest in the non-vegetated flow domain which is indicative of the increased velocities generating a strong shear layer. Further turbulence is depicted just downstream of the patch where the vegetated flow re-joins the channel and where the bisected channel flow re-joins. The lowest TKE values are present in the near-bed void beneath the patch where velocities are slow due to upstream vegetation blockage with little interference from the patch itself. Section (III) describes the streamwise variation in flow velocities throughout the water column: the greatest reduction in velocity occurs where at the bulk of the vegetation patch, beginning near the riverbed (B) and increasing in elevation to the free surface (E); the locus of velocity reduction increases in elevation downstream with the vertical position of the patch. The streamwise velocity begins to recover in the near-bed void beneath the patch, as seen in (D) and (E), and just downstream in the wake (F). Similar to the uniform arrays, the highest velocities are seen in the non-vegetated flow domains on either side of the patch due to flow bisection.

Interference from the wake of a patch upstream explains the low velocities preceding the patch in cross-section (A).

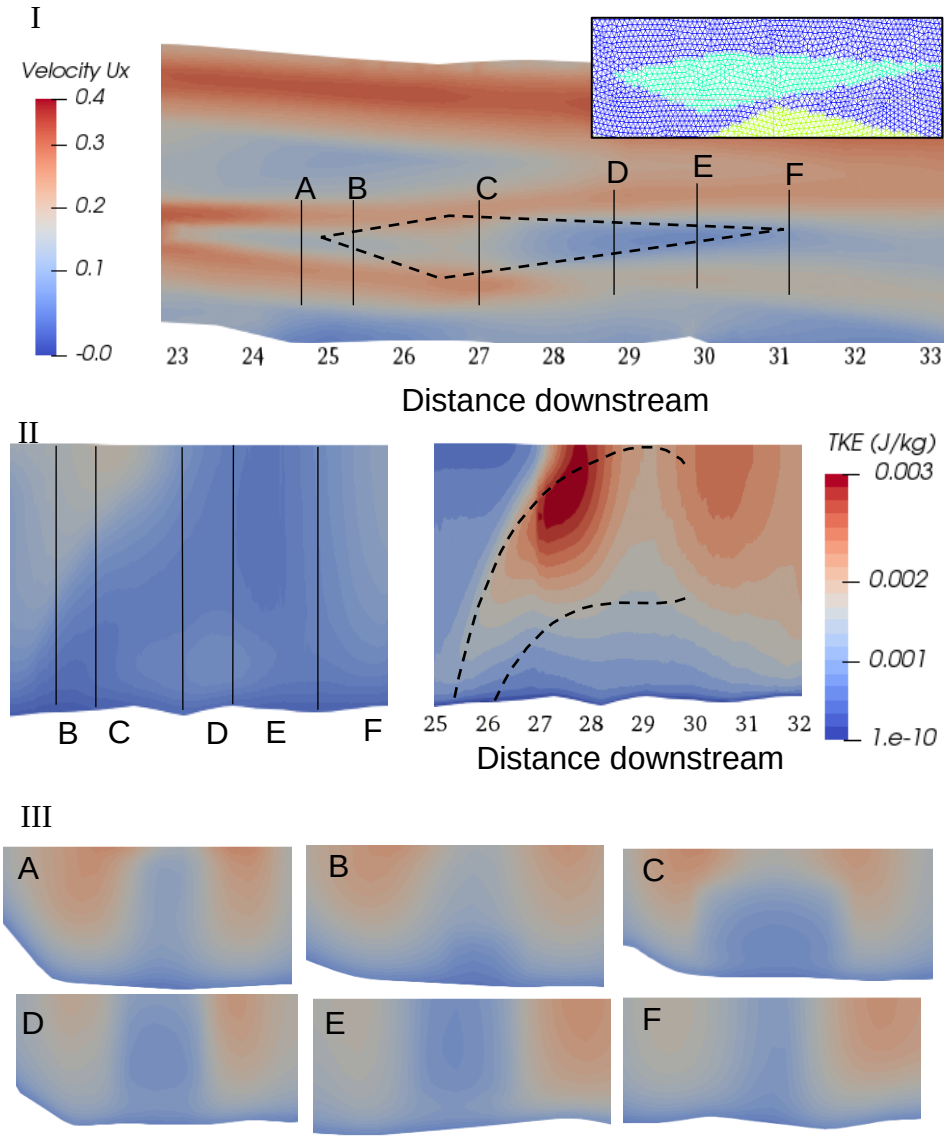


Figure 7.36. The effect of trailing vegetation on flow conveyance for the September (2001) low flow period, showing the channel distribution of surface velocity ux component in response to the vegetated nodes (inset) (I); the streamwise variation in velocity ux and turbulent kinetic energy (II), and the cross-sectional variation in velocity throughout the patch (III). The location of the cross-sections are shown in figs. (I) and (II).

## 7.6. Representing overhanging vegetation

The effects of overhanging bank vegetation disturbing the surface flow has not been widely researched, with little literature detailing how overhanging vegetation may be best represented. However overhanging vegetation can become significant to contributors flow resistance at bankfull conditions (Tabata & Hickin, 2003). In this study the effect of overhanging vegetation was represented by the application of a skin friction coefficient at the highest mesh layer i.e. the free surface. The majority of overhanging vegetation is composed of grass and herbaceous species (Rameshwaran & Naden, 2012). Previous research has identified that skin friction becomes important as grass blades assume more streamlined positions within the flow and superceding the influence of form drag (Luhar & Nepf, 2011). Luhar & Nepf (2011) represented seagrasses using a skin friction coefficient value of $C_f$ of 0.001 to 0.01, comparable to a relatively smooth surface although they noted that in reality such surfaces are likely to be rougher due to, for example, epiphyte growths. Skin friction drag was estimated using (Hervouet, 2004):

$$C_{vf} = 2n^2 g/h^{(1/3)}$$

where $C_{vf}$ is the skin friction coefficient for overhanging vegetation estimated from a Manning's $n$ value of 0.01, $g$ is acceleration due to gravity, and $h$ is the local depth. The friction term was then calculated as:

$$F_{vi} = \sqrt{C_{vf}({U_x}^2 + {U_v}^2)}$$

where $U_x$ and $U_v$ are the average velocities over the vertical, and $F_{vi}$ is the friction term (Hervouet, 2004). The vegetative friction was represented by identifying the nodes which were affected by overhanging vegetation (Figure. 7.4) and then applying the friction term to those nodes.

Simulation runs investigating the effect of overhanging vegetation were calibrated using the same method discussed for the September cases. Again, both drag estimation methods were used.

Both methods including the effects of overbank vegetation calibrated with coefficient values closer to those for the May case for their respective method, shown in Table

7.6, suggesting that the inclusion of overbank vegetation has increased the accuracy to which the model captures the influence of vegetation on flow conveyance.

Table.7.6. Calibrated values for September and May conditions using overhanging vegetation.

| Simulation case | May | September low flow conditions | September low flow conditions *with overhanging vegetation* |
|---|---|---|---|
| Calibrated coefficient | 0.32 | 0.34 | 0.33 |
| Simulation case | May | September low flow conditions | September low flow conditions *with overhanging vegetation* |
| Calibrated coefficient | 0.04 | 0.07 | 0.06 |

Figure.7.37 shows profiles for the September low flow case at cross-section two for two bank regions with overbank vegetation, and a channel free of vegetation. Compared to the simulations without overbank vegetation applied: the simulated streamwise velocity in the near-surface region is reduced compared to profiles at the same node. This suggests that the effect of overbank vegetation on flow reducing velocities is represented effectively within the model. A larger difference throughout the water column exists at the right bank, which may be due to slower flow on the inside of the meander bend resulting in greater changes in the velocity gradient. A slight increase in velocity is observed in the central channel for the case with the overhanging vegetation, suggesting that continuity has been satisfied in the cross-$u_x$ (m/s) section.

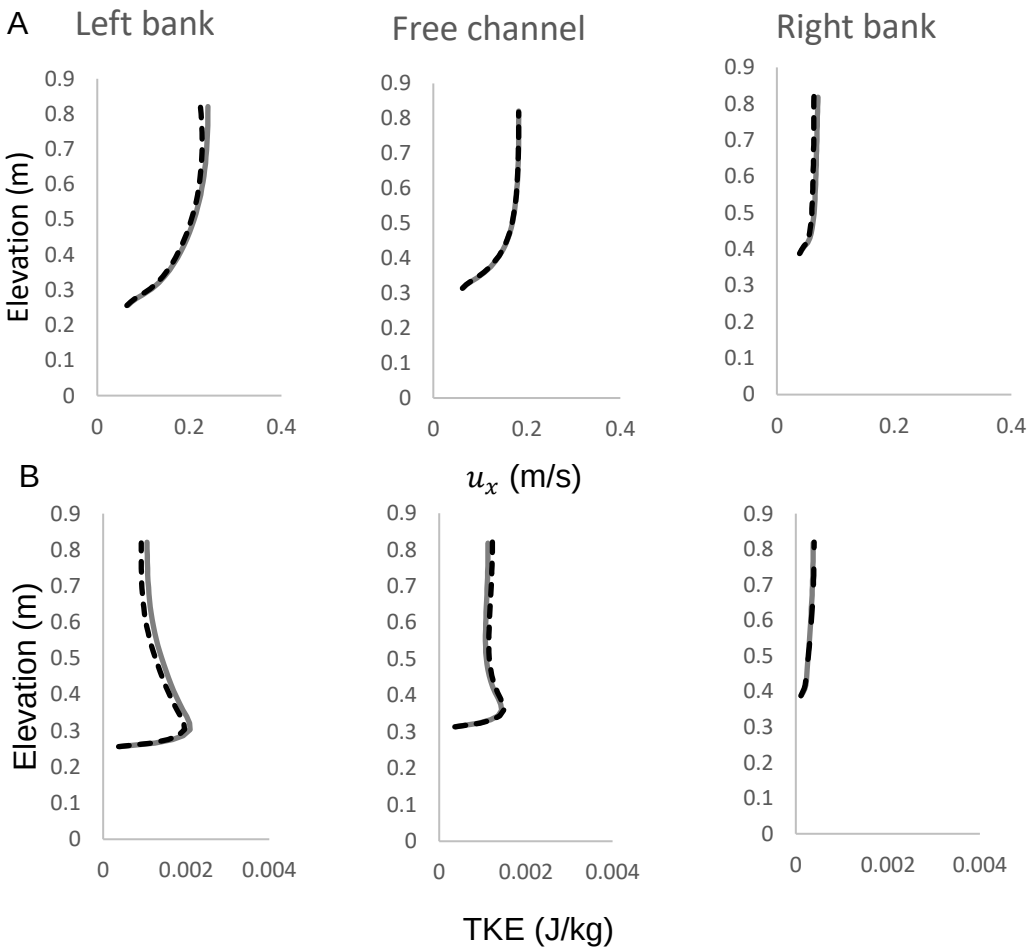


Figure 7.37. The effect of trailing vegetation on flow conveyance for the September (2001) low flow period on flow profiles for velocity (A) and TKE(B). Profiles for overhanging vegetation are the black dashed line, and profiles without overhanging vegetation are represented using the grey solid line.

## 7.7. Representing berm vegetation:

The effect of vegetation on floodplain (i.e. the berm) flow needed to be characterised to ensure that the predicted flow was realistic. The global mesh was extended to include a floodplain zone with a larger edge length (0.3m) than previous meshes (0.1m) in order to improve computational efficiency. The channel banks were extended to their full height as measured in the topographic survey and the edge length was increased to 0.2m to ease the computational burden. No data was available to either describe the vegetation occupying the berm or the flow quantities during a flood event. In order to test berm roughness the berm vegetation was characterised using site photographs and measurements of similar tree species. The floodplain vegetation was parametrised using composite drag term consisting of drag due to trees and the drag due to the effect of small shrubs and grasses. The drag term for the trees was estimated using the relationship described by Nepf (1999), and the grass drag coefficient was adjusted until a reasonable channel slope was acquired. Due to the lack of data, it was assumed that the free surface slope for the channel during a flood event would be similar to the gradient of the highest recorded flow: the September High Flow condition. The calibration method used in previous sections for slope calibration was employed, where the bulk drag coefficient for grass was incrementally adjusted until the differences between the slopes were at a minimum.

### 7.7.1. Generating the floodplain mesh

The mesh generation procedure followed the method outlined in Chapter 5. The areal extent of the berm was delineated by fitting a polygon to the topographic data. A second polygon was generated which described the maximum extent of the channel banks. A triangular mesh was then generated within the second polygon using an edge length of 0.2m, resulting in the channel sub-mesh. This was then inserted within the larger floodplain polygon which was subsequently generated with an edge length of 0.3m. The channel mesh resolution was decreased from the 0.1m previously used as the high resolution was computationally expensive due to the greater number of elements; the quicker run-time provided by using a 0.2m edge length was more practical for the scenario runs. The key area of interest in this study is the dynamics of in-stream vegetation within the channel rather than on the

floodplain. As such, the floodplain mesh resolution was set to 0.3m to ease computational burden. The assessment of accuracy for all of the above mesh resolutions were discussed previously in Chapter 6, Section 6.5. The boundaries between the floodplain mesh and channel sub-mesh were flush except at berm which was the only floodplain environment included in the data. The initial data and resulting mesh for the above procedure is illustrated in Fig. 7.38.

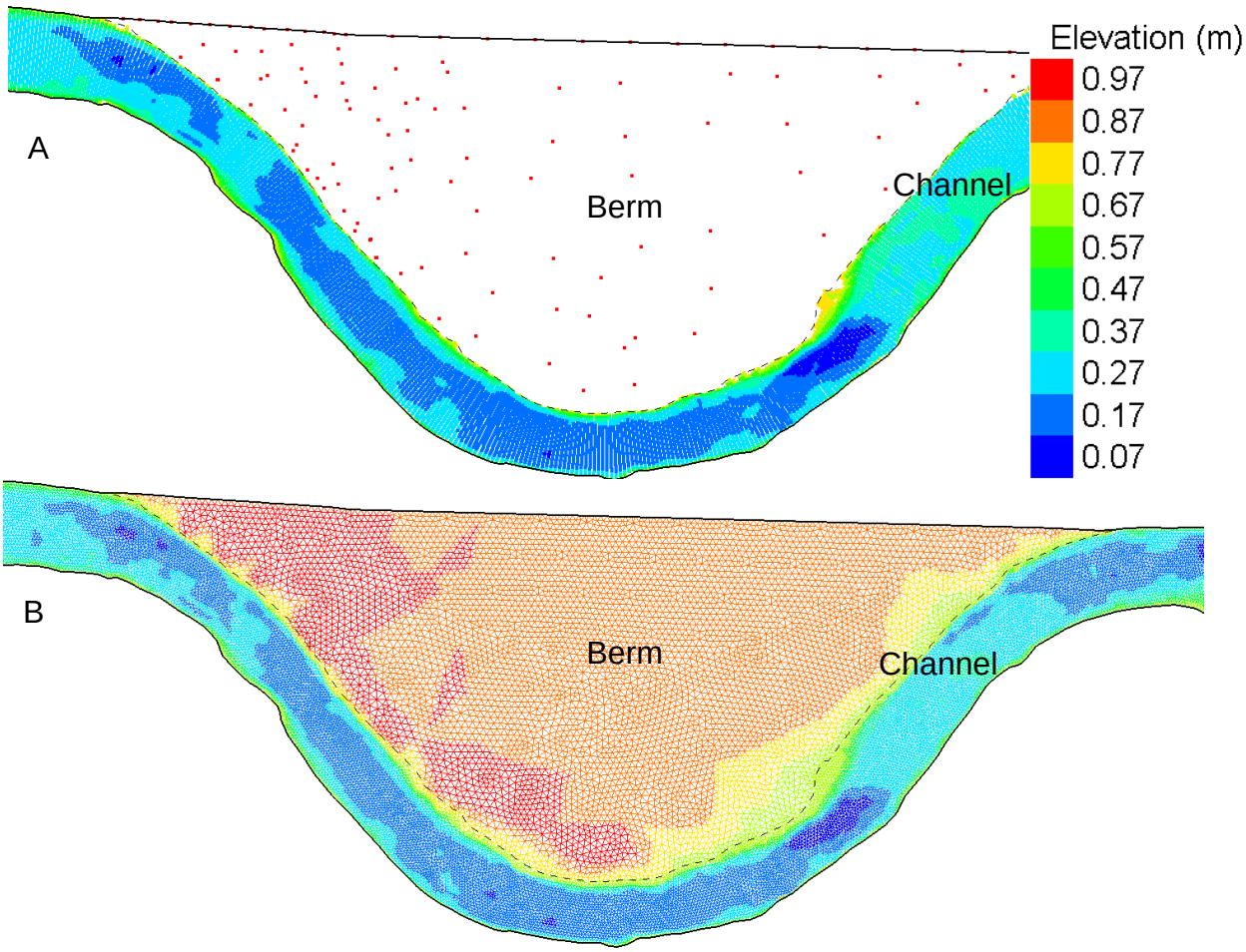


Figure 7.38. Delineation of the channel and berm topography (A), showing the sub-mesh boundary for the channel (dashed line) and the total mesh boundary (thick, solid line) inclusive of the topographic data (coloured icons), alongside the resulting mesh with interpolated topography (B).

Both the channel sub-mesh and floodplain mesh were represented using unstructured triangular meshes with regular spacing between the vertical layers. Due to the constrained geometry of the floodplain the mesh exhibits a higher resolution on the vertical compared to the channel mesh, which can be seen in Fig. 7.39.

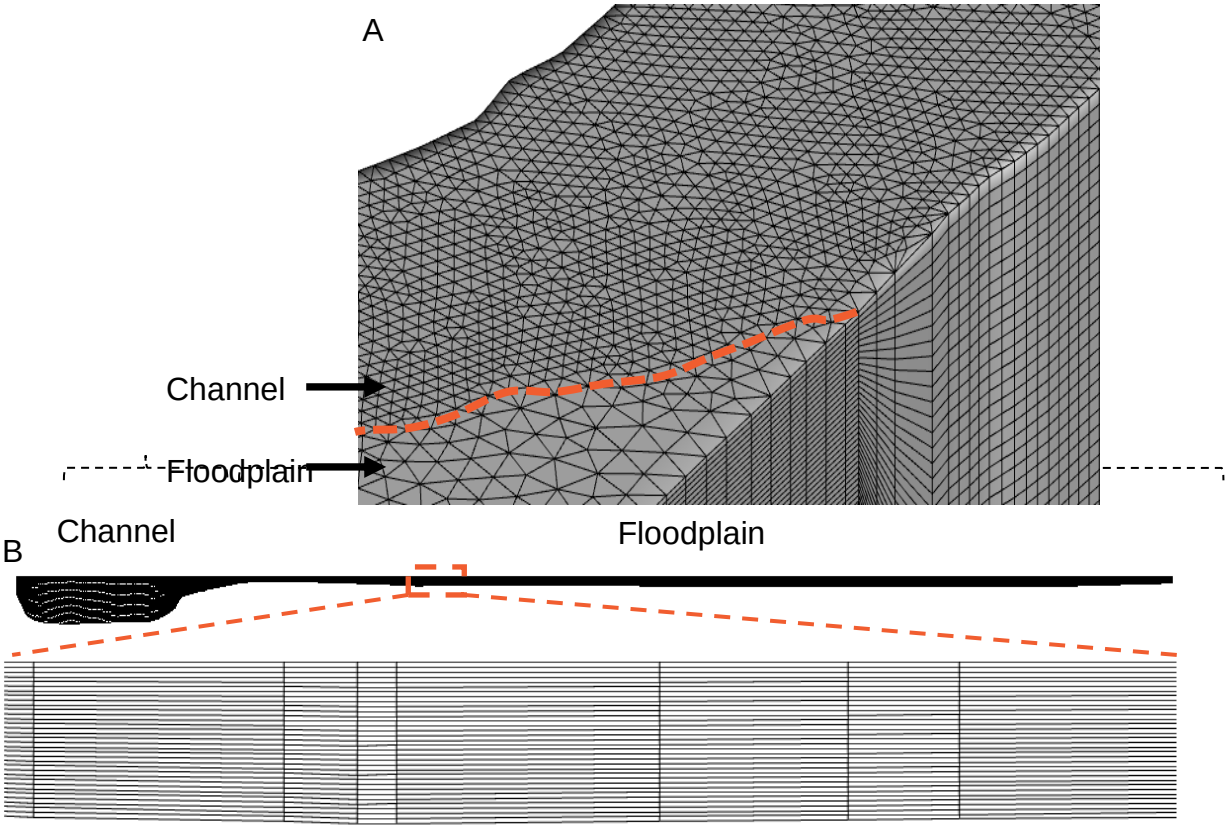


Figure 7.39. Distribution of mesh layers throughout the z-axis, comparing the 3D differences in resolution between the channel and floodplain meshes (A), and a typical cross-section of the floodplain mesh cutting through berm centre from the meander apex (B).

### 7.7.2. Characterising floodplain vegetation

Site photographs taken in May 2016 (Fig. 7.40-43) were used to assess the composition of vegetation cover, determine the extant tree species, and estimate the areal density of tree coverage. The largest roughness elements on the floodplain (the berm) were trees of the willow species *Salix caprea*. The willow species dominated the berm with few other species observed to inhabit the area. The composition of non-woody vegetation was largely grasses with some small shrubs and bushes. A resistance factor $ks$ = 0.01129622 for the soil was applied on the floodplain nodes at the first layer, where the $ks$ value was converted from the Manning's $n$ for a floodplain with only firm soil ($n$ = 0.018), as reported in Arcement & Scheider (1989). The value for a vegetated floodplain $ks$ = 0.6105295 ($n$ = 0.035) was also considered. Both values were assessed against the limit of $ks$ for application at the boundary layer where $ks$ is meaningful when ≤29.7*Z, where Z is the height of the first vertical layer (Rameshwaran et al., 2011). For the floodplain mesh 29.7*Z = 0.22737, indicating that only the firm soil value is acceptable; the vegetated floodplain value is meaningless without considerably altering the mesh to more than twice the size of $ks$/29.7. As a result, only the floodplain resistance for soil was used and vegetation was parametrised using the drag force approach.

The floodplain trees had been coppiced resulting in most exhibiting multiple trunks. This is important as during emergent flow conditions tree trunks induce a considerable level of drag on the flow (Wilson et al. 2006). To account for this, the density of *S caprea* was calculated by counting the number of trunks rather than the number of individual trees. In total thirty trunks were counted on the floodplain.


A
Flow

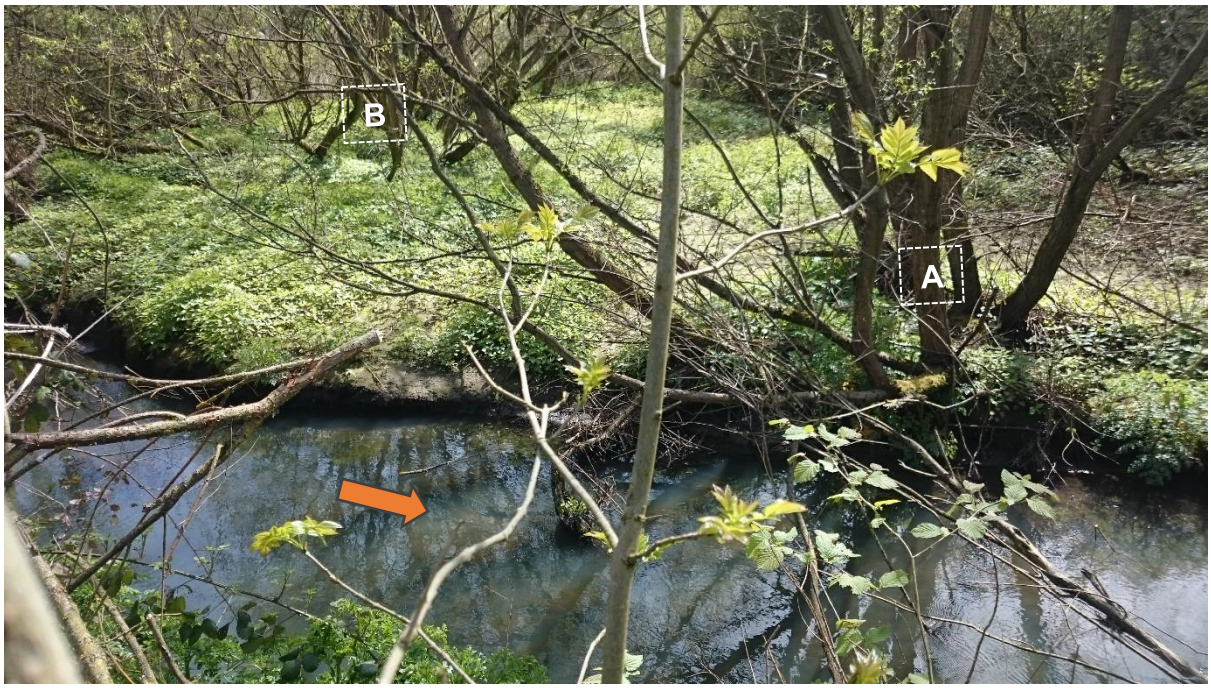
B
A


Figure 7.40-43. Selected field site photos of the berm. Taken May 2016. The orange arrow represents flow direction. Selected trees were labelled A & B to present spatial consistency throughout the photos.

To calculate the appropriate drag term the trunks of *S. caprea* were assumed to be cylindrical with a uniform diameter and distributed regularly across the berm. Similar to the in-stream vegetation, estimating appropriate drag terms for trees is difficult due to large variations in trunk geometry and biomechanical characteristics (for example, flexibility) both between species and individual plants (Nepf, 1999; Kothyari, Hayashi, & Hashimoto, 2009). In reality, trees exhibit increasingly complex geometry with greater elevation due to complex branching in the main canopy region. However, the maximum flood height over the floodplain is considerably below the main canopy region and exhibits relatively fewer branches. Therefore, the model represents the tree trunks below the canopy and the effect of any branches are assumed to be negligible compared to that of the trunks. In this case, representing the trunks as cylinders was deemed appropriate. This approach is frequently adopted within the literature (for example, see: Stoesser et al., 2003; Wislon et al., 2006; Tanino & Nepf, 2008; Aberle & Järvelä, 2013; Mulahasan et al., 2017) when modelling the effect of trees inundated below the main canopy level; although this simplification means that the effect of any flexible woody vegetation on the velocity field below the main canopy is uncharacterised, Wilson et al. (2006) mention that this may be adequate for modelling flood inundation extent.

The density of the trees was calculated by dividing the number of trees (30) by the area of the berm (839.877 $m^2$). The berm area was calculated using measured site data (see Chapter 3, Section 3.3.2). The width of the trees was determined by measuring the diameter of similar *Salix* species at breast height (1.4 m) using a flexible measuring tape. Breast height is conventionally used by foresters and ecologists to ensure consistency between tree measurements (Broad, 2015), and thus was deemed appropriate in order to keep the study in line with literature. The average diameter was then used to compute the appropriate drag imposed by the trunk on the flow in each Cartesian direction using the drag equation previously described in Chapter 4, Section 4.3. Flow in the z-direction was calculated using the equation:

$$A_s = (nt\pi DTC)/(AC)$$

where $AS$ is the surface area of the trunk diameter ($m^2$), $nt$ is the numb er of trees on the berm, $DT$ is the average trunk diameter (m), $C$ is equal to 1.0, and $A$ is the berm area ($m^2$). For flow in the x- and y-direction the area was calculated as:

$$A_p = (nDTC)/(AC)$$

where $AP$ is the projected area of the tree trunk ($m^2$). The values calculated were $AS$ = 0.00581717408 $m^2$ and $AP$ = 0.00185166399 $m^2$. Both were then inserted into the drag equation and the model was then run until convergence was reached.

There was a lack of data monitoring describing high flow over the berm, as such an appropriate calibration method was unable to be performed. To investigate whether the roughness effects on the berm appropriately emulated the free surface slope, the slope for over-berm flow were compared to that of the previously calibrated high flow for the September period. A lack of data monitoring bank exceedance meant that it was inappropriate to compare free surface elevation at the banks and instead the channel centreline was used to compare free surface slopes. The channel centreline was used to select the free surface values to ensure that there was a spatial similarity between the runs. The reduced resolution of the mesh meant that a direct comparison could not be made on a node-by-node basis using statistical methods (for example, RMSE method) therefore simple regression was used to compare the slopes.

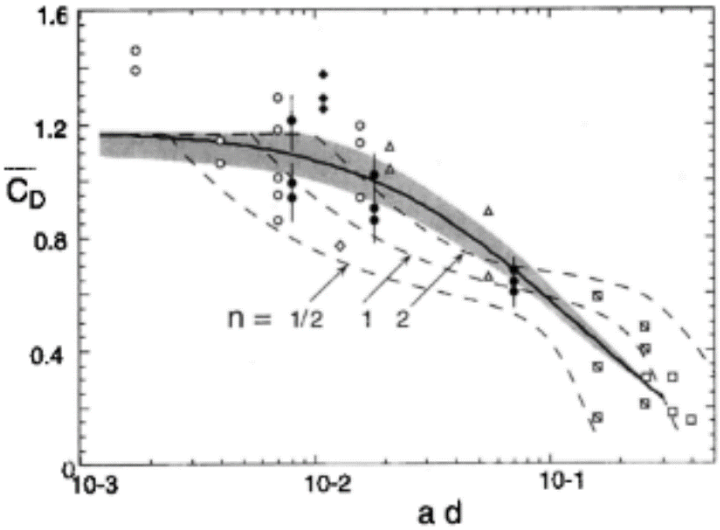


Figure 7.44. Decreasing bulk drag coefficient ($C_D$) with increasing array density ad for randomised (solid line) and staggered (dashed line) arrays of cylinders (Nepf.,1999).

Previous research investigating the representation of woody riparian vegetation identified that the drag coefficient $C_D$ should be close to 1.0: Schlichting (1962) discussed how an array of smooth, emergent cylinders with a range of Reynolds numbers of 1000<$Re_{cylinder}$<10000 the drag coefficient was about 1.0. Nepf (1999) investigated how wake formation by cylinders can diminish the drag coefficient of downstream cylinders (Fig.7.44). Rameshwaran & Shiono (2007) used a wake interference model developed by Nepf (1999) and calculated a bulk drag coefficient of 1.0. In the case where there's little data and an unknown drag coefficient it is therefore common practice to set the drag coefficient $C_{DT}$ to a fixed value, where $C_{DT}$ is the drag coefficient for trees on the floodplain. Nepf (1999) showed that an increasing density of a cylinder array will result in a non-linear decrease to the bulk drag coefficient $\overline{C_D}$. This relationship can be used to estimate an appropriate value for $C_{DT}$ assuming the tree trunks are uniform cylinders. The dimensionless population density $ad$ for the berm was calculated using the equation (Nepf, 1999):

$$ad = DT^2/\Delta S^2$$

where $DT$ is the circular diameter, and $\Delta S$ is the average space between cylinders and is assumed to be uniform, calculated as the number of trees divided by the area of the berm. In reality, the spacing between trunks across the berm is irregular. The values used are given later in Table 7.7. Nepf (1999) states that the dimensionless

population density $ad$ represents the fractional volume of the flow domain. The bulk drag coefficient $\overline{C_D}$ was obtained by using the relationship in Fig. 7.44 which was equal to 0.86. This is slightly lower than the standard value of $C_D$ = 0.1 used in the literature (for example: Tang & Knight, 2009), however this value was derived from experiments considering a single cylinder rather than the array as used by Nepf (1999) which is known to result in lower values compared to those attained from individual cylinders.

The composite drag for trees on the berm was then calculated as $C_{DT}$*$A_t$, where $A_t$ represents the characteristic area defined as either $A_s$ or $A_p$ for the respective Cartesian flow direction. The areal values for the grasses $A_{TGR}$ was unknown, thus the drag coefficient for floodplain grasses $C_{DGR}$ was adjusted to estimate the free surface slope using the method above. The drag equation for flow over the riparian floodplain zone was characterised as:

$$F_{bx} = \frac{1}{2}(C_{DT}S_{fT} * A_{PT} + C_{DGR}S_{fGR} * A_{PGR})|\langle\bar{u}\rangle|\langle\bar{u}\rangle$$

$$F_{by} = \frac{1}{2}(C_{DT}S_{fT} * A_{PT} + C_{DGR}S_{fGR} * A_{PGR})|\langle\bar{u}\rangle|\langle\bar{u}\rangle$$

$$F_{bz} = \frac{1}{2}(C_{DT}S_{fT} * A_{ST} + C_{DGR}S_{fGR} * A_{PGR})|\langle\bar{u}\rangle|\langle\bar{u}\rangle$$

Where $F_{bi}$ is the drag force implemented over the berm, $C_{DT}S_{fT}$ is the composite term for drag exerted by the willows, $C_{DGR}S_{fGR}$ is the composite term for drag exerted by berm grasses and $A_{PGR}$ and $A_{SGR}$ are the respective vegetative projected area and surface area for grasses, and, together with the composite drag term for grasses $C_{DGR}S_{fGR}$, theoretically equal the calibrated $C_{DG}$ term. Drag was applied to the floodplain zone on the mesh by selecting the nodes representing the floodplain using a polygon berm. The floodplain nodes were then inserted into the code in a similar fashion described in Section 7.3.1. Values for the parameters tested above are provided in Table 7.7

Table 7.7. Floodplain parameters for grasses and trees.

| | |
|---|---|
| Berm area ($m^2$) | 839.877 |
| Number of *S. caprea* trunks | 30 |
| Average width (m) | 0.053174 |
| $A_{PT}$ ($m^2$) | 0.00185166399 |
| $A_{ST}$ ($m^2$) | 0.00581717408 |
| $C_{DT}S_{fT}$ | 0.86 |

The composite grass drag coefficient $C_{DGR}S_{fGR}$ was estimated using the same method used for previous calibrations: the coefficient value was incrementally adjusted until the differences in slope between the observed and modelled data were at a minimum. To ensure that the berm drag was having an appropriate impact on overland flow the calibration scenario used boundary condition values for inlet discharge and outlet stage taken from the highest observed flow in September: 1.09 $m^3/s$ and 1.242m respectively. The slope value for the modelled free surface was compared to the slope value for the observed September-High period. The September High period had a slope of 0.00053m. The modelled slope for the berm test case had a slope of 0.00053m with a bulk drag coefficient $C_{DGR}S_{fGR}A_{PGR}$ of 0.36 (Fig.7.45). In the literature it is typical to observe how bulk drag coefficients estimated for floodplain vegetation varies with Reynolds number. Using the depth-averaged streamwise velocity for the September high flow condition, the Reynolds number for the maximum extent of the apex cross-section was 646636.09. In flume experiments Reynolds numbers are often lower, largely ranging below $10^{-4}$ (for example, see: Järvelä (2002); Mulahasan et al., 2017). Previous studies have demonstrated that coefficients are highly sensitive, with the drag coefficient dependant on the Reynolds number and the density and configuration of cylinders: previous research has described how the drag coefficient decreases as Reynolds numbers increases (Tanino & Nepf (2008); Cheng & Nguyen (2011)). Additionally, Tanino & Nepf (2008) discussed how the range of measured drag coefficients increases with decreasing rod diameter. Little data is available exploring the calibrated range for a floodplain composite drag coefficient inclusive of cylinder drag

and calibrated using the drag for low-level vegetation. The slope for both the September High period and the berm test case are presented in Fig.7.45.

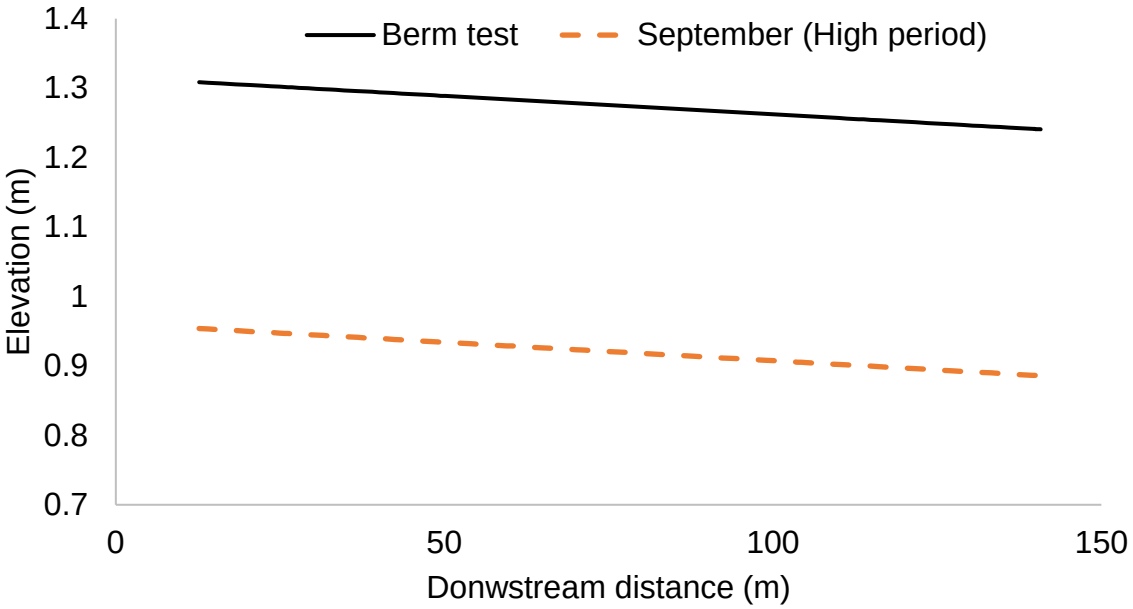


Figure 7.45. Calibrated free surface slopes for the non-berm ($C_{DGR}S_{fGR}$ = 0.34; orange, dashed line) and berm ($C_{DGR}S_{fGR}A_{PGR}$= 0.36; black, solid line) cases.

### 7.7.3. Assessment of berm flow characteristics

Flow patterns for the calibrated September High Flow case and the berm case were compared. Fig.7.46 describes the streamwise velocity patterns for the same cross-section. Both flow cases share the same vegetation distribution in the channel; the key difference in their parametrisation is that the berm case includes additional mesh elements representing the berm and associated higher banks, the drag effects of berm vegetation, and increased values for discharge and stage for the initial conditions.

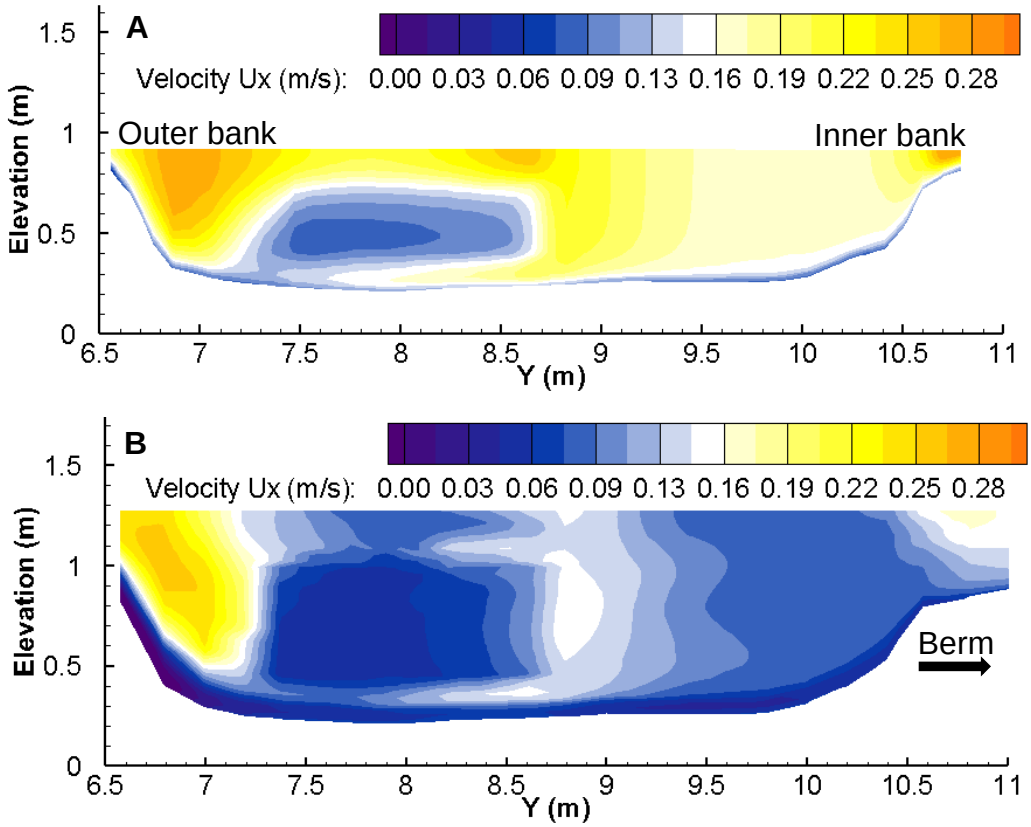


Figure 7.46. Streamwise velocities (m/s) for no-berm (A) and berm (B) cases. Both cross-sections were taken from the same location and using the same distribution of vegetation patches.

Streamwise velocities are generally higher for the no-berm cases; two loci of high velocity are apparent above the vegetation patch and at the inner bank for the no-berm case. In the berm case these loci have considerably lower velocity values. This is likely a result of the reduced hydraulic space within the no-berm case as the flow is restricted between the topography and free surface. For both cases the maximum velocity values are located at the outer bank, and the trailing biomass is clearly represented as a zone of reduced velocity. In addition, the velocities at the vegetation boundary are higher compared to the non-vegetation channel for both cases and roughly occupy the same lateral extent across the cross-section.

The respective free surfaces across each apex cross-section for both cases was also assessed. In a natural meander, centrifugal forces act on the flow resulting in higher velocities and flow depths towards the outer bank. The modelled free surfaces for both cases showed a slightly higher elevation in flow depth at the outside bank compared to the inside bank (Fig.7.46) suggesting that the model has captured the natural dynamics of flow through a meander.

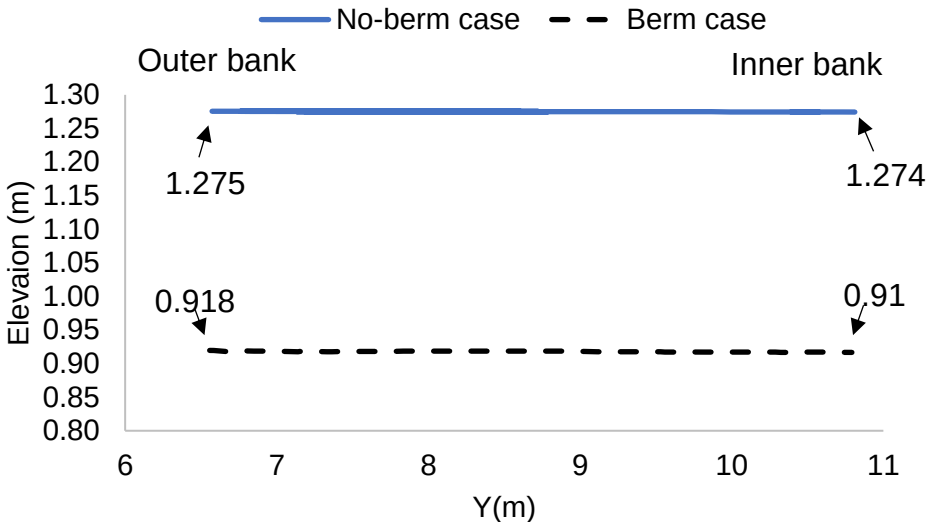


Figure 7.47. Differences in free surface elevation at the inner and outer banks for both berm and non-berm cases.

Secondary circulation was also compared between both cases (Fig.7.48) by considering the direction of the circulation and the magnitude of the vectors for velocity. Flow circulation for both cases follow a similar direction with the entirety of the flow column moving towards either the outside or inside bank depending on is position relative to the channel centre. Both cases capture a vertical bifurcation of the flow around the vegetation. The berm case exhibits more explicit deformation within the bank-ward flow direction, with rotational cells occurring at the right-hand edge of the vegetation patch at both the base and the canopy top. Generally, visual analysis suggests that the no-berm case exhibits stronger vector magnitudes than the berm case. The differences are the most explicit at the channel centre, with the Berm case have weaker circulation compared to the vectors in the no-berm case.

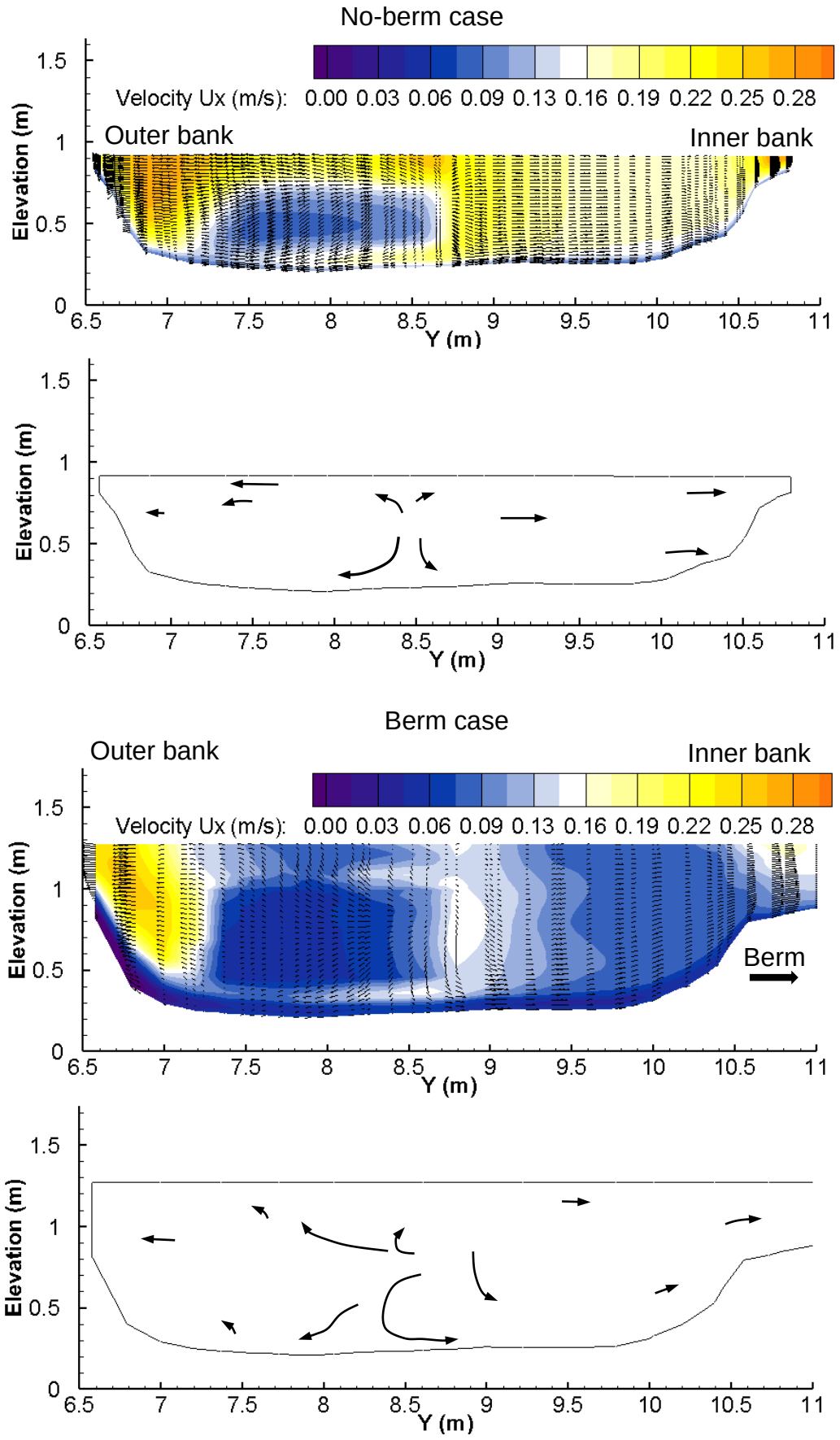


Figure 7.48. Patterns and vector magnitudes for secondary circulation for vegetated non-berm (A) and vegetated berm (B) simulations.

Turbulent kinetic energy was compared between the berm and non-berm cases (Fig. 7.49). Considerably higher quantities of turbulence are evident within the non-berm case compared to the berm case, reflecting the lower velocities exhibited within the channel and thus the reduced shearing. Similarities between the spatial distribution of TKE is observed, with the higher values located at the upper canopy boundary for the vegetation patch where the greatest levels of shearing occur.

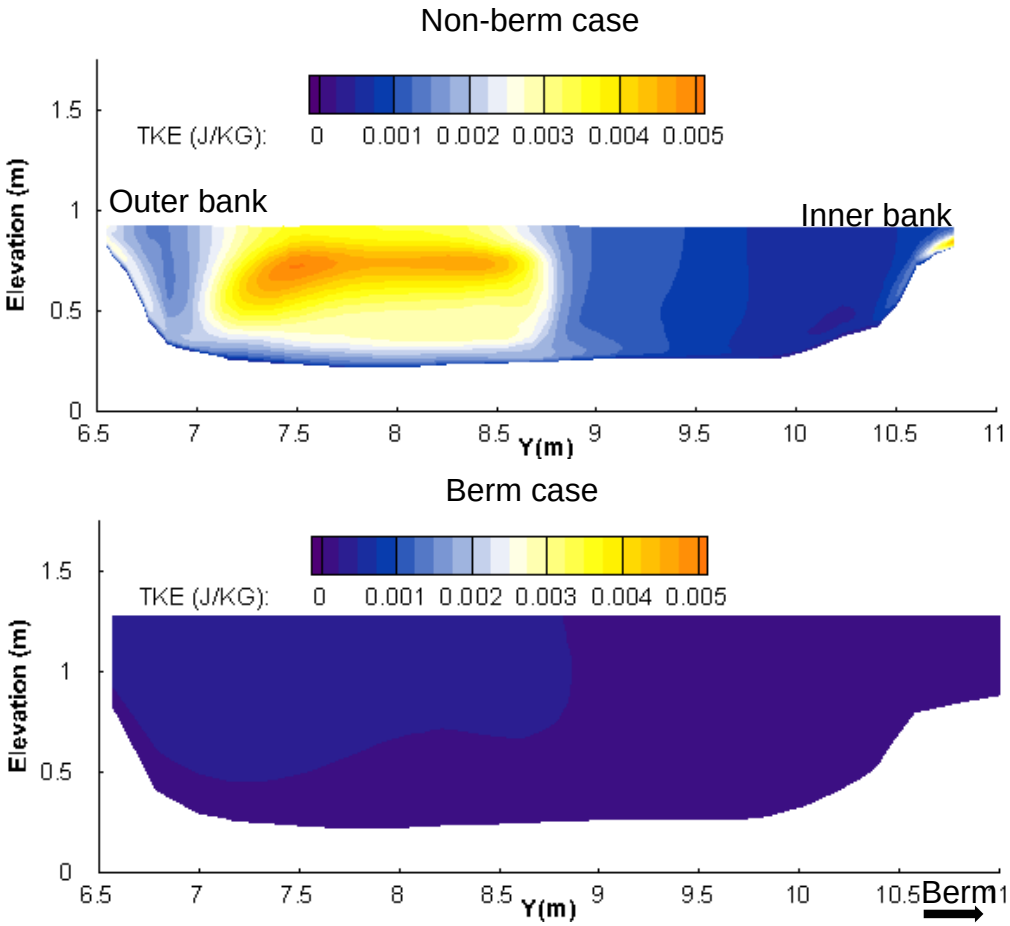


Figure 7.49. Distribution of TKE values for vegetated non-berm (A) and vegetated berm (B) simulations.

To assess whether the flow during flood conditions were reasonable the velocity magnitudes, secondary circulation, and TKE values for the non-vegetated case were also assessed. No cross-sectional measurements were available for non-vegetated flood conditions. To allow for slope comparison, the depth value closest to the value for the September High comparison was used. Whilst it is assumed that the slopes for similar depths would also be similar, it is noted that the September High-flow condition is vegetated which will exhibit considerably different control compared to the non-vegetated flow which is dominated by topographic controls. Considering this

the magnitude of flow quantities and circulation was compared to similar studies in the literature to determine its efficacy. The non-vegetated February flow previously used to calibrate in the non-vegetated case (Chapter 6, Section 6.3) was deemed unreasonable to compare to due to the considerably lower flow depths altering the slope and hydraulic radius, altering the significance of topographic control on flow quantities. The initial conditions for the non-vegetated flood condition are detailed in Table 7.8.

Table 7.8. Initial conditions for the non-vegetated flood condition.

| Initial conditions | January | September (High Flow) |
|---|---|---|
| Stage (m) | 1.241 | 2.15 |
| Discharge ($m^3/s$) | 1.242 | 1.09 |

The slope for the January flow was 0.00058m, which is 0.00004m higher than the September High Flow slope of 0.00053m. Differences between the two are likely due to the control exerted by vegetation for the September High Flow condition compared to the dominance of topographic drag force for the January run, as well as differences due to January's higher discharge. The slopes for both are compared in Fig. 7.50.

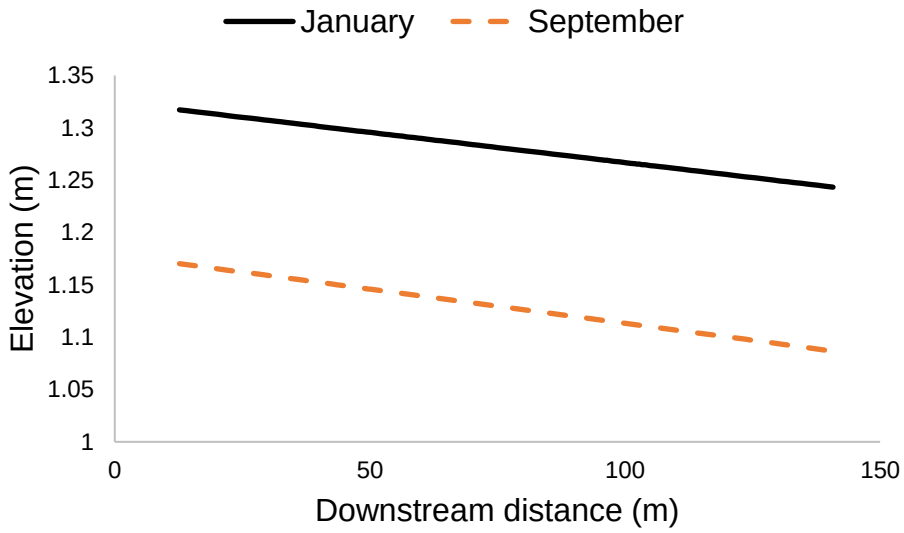


Figure 7.50. Free surface slopes for the entire reach as measured along the channel centreline for both the January (solid, black line) and the calibrated September High Flow condition (dashed, orange line).

The flow quantities for the same flow condition are shown in Fig.7.51.

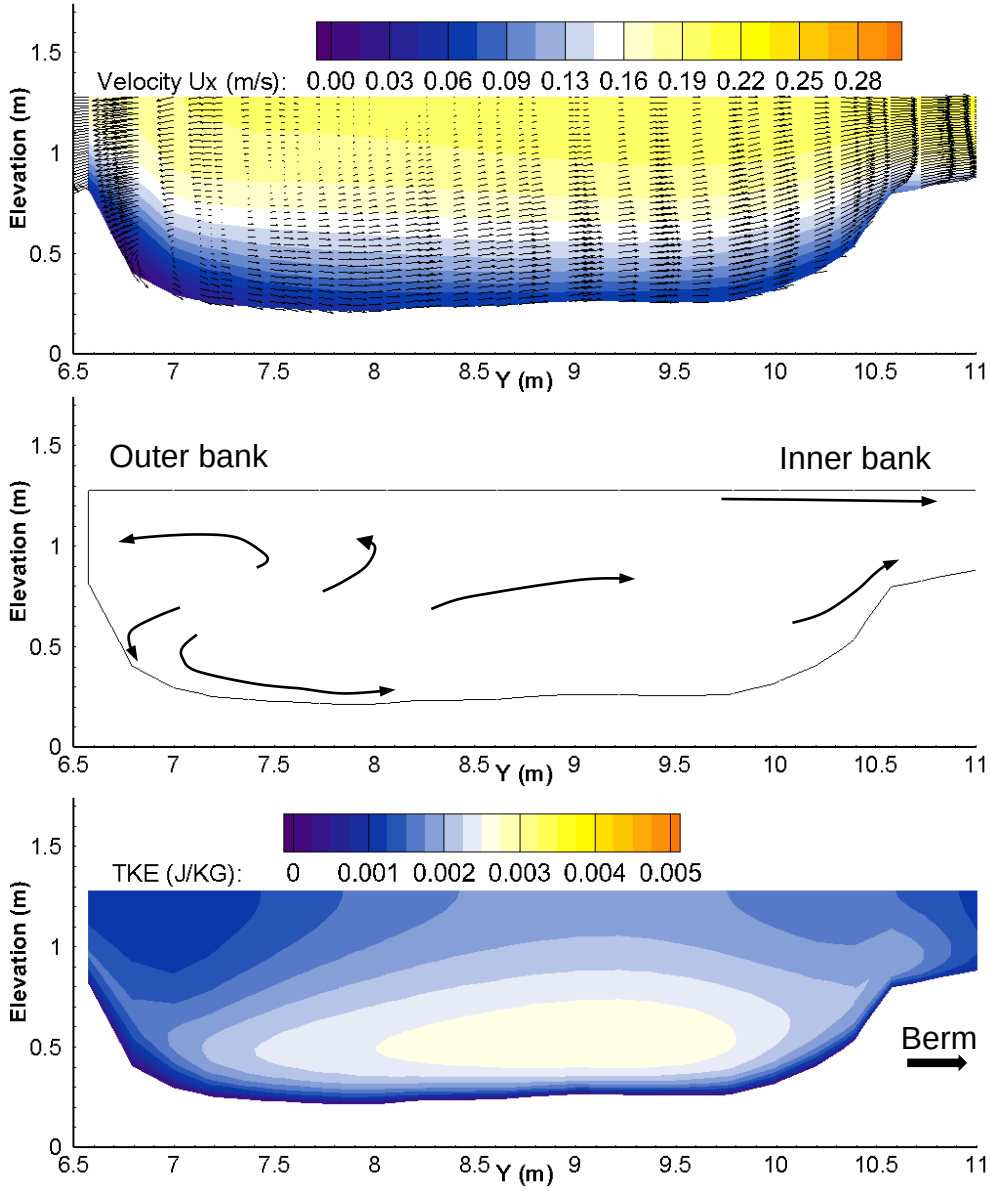


Figure 7.51. Patterns and vector magnitudes for secondary circulation (A, B) and distribution of TKE values (C) for the non-vegetated berm case.

The distribution of magnitudes for the streamwise velocity is similar to velocity patterns in channels dominated by topographic controls: the flow is slowest at the near-bed and bank regions where the flow is most affected by drag and the maximum velocity is evident at and just below the free surface. This is similar to the velocity patterns described for non-vegetated flow in Chapter 6, Section 6.3 and flow patterns observed in the literature (for example: Ferguson et al., 2003). Secondary flow vectors detail a large circulation near the outer bank rotating towards the outer bank near the surface and towards the inner bank near the bed. Similar circulation

patterns have been captured at the outer banks for other simulations. TKE energy is greatest just above the near-bed region indicating turbulent flow generated by shearing from the gravel-layers. This distribution of TKE values is similar to that found in literature, with the magnitude of TKE being within the same range of values found for similar studies (for example: Rameshwaran & Naden, 2004; 2011). Mass flow rates were compared between the berm and non-berm flow for the non-vegetated flows. The mass flow rate (discharge) was calculated by integrating the flow quantities throughout the flow layers for a slice at either the channel or the floodplain at the meander apex. For the berm flow, the mass flow rate was 1.452m3/s over the floodplain and 6.821m3/s in the channel i.e. flow rates over the floodplain is 21.29% of the main channel flow without vegetation. With vegetation the berm flow had a mass flow rate of 0.9255m3/s whilst a flow rate of 0.1593 was integrated from channel flow.

## 7.8. Summary

Vegetation was integrated within the numerical model using the double averaged Navier Stokes method. The parameters used in the vegetation drag equations were taken from measurements previously mentioned in Chapter 4, Section 4.3. The model simulates the effect of three vegetation types: in-stream vegetation, overhanging bank vegetation, and berm (floodplain) vegetation. In this chapter, the distribution of in-stream and overhanging bank vegetation within the channel was described using data measured on-site, the methodology for which can be found in Chapter 3, Section 3.2.2. The method for representing the 3D profile of in-stream vegetation was given for two morphotypes: the uniform patches based on the physical morphology of the macrophyte species *S.erectum*, and the trailing patches based on *S.erectum*. The calibration approach was then described for two different periods of vegetation abundance, May and September, and three flow conditions, May flow, September low flow, and September high flow. The method used for simulating the effect of overhanging flow vegetation on surface flow was then detailed. A description of the approach for representing the effects of floodplain vegetation was provided which detailed the generation of the floodplain mesh and how floodplain vegetation was characterised in the model. Finally, an assessment of the effects of vegetation on floodplain flow illustrated its impact on the 3D flow field.

# Chapter 8 | Scenario-based simulations for the vegetation-change model

## 8.1. Introduction:

This chapter details the design and results of the modelled scenarios for future climate change flood events with respect to differences in seasonal flow, flow rates, and vegetation patch size. First, the scenario design is presented alongside the method used to estimate changes to future flow rates and vegetation abundance. Second, a summary of the mean floodplain flow is given, which considers changes in flow elevation, streamwise velocities, and turbulent kinetic energy (TKE) for each scenario. Third, a reach-scale assessment of flow patterns across for the floodplain and adjacent river channel is presented. Lastly, the impact of vegetation on the local flow field is assessed by considering a single patch for both the *S. erectum* and *S. emersum* species.

## 8.2. Scenario design

Decision-making is limited by both a lack of information and the perception of limited information (Moser and Ekstrom, 2010), requiring an assessment of multiple possible futures to build, test, and implement solutions (Adger et al., 2009). Because of this, scenario-based approaches are useful for informing river management practitioners.

The scenarios were built on two key assumptions: firstly, that a future increase in global average temperatures will intensify storm intensity and longevity during the autumn and winter months to result in increased river flow rates; secondly, that temperature increases will alter channel vegetative abundance and delay peak biomass until later in the year. The research behind the above assumptions have been detailed in Chapter 2. Each scenario was represented by the peak of a flood event on the reach. The seasonal differences which affect channel flow conditions were represented by selecting flow rates for flood events of the greatest magnitude in the historical record for both the summer and autumn seasons.  Future changes to flood events were represented by altering the flow rate prescribed for the inlet boundary condition to reflect changes in flow rate predicted for the Thames region

for the year 2050. Future changes to local macrophyte abundance used observations of vegetation change reported in the literature. This change was represented within the model by increasing the size of the patch planform uniformly in each cartesian direction, thereby increasing the number of vegetated nodes laterally across the channel. The spatial distribution of patches in the summer and autumn scenarios remain the same and as mentioned in Chapter 7, Section 7.2. In this manner the scenarios can be seen to represent a 'snapshot' of a seasonal flood event at peak flow as influenced by future changes in flow rate and vegetation coverage.

The criteria for selecting the parameters to represent baseline conditions for both the summer and autumn are detailed below. The summer months were defined as the period June – August, and the autumnal periods was defined as the months September – November. For both seasons the maximum stage value was selected from the historical record to represent the baseline conditions, which reflected the maximum observed flood depth per season for the River Blackwater. The maximum stage was selected from the longest data record available, between 1994 and 2018. Once the stage was selected the associated flow rate was also chosen and both were used as the initial flow parameters (Table 8.1).

Table 8.1. Baseline flow parameters for the summer and autumn flow.

| | Observed maximum stage (m) | Observed flow rate ($m^3/s$) |
|---|---|---|
| Summer | 1.42 | 2.87 |
| Autumn | 1.51 | 5.22 |

No observational data describing the free surface slope was available for either the summer or autumn flow conditions. To ensure a realistic free surface gradient was simulated, the slope for each scenario was compared to the highest measured slope: the free surface of the September high flow condition previously discussed in Chapter 7, Section 7.5. For each scenario run, the outlet stage was adjusted until the differences between the simulated free surface gradient and the September high

flow gradient were at a minimum. The results for the stage-adjusted simulations are assessed later in this chapter.

A bankfull flow condition was also used to represent flood conditions in which the maximum surface elevation equalled the maximum bank elevation. Elevation is defined in relation to the lowest point of the riverbed. A lack of observational data describing bankfull flow conditions meant a different treatment was necessary for estimating flow depth, flow rate, and free surface slope. The near bank was higher than both the berm and the far bank, and so bankfull in this case refers to scenarios where flood events have submerged the berm but have not encroached on the southern floodplain. The flow parameters were estimated as follows: first, the highest recorded bank elevation for the near bank was identified using the topographic data (see: Chapter 3, Section 3.3.2). This elevation was used for the “bankfull depth” (2.65m) which assumed a uniform bank height. In reality, the bank elevation exhibits a general decrease in elevation with downstream distance due to the channel slope whilst being highly variable locally. Second, the data for the flow rates & inlet depths previously used to parameterise the other scenarios was linearly interpolated to estimate the flow rate for bankfull depth at the inlet. The inlet bankfull depth was calculated for both the autumn and summer conditions, and the free surface slope for each scenario was estimated using the free-surface slope adjustment method performed for previous scenarios: the outlet depth was adjusted until the slope difference between the September high flow data and the new free surface slope was at a minimum. The estimated free surface slopes had a maximum flow elevation equal to the maximum bank elevation at the inlet (i.e. the region with highest free surface slope elevation). The calculated flow rate was higher than those observed for the summer flow, but less that the flow rates observed than the winter flow.

The impact of climate change on flow rate was represented by the percentage increase in flow rate for the Thames valley region as described by Sayers et al (2017); changes to peak flow were calculated for multiple years assuming a $2^0$C and $4^0$C increase in global mean temperature by the 2080s. In this study the year 2050 was chosen as the representative year for model scenarios for both the $2^0$C and $4^0$C climate projections. The changes to flow rate for both the $2^0$C and $4^0$C projection were based on FD2020 (Reynard et al., 2010) and calculated by Sayers et al. by interpolating between ‘change factors’ quantify the potential change in river flood

flow relative to the 1961-90 baseline. Change factors are based on UKCP09 probability distributions for projections of rainfall and temperature for river flow with a 2% (1-in-50) chance of occurring in a given year (Environment Agency, 2012). The 'medium' change factor is based on the A1B (Medium) emission scenario, whilst upper and lower change factors represent the upper and lower limits of scenario uncertainty, respectively. Sayers et al. (2017) calculated change in peak flow for the $2^0$C projection by interpolating between the lower and medium change factor, whilst for the $4^0$C projection change in peak flow was calculated by interpolating between the upper and medium change factor. In this study, the scenario flow parameters per season were thus: the baseline peak flow conditions (i.e. the historical maximum), change to peak flow under $2^0$C of warming, and changes to peak flow under $4^0$C of warming. Future warming scenarios represented changes in flow rate for the year 2050. The chosen scenarios allowed for comparisons between current (baseline), likely ($2^0$C warming), and unlikely ($4^0$C warming) climate outcomes by 2050. The use of an unlikely scenario was included because extreme scenarios are useful for enabling a better understanding of low probability events which may be disruptive if poorly anticipated and planned for, or which exceed futures currently considered probable or possible and therefore unanticipated (Fischbacher-Smith, 200). A detailed description of how they were calculated can be found in Sayers et al. (2017). The final flow parameters for all scenarios are presented in Table 8.2.

Table 8.2. Finalised parameters for flow rate.

| Climate scenario (2050) | Percentage change to flow rate | Summer ($m^3/s$) | Autumn ($m^3/s$) |
|---|---|---|---|
| Baseline | 0% | 2.87 | 5.22 |
| $+2^0C$ | 3% | 2.96 | 5.38 |
| $+4^0C$ | 24% | 3.56 | 6.47 |
| N/A (*bankfull flow condition*) | Summer: 54.18%<br>Autumn: -14.34% | 4.4251 | 4.4712 |

The future change to vegetation patch size was represented using the data reported by Grînberga & Sprioìe (2008), who observed increases in the total vegetative biomass by measuring the mean average percentage of macrophyte cover per river reach for seven reaches of the River Salaca, Latvia, from 1986 – 2002. The reported data was considered appropriate for this study as the change in-stream vegetation biomass was attributed to climatic influences: the anthropogenic influence on the river flow was estimated as "very low" whilst an upward trend in annual mean temperatures were recorded throughout the period during which an increase in vegetation abundance occurred. Additionally, the river featured populations of *S. emersum* and *S. erectum*. This study used three reaches reported by Grînberga & Sprioìe (2008) and which were selected because the change to the mean percentage macrophyte cover for a given reach included increases in both *S. emersum* and *S. erectum* species. Three reaches were used: "Reach 1) Mazsalaca – River Ramata", "Reach 2) River Ramata – River Ige", and "Reach 4) Staicele – River Puzupe". Predictive studies estimating the future vegetation growth typically use allometric scaling based on observations on characteristics such as plant mass. However, a lack of allometric data made it difficult to determine how both species would change over the period covered by the scenarios in this study. To represent future changes in vegetation patch size the mean change in macrophyte abundance was used instead. A mean increase in abundance of 30% was calculated for all three reaches over 21 years. In reality, changes in patch size will be different over a longer time period. This dearth in reach-scale observations and research into macrophyte change under climate change suggests this is an area requiring further research.

Each scenario representing an increase in vegetation abundance increased the patch size for both *S. emersum* and *S. erectum* species by 30%.

Scenarios simulating change in patch size for only one of the dominant species, i.e. *S. erectum* or *S. emersum*, were also run. Previous research has identified differences in the hydraulic resistance between macrophyte species. Scenarios which allow for comparisons between changes to vegetation patches by morphotype would better inform how different plant morphotypes and, by extension, different species affect flood flow. Both species are represented in the model with a different morphotype, described in Chapter 7, Section 7.3, with both the *S. erectum* and *S. emersum* species shown to have a different effect on the local flow field. Scenarios increased the patch size for one species by 30% whilst the patches belonging to the other species were left unchanged. For example, a scenario featuring a 30% increase to *S. erectum* patches would feature *S. emersum* patches with a 0% increase in patch size. These “morphotype-specific” scenarios were simulated for both the autumn baseline and autumn bankfull conditions, thus bringing the total number of simulated scenarios to 12. The final flow rate parameters prescribed at the inlet for each scenario is presented in Table 8.3 alongside the final flow rates simulated for each run.

Henceforth, individual scenarios will be referenced using the typographic X.1.2, where “X” denotes the season, either summer (S) or autumn (A); “1” denotes the percentage change in flow rate (either 0%, 3%, 24%, 54% for summer bankfull conditions, or -14% for autumn bankfull conditions); “2” denotes the percentage increase in patch size (0% or 30%). For example, a scenario parameterised for summer flow, with a 3% increase in flow rate, and a 30% increase in patch size would be referred to as scenario S.3.30. For morphotype-specific scenarios the scenario reference additionally notes the species which featured an increase in patch size: either SER (*S. erectum*) or SEM (*S. emersum*). For example, if scenario S.3.30 instead only featured an increase in the patch size for *S. erectum* the scenario would be denoted S.3.30.SER.

Table 8.3. Flow rates prescribed per scenario.

| Summer | Patch: 0% increase | | | | Patch: 30% increase | | | |
|---|---|---|---|---|---|---|---|---|
| Flow scenario: | 0% | 3% | 24% | 54.18314% (bankfull) | 0% | 3% | 24% | 54.18314% (bankfull) |
| Prescribed Q: | 2.87 | 2.96 | 3.56 | 4.425 | 2.87 | 2.96 | 3.56 | 4.425 |
| Simulated Q: | 2.87 | 2.959 | 3.56 | 4.425 | 2.87 | 2.96 | 3.56 | 4.425 |
| Autumn | Patch: 0% increase | | | | Patch: 30% increase | | | |
| Flow scenario: | 0% | 3% | 24% | -14.3448% (bankfull) | 0% | 3% | 24% | -14.3448% (bankfull) |
| Prescribed Q: | 5.22 | 5.38 | 6.47 | 4.471 | 5.22 | 5.38 | 6.47 | 4.47 |
| Simulated Q: | 5.22 | 5.38 | 6.47 | 4.471 | 5.22 | 5.38 | 6.47 | 4.47 |
| Autumn | *S. erectum*: 30% increase | *S. erectum*: 30% increase | *S. emersum*: 30% increase | *S. emersum*: 30% increase | | | | |
| Flow scenario: | 0% | 14.3448% (bankfull) | 0% | -14.3448% (bankfull) | | | | |
| Prescribed Q: | 5.22 | 4.47 | 5.22 | 4.47 | | | | |
| Simulated Q: | 5.22 | 4.47 | 5.22 | 4.47 | | | | |

A single bulk drag coefficient representative of vegetation drag was chosen to be applied across all flow scenario designs. Variation between calibrated vegetation drag is expected: differences in flow rate and patch distribution affects the degree which to the coefficient value is adjusted to match the energy slope, whilst morphological changes to patches during the growth season affects vegetation surface area and the patch profile which are potential sources of error. To ensure that the vegetation drag coefficient was consistent between scenarios a universal coefficient value was chosen from the range of CD0 values calibrated for the May (Chapter 7, Section 7.4), September low flow and September high flow cases (Chapter 7, Section 7.5) (Table.8.4).

Table 8.4. RMSE for free-surface slope used assessing the CD0 parameter. The calibrated CD0 is in blue.

| **CD0 /Case** | **CD0 0.32** | **CD0 0.33** | **CD0 0.34** | **CD0 0.35** |
|---|---|---|---|---|
| **May** | 0.0035 | 0.0036 | 0.0037 | 0.0043 |
| **September (low flow)** | 0.002 | 0.0019 | 0.0019 | 0.0019 |
| **September (high flow)** | 0.0015 | 0.0014 | 0.0007 | 0.0015 |

The representative vegetation drag coefficient was selecting the coefficient with the smallest difference in RMSE from each respective calibrated case. The coefficient CD0 0.33 was selected to represent vegetation roughness for all patches as it had the smallest differences in RMSE for each case when assessing the relative change in accuracy from the calibrated value (Table 8.5).

Table 8.5. The chosen universal coefficient CD0 (green) with the respective differences in RMSE for each case. Differences are shown as a percentage (%).

| CD0 /Case | CD0 0.32 | CD0 0.33 | CD0 0.34 | CD0 0.35 |
|---|---|---|---|---|
| **May** | 0 | 2.25 | 5.00 | 16.21 |
| **September (low flow)** | 7.39 | 3.19 | 0 | 0.32 |
| **September (high flow)** | 38.46 | 33.24 | 0 | 42.24 |

The spatial distribution for the vegetative drag terms is summarised in Fig.8.1; the drag terms representing in-channel vegetation patches are found within the reach (blue), whilst grass and tree vegetation are located on the berm (yellow), and grass only is on the bank wall (red). Not shown is the drag region for overhanging bank vegetation, which is detailed in Chapter 7, Section 7.6.

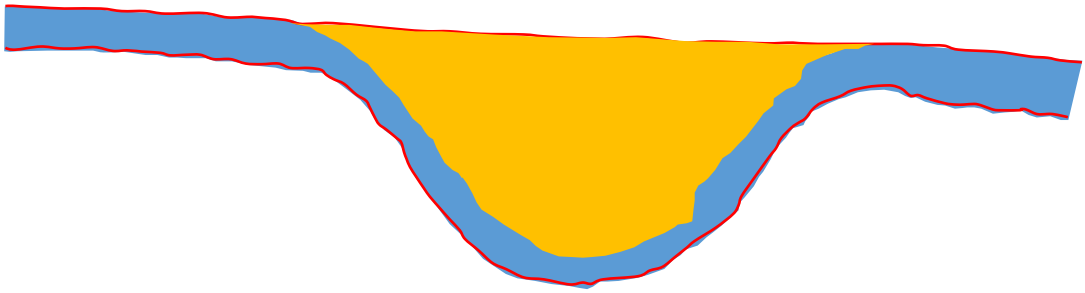

Figure 8.1. Zones of the reach within which different vegetation drag terms are applied.

## 8.2.1 Flow rate assessment:

To ensure that the model had effectively simulated the prescribed flow conditions, the flow rate for each simulated result was calculated and compared to the prescribed flow rate. The mass continuity principle states that flow rate should remain constant throughout the domain, and as such the mean flow rate calculated for any given cross-section of the domain should match the value of the prescribed flow rate. To calculate the flow rate from the model results, a transect of the floodplain positioned normal to the flow was taken at 84.82m downstream of the inlet, approximately at the apex of meander. The flow rate was then calculated by integrating the streamwise velocity over the transect area. The flow rates calculated for each scenario are shown in Table 8.6. The simulated and prescribed flow rates

were identical up to two decimal places for the majority of the scenarios, with a variation of 0.01$m^{3/s}$ 0.001 $m^3/s$ noticeable for scenario S.3.0.

Table 8.6: comparison of prescribed and simulated flow rates for a single transect over the floodplain.

| Summer | Patch: 0% increase | | | | Patch: 30% increase | | | |
|---|---|---|---|---|---|---|---|---|
| Flow scenario: | 0% | 3% | 24% | 54.18314% (bankfull) | 0% | 3% | 24% | 54.18314% (bankfull) |
| Prescribed Q: | 2.87 | 2.96 | 3.56 | 4.43 | 2.87 | 2.96 | 3.56 | 4.43 |
| Simulated Q: | 2.87 | 2.959 | 3.56 | 4.43 | 2.87 | 2.96 | 3.56 | 4.43 |
| Autumn | Patch: 0% increase | | | | Patch: 30% increase | | | |
| Flow scenario: | 0% | 3% | 24% | -14.35% (bankfull) | 0% | 3% | 24% | -14.35% (bankfull) |
| Prescribed Q: | 5.22 | 5.38 | 6.47 | 4.47 | 5.22 | 5.38 | 6.47 | 4.47 |
| Simulated Q: | 2.87 | 2.96 | 3.56 | 4.43 | 2.87 | 2.96 | 3.56 | 4.43 |
| Autumn | S. erectum: 30% increase | S. erectum: 30% increase | S. emersum: 30% increase | S. emersum: 30% increase | | | | |
| Flow scenario: | 0% | 14.3448% (bankfull) | 0% | -14.3448% (bankfull) | | | | |
| Prescribed Q: | 5.22 | 4.47 | 5.22 | 4.47 | | | | |
| Simulated Q: | 5.22 | 4.47 | 5.22 | 4.47 | | | | |

## 8.3. Berm-scale assessment:

A summary of the results is provided in this section. The depth- and spatially-averaged values for the free surface surface elevation, streamwise velocity, and turbulent kinetic energy (TKE) are reported for the simulated floodplain flow on the berm. The difference and percentage change in mean values between complementary scenario pairs are also discussed. Here “complementary scenario pairs” refers to two simulated scenarios where the sole difference in their parameterisation is the percentage increase in vegetation patch size. For example, scenarios S.0.0 and S.0.30 are considered complementary scenarios.

### 8.3.1. Floodplain mean free surface elevation:

This section details the mean floodplain mean surface elevation for scenarios featuring uniform increases in patch size across all patches. Following, an assessment of the mean surface elevation for the morphotype-specific scenarios is given. All scenarios exhibited an increase in the mean floodplain free surface elevation with increases in the flow rate, the patch size, or to both. Scenarios featuring an increase to both flow rate and patch size featured higher mean elevations than scenarios which featured increases to only flow rates. Clear differences in the mean floodplain free surface elevation are present between complementary scenarios. The mean elevations for all scenarios considered in this section are shown in Figure.8.2. The percentage changes between complementary scenarios are presented in Table.8.7.

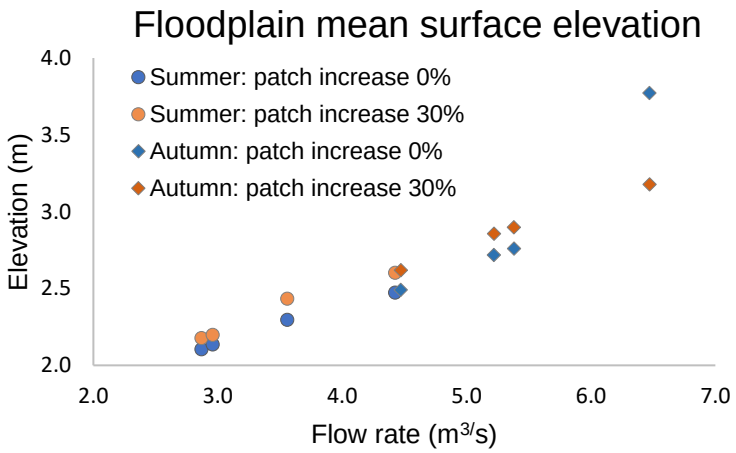


Figure 8.2. Seasonal changes in mean floodplain surface elevation with changes in patch size. Increases in patch size are applied uniformly to all morphotypes in each scenario.

Table 8.7. Percentage change in mean flow quantities from the respective baselines for Summer (S.0.0) and Autumn (A.0.0) scenarios.

| Season | Summer | | | | | | |
|---|---|---|---|---|---|---|---|
| Scenario | S.3.0 | S.24.0 | S.54.0 | S.0.30 | S.3.30 | S.24.30 | S.54.30 |
| Mean elevation (m) | 2.10 | 2.13 | 2.30 | 2.47 | 2.18 | 2.20 | 2.43 |
| Change in mean elevation (%) | 1.44 | 9.15 | 17.51 | 3.46 | 4.50 | 15.68 | 23.69 |
| Season | Autumn | | | | | | |
| Scenario | A.3.0 | A.24.0 | A.-14.0 | A.0.30 | A.3.30 | A.24.30 | A.-14.30 |
| Mean elevation (m) | 2.72 | 2.76 | 3.77 | 2.49 | 2.86 | 2.90 | 3.18 |
| Change in mean elevation (%) | 1.48 | 38.73 | -8.41 | 5.11 | 6.59 | 16.90 | -3.69 |

For all scenarios, an increase in flow rate resulted in an increase in the free surface elevation on the floodplain. Similarly, an 30% increase in patch size exhibited higher mean surface elevation than their respective complementary scenarios. For example, scenario S.54.0 exhibited an increase in mean surface elevation by 17.51% from the baseline, whilst the additional vegetation in S.54.30 increased mean surface elevation to 23.69% from the baseline, as shown in table.8.7. The scenarios for the highest flow rate, A.24.0 and A.24.30, were exceptional in that the scenario with no change to vegetation patch size (A.24.0) featured a mean surface elevation higher than the complementary scenario where vegetation patch size was increased (A.24.30).

For both seasons, scenarios featuring none-to-small increases in flow rates, such as those of 0% and 3%, an increase in vegetation patch size contributed to a greater increase in the flow elevation than scenarios which featured solely changes to the flow rate. However, this contribution diminished at higher flow rates. This vegetation contribution can be inferred given that the only difference between complementary scenarios were the changes in patch size and increasing vegetation patch size accounts for the differences between complementary scenarios. For example, the difference in mean surface elevation percentage change between S.54.0 and S.54.30 above suggests that the vegetation increase contributed an additional 6.18% increase to mean surface elevation from the baseline (Fig.8.3). For S.24.30 this vegetative contribution increased mean elevation by 6.53%, similar to that reported above for S.54.30. Scenarios with lower flow rates, i.e. S.3.30 and S.0.30, featured smaller changes in elevation as a result of abundant vegetation: an increase of 3.06% and 3.46%, respectively. For Autumn scenarios, the A.-14.30 scenario had both the lowest flow rate and the lowest vegetative contribution of 4.72%. This vegetation contribution increased to 5.11% for both the A.0.30 and A.3.30 scenarios

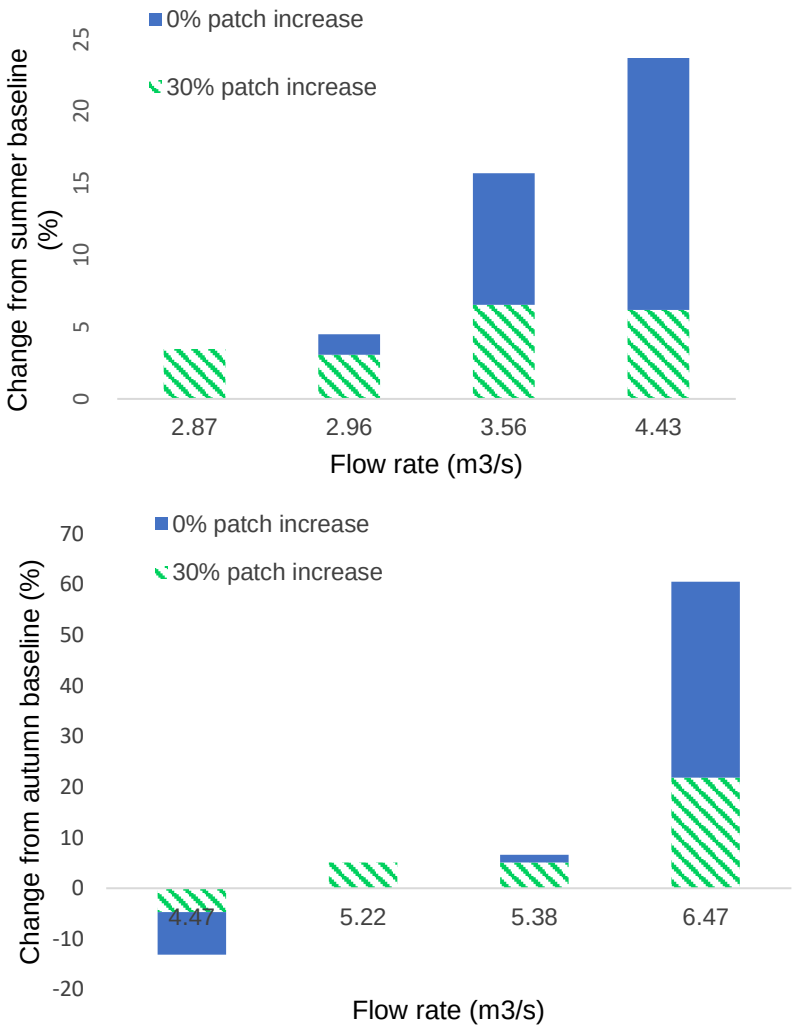


Figure 8.3. Additional percentage change in floodplain mean surface elevation due to vegetation patch increase, relative to the seasonal baseline for summer (top) and autumn (bottom).

In the above paragraph the differences in mean surface elevation relative to the baseline were attributed to changes in vegetation patch size. It is important to consider what proportion of the total change in mean elevation is attributed to vegetation change relative to the seasonal baseline. Here this proportion is the “vegetation component” of the total change in mean surface elevation relative to the seasonal baseline. Changes in the mean surface elevation were compared against the seasonal baselines for the respective scenario: either S.0.0 or A.0.0. It is difficult to determine what proportion of the floodplain flow elevation is attributable for vegetation for scenarios featuring no change in vegetation distribution. Due to this, the vegetation component was calculated solely for scenarios featuring an increase

in vegetation i.e. scenarios in which plant patches had been increased by 30%. The "total change" refers to any change in mean surface elevation that is inclusive of increases in vegetation patch size. The vegetation component calculation assumed that the difference in mean surface elevation between complementary scenarios could only be accounted for by an increase in patch size. The difference in the mean elevation between two complementary scenarios was used to calculate the percentage change relative to the seasonal baseline. This percentage change was then attributed to an increase in vegetation (Table.8.8).

Table 8.8. Component of mean elevation change in surface elevation for floodplain flow attributable to an increase in vegetation patch size compared against the baseline scenario (S.0.0 and A.0.0, respectively). Percentage change in mean elevation between complementary scenarios are calculated relative to the baseline. The vegetation component accounts for the percentage of flow increase accounted for by an increase in vegetation patch size.

| Season | Summer | | | |
|---|---|---|---|---|
| Scenario | S.0.0 | S.3.30 | S.24.30 | S.54.30 |
| Change from complementary scenario (m) | 0.07 | 0.07 | 0.14 | 0.13 |
| Change from complementary scenario, relative to baseline (%) | 3.5 | 3.1 | 6.5 | 6.2 |
| Vegetation component (%) | 100.000 | 68.1 | 41.7 | 26.1 |
| Season | Autumn | | | |
| Scenario | A.-14.30 | A.0.30 | A.3.30 | A.24.30 |
| Change from complementary scenario (m) | 0.13 | 0.14 | 0.14 | -0.59 |
| Change from complementary | 4.7 | 5.1 | 5.1 | -21.8 |

| | | | | |
|---|---|---|---|---|
| scenario, relative to baseline (%) | | | | |
| Vegetation component (%) | 78.37 | 100.000 | 77.57 | 22.59 |

Generally, the vegetation component of total change decreased as the flow rate increased, suggesting that role of vegetation diminished with more extreme flood events. Conversely, scenarios with low flow conditions were more influenced by vegetation change than flow rate: for both the summer and autumn, the scenarios which featured a 3% increase in the flow rate an increase in patch size was attributed 68.1% and 78. 37% of the total change in mean surface elevation (Table.8.8). For higher flow conditions in the summer, the vegetation component decreased to 41.65% and 26.09% for S.24.30 and S.54.30, respectively. Similarly, for the Autumn, the vegetation component fell from 78.37% to 22.59%, for A.-14.30 and A.24.30, respectively. The Autumn scenarios all exhibited a higher vegetation component compared to the Summer except for the highest flow scenario A.24.30. This indicates that the influence of in-stream vegetation on flow elevation is considerable, with mean elevation higher for all scenarios featuring increases in vegetation patch size.

In summary, scenarios featuring a 30% increase in vegetation patch size exhibited a higher mean surface elevation compared to their complementary scenarios featuring no change in patch size. This occurred across every scenario except for the autumn scenario with the highest flow rate. The difference in mean surface elevation between complementary scenarios increased with flow rate; complementary scenarios with higher flow rates exhibit greater differences in mean flow elevation than scenario pairs with lower flow rates. These differences are discussed further in Section 8.3.3. A notable deviation from this pattern occurs for the highest flow condition, where the mean flow elevation for scenario A.24.0 is considerably higher than the scenario with an increase in patch size, A.24.30. This is likely the result of the greater recirculation, which is later described in the flow visualisation section, Section 8.4. For lower flows, the vegetation component of total flow was high with increases in patch size resulting in over a 60% increase in mean depth above their

complementary scenario. However, the vegetation component decreased with increases in the flow rate; at higher flow rates an increase in vegetation patch size resulted in increases in mean surface elevation of less than 30%. The highest mean surface elevations were observed for flow conditions which represented the greatest impact of climate change: for example, A.30.24 and A.30.0. The lowest mean elevations were observed where the impact of climate change was at a minimum: for example, A.0.0 and A.0.30. For all scenarios, differences between complementary scenarios exceeded their respective standard deviation indicating that changes in mean elevation cannot be attributed to local variation in the free surface.

*8.3.1.2. Morphotype-specific changes to flow elevation:*

The surface elevation for scenarios A.-14.0, A.-14.30.SER, A.-14.30.SEM, A.0.0, A.0.0.SER, and A.-0.0.SEM are shown in Figure 8.4.

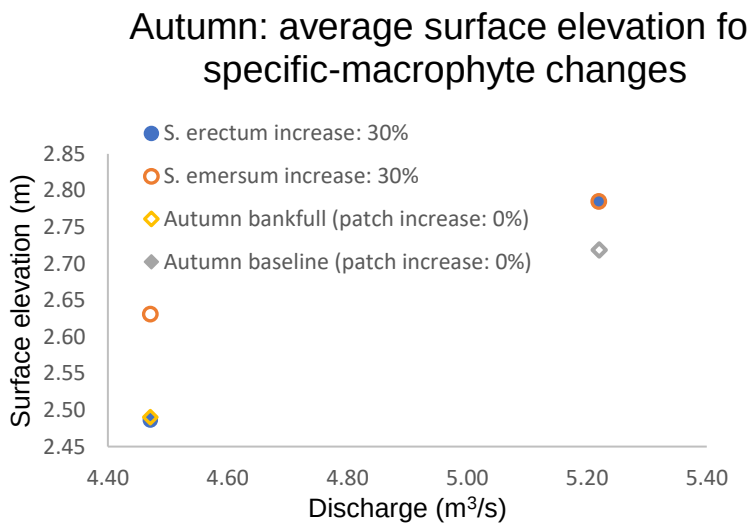


Figure 8.4. Mean surface elevation for morphotype-specific changes to patch size; patch size increases affect either *S. erectum* or *S. emersum* only. Autumn scenarios (-14.0, A.-14.30.SER , A.-14.0.SEM) featuring lowest flow rate, the bankfull flow conditions (4.47 $m^3$/s or -14% change from the baseline), and scenarios with high flow rates (A.24.0, A.24.30.SER , A.24.0.SEM) were considered.

For the bankfull flow conditions featuring patch size increases, A.-14.30.SER and A.-14.30.SEM, the differences between the mean surface elevations for *S. emersum* and *S. erectum* were pronounced: the mean surface elevation for S. *emersum* was

0.15m higher than both the mean surface elevation of A.-14.30.SER and the bankfull scenario featuring non-adjusted vegetation patches, A.-14.0. The difference in mean elevation between A.-14.30.SER and A.-14.0 were negligible, with differences in mean elevation within the 0.003m standard deviation for scenarios. This is reflected in the percentage change in mean surface elevation from the non-adjusted scenario: A.-14.30.SEM increased by 0.1% whilst a very slight decrease in the mean elevation was calculated for A.-14.30.SER (Table 8.9). Increases in only the *S. emersum* patches had a greater effect on increasing the mean surface elevation than scenarios which featured uniform increases for all vegetation patches, whilst increases to only *S. erectum* patches had no considerable impact on the mean surface elevation. For the baseline flow scenarios, A.0.30.SER and A.0.30.SEM, little difference was evident between the mean surface elevations: a small variation in mean elevation was captured within the standard deviation of both, as shown in able 8.10. For the baseline flow scenarios, A.0.30.SER and A.0.30.SEM, little difference was evident between the mean surface elevations: small variation in mean elevation was captured within the standard deviation of both, as shown in Table 8.10.

The scenarios were also compared to the autumn baseline, A.0.0. The difference in percentage change from the baseline for both scenarios were again minimal: both scenarios were higher than the baseline condition, A.0.0, by 0.06m. The surface elevation for A.0.30.SER had increased by 2.44% and for A.0.30.SEM had increased by 2.43%. For the higher flow condition uniform changes in vegetation patch size for all patches had a greater effect on floodplain mean surface elevation than scenarios where only one morphotype was increased. Additionally, the choice of morphotype did not appear to have any considerable effect on floodplain flow elevation with differences in mean elevation negligible between the two.

Table 8.9 Percentage change in mean flow quantities for each scenario. Changes are calculated using the baseline for the respective flow condition. E.g., the baseline scenario for A.-14.30.SER is the bankfull flow condition A.-14.0, and the baseline scenario for A.0.30.SER is the unmodified flow, or baseline flow, scenario A.0.0.

| Season | Autumn | | | |
|---|---|---|---|---|
| Scenario | A.0.30.SER | A.-14.30.SER | A.0.30.SEM | A.-14.30.SEM |
| Change in mean elevation from baseline (%) | 0.1 | 0.0 | 0.1 | 0.1 |
| Change in mean streamwise velocity from baseline (%) | 0.0 | 0.0 | 0.1 | -2.3 |
| Change in mean TKE from baseline (%) | 0.0 | 0.0 | 0.0 | -2.5 |

Table 8.10. Standard deviations, surface elevation maximum, and surface elevation minimum for morphotype-specific scenarios.

| Season | Autumn | | | |
|---|---|---|---|---|
| Scenario | A.0.30.SER | A.-14.30.SER | A.0.30.SEM | A.-14.30.SEM |
| Mean elevation with standard deviation (m) | 2.79±0.002 | 2.49±0.003 | 2.79±0.003 | 2.63±0.002 |
| Surface elevation maximum (m) | 2.79 | 2.49 | 2.62 | 2.64 |
| Surface elevation minimum (m) | 2.76 | 2.45 | 2.58 | 2.61 |

8.3.2. Floodplain mean velocity $U_x$ and turbulent kinetic energy (TKE):

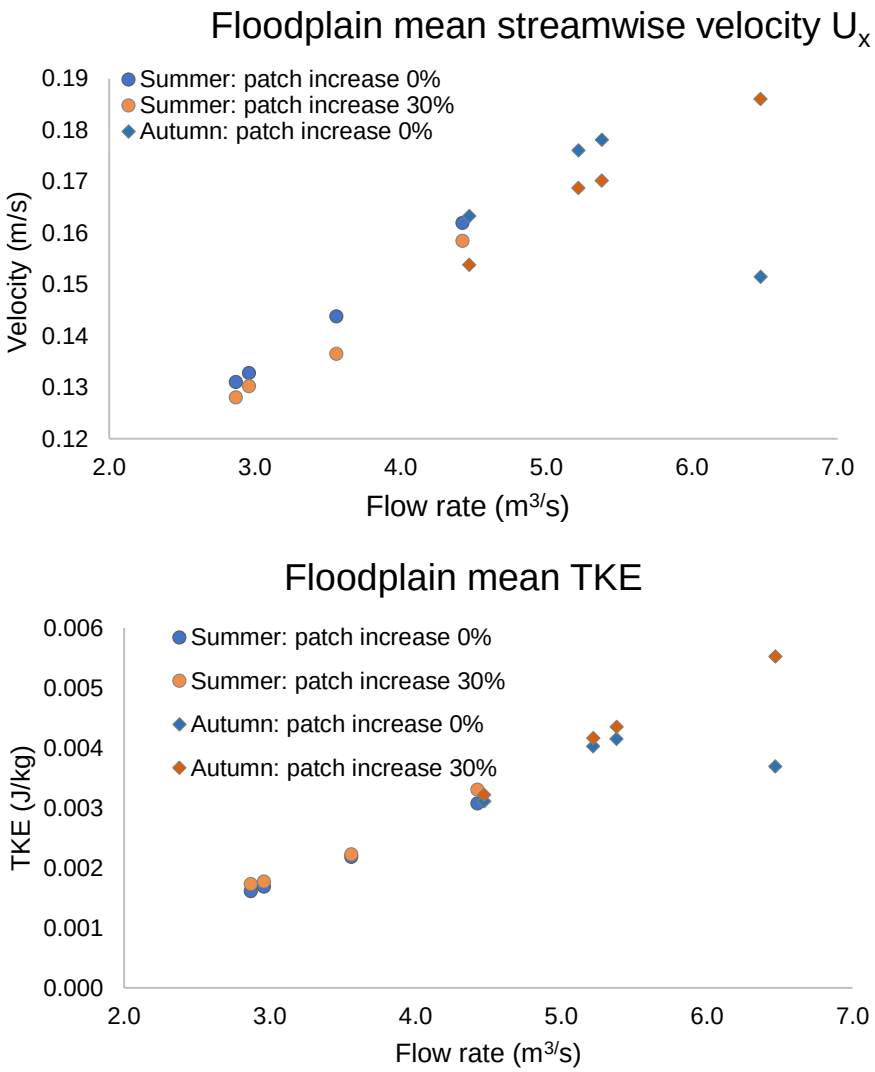


Figure 8.5. Seasonal changes in mean velocity (top) and TKE (bottom) floodplain surface elevation with changes in patch size. Increases in patch size are applied uniformly to all morphotypes in each scenario.

The floodplain mean velocities increased with flow rate: Figure. 8.5 shows that the higher flow conditions for the autumn resulted in higher mean velocities compared to the summer scenarios, whilst scenarios featuring greater increases in flow rate due to climate change exhibited higher velocities for both the autumn and the summer. Mean velocity values were slightly higher for scenarios featuring no uniform increase in patch size compared to scenarios which featured a 30% increase in patch size. For example, S.3.0 had a mean velocity 0.03 (m/s) higher than S.3.30. This pattern was preserved for higher flow rates with S.54.0 exhibiting a mean velocity of 0.05(m/s) higher than S.54.30. Higher flow rates also resulted in a greater

percentage increase from the baseline: S.3.0 featured an increase in the mean velocity by 1.33% relative to the baseline, whilst S.54.0 increase by 20.94% (Table. 8.11). The autumnal high flow scenarios, A.24.0 and A.24.30, exhibited the reverse: the mean velocity was lower for the scenario with no patch-size increase, A.24.0, than that of the scenarios with an increase in patch size, A.24.30.

Table 8.11. Floodplain mean streamwise velocity and TKE, and the change relative to the baseline.

| Season | | Summer | | | | | | |
|---|---|---|---|---|---|---|---|---|
| Scenario | S.0.0 | S.3.0 | S.24.0 | S.54.0 | S.0.30 | S.3.30 | S.24.30 | S.54.30 |
| Mean streamwise velocity (m/s) | 0.131 | 0.133 | 0.144 | 0.162 | 0.128 | 0.130 | 0.136 | 0.158 |
| Mean streamwise velocity (%) | n/a | 1.33 | 9.74 | 23.62 | -2.27 | -0.63 | 4.20 | 20.94 |
| Mean TKE (J/kg) | 0.0016 | 0.0017 | 0.0022 | 0.0031 | 0.0017 | 0.0018 | 0.0022 | 0.0033 |
| Mean TKE (%) | n/a | 4.57 | 35.36 | 90.62 | 7.14 | 9.77 | 37.76 | 104.58 |
| Season | | Autumn | | | | | | |
| Scenario | A.-14.0 | A.0.0 | A.3.0 | A.24.0 | A.-14.30 | A.0.30 | A.3.30 | A.24.30 |
| Mean streamwise velocity (m/s) | 0.163 | 0.176 | 0.178 | 0.151 | 0.154 | 0.169 | 0.170 | 0.186 |
| Mean streamwise velocity (%) | -7.25 | n/a | 1.16 | -13.99 | -12.66 | -4.15 | -3.37 | 5.65 |

| | | | | | | | | |
|---|---|---|---|---|---|---|---|---|
| Mean TKE (J/kg) | 0.0031 | 0.0040 | 0.0042 | 0.0037 | 0.0032 | 0.0042 | 0.0044 | 0.0055 |
| Mean TKE (%) | -22.77 | n/a | 3.05 | -8.44 | -20.05 | 3.31 | 7.99 | 37.07 |

Generally, for both seasons the differences between mean velocities for complementary scenarios were greater with increases in the flow rate (Table 8.12). For example, mean velocity decreased by 0.003m/s from scenario S.0.0 to S.0.30 and decreased by 0.007m/s for S.24.30, a change of -2.27% and -5.5% relative to the baseline respectively. Changes in mean velocity between complementary scenarios did not consistently increase with increases to flow rates. For example, the change in mean velocity between scenario S.54.0 and S.54.30 was -2.268%, which was smaller than the change of -5.54% between S.24.0 and S.24.30. This was despite scenario S.54.0 and S.54.30 featuring a higher flow rate. The standard deviation in mean velocities for S.54.0, 0.05 m/s, exceeded the mean velocity difference between their respective complementary scenarios, 0.0073m/s. This indicated that the variation in velocity values across the berm was greater than the difference between scenario means.

For the floodplain mean TKE, scenarios with an increase in flow rate also had a small increase in mean TKE, with winter scenarios exhibiting a higher mean TKE than the summer scenarios. However, changes in mean TKE were not consistently higher with increases in flow rate: scenarios featuring an increase in patch size had higher mean TKE values than their complementary scenario. Differences in the mean TKE values for complementary scenarios were smaller for scenarios with low rates, but these differences increased considerably for scenarios featuring higher flow rates. Overall, the increases were negligible except for the highest flow scenarios, A.24.0 and A.24.30. For example, S.24.30 and S.3.30 both had standard deviations of 0.0053 J/kg and 0.0056 J/kg, respectively, which were both greater than the differences between complementary scenarios, 0.0001 J/kg and 0.00004 J/kg. The highest flow scenarios showed considerable change in TKE on the floodplain: the mean TKE for scenario A.24.30, 0.0055 J/kg, was 45.5% higher than its complementary scenario A.24.0 which had a mean TKE of 0.0037 J/kg.

Table 8.12. Component of mean change in velocity *u*x and TKE compared against the baseline scenario (S.0.0 and A.0.0, respectively). Percentage change in the mean velocity and TKE between complementary scenarios are calculated relative to the baseline.

| Season | Summer | | | |
|---|---|---|---|---|
| Scenario | S.0.0 | S.3.30 | S.24.30 | S.54.30 |
| Change in mean velocity from complementary scenario (m/s) | -0.0030 | -0.0026 | -0.0073 | -0.0035 |
| Change in mean velocity from complementary scenario (m/s), relative to baseline (%) | -2.3 | -2.0 | -5.5 | -2.7 |
| Change in TKE from complementary scenario (J/kg) | 0.0001 | 0.0001 | 0.00004 | 0.0002 |
| Change from complementary scenario, relative to baseline (%) | 7.1 | 5.2 | 2.4 | 14.0 |
| Season | Autumn | | | |
| Scenario | A.-14.30 | A.0.30 | A.3.30 | A.24.30 |
| Change in mean velocity from complementary scenario (m/s) | -0.0095 | -0.0073 | -0.0080 | 0.0346 |
| Change in mean velocity from complementary scenario (m/s), relative to baseline (%) | -5.4 | -4.2 | -4.5 | 19.6 |
| Change in TKE from complementary scenario (J/kg) | 0.0001 | 0.0001 | 0.0002 | 0.0018 |
| Change from complementary scenario, relative to baseline (%) | 2.7 | 3.3 | 4.9 | 45.5 |

*8.3.1.2 Specific-morphotype changes to velocity and turbulent kinetic energy:*

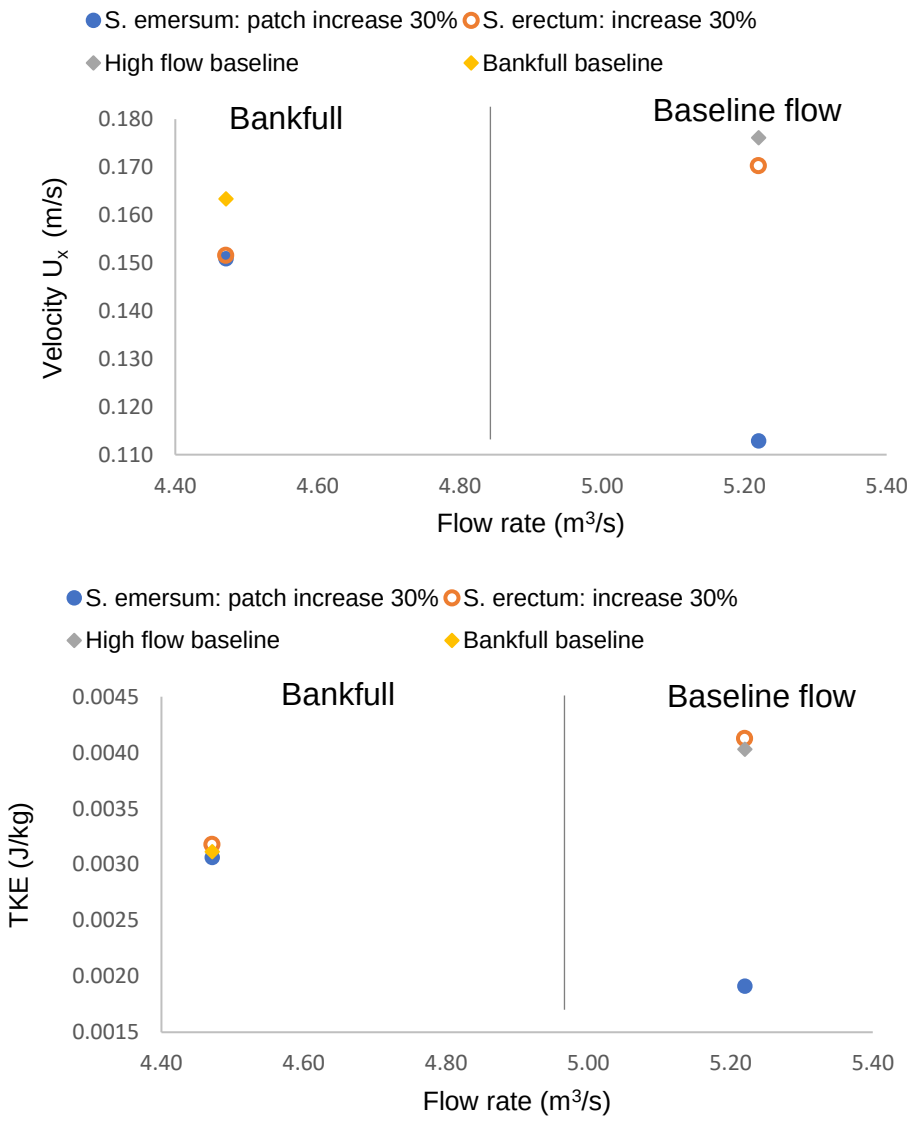


Figure 8.6 Mean velocity Ux and TKE (J/kg) for the morphotype-specific Autumn flow scenarios with bankfull flow (A.-14.0, A.-14.30.SER , A.-14.0.SEM) and scenarios with baseline flow rates (A.24.0,, A.24.30.SER , A.24.0.SEM).

For the mean floodplain velocity, the scenarios with bankfull flow conditions featuring an increase in the patch size for either *S.erectum* or *S. emersum* morphotypes exhibited a similar decreases in the floodplain mean velocities. No clear difference in the effect on the velocity was evident between the species with both A.-14.30.SER and A.-14.0.SEM scenarios reducing the mean velocity from the bankfull baseline by 0.66% (Fig. 8.6). No significant difference was evident between the two scenarios:

differences between the two were small at 0.001 m/s, which was within the standard deviation for both of 0.04m/s. For the baseline flow condition, both scenarios had lower mean floodplain velocities however the scenario featuring only an increase *S. erectum* exhibited higher mean velocity than the *S. emersum*-only scenario. For example, the A.-14.0.SEM scenario mean velocity decreased by 35.91% relative to the baseline. By comparison, the A.-14.30.SER scenario decreased by 3.33%. In summary, whilst increasing the patch size for either *S.erectum* or *S. emersum* reduced mean floodplain velocity, at the higher flow condition a 30% increase in patch size for *S. emersum* had a greater effect on flow deceleration than the same percentage increase in patch size for *S.erectum* morphotypes.

For mean floodplain TKE, at bankfull flow both the *S. erectum*-only and *S. emersum*-only scenarios featured a similar increase in mean TKE relative to the baseline: an increase of 1.61% and 1.62%, respectively. However, the increase in mean TKE for both were within the standard deviation for the baseline (Table. 8.13.). Therefore, it is difficult to discount the effect of natural variability on the mean floodplain TKE and attribute changes to the floodplain mean TKE to changes in patch size for either morphotype. For the baseline flow condition, the *S. erectum*-only scenario had little effect on mean TKE however the same percentage increase in patch size for *S. emersum* affected a decrease in the floodplain mean TKE: scenario A.0.30.SER featured an increase in mean TKE of 2.37% which was within the 0.0006(J/kg) standard deviation for the baseline. Comparatively, scenario A.0.30.SEM featured a 52.57% decrease relative to the baseline Table. 8.14).

Table 8.13. Mean TKE for macrophyte-specific scenarios.

| | Autumn | | | |
|---|---|---|---|---|
| Scenario | A.0.30.SER | A.-14.30.SER | A.0.30.SEM | A.-14.30.SEM |
| Mean streamwise velocity (m/s) | 0.17 ±0.05 | 0.23 ±0.04 | 0.11 ±0.05 | 0.23 ± 0.04 |
| Mean TKE (m/s) | 0.0042 ± 0.001 | 0.0032 ±0.001 | 0.004 ±0.001 | 0.0031 ± 0.001 |

Table 8.14. Differences in floodplain mean TKE and the change relative to the baseline for complementary scenarios.

| Season | Summer | | | |
|---|---|---|---|---|
| Scenario | S.0.0 | S.3.30 | S.24.30 | S.54.30 |
| Change in streamwise velocity from complementary scenario (m/s) | -0.0030 | -0.0026 | -0.0073 | -0.0035 |
| Change in streamwise velocity from complementary scenario (%). | -2.3 | -2.0 | -5.5 | -2.7 |
| Change in TKE from complementary scenario (J/Kg) | 0.0001 | 0.0001 | 0.00004 | 0.0002 |
| Change in TKE from complementary scenario (%). | 7.1 | 5.2 | 2.4 | 14.0 |
| Season | Autumn | | | |
| Scenario | A.-14.30 | A.0.30 | A.3.30 | A.24.30 |
| Change in streamwise velocity from complementary scenario (m/s) | -0.0095 | -0.0073 | -0.0080 | 0.0346 |
| Change in streamwise velocity from complementary scenario (%). | -5.4 | -4.2 | -4.5 | 19.6 |

| | | | | |
|---|---|---|---|---|
| Change in TKE from complementary scenario (J/Kg) | 0.0001 | 0.0001 | 0.0002 | 0.0018 |
| Change in TKE from complementary scenario (%). | 2.7 | 3.3 | 4.9 | 45.5 |

### 8.3.3 Discussion:

The results show that increases to in-channel vegetation patches alter the mean floodplain flow, and that the degree to which floodplain flow is affected is dependent on the channel flow rate. The data suggests that climate change will increase flood magnitudes as higher global mean temperatures in turn increases vegetation abundance and flow rates. Flow behaviour aligns with phenomena reported in the literature, with vegetation-induced deceleration resulting in local increases to flood elevation (for example: Kothayari et al., 2009; Nehal et al., 2012; Mulahasan & Stoesser, 2017). Clear differences are apparent between scenarios with different flow rates and between complementary scenarios which differ in vegetation patch size: scenarios featuring a greater vegetation abundance had slightly larger mean TKE and lower mean velocity, and consequentially an increase in surface elevation. This resulted in greater differences in mean floodplain elevation for complementary scenarios with high flow rates compared to those with low flow rates. This is likely due to increases in drag as higher velocity flow interacts with the vegetation patch. A similar effect was reported by Mulahasan & Stoesser (2017) who noted that water depth was higher when vegetation density was increased and that this effect became more apparent at higher flow rates. They noted that the relationship between vegetation density and flow rate resulted in steeper gradients for increases in flow depth for cases with high vegetation density compared to the shallower curves exhibited for cases with low vegetation density or no vegetation array. Nehal et al. (2012) similarly reported steeper gradients and higher flow depths with dense vegetation patches as flow rates increased. This vegetation-flow interaction was consistent between summer and autumn scenarios. Of the total percentage change in flow elevation the proportion attributable to vegetation change was greater for scenarios with lower flow rates, indicating that future changes to vegetation will have a greater effect on flood events which occur during periods of low flow than higher flow conditions representative of high impact, low probability flood events. As such, whilst a greater abundance of in-stream vegetation resulting from a warmer climate will increase flood levels overall, the impact of vegetation on flood conveyance is more apparent under the $2^0$c projection than the $4^0$c projection.

Scenarios featuring higher mean elevations also featured increased TKE and decreased mean velocity. Increases in the mean TKE are indicative of the greater

friction experienced at the vegetation-flow boundary as a result of faster flow interacting with the vegetative biomass. Higher mean TKE values for scenarios featuring a 30% increase in vegetation patch size of a given complementary scenario pair reflects how increases in the patch area cause greater turbulent intensities: an increase in the size of the interface between high-velocity channel flow and low-velocity patch flow in turn increases the shear zones at the vegetation-flow boundary. The result is a deceleration of the flow and an overall reduction in the reported mean velocity values. Although a general upward trend in the mean TKE and a downward trend in the mean velocity was reported a considerable amount of uncertainty made it difficult to attribute changes in flow to the scenario parameterisation. This is likely a product of flow acceleration as it is redirected through narrow cross-sectional channels between vegetation patches before entering the floodplain. Whilst the mean values aid in depicting the general trends in mean elevation it is difficult to appreciate the nuance of more sensitive flow quantities like TKE.

A key difference between the morphotypes was the degree to which their effect on flow elevation changes with flow rate: the trailing *S. emersum* morphotype consistently resulted in considerably higher flow elevations than the baseline however this difference was reduced for the higher flow rate. However, the uniform *S. erectum* morphotype showed little changed from the baseline flow condition for the lower flow condition. For the high flow elevation, the mean elevation was similar to *S. emersum.* The predominant influence of *S. emersum* is similar to the observations reported by Naden et al. (2006) who investigated the effect of *S. emersum* and *S. erectum* patches on flow for the same 140m reach of the River Blackwater during the May and September months. They noted that the increased abundance in *S. emersum* patches in September and within the channel centre were the dominant influence on flow, as the increased drag in the central channel resulted contributed to deceleration and subsequent increases in flow depth. By comparison, established *S. erectum* patches during the May month redirected flow into narrower sections of the channel resulting in higher velocities rather than increases in flow depth. This holds significance for river management strategists incorporating species composition into their flood mitigation schemes: differences in recovery times between species means that faster-growing species are more likely to become

predominant within river channels following weed cutting efforts. The results suggest that river strategists should take caution when managing channels occupied by fast-growing species which exhibit trailing morphotypes which may become dominant during the following growing season and exert greater control over flood conveyance. Whilst unknowns remain with regards to changes in growth rate per individual macrophyte species under future warming, an increase in the abundance of trailing morphotypes under climate change may exacerbate flood levels. As such, the predominance of trailing species after weed cutting may frustrate weed cutting initiatives seeking to reduce local flood risk in the future. However, this may be beneficial at reaches adjacent to floodwater detention zones.

## 8.4. Visualisations of berm flow:

Depictions of flow over the berm, or the local floodplain, and adjacent channel sections are shown for the flow surface and at halfway through the flow depth as measured from the lowest datum for elevation to the highest flow elevation, 1.328m. This elevation was chosen to capture changes in flow around patches otherwise absent when solely focusing on changes at the surface. General flow patterns were largely consistent across scenario runs: patterns for velocity $u_x$ at the surface and at-depth indicated that flow was considerably influenced by spatial variation in drag, and that this influence changed as flow rate increased.  Fig. 8.7 shows that the highest velocity values were located within the straight channel sections immediately preceding and succeeding the meander and floodplain zone. High velocity zones also influenced downstream flow. For example, a region of high surface velocity which developed in the straight channel section upstream of the floodplain caused higher velocities in the floodplain region. Increases in flow rates and vegetation patch size resulted in the higher velocity flow penetrating further into the floodplain region. This was also indicative of flow redirection and the potential for a meander cut-off. Streamwise velocity values were at their lowest velocities in the flow region centred at the meander apex and which expanded to include both meander limbs and much of the floodplain as flow rates increased and the vegetation patch size was increased. Scenarios A.24.40 and S.54.30 exhibited both the largest low velocity zones and greatest penetration by redirected flow when compared to other scenarios in their respective season.

For summer scenarios, both straight channels featured low velocity zones at the surface which corresponded with the distribution of the vegetation patches and the occurrence of downstream wakes.  These low velocity zones were absent for scenarios featuring flow rates of 3.56$m^3$/s and above after which the patch was submerged. At 1.328m flow depth, Fig. 8.8 shows the comparative effect between increased and unchanged vegetation patch sizes: scenarios: a 30% increase in patch size resulted in larger regions of low velocity due to flow deceleration within the patch and subsequent wake generation. Similar to surface flow velocities, high velocity zones developed in the straight channel preceding the floodplain. Increases in patch size and flow rates also increased area occupied by the high velocity zone close to the far bank, whilst also increasing the low velocity zone centred over the meander apex. The continuation of velocity zones at-depth suggested that the velocity flow regions were not isolated to surface flow and affected a considerable portion of the water column. A small circulation cell was evident near the meander apex, indicating that the negative velocity values were the result of a recirculation cell occurring over the apex.

Figure 8.7. Plan view of surface velocity flow at the floodplain for summer scenarios: S.0.0, S.0.30, S.24.30, S.24.30

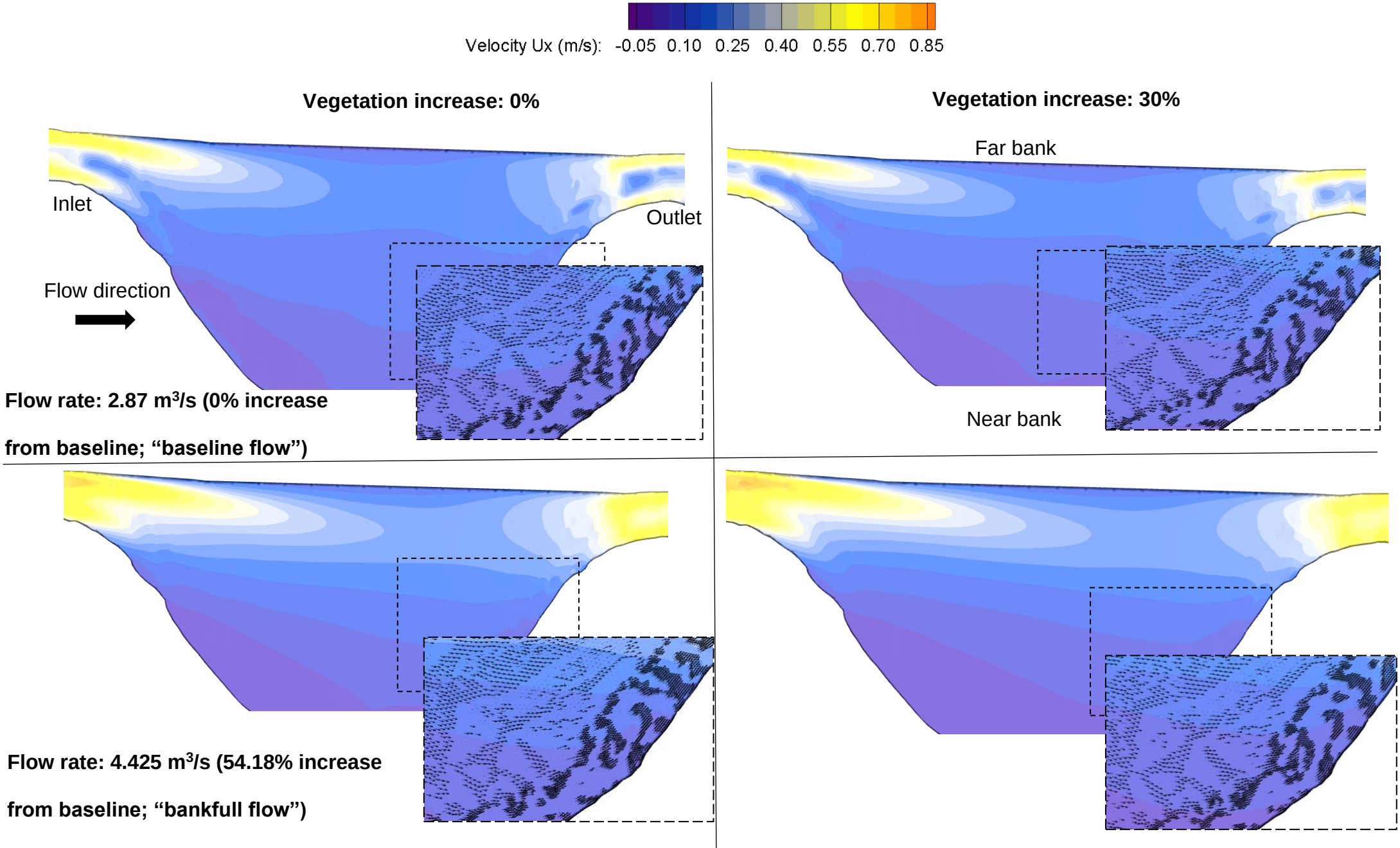

Figure 8.8. Plan view of velocity at 1.326m depth on the floodplain for summer scenarios: S.0.0, S.0.30, S.24.30, S.24.30

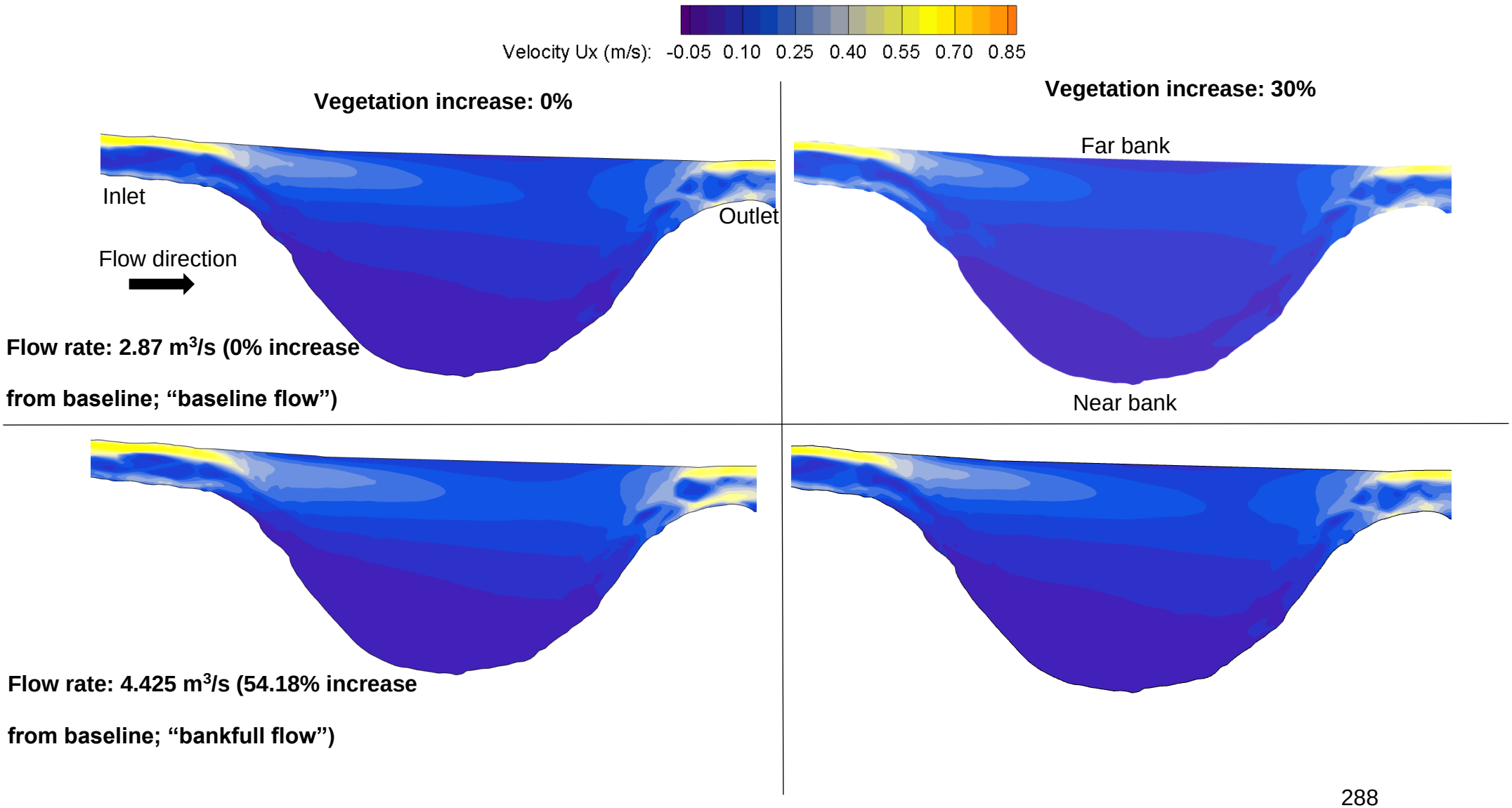

The autumn scenarios lacked the surface deceleration zones associated with the patch distributions which were observed in the summer scenarios (Fig. 8.9). This was due to the high autumnal flow rates which submerged all patches for all scenarios and resulted in an absence of discrete zones of velocity reduction and wake generation at the surface. The high flow zone located in the straight channel section upstream of the floodplain which was present in the summer scenarios was also present in the autumn scenarios. In all autumn scenarios the high velocity zone penetrated further across the floodplain compared to summer scenarios which suggested the distribution of high velocity zone was a function of flow rate. Additionally, the autumn scenarios also featured zone of high velocity at the channel-floodplain threshold which was located in the same channel region as the above. The distribution of high velocity values also increased with increases in the flow rate and patch size.

The low velocity zone centred over the meander apex was also present for autumn scenarios and which occupied a greater area of the meander and floodplain as flow rate and vegetation patches were increased. Negative velocities were observed to occur near the meander apex, the occurrence of which increased as the low velocity zone occupied more of the meander and floodplain. For all scenarios except the bankfull and baseline scenarios a large recirculation cell occurred over the meander apex which rotated right and down towards the near bank and left and up towards the far bank. This recirculation cell increased in size alongside the expansion of low velocity zone. For the 1.328m depth flow, the autumnal scenarios exhibited similar changes in flow distribution to that reported for the summer scenarios: Fig.8.10 shows that an increase in patch size and flow rate resulted in greater zones of velocity deceleration in vegetated regions, higher velocities, and deeper penetration of the floodplain from the upstream channel straight, and an expansion of the low flow zone over the meander apex to occupy more of the meander and floodplain.

Zones of high velocity are located between the vegetated regions and the channel bank for all scenarios are indicative of flow bifurcation resulting in flow acceleration. Notably scenario A.-14.30 features lower velocity values in these zones when compared to its complementary scenario, A.-14.0, despite the increase in patch size. In turn, the high velocity zone in the straight channel upstream of the floodplain occupies a larger surface area and penetrates deeper into the floodplain. The lower

flow velocities occurring near the channel boundaries in the 1.328m visualisation may be the result of flow being redirected towards the surface, resulting in higher surface velocities and lower near-bank velocities for A.-14.30 than those observed for A.-14.0. Scenarios A.24.0 and A.24.30 do not feature this differentiation between complementary scenarios with both exhibiting high velocity values both at the surface and in the near bank regions at 1.328m, suggesting that higher flow rates may overcome the dampening effect of vegetation near to the channel bank. Generally, flow velocity is lower in the channel flow region for scenarios featuring an increase in patch size.

Figure 8.9. Plan view of surface velocity flow at the floodplain for autumn scenarios: A.0.0, A.0.30, A.24.0, A.24.30

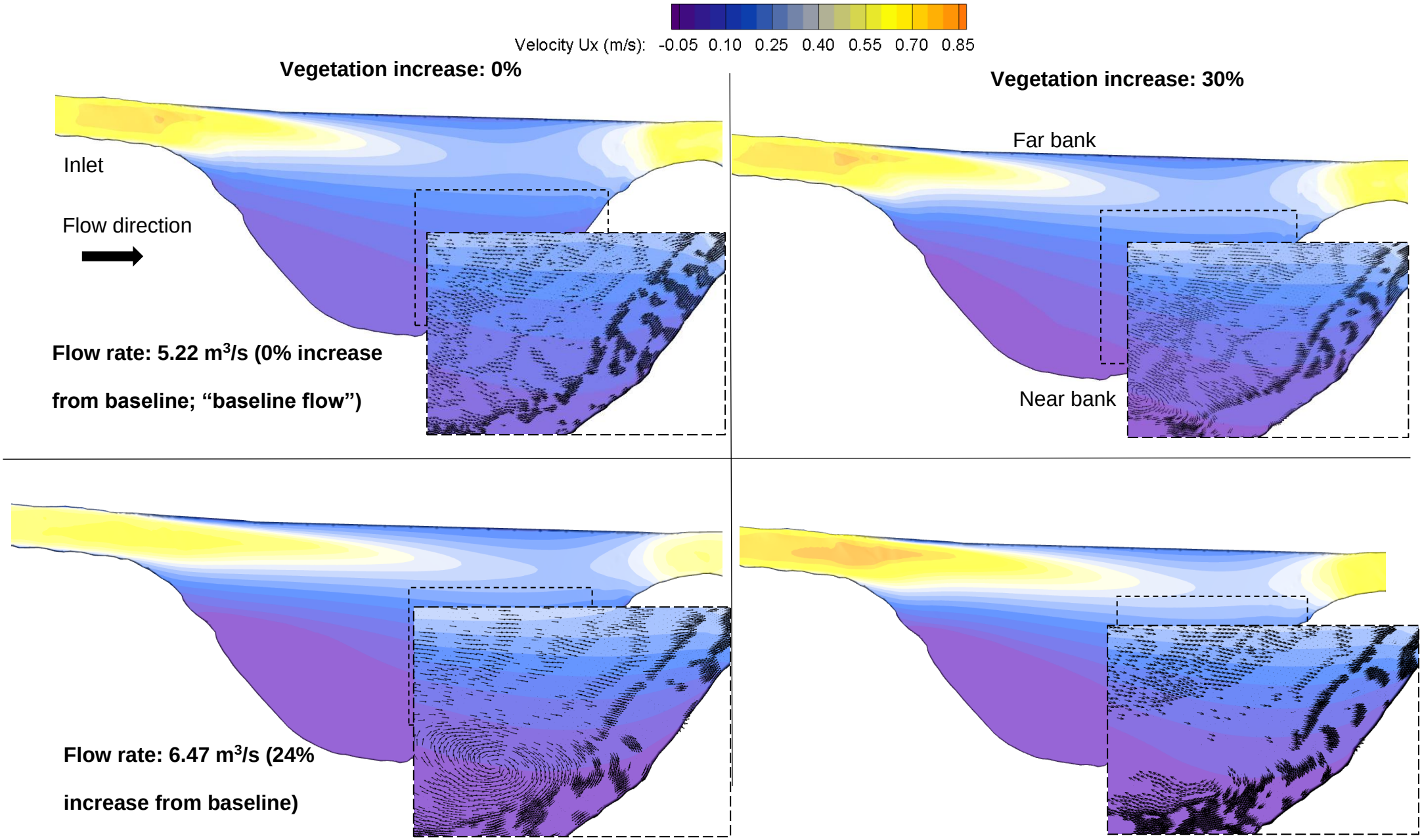

Figure 8.10. Plan view of velocity flow at depth (1.326m) at the floodplain for autumn scenarios: A.0.0, A.0.30, A.24.0, A.24.30

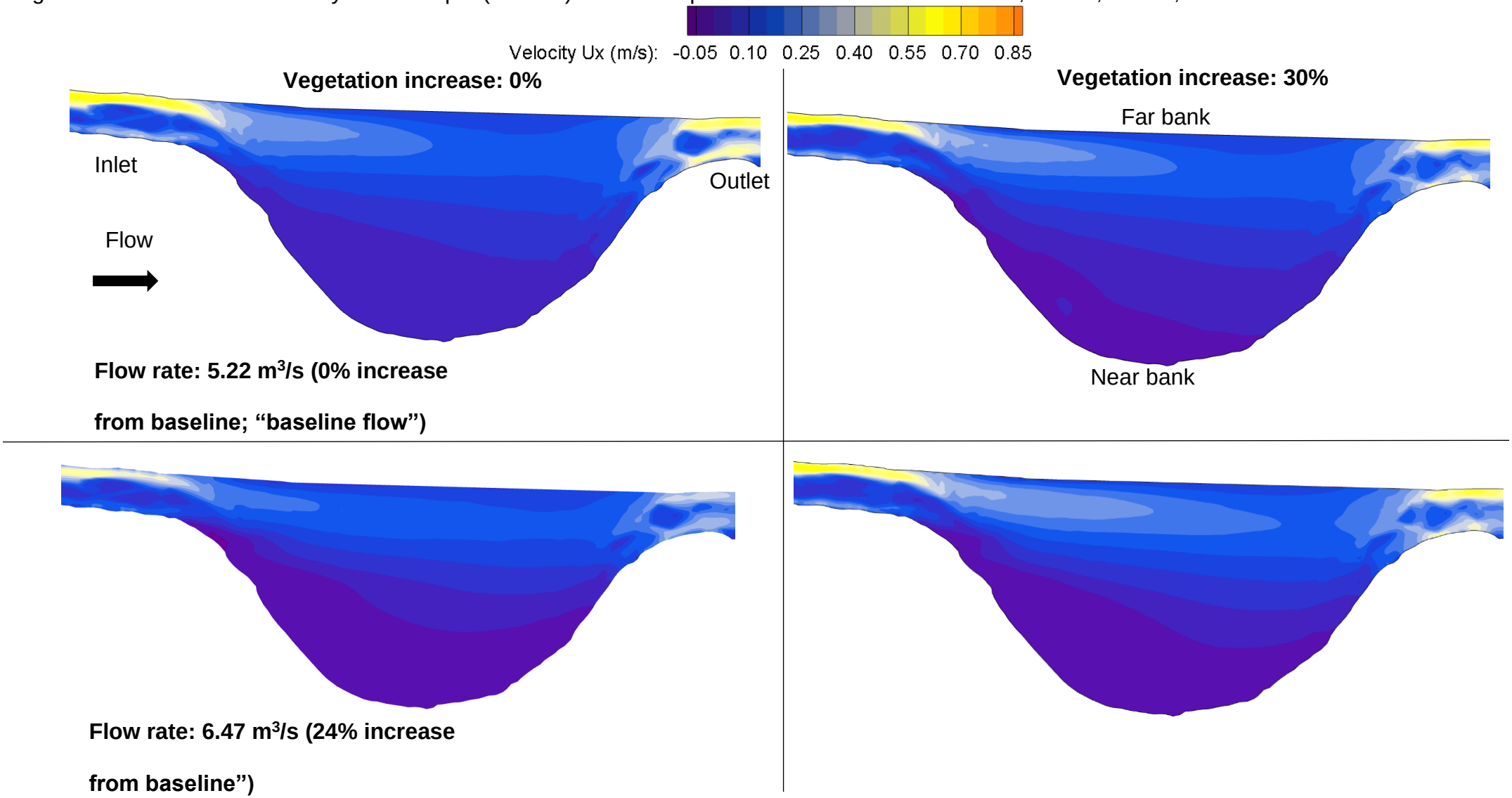

Generally, surface TKE values were highest in discrete zones in the straight channel immediately regions preceding and succeeding the meander (Fig.8.11 & Fig.8.12). TKE values were lowest over the meander apex. For both seasons, zones of high TKE were located along boundaries of vegetation patches and at the floodplain-channel threshold. At this threshold, the size of the high TKE zone changed as scenario variables were altered, with the zone increasing in size as the flow rate, vegetation patch size, or both were increased. Depending on the variable which was altered the shape of the zone also changed: an increase in just the flow rate resulted in a broader surface area occupied by high TKE values, whilst if just the patch size was increased then the TKE zone lengthened and penetrated further downstream. As such, vegetation-induced turbulence may have a greater impact downstream as the abundance of vegetation increases. For both seasons, the 1.328m visualisations (Fig.8.13 & Fig.8.14) showed the zones with the highest TKE values occurred at patch boundaries. These zones appeared to be clearly defined for scenarios featuring no increase in vegetation patch size however this definition was lost when patch size increased. For scenarios featuring increases in vegetation patch size higher TKE values occurred across greater breadths of the channel. The greater occupation of vegetation throughout the channel may reduce the discrete boundaries of individual patches whilst establishing an effective vegetation boundary inclusive of multiple patches with a contiguous vegetative influence on the flow. Both the summer and autumn scenarios featured the above effects in regions similar to those shown at 1.328m depth. This autumn scenarios featured a similar distribution of high and low TKE zones at 1.328m; zones with high TKE increased in magnitude and size with increases to both flow rate and vegetation patch size. Notably, the surface area for high TKE values was greater in autumn scenarios compared to those in the summer. For the 1.328m visualisation, scenario A-13.30 featured reduced TKE values compared to its complementary scenario A.-14.30 for turbulent zones in the same location, reflecting the lower velocities reported in the above section. Similarly, the reduction in TKE between complementary scenarios was not between scenarios A.0.30 and A.0.0.

Figure 8.11. Plan view of surface TKE at the floodplain for summer scenarios: S.0.0, S.0.30, S.24.30, S.24.30

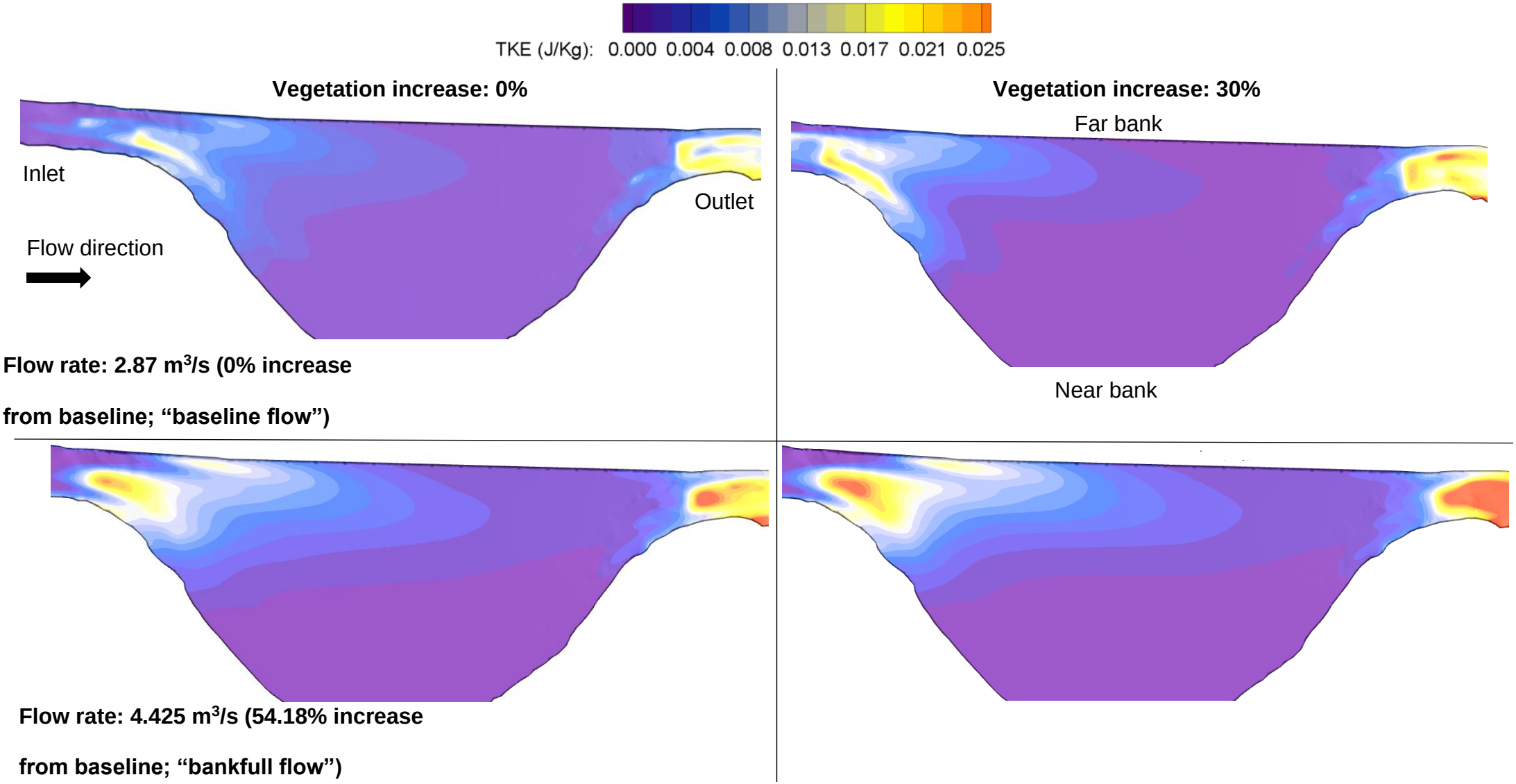

Figure 8.12. Plan view of surface TKE at the floodplain for autumn scenarios: A.0.0, A.0.30, A.24.0, A.24.

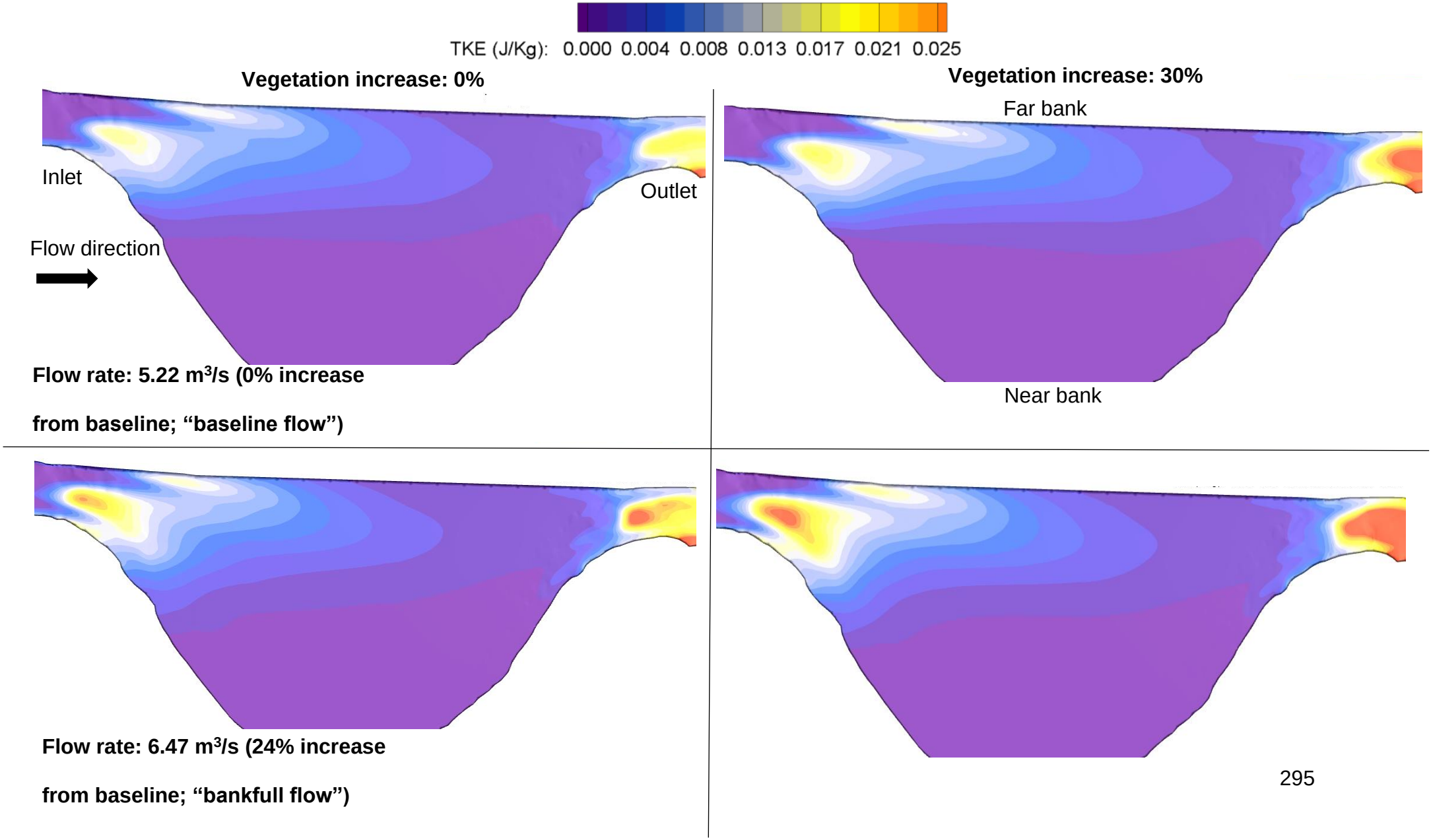

Figure 8.13. Plan view of TKE at depth (3.126m) at the floodplain for summer scenarios: S.0.0, S.0.30, S.24.30, S.24.30

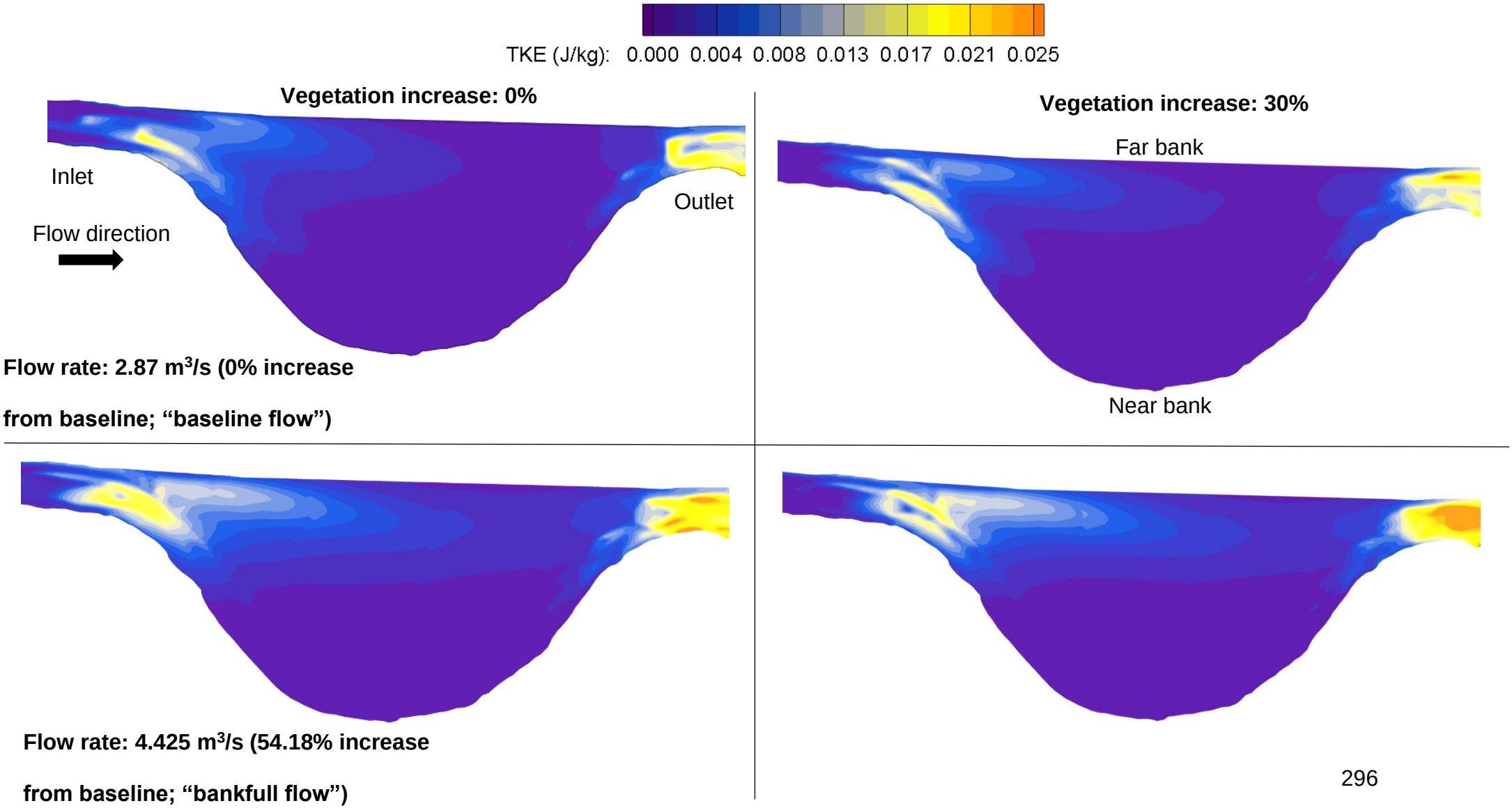

Figure 8.14. Plan view for TKE at depth (3.126m) at the floodplain for autumn scenarios: A.0.0, A.0.30, A.24.0, A.24.30

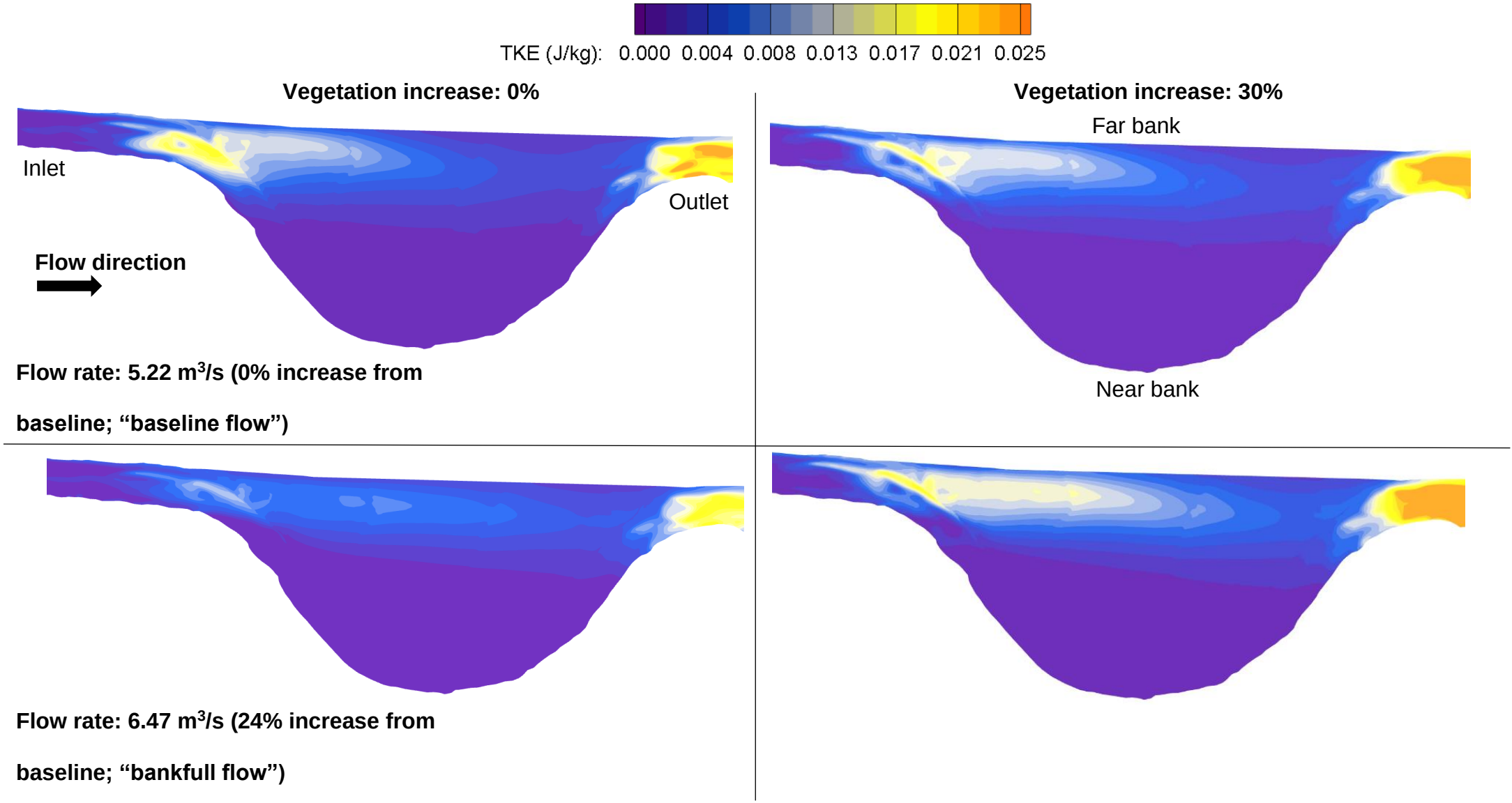

A transect positioned at the meander apex was used to assess representative changes to flow quantities throughout the water column on the floodplain. A zone of high velocity developed near to the far bank in the near-surface region (right side in Fig. 8.15). Increases in flow rate resulted in a greater area of the water column occupied by high velocity. Increases in flow rate also resulted in more flow deceleration in the channel at the meander apex throughout the whole water column; scenarios with higher flow rates featured a larger low velocity zone which occupied more of the floodplain compared to scenarios with low flow rates. Compared to increases in flow rates, increases in patch size resulted in smaller changes to the higher velocity zone; flow redirected over the floodplain due to increases in plant size were of lower velocity values than scenarios featuring high flow rates. Compared to their complementary scenarios, the scenarios featuring a 30% increase in patch size also featured a larger region of low velocity and higher surface elevations. This suggests the increase in vegetation patch size decreased flow velocities throughout the water column which in turn increased flow depths.

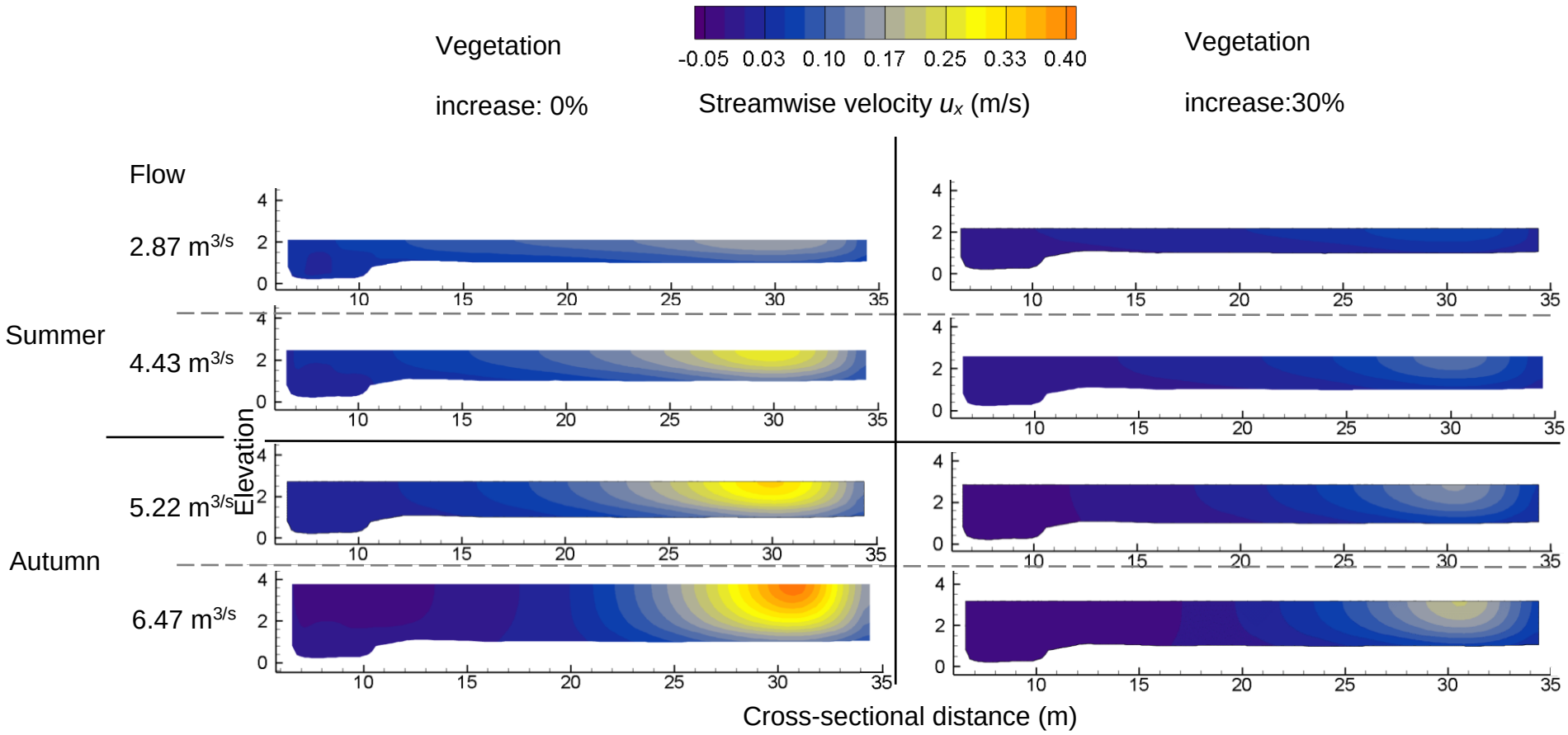


Figure 8.15. Cross-sectional profiles of depth-averaged streamwise velocity for scenarios S.0.0, S.0.30, S.54.0, S.54.30, A.0.0, A.0.30, A.24.0, A.24.30. Scenarios were chosen to show the differences in seasonal extremes and their complementary scenarios exhibiting changes in vegetation patch size.

### 8.4.3 Discussion

At the reach-scale the model exhibited phenomena observed in the literature, including the bifurcation of flow around patches (Bouteiller & Venditti, 2015), flow deceleration within patches (Tang et al., 2020), and wake production immediately downstream of patches (Follett and Nepf, 2012). High velocity values occurred at the surface and near-surface regions of the flow whilst lower values occurred at depth. For all scenarios flow was redirected over the floodplain in a jet-like flow pattern. This redirected flow strengthened with both increases in vegetation patch size and flow rates. As result of the flow diversion over the floodplain velocities were reduced in the meander. Negative velocity values in this region can be attributed to large recirculation cells which increased in size with increases in flow rates. Similar phenomena were reported by Lin et al. (2012) who characterise the recirculation zone as a negative velocity sub-zone whose boundary is defined as zero-velocity points adjacent to positive streamwise velocity. The presence of a recirculation cell adjacent to a jet-like flow has previously been reported in the literature. For example, MacVicar and Roy (2007) reported a large stationary gyre adjacent to a jet-like flow in a gravel-bed river. Few studies have considered the effect of in-stream vegetation on flow characteristics at meanders making a direct comparison of the results with the literature difficult, however Schaunder & Sukhodov (2012) observed a jet-like flow in a vegetated meander which, along with the adjacent recirculation cells, strengthened with increases in flow rate. Schaunder & Sukhodov (2012) report similar flow behaviour to the floodplain jet-like flow and recirculation zones in this study suggesting that the model may be an effective tool for simulating flow redirection and its possible consequences, such as effecting a meander cut-off.

Seasonal differences were apparent, with the lower flow rates for the summer resulting in vegetation effecting a conspicuous low velocity zone upon surface flow and accelerated flow in adjacent non-vegetated channel sections. In these conditions the vegetation patches occupied the total flow column; *S. erectum* can be considered to be emergent whilst for *S. emersum* the maximum elevation of the canopy is equal to free surface elevation. During the autumnal scenarios the vegetation patches were fully submerged, and flow was largely unimpeded near the surface in the channel centre. This result is consistent with the literature, where unimpeded flow above vegetation patches exhibits higher velocity than the flow within patches (Tinoco &

Coco, 2018). Clear differences were observed between scenarios which featured no increase in vegetation patch size and scenarios which featured a 30% increase in patch size: for scenarios featuring no increase in vegetation size low velocity zones both at the surface and at-depth are largely coherent with patch geometry. However, patch geometry became indiscernible for scenarios where patch size increased by 30%. Instead, the channel centre appears a contiguous interaction of patch-flow interactions with flow diverted and accelerating in narrow channels near the banks. Differences were also apparent on the floodplain despite no vegetative change having occurred in this region: the redirected flow exhibited lower velocity values for scenarios featuring an increase in patch size compared to scenarios with no increase but with the same flow rate.

## 8.5 Flow around patches:

The study sought to represent the real-life morphology of in-stream vegetation by using field measurements and the methods described in Chapter 3, Section 3.2.3. To understand the effect of vegetation morphotypes on the local flow field, longitudinal and lateral transects were extracted for a single patch for both *S. erectum* and *S. emersum* morphotypes. The patches selected were chosen for having the maximum distance possible from other plant patches upstream or downstream, being situated within the fully developed flow (i.e. vegetation patches near to the input boundary were not considered), and which occupied a channel area outside of the meander low-velocity zone. Lateral and longitudinal contour plots, alongside vertical profiles for flow variables equivalent to the longitudinal contour plot, were produced for both patches.

To investigate changes to local flow a patch representative of other patches in the reach was identified. For the *S. emersum* morphotype a patch was selected from the A.24.30 scenario which was 2.11m in length, had no neighbouring patch downstream, and its nearest neighbouring patch upstream separated by 3.09m. The patch was situated outside of the meander bend within the channel straight, ensuring that flow-vegetation interaction could be observed even during high flow conditions. In this scenario the patch is fully submerged.

8.5.1. Patch-scale flow: *S. emersum*:

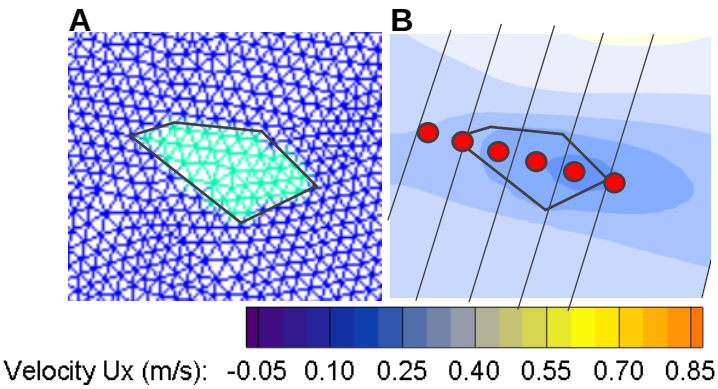


Figure 8.16. Plan view of the *S. emersum* patch showing the discrete patch geometry in in relation to the mesh nodes (A), and the patch geometry in relation to surface mean streamwise velocity showing the position of the cross-sectional slices used in Fig. 8.17 (black lines) and the co-ordinate locations used to extract flow profiles in Fig. 8.18 (red dots).

The longitudinal transects (Fig. 8.17) show flow deceleration within the vegetation patch. Flow through the patch was characterised by a velocity gradient, with the highest velocities located in the vegetated region adjacent to the upper canopy boundary and which faced the upstream flow. The lowest velocities were at the lower boundary towards the patch terminus. Immediately downstream of the patch the velocity values remained low, indicative of wake formation. Considering both vegetated and near-vegetation flow regions the lowest velocity values were located in the non-vegetation zone below the lower canopy boundary and below the patch terminus. The low velocity region below the canopy suggested that a sheltering effect was imbued by the trailing canopy, where flow within the space further deaccelerated and did not accelerate like other downstream flow regions until the flow re-joined with the wake further downstream. The highest velocity values for the patch were located at the point of maximum elevation on the upper canopy boundary. Above this point velocity values continued to increase as the flow transitioned into the free flow layer and achieved maximum velocity values at the surface. The loci of high velocity values on the upper canopy boundary were also the location of the highest TKE values. The lowest TKE vales were located near the riverbed. The highest Reynolds stress were located along the upper canopy boundary which faced the upstream flow. The lowest were located below the lower canopy boundary in the sheltered flow zone.

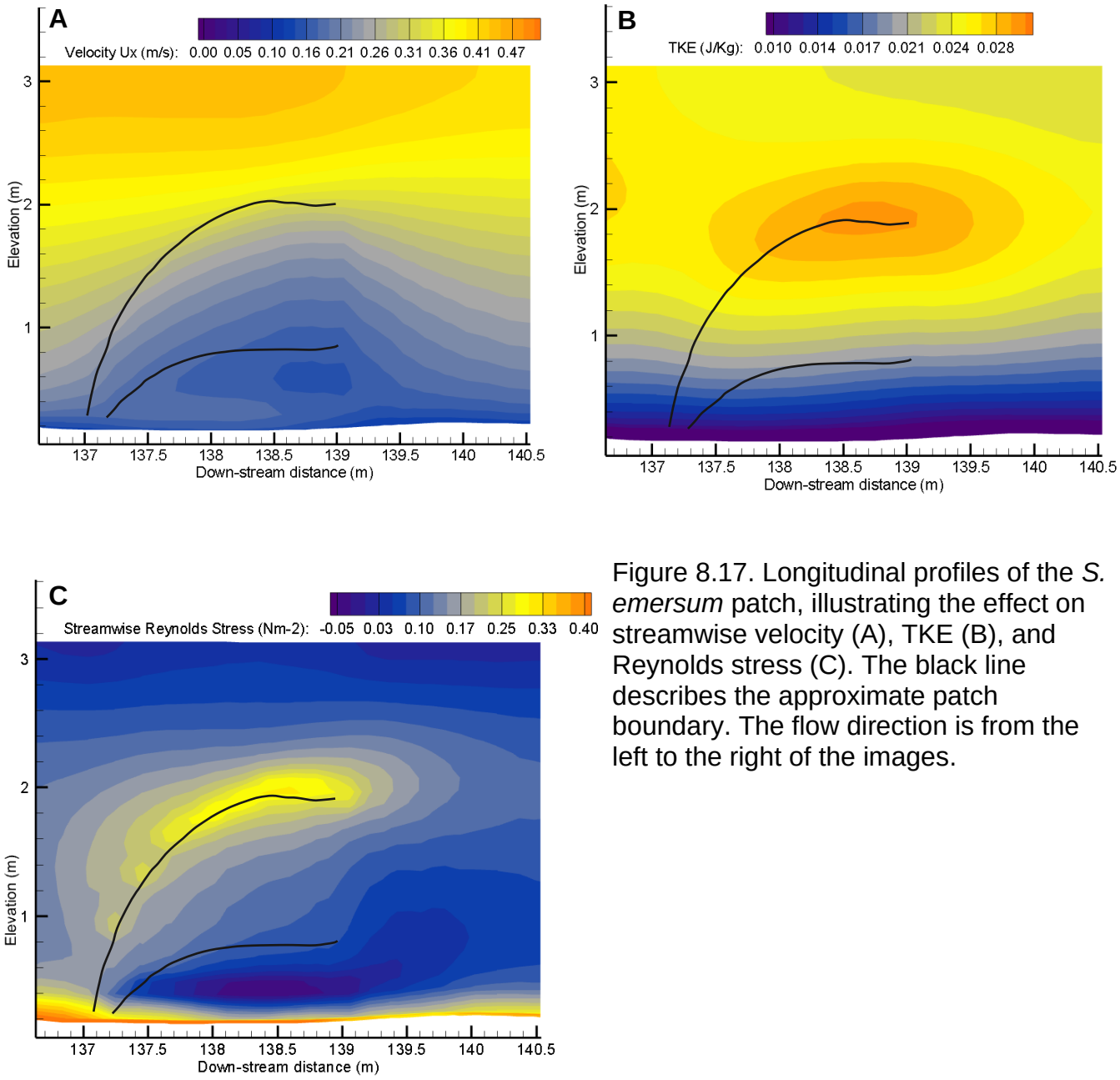


Figure 8.17. Longitudinal profiles of the *S. emersum* patch, illustrating the effect on streamwise velocity (A), TKE (B), and Reynolds stress (C). The black line describes the approximate patch boundary. The flow direction is from the left to the right of the images.

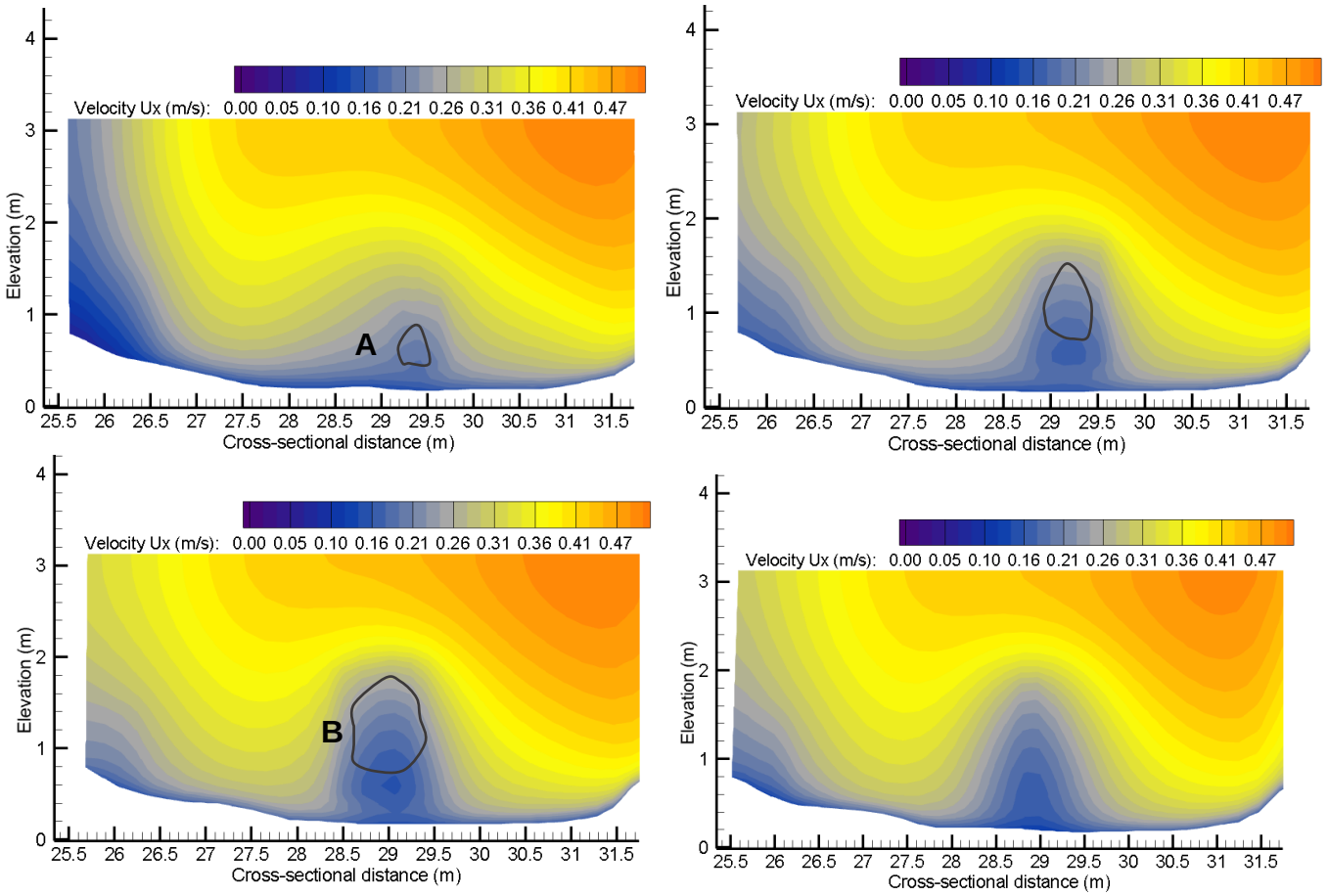


Figure 8.18. Lateral profile of the *S. emersum* vegetation patch, illustrating the effect of the patch on streamwise velocity. The approximate patch boundary is described by the black line. The flow direction is towards the viewer; the near bank is at the left of the cross-section and the berm bank is at the right.

Lateral transects of the channel describe the changing effect of the vegetation: a loci of low velocity values roughly corresponds to the vegetative region (Fig. 8.18) with the low velocity zone at the riverbed corresponding to where the patch is attached to the bed (A). As the patch extends both up through the water column and downstream the low velocity zone occupies a higher elevation (B). Immediately downstream of the patch the low velocities persist, indicating the presence of the wake. Velocity values are higher in the non-vegetated flow regions adjacent to the patch where the flow is unimpeded.

Vertical profiles for the streamwise velocity, TKE, and Reynolds stress were extracted upstream of the patch, throughout the patch, and downstream of the patch at intervals of 0.75m. Values for the velocity and Reynolds stress were calculated to represent the Cartesian streamwise direction using the method previously in Chapter 7, Section 7.4.1. Six vertical profiles were extracted for each variable and are presented in Figure 8.19. The upstream vertical profile shows a gradual increase in velocity with depth with a key perturbation in the profile in the near-bed region where velocity is much reduced (A). However, as flow interacted with the patch, the distribution of values became distorted for vegetative profiles (B-E) relative to the upstream profile. The velocity profiles showed flow deceleration within the patch whilst values increased above the patch, resulting in the characteristic serpentine “S” shape reported in the literature (Li et al., 2019). TKE values were highest at the upper patch boundary between vegetated flow and the free flow layer. This complements the literature where turbulent maximums occurring at the top of submerged canopies has previously been reported (Nezu & Onitsuka, 2001). Reynolds stress is highest at the riverbed where shearing occurs as a result flow interacting with the gravel-bed drag elements. High Reynolds stress values also occur at the top of the patch canopy where shearing occurs because of the faster turbulent flow layer encountering the vegetative boundary. The effect of the vegetation on flow appeared to increase with distance downstream: for all three quantities the vertical profiles near to the patch head (B) were less distorted relative to the non-vegetated profile (A) when compared to the profile at the patch terminus (E). For example, streamwise velocity profiles at the patch head (B) exhibit less change throughout the vertical profile compared to subsequent downstream locations, whilst the maximum value for TKE and Reynolds stress occurred in profile

E. This suggests that the cumulative effect of drag results in greater differences in flow velocity at the near-canopy layer and the turbulent flow layer, increasing shear and turbulence generation. Patterns in velocity reduction, and increases to both TKE and Reynolds stress, occurs immediately downstream of the patch suggesting the prevailing influence of vegetation on flow and the formation of a wake.

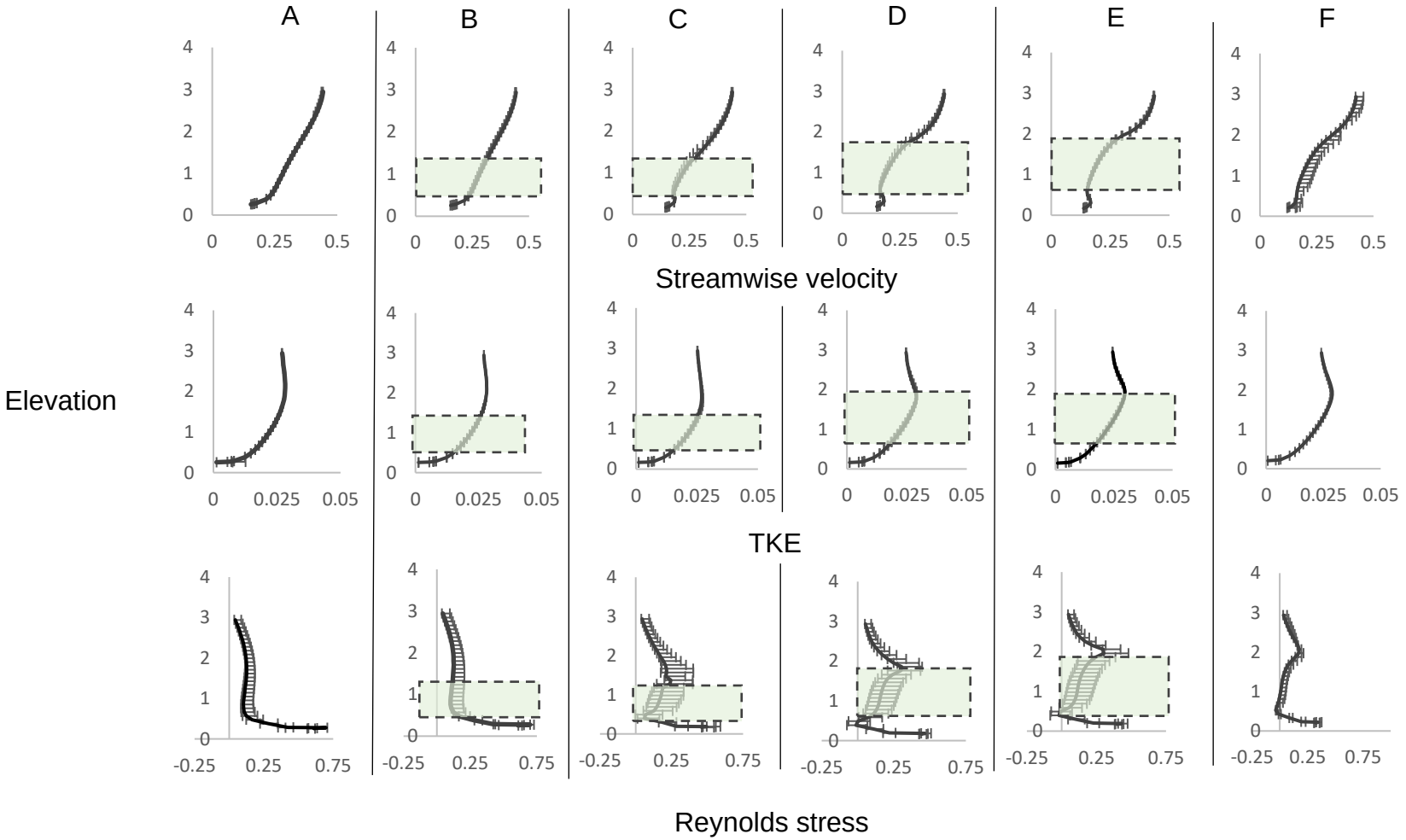


Figure 8.19. Flow profiles at six locations within or adjacent to the *S. emersum* patch. Figures are ordered from the upstream (A) to the downstream (B) points described in Fig. 8.16. The green squares show the approximate location of the patch within the water column.

For the *S. erectum* morphotype a patch was selected from the S.24.0 scenario which was 2.91m in length, and was distanced from patches upstream and downstream by 2.67m and 0.83m respectively.

8.3.2. Patch scale flow: *S. erectum*

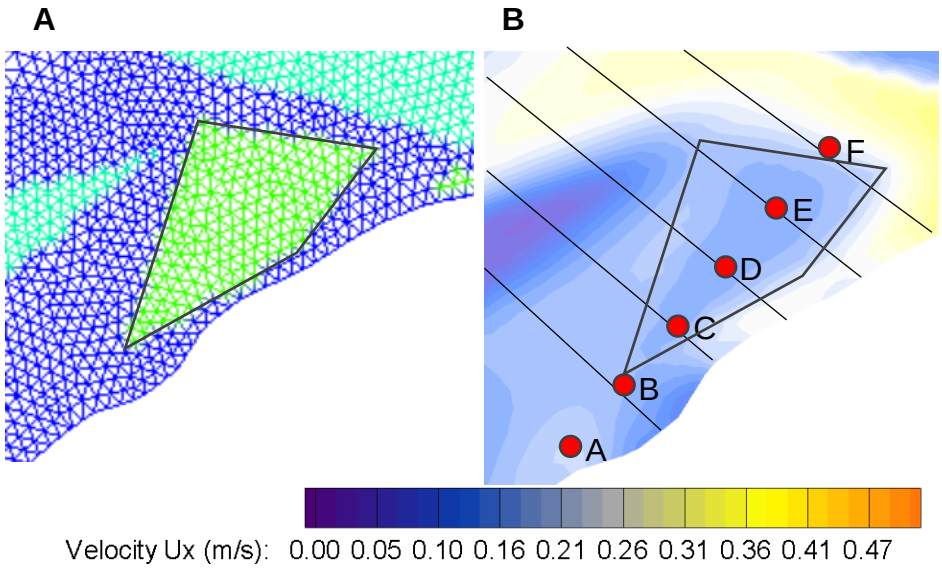


Figure 8.20. plan view of the *S. erectum* patch showing the discrete patch geometry in in relation to the mesh nodes (A), and the patch geometry in relation to surface mean streamwise velocity with the position of the cross-sectional slices used in Fig. 8.21. shown (black lines) alongside the co-ordinate locations used to extract flow profiles in Fig. 8.22 (red dots).

For the *S. erectum* morphotype the flow profiles were extracted from the S.24.0 scenario, i.e. the highest flow condition and which featured no increase in vegetation patch size. In this scenario, the *S.erectum* patch is fully submerged. The longitudinal transects (Fig. 8.21) showed low velocity values which shared the same spatial distribution as the vegetation patch, indicating a deceleration of the flow within the patch. Low velocity values were also present immediately downstream of the patch, indicating wake formation. Within the patch, the low velocity values shared a similar gradient throughout: velocity was highest towards the patch canopy and decreased with proximity to the riverbed. Above the patch velocity values were higher and increased in the downstream direction with distance along the canopy. A local velocity maxima was reached at the patch terminus, suggesting flow acceleration

due to bifurcation. The near-canopy flow layer adjacent to the upper patch boundary exhibited high TKE values. The highest TKE values were located in the same region as the velocity maxima. The lowest TKE values occurred at the riverbed. The highest Reynolds stress values were present along the upper patch boundary and the riverbed boundary. The lateral transects (Fig. 8.22) of the patch showed an a decreased in flow velocities for all vegetated regions, with the lowest velocities distributed towards the base of the patch. This distribution was absent for the upstream transect but present for the downstream transect which was identified as a wake. Velocities were slightly higher in the free flow regions beside the patch and highest at the free surface region.

Figure 8.21. Longitudinal profiles of the *S. erectum* patch, illustrating the effect on streamwise velocity (A), TKE (B), and Reynolds stress (C). The black line describes the patch boundary. The flow direction is from the left to the right of the images.

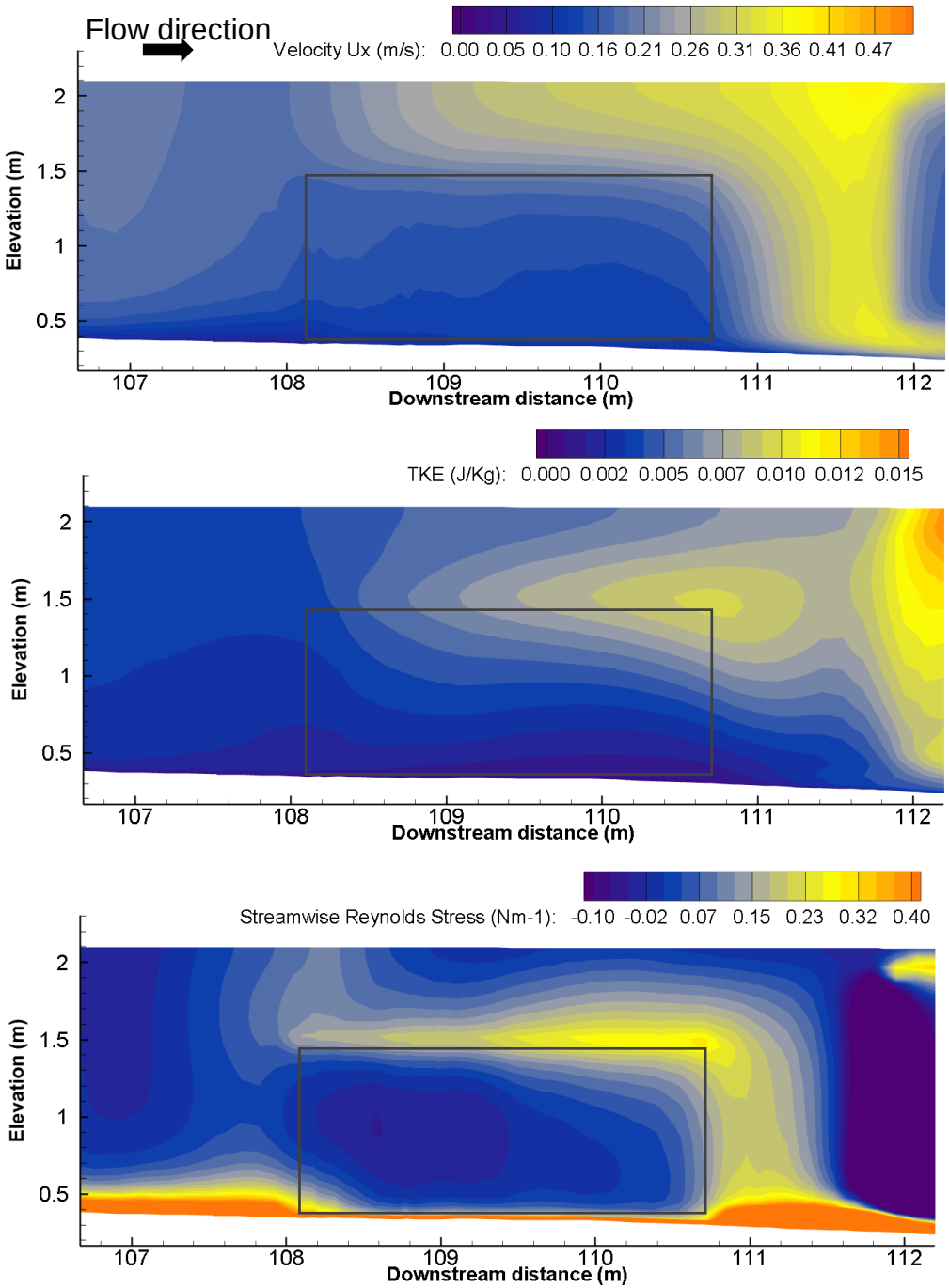

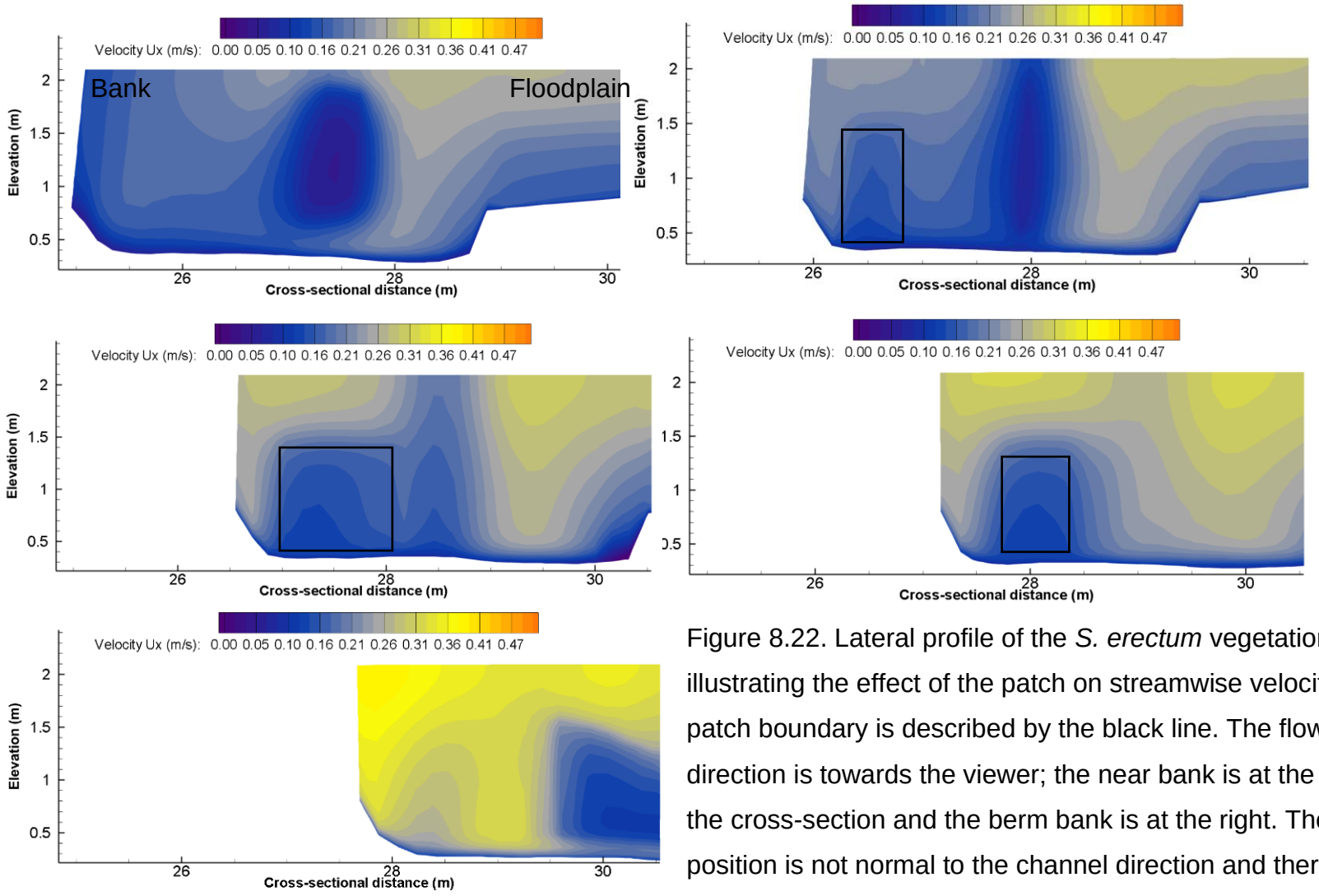


Figure 8.22. Lateral profile of the *S. erectum* vegetation patch, illustrating the effect of the patch on streamwise velocity. The patch boundary is described by the black line. The flow direction is towards the viewer; the near bank is at the left of the cross-section and the berm bank is at the right. The patch position is not normal to the channel direction and therefore the lateral dimensions are not consistent.

For the vertical flow profiles, three distinct flow layers were present in in Figure 8.23 B-F: the near-bed layer, the vegetated patch layer, and the free flow layer. The near-bed layer exhibited the lowest values for streamwise velocity and TKE whilst showing the highest values of Reynolds stress. The high Reynolds stress values were indicative of high levels of shearing on the riverbed. The vegetated patch layer was a region of low velocity which extended through the flow column until 1.5m, the maximum extensions of the vegetation patch, and where velocity values increased. At the 1.5m threshold both the TKE and Reynolds stress increased, with the TKE being highest in this region. The high TKE values suggested that the flow is experiencing higher levels of drag at the vegetation boundary than elsewhere in the water column. Above the patch the velocity values reached their highest whilst TKE production and Reynolds stress are reduced, indicative of fast flow regions unimpeded by form drag. The above behaviours become exaggerated with downstream distance from the patch head: the difference between the velocities just above the 1.5m threshold and those below appears to increase until the patch terminus at point E. The TKE values are also highest at this point and suggests that the vegetation drag has a cumulative effect on the flow. Additionally, the effect of vegetation drag still prevails immediately downstream of the patch (point F) which is indicative of a wake.

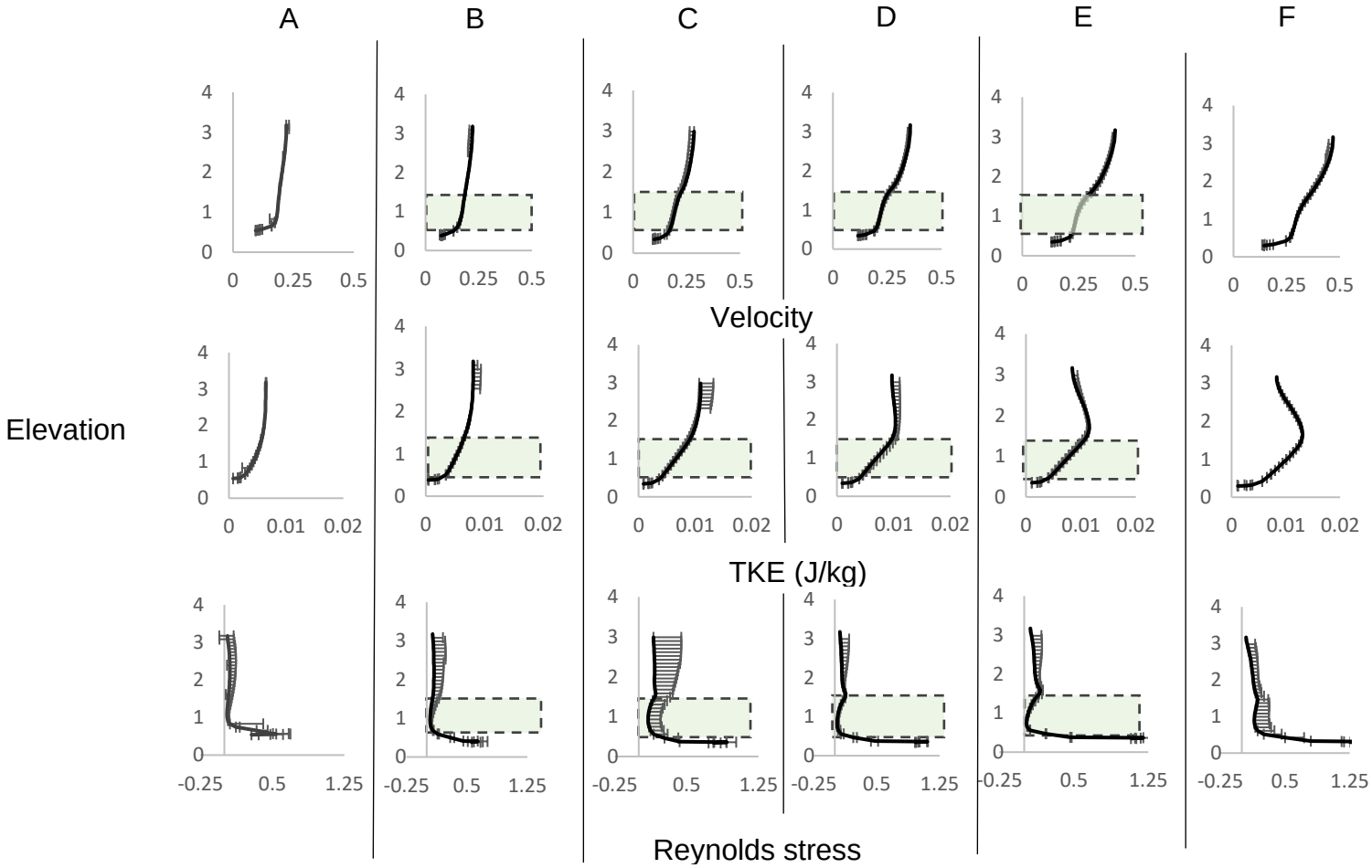


Figure 8.23. Flow profiles at six locations immediately upstream of the patch, immediately downstream, and within the *S. erectum* patch. Figures ordered from the upstream (A) to the downstream (B) points described in Fig. 8.20. The green squares show the approximate location of the patch within the water column.

### 8.3.4 Discussion.

For both morphotypes flow decelerates within the plant patch and then gradually accelerates immediately downstream in the wake region, whilst flow velocities are at their highest towards the patch terminus in the near-canopy flow layer just above the upper patch boundary. Within the patch the distribution of velocity gradients is related to the upper patch boundary: the curved boundary of *S. emersum* results in a diagonal distribution of velocities as flow near the patch bottom slows down quicker compared to flow near to the patch top having interacted with more vegetative volume by the same point. For *S. erectum* the uniform elevation of the upper boundary results in a somewhat regular gradient within the patch with flow velocity decreasing with depth. Both patches exhibit their lowest velocities immediately before the patch terminus, however for *S. emersum* the zone of lowest velocity appears to be more concentrated and occurs in the sheltered non-vegetated zone immediately below the bottom vegetative boundary.

For both morphotypes the occurrence of acceleration in the near-canopy boundary flow region has previously been reported in the literature (Nepf & Vivoni, 2000). However, the distribution of high velocity values within the near-boundary region is different between the two morphotypes: for *S. emersum* high velocity values are limited to the patch terminus and this small locus of high velocity marks a threshold above which velocity increases with height and but decreases with height below. The deepest section of the upper boundary which meets the riverbed has very low velocities. For *S. erectum* high velocity values occur across the entire upper boundary likely a result of its uniform geometry maintaining the upper boundary at the same elevation for the length of the patch. Both patches exhibit a gradient in velocity values throughout the near-boundary flow region, however for *S. emersum* the change in velocity along the upper boundary appears to be a function of height as velocities increase as the upper boundary extends up throughout the flow column. For *S. erectum* the gradient appears to be dominated by flow redirection: whilst the elevation remains the same the velocity values increase with distance downstream as water is squeezed between the canopy and free surface.

The results suggest that flow-vegetation interactions produce complex phenomena which are dependent on vegetation morphology. For both morphotypes flow

acceleration above the vegetation patch induces high shearing, which in turn generates turbulence. Previous research has observed flow acceleration above vegetation patches and deceleration within patches (Li et al, 2019) and high Reynolds stress at the vegetation boundary. In this study, negative Reynolds stress above patches was also identified. Negative Reynolds shear stress is indicative of a positive velocity gradient (Yan, Wai, & Li, 2016) and hence decreases with an increase in both downstream and vertical distance from the patch as the flow increases. The high negative values located above the canopy is indicative of shearing induced by flow acceleration above the canopy, a phenomena previously reported by Nepf and Ghisalberti (2009). The spatial heterogeneity in Reynolds stress reported here has previously been reported in the literature: Neary et al., (2012) reported low shear stress within vegetation patches whilst higher values were noted by Tinoco & Coco (2018) at the vegetation boundary. The trailing morphotype of the *S. emerusm* species exhibited a somewhat different distribution of streamwise velocity, TKE, and Reynolds stress compared to the *S. erectum species.* A scarcity of data describing variation in turbulence generation for natural, in-stream river plants suggests that the simulated velocity, TKE, and Reynolds stress data produced in this study is a novel contribution to the field. The results suggest that patch length plays an important role in flow acceleration in adjacent non-vegetative flow regions for species with regular canopy shapes. For flow through the patches, the vertical gradient of velocity values within the *S.erectum* patch suggests greater flow deceleration occurs with elevation. The vertical velocity gradient is extant to a lesser degree for *S. emerusm*, with velocity highly influenced by proximity to the upper boundary layer which serves ingress for flow entering the patch, and by proximity to the lower patch boundary where flow exits the patch and the lowest velocity values occur. Because flow acceleration initiates shearing and, in turn, turbulence production, both the values for TKE and Reynolds stress are dependent on this pattern. Both patches achieve their maximum decelerative values immediately before their terminus.

## 8.6. Summary

This chapter has described the design philosophy of the future flood scenarios and assessed the impact of changing river flow rate and vegetation patch size on flow.

For the scenario results the following were considered: the overall impact of changes in flow rates and vegetation change on mean floodplain flow, a floodplain-scale assessment of model results, and changes to flow behaviour at the patch scale per morphotype.

The effect of future changes to river vegetation, river flow rate, and the vegetation-flow interactions are: increases in vegetation patch size resulted in higher surface elevations, with the degree to which vegetation contributes to the total change in surface elevation being dependant on the flow rate. Increases in mean floodplain elevation occurred alongside decreases in streamwise flow velocity and increases in TKE. These changes were observed for both velocity and TKE across the summer and autumn scenarios. The contribution vegetation has at increasing flow rates, here termed the vegetation component, decreases with higher flow rates. The reduced influence of vegetation is likely due to the greater hydraulic area occupied by the turbulent flow layer which allows for a greater volume of water to be uninhibited by vegetation drag. The increase in the floodplain surface elevation for scenarios with higher flow rates and a smaller vegetation component suggests that changes in surface elevation are not wholly dependent on changes to vegetation patch size. This phenomenon may be the result of the vertical distribution of floodplain drag remaining unchanged, with flow height allowing trees to dominate drag production. At lower flow rates the uniform morphotype that typified the *S. erectum* patch profile had a lesser effect on flow compared to the trailing morphotype more typical of *S. emersum* patches. However, these differences were reduced when the flow rate increased. Overall, changes to vegetation patch size and the resultant impact on vegetative drag, floodplain conveyance, and flow elevation suggests that plant abundance is a key control for the velocity and depth of river flow. This effect is particularly stronger for scenarios with lower flow rates, however at higher flow rates the impact of vegetation is lessened. The changes to mean flow quantities suggests that a future increase in vegetation abundance is more important in the assessment of flood risk for high frequency, low magnitude flood events than extreme flood events, where changes to vegetation patch size exerts a greater control on flood levels. Incorporating an understanding of plant abundances is critical when assessing the frequency that bankfull flows may occur.

At floodplain-scale the effect of changes to flow rates and vegetation patch size were considered for streamwise flow velocity and TKE. Changes to both quantities were assessed in terms of the surface flow and flow-at-depth. The flow distribution was highly heterogenous, with higher values for TKE and velocities located in straight channel regions preceding and succeeding the meanders whilst regions of very low flow and TKE were located in the region of the meander apex. For a given season, increases in both flow rate and vegetation patch size diverted channel flow over the floodplain which experienced higher velocities whilst the greater portion of the meander and the adjacent floodplain were occupied by a low-velocity region. Additionally, as flow rates increase a larger region of both the meander and the floodplain is occupied by a recirculation cell. A larger survey of the surrounding floodplain topography and the characteristics of local floodplain vegetation would be needed to expand the mesh to investigate the broader changes in floodplain flow. A single cross-section across the centre of the floodplain was used to assess the overall distribution of velocity throughout the water column and showed that high velocity regions were concentrated near the surface whilst the low velocity region near the meander apex were consistent through the entire water column.

The flow pattern at patch-scale exhibited complex behaviour resulting from the relative acceleration and deceleration of flow as it interacted with the vegetation geometry for both morphotypes. The distribution of flow was different for both morphotypes, with the trailing profile for *S. emersum* exhibiting very low velocity just below the profile in the non-vegetative region above the bed and high Reynolds stress on the upstream-facing boundary, whilst the uniform profile for *S. erectum* exhibited low velocity along the riverbed for the length of the patch and high Reynolds stress along the top of the patch profile. Both exhibited a zone of high TKE at the downstream terminus of their respective upper boundaries.

The model shows promise for representing dynamic three-dimensional flood responses to both climate change and vegetation change. The flow phenomena described for both within vegetation patches and in patch-adjacent flow regions reflect phenomena reported in the literature, suggesting the model has effectively represented current understanding of flow-vegetation interaction. An assessment of mean floodplain flow indicates that the model is useful for simulating future flood magnitudes. However, the effective representation of in-stream vegetation within 3D

models is nascent, with further study required to investigate the integration of vegetation biomechanics, such as vegetation flexibility within fluid models. This study produced novel results describing the influence of two vegetation morphotypes on key flow characteristics under different flood conditions in a gravel-bed river, generating a new understanding of flow-vegetation interaction.

# Chapter 9 | Summary of study results

## 9.1. Introduction

Future increases to in-stream vegetation patch size due to climate change have a considerable impact on flood events for a chalk river. In addition, the contribution of in-stream vegetation to total flood magnitude changes with the flow rate. This project has considered the key role in-stream vegetation has in influencing flood flow due to changes in channel capacity, differences between species morphology, and interactions between vegetation and predicted changes to river flow under future climate change. In doing so this project has addressed a key research gap in understanding the changing impact of vegetative controls on three-dimensional flow within a natural channel under different future climate scenarios. This outcome was achieved by using a three-dimensional numerical model to simulate the topographical, ecological, and hydraulic components of a reach situated in the River Blackwater, Hampshire, UK. The model was calibrated using four scenarios which considered three conditions of seasonal vegetation abundance (February, non-vegetated channel; May, low vegetation abundance; September, high vegetation abundance) and four different flow conditions (February flow, May flow, September low flow, September high flow). The gravel-bed bulk drag coefficient was calibrated using the February abundance scenario and flow. The vegetated bulk drag coefficient was calibrated using the May vegetation abundance and May flow condition, as well as the September vegetation abundance scenario for both low and high flow conditions. The influence of overhanging bank and floodplain vegetation was also incorporated into the model. Two different vegetation morphotypes were represented which describe the effect of patch morphology on channel flow. Both morphotypes were informed by the geometry for the two dominant macrophyte species, *Sparganium erectum* and *Sparganium emersum*, and incorporated into the model through the three-dimensional distribution of the vegetation drag term. A scenario-based approach was used to simulate the effect of changing vegetation abundance and flow rates on peak flow. The model flow scenario design was informed by estimated changes to future flow rate for the Thames valley region, observed in-stream vegetation change reported in the literature, and the observed

maximum seasonal peak flood elevations reported from an on-site river gauge. Eight flow scenarios considered changes in vegetation abundance for four flow conditions across two seasons. An additional four scenarios considered changes in only one morphotype for two flow conditions. This was done for both morphotypes, bringing the total number of model scenarios to twelve.

This chapter addresses the research questions previously mentioned in Chapter 2, Section 2.9 and which are re-stated here:

1. How do changes to in-stream vegetation patches and river flow effect floodplain flow under future climate change?
2. What is the impact of different vegetation morphologies on floodplain inundation under climate change?

## 9.2. How might changes to in-stream vegetation patches and river flow effect floodplain flow under future climate change?

In the UK, climate change is expected to alter both future river flow and the abundance of in-stream vegetation. As such, the model scenarios considered independent changes to vegetation abundance, changes to river flow rate due to climate change, and changes to flow rate due to seasonality. Flow-vegetation interactions involve three-dimensional mechanisms and phenomena. This necessitated the development of a numerical model which used double-averaged Navier-Stokes (DANS) equations which average simulated quantities in both time and space to represent the three-dimensional drag effect exerted on the flow. This drag force approach was used to simulate flow interactions with the gravel riverbed, in-stream channel vegetation, overhanging vegetation, and vegetation on the local floodplain, also referred to as the berm. The gravel-bed drag was parameterised using the measurements of gravel dimensions taken during a field survey of the River Blackwater. The in-stream vegetation was parameterised by using the measurements of the vegetation patch planform, patch distribution within the channel, vegetative surface area, and vertical distribution of the vegetation patches, as well as a factor describing the proportionate relationship between patch planform geometry and drag. The floodplain vegetation was represented by a composite term drag for grasses and trees. The tree drag was parameterised using the calculated

mean vegetation geometry and the dimensionless population density which represented the spacing of vegetation on the berm. Due to a lack of information detailing the areal values of the floodplain grasses, the grass coefficient was adjusted using the same method for vegetation patch calibration. Bank vegetation was represented by the drag coefficient for floodplain grass. The calibrated values for both the gravel and vegetative bulk drag coefficients were within the same order of magnitude as similar studies. The model performed reasonably well, with the simulated profiles for vertical velocity and TKE reasonably matching the profiles for the measured values whilst flow heterogeneity resulting from flow-vegetation interaction reflected phenomena reported in the literature. The model assessment revealed a greater level of uncertainty at shear zones, as well as for the $u_z$– component of velocity and TKE. Greater model uncertainty at shear zones is not unexpected, whilst the $u_z$–component of velocity and TKE has a higher sensitivity to mesh resolution. Both phenomena have previously been reported in the literature. Following assessment, the model scenarios were then designed to consider how flood conveyance over the floodplain is influenced by changes in vegetation patch size, flow rate, seasonality, and species morphotype. Future changes to vegetation patch size for the in-stream species *Sparganium erectum* and *Sparganium emersum* was based on observational data taken from the literature, where the same species were monitored for changes in abundance resulting from a warming climate over a 23-year period. Future changes to flow rate were based on the percentage change to peak flow for the year 2050 for two climate change projections which estimate an increase in global mean temperature by $2^0$c and $4^0$c by 2080. The results considered the mean floodplain values, flow phenomena at the submerged meander, and patch-scale flow phenomena. The mean flow summary showed increases in the mean floodplain free surface elevation, mean TKE, and decreases in the mean velocity for scenarios featuring a 30% increase in vegetation patch size when compared to scenarios with the same parameters but no increase in patch size. This difference in mean floodplain surface elevation increased with higher flow rates, indicating that scenarios with a higher vegetation abundance and a higher flow rate had a greater impact on flood magnitude. The proportional change to total flow elevation resulting from an increase in vegetation patch size was larger at lower flow rates but decreased as flow rate increased. This suggested that the impact of vegetation

abundance on flood levels was greater for less powerful flood events. These effects were consistent between both the summer and the autumn scenarios. The implication of this study is that the unchecked growth on in-stream vegetation resulting from a warmer climate will result in higher flood levels for both summer and the autumn. The greater change in mean flow elevation for autumnal flows showed that the autumn flood events would experience the greatest change in flood levels due to the co-occurrence of higher abundance of in-stream vegetation and a period of intensified flow. Vegetation appears to exert a greater control on flow conveyance at lower flow rates, highlighting the importance of incorporating vegetation management into strategies seeking to mitigate low impact, higher frequency flood events in the future. The results also imply that in-stream vegetation may also be used to selectively flood designated detention basins situated away from population centres. Such natural flood management schemes have become increasingly popular in the UK and may serve as a mechanism for mitigating against future river flooding.

The visualisations of floodplain flow showed phenomena at the vegetation-flow interface which had previously been reported in the literature. A jet-like flow pattern was apparent on the floodplain due to flow redirected from the channel immediately preceding the meander. The redirected flow exhibited increases in both the surface and near-surface velocity and penetrated further across the floodplain with increases in vegetation abundance, increases in flow rates, or increases in both. The flow region over the meander apex exhibited very low of negative velocity throughout the flow depth which was indicative of a recirculation zone. Increases in patch size resulted in a contiguous area of vegetation drag within the vegetation channel as the boundaries between vegetation patches became less distinct. This resulted in an increase in velocities at the near-bank region due to greater flow bifurcation. Seasonal differences were apparent: except for the highest flow condition, vegetation patches for summer scenarios exhibited a strong influence on surface flow which was not evident for the higher flow conditions during the autumn when all patches were submerged. These results suggest changes to in-stream vegetation is important for meander management: the high velocity, redirected flow may have geomorphological implications which threaten bank stability by exacerbating the development of a meander cut-off. Both velocity and the penetration depth of the jet-

like flow across the floodplain increased as flow rates and patch size were adjusted to reflect higher global mean temperatures, indicating that the effect of climate change on intensifying flow phenomena that result from vegetation-flow interactions may have important implications for geomorphological processes at meanders. The study contributed novel findings which detail flow processes which result from changing vegetation-flow interactions and their impact on flow behaviour on a submerged meander.

## 9.3. What is the impact of different vegetation morphologies on floodplain inundation under climate change?

Different species of macrophytes have associated morphotypes: three-dimensional geometries which describe the extent to which the vegetation biomass extends up and throughout the flow layers. Morphotypes can considerably alter how the vegetation biomass interacts with the surrounding flow. To identify how different species may affect changes in flood magnitudes and how they influence local flow profiles two different morphotypes representing the dominant in-stream species, *Sparganium erectum* and *Sparganium emersum*, were numerically represented within the mesh (Chapter 7, Section 7.3). To simulate how flow conveyance changes when the flow interacts with a given morphotype the study featured scenarios where increases in vegetation patch size only occurred for one of the dominant species, termed in this study as “morphotype-specific” scenarios. For a given morphotype-specific scenario two flow conditions were used which captured the lowest and highest estimated flow rates for the autumn season, which was the season with the highest peak flow. The results for mean floodplain surface elevation suggested that the trailing morphotype associated with the *S. emersum* species had a greater effect on increasing flood magnitudes than the uniform *S. erectum* species: increasing the channel cover of only the *S. emersum* patches increased mean surface elevations by 5.67% at the low flow condition, respective to the baseline. In the scenarios which featured an increase in only the *S.erectum* patches, the mean surface flow had no significant change from the baseline for the low flow condition. This effect appeared to be dependent on flow rates with both species having the same influence on mean surface elevation at the higher flow rate: both morphotype-specific scenarios featured an increase in mean elevation by 2.4% respective to the baseline. This

suggests that the importance of morphotypes may be crucial for understanding the interaction between vegetation and flood conveyance at lower flow rates. At the patch-scale the results described flow behaviour consistent with the literature for both morphotypes: flow deceleration occurred within the patch and immediately downstream for both patch morphotypes, flow acceleration occurred in the free flow region immediately above the upper canopy boundary, and a high Reynolds stress was evident along the upper canopy boundary but very low within the patch. Differences in the gradient and distribution of the above phenomena was evident: for the *S. erectum* morphotype, flow acceleration above the canopy boundary was the result of the flow continually being squeezed between the uniform patch boundary and the free surface. For *S. emersum,* flow acceleration on the upper boundary appeared to be more related to patch height, with a zone of high velocity occurring where the canopy peak interacted with the faster-flowing uninhibited flow region above the patch. Differences in the distribution of low velocity regions was also apparent: for the *S. erectum* morphotype, the zone of lowest velocity occurred close to the bed and within the patch immediately before the patch terminus. In contrast, for the *S. emersum* morphotype, the lowest velocity zone occurred outside of the patch immediately below the terminus of the lower canopy in a region sheltered from the main channel flow. These differences in velocity distribution resulted in different levels of shearing and turbulence generation between the two morphotypes. The local changes in velocity distribution were the result of differences in the vertical velocity gradient that developed between the two morphotypes: flow interacting with the vegetation was affected by the shape of the vegetation patch throughout the water column, indicating that the vegetation morphotype is an important control of the vertical velocity gradient. The cumulative effect on flow resulting from these different vegetation-flow interactions may explain some of the difference in mean surface elevation between morphotype-specific scenarios at lower flows. This study reveals that a dynamic interaction between different vegetation morphotypes and flow rate exists which determines the vegetative control exerted on flood conveyance. This suggests that an understanding of how different, three-dimensional vegetation morphotypes influence flow is critical for assessing the impact of in-stream vegetation have on flood events. In particular, the study suggests that rising global mean temperature and an associated increase in the abundance of

trailing vegetation morphotypes, such as *S. emersum*, will contribute to higher flood levels when compared to uniform morphotypes for flood events with flow rates similar to the low flow condition estimated from the $2^0$c climate change projection. With increases in global meant temperatures likely to exceed $1.5^0$c by 2050 the interaction reported in this study provides a foundation for river managers to anticipate how vegetation-flow interactions may shape flood events in the coming future. Key to understanding the role of in-stream vegetation as a flood control is the inclusion of patch geometries within numerical models which are representative of different morphotypes. The clear differences in effect between morphotypes for scenarios with low flow rates suggests that vegetation morphotypes are crucial to the understanding of how vegetation affect less extreme but more common flood events as a result of the future interaction between abundant in-stream vegetation and intensified flow rates.

## 9.4 Recommendation for future research

The results of this study have shown the importance of in-stream river vegetation as a control on future flood levels, revealing a new understanding on how changes to in-stream patch size and flow rates affects local flow phenomena and flood flow patterns under climate change. To expand this knowledge, further investigation into the simulating the influence of vegetation abundance and three-dimensional vegetation geometries, and the application of ecohydraulics tools for effective flood mitigation strategies under climate change are necessary.

For the former, more long-term reach-scale observational studies monitoring changes in the abundance of different macrophyte species is necessary to produce better informed assessments of the climatic impacts on vegetation-flood interactions. In the current state of the literature much of the focus has been given to broad national, multi-national, or supra-national changes in species distribution because of changes in the climate, however a dearth of observations is evident at the reach-scale. Observations detailing the changes in abundance for different in-stream vegetation would increase the accuracy with which future models can simulate increases in vegetation abundance. This would allow for changes in vegetation-flow interaction to better reflect those found in natural streams and anticipate scenarios helpful to flood mitigation strategists. Regarding three-dimensional patch profiles, the

model in this study made numerous assumptions as a result of uncertainty: a lack available information within the literature meant that the turbulence closure coefficients were assumed to the same as those for a standard $k - \varepsilon$ model. Porosity terms were neglected, and the effect of porosity was assumed to be captured by the bulk drag coefficient. However, the absence of a porosity term means that the model neglects spatial variation in vegetation blockage. Similarly, the vegetation profiles assumed no vegetation flexibility, with the effects of patch flexibility assumed negligible compared to the mesh resolution. Key to reducing uncertainties concerning flow resistance is research into flexible ins-stream vegetation: unlike some of the cases for rigid vegetation, studies concerned with detailing flow resistance for flexible vegetation focus on parameterising flow for individual morphotypes rather than deriving any law for flow resistance. The resulting literature has rendered meaningful comparisons difficult. However, research has shown the patch movement may impact overall vegetation drag and hence also effect the bulk vegetative drag coefficient. Research concerned with detailing flow resistance for flexible vegetation should work towards producing comprehensive guidance. Such guidance would need to relate vegetation geometry and biomechanical characteristics to changes in, for example, location, density, species, seasonality, and age. The high resolution required to classify vegetation in such a manner would require the development and application of remote sensing methods. Research into flexible vegetation must also consider plant dynamics, with more measurement required to identify the thresholds at which the influence of vegetation peaks. To do so, studies must consider how vegetation bend, breaks, or is wholly uprooted during flood conveyance. Additionally, studies must consider how the influence changes for both induvial plants and for patches.  More broadly, the inclusion of more, different morphotypes for vegetation species with known high hydraulic resistances would better inform guidance for river management strategies concerned with weed cutting. In this study the changes in patch distribution reflected those observed between seasons, however including different patch patterns as a scenario variable would likely elicit different responses in flood magnitude. A better understanding of the uncertainties affecting changes to flood levels may also be obtained by increasing the number of scenarios to generate an ensemble which captures a larger diversity of increases to flow rates, increases to vegetation cover, and different years.

Relating the flow scenarios to return years would also help quantify an approximation of flood risk. More research is required at liminal systems, such as the floodplain-bank interface to better understand how the presence of vegetation alters mass transfer between both regions, and which may impact the viability of floodplain detention zones. Vegetation patch patterns also influence flood levels by how they alter flow conveyance. Different patch patterns were not explored in this study, however the dominance of a given morphotype can change after vegetation die-back and therefore change flood response over time scales longer than a year. As different plant species exhibit varying responses to changes in mean temperature, how patches will be altered by future climate change is also important for understanding the overall changes to future flood conveyance. Thus, introducing different patch patterns as a variable is key for reducing the uncertainties surrounding the mitigative impacts of vegetation. Doing so may help practitioners understand the uncertainties in effective flood mitigation for a given vegetation abundance. Importantly, the interaction between vegetation and flow is more than a two-way phenomena, it is part of a complex, dynamic system interrelated with sediment transport and geomorphology (Tsujimoto,1999). However, the interactions between vegetation, sediment transport, and geomorphology remain poorly understood (D'Ippolito et al., 2021). Multi-disciplinary approaches invoking environmental engineering, climatology, hydraulics, hydrology, and geomorphology are thus necessary for exploring fields of research concerned with changes to flow resistance in relation to feedback cycles which vary across time and space. Understanding their interaction and the subsequent on flood flow conveyance requires input from multiple disciplines investigating complex feedback systems which vary through time and space. Whilst this study has attempted to elucidate the connection between hydrological, ecological, and climatic disciplines other research investigating in-stream vegetation and sediment transport, erosion, and deposition suggests there is an opportunity to develop a more comprehensive assessment of climate change impacts on river flooding through the inclusion of geomorphological processes.

Finally, it would be useful for flood management strategies to consider entire hydrographs to understand how differences in vegetation coverage and morphotype influences flow conveyance throughout the entire duration of a flood event where this

study considered the effect of vegetation-flow interactions on peak flow and described the resulting effect during flood maxima. Because the influence of a given abundance of in-stream vegetation on flood magnitude changes depending on the flow rate, expanding the range of scenarios to encompass different event thresholds would allow for river managers to better anticipate flood flow behaviour. Thresholds are currently used by the UK government and environmental organisations to advise on the implementation of measures for flood mitigation and adaption. For example, flood risk assessments for building constructions in areas which have a flood probability of 1 in 100 years should ability and above should use low permeable building materials for floodwaters below 0.3m. Exceeding this threshold requires additional measures to be implemented, such as resilient materials or “flood-proof” designs for electrical components (EA, 2014). Therefore, identifying how much changes in the abundance of vegetation patches may influence floodwaters to exceed these thresholds would help provide better understanding of the mitigative services provided in-stream vegetation, allowing practitioners to anticipate when this service provision would be most effective. Thresholds may take for form of numerous parameters such as risk to life and livelihood, ecological and environmental change with further consideration of possible geomorphological implications, or financial cost. Implementing thresholds for financial cost may, for example, help practitioners understand how effective in-stream vegetation could be as a flood mitigation tool when looking to avoid undesirable trade-offs between flood risk and mitigations costs. Knowing when flood magnitudes exceed the mitigative potential of in-stream vegetation may inform how river managers implement riparian flood detention measures; understanding both the local hydrometeorological context and morphotype of in-stream vegetation can inform the number and capacity of detention zones on the floodplain. This would also necessitate further research to understand the implications of other mitigative environmental provisions whose processes overlap with in-stream flow-vegetation dynamics. This provide further insight into how different environmental solutions interact; decreasing the abundance of in-stream vegetation may produce diminishing returns where the detrimental ecological effects outweigh the costs of a given flood threshold. A threshold-based approach would also be suitable for verifying the performance of both flow conveyance models and river management strategies, such as in the case of reproducing historical

flooding, allowing for the design of risk reduction methods. For example, simulating historical events with different in-stream vegetation abundances may show how flood levels could be exacerbated when abundances are increased in the local region, whilst describing how said levels might be reduced if vegetation is introduced upstream.

# Bibliography

Aberle, J. and Järvelä, J. (2013) ‘Flow resistance of emergent rigid and flexible floodplain vegetation’, *Journal of Hydraulic Research*, 51(1), pp. 33–45. doi: 10.1080/00221686.2012.754795.

Aberle, J. and Järvelä, J. (2015) ‘Hydrodynamics of vegetated channels’, in *GeoPlanet: Earth and Planetary Sciences*. Springer Verlag, pp. 519–541. doi: 10.1007/978-3-319-17719-9_21.

Alahuhta, J., Heino, J. and Luoto, M. (2011) ‘Climate change and the future distributions of aquatic macrophytes across boreal catchments’, *Journal of Biogeography*, 38(2), pp. 383–393. doi: 10.1111/j.1365-2699.2010.02412.x.

Albayrak, I. *et al.* (2012) ‘Flow-plant interactions at a leaf scale: Effects of leaf shape, serration, roughness and flexural rigidity’, *Aquatic Sciences*, 74(2), pp. 267–286. doi: 10.1007/s00027-011-0220-9.

Albertson, M. L., Simons, D. B. and Barton, J. R. (1960) *Fluid mechanics for engineers*. Prentice Hall.

Allan, R. P. (2011) ‘Climate change: Human influence on rainfall’, *Nature*. Nature Publishing Group, pp. 344–345. doi: 10.1038/470344a.

Allaoui, N. El *et al.* (2015) ‘Modified hydrodynamics in canopies with longitudinal gaps exposed to oscillatory flows’, *Journal of Hydrology*.

Allen, M. R. *et al.* (2009) ‘Warming caused by cumulative carbon emissions towards the trillionth tonne’, *Nature*. Nature Publishing Group, 458(7242), pp. 1163–1166. doi: 10.1038/nature08019.

Anjum, N. *et al.* (2018) ‘To Investigate the Flow Structure of Discontinuous Vegetation Patches of Two Vertically Different Layers in an Open Channel’, *Water*.

doi: 10.3390/w10010075.

Armanini, A., Righetti, M. and Grisenti, P. (2005) ‘Direct measurement of vegetation resistance in prototype scale’, *Journal of Hydraulic Research*. International Association of Hydraulic Engineering Research, 43(5), pp. 481–487. doi: 10.1080/00221680509500146.

ASME (1993) ‘Journal of Fluids Engineering editorial policy statement on the control of numerical accuracy.’, *ASME Journal of Fluids Engineering*, 115(399).

Augustin, L. N., Irish, J. L. and Lynett, P. (2008) ‘Laboratory and numerical studies of wave damping by emergent and near-emergent wetland vegetation’, *Coastal Engineering*, 56, pp. 332–340. doi: 10.1016/j.coastaleng.2008.09.004.

Baattrup-Pedersen, A. *et al.* (2006) ‘Macrophyte communities in unimpacted European streams: variability in assemblage patterns, abundance and diversity’, *Springer*, 566(1), pp. 179–196. doi: 10.1007/s10750-006-0096-1.

Bai, K., Katz, J. and Meneveau, C. (2015) ‘Turbulent Flow Structure Inside a Canopy with Complex Multi-Scale Elements’, *Boundary-Layer Meteorology*. Kluwer Academic Publishers, 155(3), pp. 435–457. doi: 10.1007/s10546-015-0011-2.

Bal, K. *et al.* (2011) ‘How do macrophyte distribution patterns affect hydraulic resistances?’, *Ecological Engineering*.

Bal, K. and Meire, P. (2009) ‘The influence of macrophyte cutting on the hydraulic resistance of lowland rivers’, *Journal of Aquatic Plant Management*.

Baptist, M. J. *et al.* (2007) ‘On inducing equations for vegetation resistance’, *Journal of Hydraulic Research*. International Association of Hydraulic Engineering Research, 45(4), pp. 435–450. doi: 10.1080/00221686.2007.9521778.

Barrat-Segretain, M. H. (1996) ‘Strategies of reproduction, dispersion, and competition in river plants: A review’, *Vegetatio*. Springer Netherlands, pp. 13–37.

doi: 10.1007/BF00044885.

Barrett, P. R. F., Greaves, M. P. and Newman, J. R. (1999) *Aquatic weed control operation. Best practice guidelines*. Environment Agency.

Barrow, E. and Hulme, M. (2014) *Climates of the British Isles: present, past and future*. Routledge.

Beck, H. E. *et al.* (2013) 'Global patterns in base flow index and recession based on streamflow observations from 3394 catchments', *Water Resources Research*. John Wiley & Sons, Ltd, 49(12), pp. 7843–7863. doi: 10.1002/2013WR013918.

Bennett, O. and Hartwell-Naguib, S. (2014) 'Flood defence spending in England', *House of Commons Library: Science and Environment.*

Bennett, S. J., Pirim, T. and Barkdoll, B. D. (2002) 'Using simulated emergent vegetation to alter stream flow direction within a straight experimental channel', *Geomorphology*. Elsevier, 44(1–2), pp. 115–126. doi: 10.1016/S0169-555X(01)00148-9.

Van den Berg, B. (1975) 'A three-dimensional law of the wall for turbulent shear flows', *Journal of Fluid Mechanics*.

Berger, C. J., Wells, S. A. and Asce, M. (2008) 'Modeling the Effects of Macrophytes on Hydrodynamics', *Journal of Environmental Engineering*. doi: 10.1061/ASCE0733-93722008134:9778.

Bertola, M. *et al.* (2020) 'Flood trends in Europe: are changes in small and big floods different?', *Hydrology and Earth System Sciences*. doi: 10.5194/hess-2019-523.

Berz, G. *et al.* (2001) 'World map of natural hazards - a global view of the distribution and intensity of significant exposures', *Natural Hazards*. Springer, 23(2–3), pp. 443–465. doi: 10.1023/A:1011193724026.

Bilskie, M. V. and Hagen, S. C. (2013) 'Topographic accuracy assessment of bare

earth lidar-derived unstructured meshes', *Advances in Water Resources*. Elsevier, 52, pp. 165–177. doi: 10.1016/j.advwatres.2012.09.003.

Birnir, B. (2008) 'Turbulent rivers', *Quarterly of applied mathematics*.

Biron, P. M. *et al.* (2007) 'Assessing different methods of generating a three-dimensional numerical model mesh for a complex stream bed topography', *International Journal of Computational Fluid Dynamics*. Taylor & Francis Group , 21(1), pp. 37–47. doi: 10.1080/10618560701374411.

Blevins, R. (2003) *Applied fluid dynamics handbook*. Krieger Publishing Company, USA.

Bloomfield, J. P., Allen, D. J. and Griffiths, K. J. (2009) 'Examining geological controls on baseflow index (BFI) using regression analysis: An illustration from the Thames Basin, UK', *Journal of Hydrology*. Elsevier, 373(1–2), pp. 164–176. doi: 10.1016/j.jhydrol.2009.04.025.

Blöschl, G. *et al.* (2019) 'Changing climate both increases and decreases European river floods', *Nature*. Nature Publishing Group, 573(7772), pp. 108–111. doi: 10.1038/s41586-019-1495-6.

Boerema, A. *et al.* (2014) 'Economic valuation of ecosystem services, a case study for aquatic vegetation removal in the Nete catchment (Belgium)', *Ecosystem Services*, 7, pp. 46–56. doi: 10.1016/j.ecoser.2013.08.001.

Boothroyd, R. J. *et al.* (2016) 'The importance of accurately representing submerged vegetation morphology in the numerical prediction of complex river flow', *Earth Surface Processes and Landforms*. John Wiley and Sons Ltd, pp. 567–576. doi: 10.1002/esp.3871.

Boothroyd, R. J. *et al.* (2017) 'Modeling complex flow structures and drag around a submerged plant of varied posture', *Water Resources Research*. Blackwell Publishing Ltd, 53(4), pp. 2877–2901. doi: 10.1002/2016WR020186.

Bouma, T. J. *et al.* (2005) ‘Trade-offs related to ecosystem engineering: A case study on stiffness of emerging macrophytes’, *Ecology*. Ecological Society of America, 86(8), pp. 2187–2199. doi: 10.1890/04-1588.

Le Bouteiller, C. and Venditti, J. G. (2015) ‘Sediment transport and shear stress partitioning in a vegetated flow’, *Water Resources Research*. Blackwell Publishing Ltd, 51(4), pp. 2901–2922. doi: 10.1002/2014WR015825.

Bradshaw, P. and Huang, G. P. (1995) ‘The law of the wall in turbulent flow’, *Proceedings - Royal Society of London, A*, 451(1941), pp. 165–188. doi: 10.1098/rspa.1995.0122.

Braudrick, C. A. *et al.* (2009) *Experimental evidence for the conditions necessary to sustain meandering in coarse-bedded rivers*, *PNAS October*.

Bravard, J. and Petit, F. (2009) *Geomorphology of Streams and Rivers*, *Encyclopedia of Inland Waters*.

Broad, K. (2015) *Caring for small woods*.

Burke, R. and Stolzenbach, K. (1983) *Free surface flow through salt marsh grass*.

Burnett, H. S. (2007) *Climate Change: Consensus Forming around Adaptation*, *ncpathinktank.org*..

Busari, A. O. and Li, C. W. (2016) ‘Bulk drag of a regular array of emergent blade-type vegetation stems under gradually varied flow’, *Journal of Hydro-Environment Research*. Elsevier B.V., 12, pp. 59–69. doi: 10.1016/j.jher.2016.02.003.

Chanson, H. (2006) *Environmental Hydraulics of Open Channel Flows*, *Cambridge University Press*.

Chappuis, E., Gacia, E. and Ballesteros, E. (2014) ‘Environmental factors explaining the distribution and diversity of vascular aquatic macrophytes in a highly heterogeneous Mediterranean region’, *Aquatic Botany*.

Chen, Z. *et al.* (2012) ‘The wake structure behind a porous obstruction and its implications for deposition near a finite patch of emergent vegetation’, *researchgate.net*, 48(9). doi: 10.1029/2012WR012224.

Cheng, N.-S. *et al.* (2011) ‘Evaluation of Flow Resistance in Smooth Rectangular Open Channels with Modified Prandtl Friction Law’, *ascelibrary.org*. American Society of Civil Engineers (ASCE), 137(4), pp. 441–450. doi: 10.1061/(ASCE)HY.1943-7900.0000322.

Cheng, N.-S. (2013) ‘Calculation of Drag Coefficient for Arrays of Emergent Circular Cylinders with Pseudofluid Model’, *Journal of Hydraulic Engineerin*. doi: 10.1061/(ASCE)HY.1943-7900.0000722.

Cheng, N. S. (2011) ‘Representative roughness height of submerged vegetation’, *Water Resources Research*, 47(8). doi: 10.1029/2011WR010590.

Cheng, N. S. and Nguyen, H. T. (2011) ‘Hydraulic radius for evaluating resistance induced by simulated emergent vegetation in open-channel flows’, *Journal of Hydraulic Engineering*, 137(9), pp. 995–1004. doi: 10.1061/(ASCE)HY.1943-7900.0000377.

Chirol, C. *et al.* (2015) ‘The Influence of Bed Roughness on Turbulence: Cabras Lagoon, Sardinia, Italy’, *Journal of Marine Science and Engineering*.

Choi, S.-U. and Kang, H. (2004) ‘Reynolds stress modeling of vegetated open-channel flows’, *Journal of Hydraulic Research*. International Association of Hydraulic Engineering Research, 42(1), pp. 3–11. doi: 10.1080/00221686.2004.9641178.

Chow, V. (1959) ‘Open-channel hydraulics’, *McGraw-Hill civil engineering series*.

Christensen, J. and Christensen, O. (2003) ‘Severe summertime flooding in Europe’, *Nature*.

Clarke, A. *et al.* (2007) *River Blackwater Flood Study: Final Flood mapping Report*.

Conner, J. T. and Tonina, D. (2014) ‘Effect of cross-section interpolated bathymetry on 2D hydrodynamic model results in a large river’, *Earth Surface Processes and Landforms*. John Wiley and Sons Ltd, 39(4), pp. 463–475. doi: 10.1002/esp.3458.

Cotton, J. *et al.* (2006) ‘The effects of seasonal changes to in-stream vegetation cover on patterns of flow and accumulation of sediment’, *Geomorphology*.

D’ippolito, A. *et al.* (2021) ‘Flow resistance in open channel due to vegetation at reach scale: A review’, *Water (Switzerland)*. MDPI AG, p. 116. doi: 10.3390/w13020116.

Darby, S. E. (1999) ‘Effect of Riparian Vegetation on Flow Resistance and Flood Potential’, *Journal of Hydraulic Engineering*, 125(5), pp. 443–454. doi: 10.1061/(ASCE)0733-9429(1999)125:5(443).

Deconinck, H., Ricchiuto, M. and Sermeus, K. (2003) ‘Introduction to residual distribution schemes and comparison with stabilized finite elements’, *3rd Computational Fluid Dynamics Course, von Karman Institute for Fluid Dynamics (2003)*.

Dhir, B. (2015) ‘Status of Aquatic Macrophytes in Changing Climate: A Perspective’, *Article in Journal of Environmental Science and Technology*. doi: 10.3923/jest.2015.139.148.

Dingman, S. (2009) *Fluvial hydraulics*.

de Doncker, L. *et al.* (2009) ‘Relation between resistance characteristics due to aquatic weed growth and the hydraulic capacity of the river AA’, *River Research and Applications*, 25(10), pp. 1287–1303. doi: 10.1002/rra.1240.

De Doncker, L. *et al.* (2009) ‘Determination of the Manning roughness coefficient influenced by vegetation in the river Aa and Biebrza river’, *Environmental Fluid Mechanics*, 9, pp. 549–567. doi: 10.1007/s10652-009-9149-0.

De Doncker, L. *et al.* (2011) ‘Deriving the relationship among discharge, biomass and Manning’s coefficient through a calibration approach’, *Hydrological Processes*. John Wiley & Sons, Ltd, 25(12), pp. 1979–1995. doi: 10.1002/hyp.7978.

Downton, M. W. and Pielke, R. A. (2001) ‘Discretion without Accountability: Politics, Flood Damage, and Climate’, *Natural Hazards Review*. American Society of Civil Engineers (ASCE), 2(4), pp. 157–166. doi: 10.1061/(asce)1527-6988(2001)2:4(157).

Džigurski, D. *et al.* (2015) ‘Impact of climate changes on aquatic vegetation of hydromeliorative facilities’, *Contemporary Problems of Ecology*. Maik Nauka Publishing / Springer SBM, 8(3), pp. 295–308. doi: 10.1134/S1995425515030063.

Eça and Hoekstra (2014) ‘A procedure for the estimation of the numerical uncertainty of CFD calculations based on grid refinement studies’, *Journal of computational physics*.

Eça, L., Vaz, G. and Hoekstra, M. (2014) ‘Code Verification of ReFRESCO with a statistically periodic manufactured solution’, in *ASME 2014 33rd International Conference on Ocean, Offshore and Arctic Engineering*.

Ekström, M. *et al.* (2005) ‘New estimates of future changes in extreme rainfall across the UK using regional climate model integrations. 2. Future estimates and use in impact studies’, *Journal of Hydrology*. Elsevier, 300(1–4), pp. 234–251. doi: 10.1016/j.jhydrol.2004.06.019.

Environment Agency (2009) *Flooding in England: A National Assessment of Flood Risk*.

Environment Agency (2011) *Adapting to Climate Change: Advice for Flood and Coastal Erosion Risk Management Authorities Advice for Flood and Coastal Erosion Risk Management Authorities Adapting to Climate Change*.

Environment Agencey (2012) *Flood risk and coastal change.*

Etminan, V., Ghisalberti, M. and Lowe, R. J. (2018) ‘Predicting Bed Shear Stresses in Vegetated Channels’, *Water Resources Research*. Blackwell Publishing Ltd, 54(11), pp. 9187–9206. doi: 10.1029/2018WR022811.

Evans, E. *et al.* (2004) *Future Flooding. Scientific Summary: Volumes I and II.* | *ECONADAPT Library*.

Fathi-Maghadam, B. M. and Kouwen, N. (1997) ‘Nonrigid, nonsubmerged, vegetative roughness on floodplains’, *Journal of Hydraulic Engineering*. doi: 10.1061/(ASCE)0733-9429(1997)123.

Feijoó, C. S. *et al.* (1996) ‘Factors influencing biomass and nutrient content of the submersed macrophyte Egeria densa Planch. in a pampasic stream’, *Hydrobiologia*. Kluwer Academic Publishers, 341(1), pp. 21–26. doi: 10.1007/bf00012299.

Fenzl, R. N. (1962) *Hydraulic resistance of broad shallow vegetated channels*. University of California.

Ferguson, R. I. *et al.* (2003) ‘Flow in meander bends with recirculation at the inner bank’, *Water Resources Research*. American Geophysical Union, 39(11), p. 1322. doi: 10.1029/2003WR001965.

Field, C. *et al.* (2012) *Managing the risks of extreme events and disasters to advance climate change adaptation: special report of the intergovernmental panel on climate change*. Cambridge University Press.

Finnigan, J. (2000) ‘Turbulence in plant canopies’, *Annual review of fluid mechanics*.

Fischbacher-Smith, D. (2010) ‘Beyond the worst case scenario: Managing the risks of extreme events’, *Risk Management*. Palgrave, pp. 1–8. doi: 10.1057/rm.2009.17.

Fischenich, C. and Dudley, S. (2000) *Determining drag coefficients and area for vegetation. Ecosytem Management & Restoration Research Program SR 08*.

Fischer-Antze, T., Stoesser, T. and Olsen, N. R. B. (2001) ‘Modélisation numérique

3D d’un écoulement en canal avec végétation submergée’, *Journal of Hydraulic Research*. International Association of Hydraulic Engineering Research, 39(3), pp. 303–310. doi: 10.1080/00221680109499833.

Flood and Coastal Erosion Risk Management Research and Development Programme (2021) *Counting the cost of flooding*.

Folkard, A. M. (2011) ‘Vegetated flows in their environmental context: a review’, *Proceedings of the Institution of Civil Engineers Engineering and Computational Mechanics*, 164(1), pp. 1–3. doi: 10.1680/eacm.8.00006.

Follett, E. M. and Nepf, H. M. (2012) ‘Sediment patterns near a model patch of reedy emergent vegetation’, *Geomorphology*. Elsevier, 179, pp. 141–151. doi: 10.1016/j.geomorph.2012.08.006.

Fonseca, M. S. *et al.* (1982) ‘Influence of the seagrass, Zostera marina L., on current flow’, *Estuarine, Coastal and Shelf Science*. Academic Press, 15(4), pp. 351–364. doi: 10.1016/0272-7714(82)90046-4.

Fowler, H. and Wilby, R. (2010) ‘Detecting changes in seasonal precipitation extremes using regional climate model projections: Implications for managing fluvial flood risk’, *Water Resources Research*.

Franklin, P., Dunbar, M. and Whitehead, P. (2008) ‘Flow controls on lowland river macrophytes: A review’, *Science of the Total Environment*. Elsevier, pp. 369–378. doi: 10.1016/j.scitotenv.2008.06.018.

Freeman, G. E., Rahmeyer, W. H. and Copeland, R. R. (2000) *Determination of Resistance Due to Shrubs and Woody Vegetation Coastal and Hydraulics Laboratory*, *This Digital Resource was created from scans of the Print Resource*. Coastal and Hydraulics Laboratory (U.S.).

Gac, J. M. (2014) ‘A large eddy based lattice-Boltzmann simulation of velocity distribution in an open channel flow with rigid and flexible vegetation’, *Acta*

*Geophysica*, 62(1), pp. 180–198. doi: 10.2478/s11600-013-0178-1.

Galland, J., Goutal, N. and Hervouet, J. (1991) 'TELEMAC: A new numerical model for solving shallow water equations', *Advances in Water Resources*.

Georgiadis, N. J., Rizzetta, D. P. and Fureby, C. (2010) 'Large-eddy simulation: Current capabilities, recommended practices, and future research', *AIAA Journal*, 48(8), pp. 1772–1784. doi: 10.2514/1.J050232.

Gessner, F. (1955) *Hydrobotanik I. Energiehaushalt.* Berlin: Deutsch Ver. Wissensch., Berlin.

Getsinger, K. D., Madsen, J. D. and Koschnick, T. J. (2002) *Whole lake fluridone treatments for selective control of Eurasian watermilfoil: I. Application strategy and herbicide residues*, *J. Aquat. Plant Manage*.

Ghisalberti, M. and Nepf, H. (2009) 'Shallow flows over a permeable medium: The hydrodynamics of submerged aquatic canopies', *Transport in Porous Media*. Springer, 78(2), pp. 309–326. doi: 10.1007/s11242-008-9305-x.

Green, J. (2006) 'Effect of macrophyte spatial variability on channel resistance', *Advances in Water Resources*.

Green, J. C. (2005a) 'Comparison of blockage factors in modelling the resistance of channels containing submerged macrophytes', *River Research and Applications*. John Wiley & Sons, Ltd, 21(6), pp. 671–686. doi: 10.1002/rra.854.

Green, J. C. (2005b) 'Modelling flow resistance in vegetated streams: Review and development of new theory', *Hydrological Processes*. John Wiley & Sons, Ltd, 19(6), pp. 1245–1259. doi: 10.1002/hyp.5564.

Grīnberga, L. and Spriņge, G. (2008) 'Potential Impact of Climate Change on Aquatic Vegetation of River Salaca, Latvia Section B Natural, exact, and applied sciences', *Proceedings of the Latvian Academy of Sciences*.

Gunawan *et al.* (2008) *An Integrated And Novel Approach To Estimating The Conveyance Capacity Of  The River Blackwater*, *Citeseer*.

Gurnell, A. (2013) 'State of Science Plants as river system engineers', *Wiley Online Library*. John Wiley and Sons Ltd, 39(1), pp. 4–25. doi: 10.1002/esp.3397.

Gurnell, A., Bertoldi, W. and Corenblit, D. (2012) 'Changing river channels: The roles of hydrological processes, plants and pioneer fluvial landforms in humid temperate, mixed load, gravel bed rivers', *Earth-Science Reviews*.

Hamed, A. M. *et al.* (2017) 'Impact of height heterogeneity on canopy turbulence', *Journal of Fluid Mechanics*. Cambridge University Press, 813, pp. 1176–1196. doi: 10.1017/jfm.2017.22.

Hamimed, A. *et al.* (2013) *Contribution to the study of the flow resistance in a flume with artificial emergent vegetation*, *Larhyss Journal*.

Hannaford, J. (2015) 'Climate-driven changes in UK river flows: A review of the evidence', *Progress in Physical Geography*. SAGE Publications Ltd, 39(1), pp. 29–48. doi: 10.1177/0309133314536755.

Hannaford, J. and Buys, G. (2012) 'Trends in seasonal river flow regimes in the UK', *Journal of Hydrology*.

Hannaford, J. and Marsh, T. J. (2008) 'High-flow and flood trends in a network of undisturbed catchments in the UK', *international journal of climatology*, 28(10), pp. 1325–1338. doi: 10.1002/joc.1643.

Hardy, R. J. *et al.* (2009) 'Coherent flow structures in a depth-limited flow over a gravel surface: The role of near-bed turbulence and influence of Reynolds number', *Journal of Geophysical Research: Earth Surface*. Blackwell Publishing Ltd, 114(1), p. 1003. doi: 10.1029/2007JF000970.

Haslam, S. . (2006) *River Plants:  The Macrophytic Vegetation of Watercourses*,

*Forrest Text, Cardigan.* Forrest Text, Cardigan.

Heikkinen, R. K. *et al.* (2009) ‘Predicting distribution patterns and recent northward range shift of an invasive aquatic plant: Elodea canadensis in Europe Biodiversity & Ecosystem Risk Assessment’, *BioRisk*, 2, pp. 1–32. doi: 10.3897/biorisk.2.4.

Helmiö, T. (2004) ‘Flow resistance due to lateral momentum transfer in partially vegetated rivers’, *Wiley Online Library*. American Geophysical Union, 40(5), p. 5206. doi: 10.1029/2004WR003058.

Hervouet, J.M. and Jankowski, J., (2000). "Comparing numerical simulations of free surface flows using non-hydrostatic Navier–Stokes and Boussinesq equations". *Electricité de France, Groupe Hydraulique Fluviale, Division Recherche et Développement/Institut für Strömungsmechanik im Bauwesen der Universität Hannover (unveröffentlicht)*, *182*.

Hervouet, J.-M., Pavan, S. and Ricchiuto, M. (2017) *Residual distribution advection schemes in TELEMAC*.

Hervouet, J., Pavan, S. and Ata, R. (2015) ‘Distributive advection schemes and dry zones, new solutions’, in *Proceedings of the XXII TELEMAC-MASCARET Technical User Conference October 15-16, 2016*.

Hickin, E. (2004) ‘The nature of turbulence and velocity distributions in rivers’, *River Hydraulics and Channel Form*.

Horritt, M. S. (2006) ‘A methodology for the validation of uncertain flood inundation models’, *Journal of Hydrology*. Elsevier, 326(1–4), pp. 153–165. doi: 10.1016/j.jhydrol.2005.10.027.

Horritt, M. S., Bates, P. D. and Mattinson, M. J. (2006) ‘Effects of mesh resolution and topographic representation in 2D finite volume models of shallow water fluvial flow’, *Journal of Hydrology*. Elsevier, 329(1–2), pp. 306–314. doi: 10.1016/j.jhydrol.2006.02.016.

Horstman, E. M. *et al.* (2018) ‘Are flow-vegetation interactions well represented by mimics?  A case study of mangrove pneumatophores’, *Advances in water resources*.

Huai, W. xin *et al.* (2019) ‘The structure of turbulent flow through submerged flexible vegetation’, *Journal of Hydrodynamics*. Springer International Publishing, 31(2), pp. 274–292. doi: 10.1007/s42241-019-0023-3.

Huntington, K. W., Blythe, A. E. and Hodges, K. V. (2006) ‘Climate change and Late Pliocene acceleration of erosion in the Himalaya’, *Earth and Planetary Science Letters*. Elsevier, 252(1–2), pp. 107–118. doi: 10.1016/j.epsl.2006.09.031.

Huthoff, F., Augustijn, D. C. M. and Hulscher, S. J. M. H. (2007) ‘Analytical solution of the depth-averaged flow velocity in case of submerged rigid cylindrical vegetation’, *Water Resources Research*. John Wiley & Sons, Ltd, 43(6), p. 6413. doi: 10.1029/2006WR005625.

IPCC (2007) *Climate change 2007. Impacts, adaptation and vulnerability. Contribution of Working Group II to the fourth assessment report of the Intergovernmental Panel on Climate Change*.

IPCC (2013) *Climate Change 2013: The Physical Science Basis. Contribution of Working Group I to the Fifth Assessment Report of the Intergovernmental Panel on Climate Change*.

IPCC (2014) *Climate Change 2014 Impacts, Adaptation, and Vulnerability Part A: Global and Sectoral Aspects Working Group II Contribution to the Fifth Assessment Report of the Intergovernmental Panel on Climate Change Edited by*. Edited by C. B. Field et al.

James, C., *et al.* (2004) ‘Flow resistance of emergent vegetation’, *Journal of Hydraulic Research*.  Taylor & Francis Group , 42(4), pp. 390–398. doi: 10.1080/00221686.2004.9641206.

Järvelä, J. (2002) ‘Determination of flow resistance of vegetated channel banks and

floodplains', *River Flow*.

Järvelä, Juha (2002) 'Flow resistance of flexible and stiff vegetation: A flume study with natural plants', in *Journal of Hydrology*. Elsevier, pp. 44–54. doi: 10.1016/S0022-1694(02)00193-2.

Järvelä, J. (2003) 'Influence of vegetation on flow structure in floodplains and wetlands', in *Proceedings of the 3rd IAHR Symposium on River, Coastal and Estuarine Morphodynamics*. International Association of Hydraulic Engineering and Research (IAHR), pp. 845–856.

Jeffres, C., Buckland, E. and Kiernan, J. (2007) 'Baseline Assessment of Salmonid Habitat and Aquatic Ecology of the Nelson Ranch, Shasta River, California–Water Year 2007', *Prepared for the U.S. Bureau of Reclamation and the California Nature Conservancy. U.C. Davis and Watercourse Engineering, Inc.*

Jiang, B., Yang, K. and Cao, S. (2015) 'An analytical model for the distributions of velocity and discharge in compound channels with submerged vegetation', *PLoS ONE*. Public Library of Science, 10(7). doi: 10.1371/journal.pone.0130841.

Jones, P. *et al.* (2010) *UK Climate Projections science report: Projections of future daily climate for the UK from the Weather Generator*. UK Climate Impacts Programme.

Jones, P. D. and Reid, P. A. (2001) 'Assessing future changes in extreme precipitation over britain using regional climate model integrations', *International Journal of Climatology*, 21(11), pp. 1337–1356. doi: 10.1002/joc.677.

Kadlec, R. H. (1990) 'Overland Flow in Wetlands: Vegetation Resistance', *Journal of Hydraulic Engineering*. American Society of Civil Engineers (ASCE), 116(5), pp. 691–706. doi: 10.1061/(asce)0733-9429(1990)116:5(691).

Kay, A. *et al.* (2011) 'Attribution of Autumn/Winter 2000 flood risk in England to anthropogenic climate change: A catchment-based study', *Journal of Hydrology*.

Kay, A. L. and Jones, D. A. (2012) ‘Transient changes in flood frequency and timing in Britain under potential projections of climate change’, *INTERNATIONAL JOURNAL OF CLIMATOLOGY Int. J. Climatol*, 32(4), pp. 489–502. doi: 10.1002/joc.2288.

Kharin, V. V. and Zwiers, F. W. (2005) ‘Estimating extremes in transient climate change simulations’, *Journal of Climate*, 18(8), pp. 1156–1173. doi: 10.1175/JCLI3320.1.

Kharin, V. V., Zwiers, F. W. and Zhang, X. (2005) ‘Intercomparison of near-surface temperature and precipitaion extremes in AMIP-2 simulations, reanalyses, and observations’, *Journal of Climate*. American Meteorological Society, 18(24), pp. 5201–5223. doi: 10.1175/JCLI3597.1.

Kim, T. B. and Choi, S. U. (2009) ‘Depth-averaged modeling of vegetated open-channel flows using finite element’, in *Advances in Water Resources and Hydraulic Engineering - Proceedings of 16th IAHR-APD Congress and 3rd Symposium of IAHR-ISHS*. Springer-Verlag Berlin Heidelberg, pp. 411–416. doi: 10.1007/978-3-540-89465-0_72.

King, Alexandra T *et al.* (2012) ‘A k-ε turbulence model based on the scales of vertical shear and stem wakes valid for emergent and submerged vegetated flows’, *Journal of Fluid Mechanics*. Cambridge University Press, 701, p. 1. doi: 10.1017/jfm.2012.113.

Kjeldsen, T. (2011) ‘COST Action ES0901: European procedures for flood frequency estimation (FloodFreq)’, *Geophysical Research Abstracts*.

Kjeldsen, T. R., Svensson, C. and Miller, J. M. (2012) *Hydrology for a changing world*, *BHS Eleventh National Symposium*..

Kothyari, U. C., Hashimoto, H. and Hayashi, K. (2009) ‘Effect of Vegetation on Sediment Transport by Stream Flow.’, in *Proceedings of the International Conference on Water, Environment, Energy and Society (WEES-2009)*. Allied

Publishers Pvt. Limited, New Delhi.

Kothyari, U. C., Hayashi, K. and Hashimoto, H. (2009) ‘Drag coefficient of unsubmerged rigid vegetation stems in open channel flows’, *Journal of Hydraulic Research*. Taylor & Francis Group , 47(6), pp. 691–699. doi: 10.3826/jhr.2009.3283.

Kouwen, N. and Li, R. (1980) ‘Biomechanics of vegetative channel linings’, *Journal of the Hydraulics Division*.

Kouwen, N. and Unny, T. (1973) ‘Flexible roughness in open channels’, *Journal of the Hydraulics Division*.

Kozdon, Jeremy Edward *et al.* (2011) ‘Multidimensional upstream weighting for multiphase transport in porous media’, *Comput Geosci*, 15(3), pp. 399–419. doi: 10.1007/s10596-010-9211-5.

Kummu, M. *et al.* (2011) ‘How close do we live to water? a global analysis of population distance to freshwater bodies’, *PLoS ONE*. Public Library of Science, 6(6), p. e20578. doi: 10.1371/journal.pone.0020578.

Lacy, J. R. and Wyllie-Echeverria, S. (2011) ‘The influence of current speed and vegetation density on flow structure in two macrotidal eelgrass canopies’, *Limnology and Oceanography: Fluids and Environments*. Wiley-Blackwell, 1(1), pp. 38–55. doi: 10.1215/21573698-1152489.

Lane, S. N. *et al.* (2004) ‘Numerical modeling of flow processes over gravelly surfaces using structured grids and a numerical porosity treatment’, *Water Resources Research*. American Geophysical Union, 40(1). doi: 10.1029/2002WR001934.

Langan, S., Johnston, L. and Donaghy, M. (2001) ‘Variation in river water temperatures in an upland stream over a 30-year period’, *Science of The Total Environment*.

Launder, B. . and Spalding, D. B. (1974) ‘The numerical computation of turbulent flow’, *Computational Methods for Applied Mechanical Engineering*. Available at: https://ci.nii.ac.jp/naid/10014704198/ (Accessed: 13 June 2021).

Lee, A. and Ferguson, R. (2002) ‘Velocity and flow resistance in step-pool streams’, *Geomorphology*.

Lee, S. J., Lee, S. I. and Park, C. W. (2004) ‘Reducing the drag on a circular cylinder by upstream installation of a small control rod’, *Fluid Dynamics Research*, 34(4), pp. 233–250. doi: 10.1016/j.fluiddyn.2004.01.001.

Lefebvre, A., Thompson, C. and Amos, C. (2010) ‘Influence of Zostera marina canopies on unidirectional flow, hydraulic roughness and sediment movement’, *Continental Shelf Research*.

Legleiter, C. J. *et al.* (2011) ‘Effects of uncertain topographic input data on two-dimensional flow modeling in a gravel-bed river’, *Water Resources Research*. John Wiley & Sons, Ltd, 47(3), p. 3518. doi: 10.1029/2010WR009618.

Lei, J. and Nepf, H. (2019) ‘Wave damping by flexible vegetation: Connecting individual blade dynamics to the meadow scale’, *Coastal Engineering*. doi: 10.1016/j.coastaleng.2019.01.008.

Lera, S. *et al.* (2019) ‘The impact of submersed aquatic vegetation on the development of river mouth bars’, in *Earth Surface Processes and Landforms*. John Wiley and Sons Ltd, pp. 1494–1506. doi: 10.1002/esp.4585.

Li, C. W. and Zeng, C. (2009) ‘3D Numerical modelling of flow divisions at open channel junctions with or without vegetation’, *Advances in Water Resources*. Elsevier, 32(1), pp. 49–60. doi: 10.1016/j.advwatres.2008.09.005.

Li, R. M. and Shen, H. W. (1973) ‘Effect of tall vegetations on flow and sediment’, *Journal of the Hydraulics Division*. American Society of Civil Engineers, 99(HY5 (May, 1973)), pp. 793–814. doi: 10.1061/jyceaj.0003647.

Li, W. qi *et al.* (2019) ‘Effects of vegetation patch density on flow velocity characteristics in an open channel’, *Journal of Hydrodynamics*. Springer International Publishing, 31(5), pp. 1052–1059. doi: 10.1007/s42241-018-0086-6.

Liffen, T. *et al.* (2011) ‘Biomechanical properties of the emergent aquatic macrophyte Sparganium erectum: Implications for fine sediment retention in low energy rivers’, *Ecological Engineering*. Elsevier, 37(11), pp. 1925–1931. doi: 10.1016/j.ecoleng.2011.06.015.

de Lima, P. H. S., Janzen, J. G. and Nepf, H. M. (2015) ‘Flow patterns around two neighboring patches of emergent vegetation and possible implications for deposition and vegetation growth’, *Environmental Fluid Mechanics*. Kluwer Academic Publishers, 15(4), pp. 881–898. doi: 10.1007/s10652-015-9395-2.

Lin, C. *et al.* (2012) ‘Characteristics of Recirculation Zone Structure behind an Impulsively Started Circular Cylinder’, *Journal of Engineering Mechanics*. American Society of Civil Engineers (ASCE), 138(2), pp. 184–198. doi: 10.1061/(asce)em.1943-7889.0000314.

Liu, D. *et al.* (2008) ‘An experimental study of flow through rigid vegetation’, *Journal of Geophysical Research: Earth Surface*. Blackwell Publishing Ltd, 113(4), p. 4015. doi: 10.1029/2008JF001042.

Liu, X. and Zeng, Y. (2017) ‘Drag coefficient for rigid vegetation in subcritical open-channel flow’, *Environmental Fluid Mechanics*. Springer Netherlands, 17(5), pp. 1035–1050. doi: 10.1007/s10652-017-9534-z.

Liu, Z. (1998) *Sediment Transport*. Aalborg Universitetsforlag.

Lockard, D. (2010) ‘Reprint of: In search of grid converged solutions’, *Procedia IUTAM*.

López, F. and García, M. H. (2001) ‘Mean Flow and Turbulence Structure of Open-Channel Flow through Non-Emergent Vegetation’, *Journal of Hydraulic Engineering*.

American Society of Civil Engineers (ASCE), 127(5), pp. 392–402. doi: 10.1061/(asce)0733-9429(2001)127:5(392).

Lotsari, E., Thorndycraft, V. and Alho, P. (2015) ‘Prospects and challenges of simulating river channel response to future climate change’, *Progress in Physical Geography*. SAGE Publications Ltd, 39(4), pp. 483–513. doi: 10.1177/0309133315578944.

Lueck, R. G. and Lu, Y. (1997) ‘The logarithmic layer in a tidal channel’, *Continental Shelf Research*. Pergamon, 17(14), pp. 1785–1801. doi: 10.1016/S0278-4343(97)00049-6.

Luhar, M. and Nepf, H. (2013) ‘From the blade scale to the reach scale: A characterization of aquatic vegetative drag’, *Advances in Water Resources*.

Luhar, M. and Nepf, H. M. (2011) ‘Flow-induced reconfiguration of buoyant and flexible aquatic vegetation’, *Limnology and Oceanography*, 56(6), pp. 2003–2017. doi: 10.4319/lo.2011.56.6.2003.

Luo, H. *et al.* (2018) ‘Comparative 1D and 3D numerical investigation of open-channel junction flows and energy losses’, *Advances in water resources*.

Macdonald, N., Phillips, I. D. and Mayle, G. (2010) ‘Spatial and temporal variability of flood seasonality in Wales’, *Hydrological Processes*. John Wiley & Sons, Ltd, 24(13), pp. 1806–1820. doi: 10.1002/hyp.7618.

MacVicar, B. J. and Roy, A. G. (2007) ‘Hydrodynamics of a forced riffle pool in a gravel bed river: 1. Mean velocity and turbulence intensity’, *Water Resources Research*. John Wiley & Sons, Ltd, 43(12), p. 12401. doi: 10.1029/2006WR005272.

Madsen, T. and Brix, H. (1997) ‘Growth, photosynthesis and acclimation by two submerged macrophytes in relation to temperature’, *Oecologia*.

Maji, S. *et al.* (2017) ‘Hydrodynamics and turbulence in emergent and sparsely

vegetated open channel flow', *Environmental Fluid Mechanics*. Springer Netherlands, 17(4), pp. 853–877. doi: 10.1007/s10652-017-9531-2.

Maraun, D., Osborn, T. J. and Gillett, N. P. (2008) 'United Kingdom daily precipitation intensity: Improved early data, error estimates and an update from 2000 to 2006', *International Journal of Climatology*, 28(6), pp. 833–842. doi: 10.1002/joc.1672.

Marcinkowski, P., Kiczko, A. and Okruszko, T. (2018) 'Model-based analysis of macrophytes role in the flow distribution in the anastomosing river system', *Water (Switzerland)*. MDPI AG, 10(7), p. 953. doi: 10.3390/w10070953.

Marjoribanks, T. I. *et al.* (2014) 'High-resolution numerical modelling of flow-vegetation interactions', *Journal of Hydraulic Research*. Taylor and Francis Ltd., 52(6), pp. 775–793. doi: 10.1080/00221686.2014.948502.

Marjoribanks, T. I. *et al.* (2017) 'Patch-scale representation of vegetation within hydraulic models', *Earth Surface Processes and Landforms*. John Wiley and Sons Ltd, 42(5), pp. 699–710. doi: 10.1002/esp.4015.

Marjoribanks, T. I., Hardy, R. J. and Lane, S. N. (2014) 'The hydraulic description of vegetated river channels: the weaknesses of existing formulations and emerging alternatives', *WIREs Water*. Wiley, 1(6), pp. 549–560. doi: 10.1002/wat2.1044.

Marsh, T. and Dixon, H. (2012) 'The UK water balance–how much has it changed in a warming world', in *'Hydrology for a changing world', Proceedings of the Eleventh National BHS Symposium.* . Dundee: British Hydrological Society.

Mason, D. C. *et al.* (2003) 'Floodplain friction parameterization in two-dimensional river flood models using vegetation heights derived from airborne scanning laser altimetry', *Hydrological Processes*. John Wiley & Sons, Ltd, 17(9), pp. 1711–1732. doi: 10.1002/hyp.1270.

McCollum, D. L. *et al.* (2020) 'Energy modellers should explore extremes more

systematically in scenarios', *Nature Energy*. Nature Publishing Group, 5(2), pp. 104–107. doi: 10.1038/s41560-020-0555-3.

Medeiros, S. C., Hagen, S. C. and Weishampel, J. F. (2012) 'Comparison of floodplain surface roughness parameters derived from land cover data and field measurements', *Journal of Hydrology*. Elsevier, 452–453, pp. 139–149. doi: 10.1016/j.jhydrol.2012.05.043.

Meire, D. W. S. A., Kondziolka, J. M. and Nepf, H. M. (2014) 'Interaction between neighboring vegetation patches: Impact on flow and deposition', *Water Resources Research*. Blackwell Publishing Ltd, 50(5), pp. 3809–3825. doi: 10.1002/2013WR015070.

Melzer, A. (1999) 'Aquatic macrophytes as tools for lake management', in *Hydrobiologia*. Springer Netherlands, pp. 181–190. doi: 10.1007/978-94-017-3282-6_17.

Merwade, V., Cook, A. and Coonrod, J. (2008) 'GIS techniques for creating river terrain models for hydrodynamic modeling and flood inundation mapping', *Environmental Modelling and Software*. Elsevier, 23(10–11), pp. 1300–1311. doi: 10.1016/j.envsoft.2008.03.005.

Mork, M. (1996) 'The effect of kelp in wave damping', *Sarsia*, 80(4), pp. 323–327. doi: 10.1080/00364827.1996.10413607.

Morton, K. and Baines, M. (1995) *Numerical methods for fluid dynamics V*.

Moser, S. and Ekstrom, J. (2010) 'A framework to diagnose barriers to climate change adaptation', *Proceedings of the National Academy of Sciences of the United States of America*. doi: 10.1073/pnas.1007887107.

Moulinec, C. *et al.* (2011) 'TELEMAC: An efficient hydrodynamics suite for massively parallel architectures', *Computers and Fluids*. Pergamon, 51(1), pp. 30–34. doi: 10.1016/j.compfluid.2011.07.003.

Mulahasan, S. and Stoesser, T. (2017) ‘Flow resistance of in-line vegetation in open channel flow’, *International Journal of River Basin Management*, 15(3), pp. 329–334. doi: 10.1080/15715124.2017.1307847.

Mullarney, J. and Henderson, S. (2018) ‘Flows within marine vegetation canopies’, *Advances in coastal hydraulics*.

Naden, P. *et al.* (2006) ‘The influence of macrophyte growth, typical of eutrophic conditions, on river flow velocities and turbulence production’, *Hydrological Processes*, 20(18), pp. 3915–3938. doi: 10.1002/hyp.6165.

Neary, V. S. *et al.* (2012) ‘Effects of Vegetation on Turbulence, Sediment Transport, and Stream Morphology’, *Journal of Hydraulic Engineering*. American Society of Civil Engineers (ASCE), 138(9), pp. 765–776. doi: 10.1061/(asce)hy.1943-7900.0000168.

Nehal, L. *et al.* (2012) ‘Flow through non-submerged vegetation: a flume experiment with artificial vegetation’, in *Sixteenth International Water Technology Conference, IWTC 16*.

Neil, W. *et al.* (2009) ‘Are there social limits to adaptation to climate change?’, *Climatic Change*, 93(3–4), pp. 335–354. doi: 10.1007/s10584-008-9520-z.

Nepf, H. *et al.* (2007) ‘Retention time and dispersion associated with submerged aquatic canopies’, *Water Resources Research*. John Wiley & Sons, Ltd, 43(4). doi: 10.1029/2006WR005362.

Nepf, H. and Ghisalberti, M. (2008) ‘Flow and transport in channels with submerged vegetation’, *Acta Geophysica*. Springer, pp. 753–777. doi: 10.2478/s11600-008-0017-y.

Nepf, H. M. (1999) ‘Drag, turbulence, and diffusion in flow through emergent vegetation’, *Water Resources Research*. John Wiley & Sons, Ltd, 35(2), pp. 479–489. doi: 10.1029/1998WR900069.

Nepf, H. M. (2012) ‘Hydrodynamics of vegetated channels’, *Journal of Hydraulic Research*, 50(3), pp. 262–279. doi: 10.1080/00221686.2012.696559.

Nepf, H. M. and Vivoni, E. R. (2000) ‘Flow structure in depth-limited, vegetated flow’, *Journal of Geophysical Research: Oceans*. American Geophysical Union (AGU), 105(C12), pp. 28547–28557. doi: 10.1029/2000jc900145.

Nezu, I., Nakagawa, H. and Jirka, G. H. (1994) ‘Turbulence in open-channel flows’, *Journal of Hydraulic Engineering*. doi: 10.1061/(ASCE)0733-9429(1994)120.

Nezu, I. and Onitsuka, K. (2010) ‘Turbulent structures in partly vegetated open-channel flows with LDA and PI V measurements Iehisa Nezu & Kouki Onitsuka’, *Journal of hydraulic research*. International Association of Hydraulic Engineering Research, 39(6), pp. 629–642. doi: 10.1080/00221686.2001.9628292.

Nicholas, A. R. and Mclelland, S. J. (2010) ‘Computational fluid dynamics modelling of three-dimensional processes on natural river floodplains’, *Journal of Hydraulic Research*. Informa UK Limited, 42(2), pp. 131–143. doi: 10.1080/00221686.2004.9628299.

Nikora, V. *et al.* (2007) ‘Double-Averaging Concept for Rough-Bed Open-Channel and Overland Flows: Applications’, *Journal of Hydraulic Engineering*. American Society of Civil Engineers (ASCE), 133(8), pp. 884–895. doi: 10.1061/(asce)0733-9429(2007)133:8(884).

Norris, B. K. *et al.* (2019) ‘Turbulence Within Natural Mangrove Pneumatophore Canopies’, *Journal of Geophysical Research: Oceans*. Blackwell Publishing Ltd, 124(4), pp. 2263–2288. doi: 10.1029/2018JC014562.

O’Hare, J. M. *et al.* (2011) ‘Physical constraints on the distribution of macrophytes linked with flow and sediment dynamics in British rivers’, *River Research and Applications*, 27(6), pp. 671–683. doi: 10.1002/rra.1379.

O’Hare, M. T. *et al.* (2010) ‘Variability in roughness measurements for vegetated

rivers near base flow, in England and Scotland', *Journal of Hydrology*. Elsevier, 385(1–4), pp. 361–370. doi: 10.1016/j.jhydrol.2010.02.036.

Okamoto, T. and Nezu, I. (2010) 'Large eddy simulation of 3-D flow structure and mass transport in open-channel flows with submerged vegetations', *Journal of Hydro-environment research*.

Okamoto, T., Nezu, I. and Sanjou, M. (2016) 'Flow–vegetation interactions: length-scale of the "monami" phenomenon', *Journal of Hydraulic Research*. Taylor and Francis Ltd., 54(3), pp. 251–262. doi: 10.1080/00221686.2016.1146803.

Old, G. *et al.* (2014) 'Instream and riparian implications of weed cutting in a chalk river', *Ecological Engineering*. doi: 10.1016/j.ecoleng.2014.07.006.

Ortiz, A. C., Ashton, A. and Nepf, H. (2013) 'Mean and turbulent velocity fields near rigid and flexible plants and the implications for deposition', *Journal of Geophysical Research: Earth Surface*. Blackwell Publishing Ltd, 118(4), pp. 2585–2599. doi: 10.1002/2013JF002858.

Osborn, T. J. and Maraun, D. (2008) 'Changing intensity of rainfall over Britain', *Climatic Research Unit Information Sheet*. 2nd edn. doi: 10.1098/rsta.2002.1002.

Pall, P. *et al.* (2011) 'Anthropogenic greenhouse gas contribution to flood risk in England and Wales in autumn 2000', *Nature*.

Pasche, E. and Rouvé, G. (1985) 'Overbank Flow with Vegetatively Roughened Flood Plains', *Journal of Hydraulic Engineering*. American Society of Civil Engineers (ASCE), 111(9), pp. 1262–1278. doi: 10.1061/(asce)0733-9429(1985)111:9(1262).

Pavan, S., Ata, R. and Hervouet, J. M. (2015) 'Finite volume schemes and residual distribution schemes for pollutant transport on unstructured grids', *Environmental Earth Sciences*. Springer Verlag, 74(11), pp. 7337–7356. doi: 10.1007/s12665-015-4760-5.

Peralta, G. *et al.* (2008) ‘Consequences of shoot density and stiffness for ecosystem engineering by benthic macrophytes in flow dominated areas: A hydrodynamic flume study’, *Marine Ecology Progress Series*, 368, pp. 103–115. doi: 10.3354/meps07574.

Petryk, S. and Bosmajian, G. (1975) ‘Analysis of Flow Through Vegetation’, *ASCE J Hydraul Div*, 101(7), pp. 871–884. doi: 10.1061/jyceaj.0004397.

Pitlo, R. H. and Dawson, F. H. (1990) ‘Floe-resistance of aquatic weeds. ’, in Pieterse, A. and Murphy, K. (eds) *Aquatic weeds: the ecology and management of nuisance aquatic vegetation*. Oxford: Oxford University Press, pp. 74–84.

Pitt, M. (2008) *Learning lessons from the 2007 floods – full report*.

Powell, D. (2014) ‘Flow resistance in gravel-bed rivers: Progress in research’, *Earth-Science Reviews, Elsevier*.

Price, W. A., Tomlinson, K. W. and Hunt, J. N. (1969) ‘The Effect of Artificial Seaweed in Promoting the Build-Up of Beaches’, *Coastal Engineering*. American Society of Civil Engineers (ASCE), pp. 570–578. doi: 10.1061/9780872620131.036.

Prudhomme, C. *et al.* (2012) ‘Future flows climate: An ensemble of 1-km climate change projections for hydrological application in Great Britain’, *Earth System Science Data*. Copernicus GmbH, 4(1), pp. 143–148. doi: 10.5194/essd-4-143-2012.

Rameshwaran, P., Naden, P. S. and Lawless, M. (2011) ‘Flow modelling in gravel-bed rivers: Rethinking the bottom boundary condition’, *Earth Surface Processes and Landforms*. John Wiley & Sons, Ltd, 36(10), pp. 1350–1366. doi: 10.1002/esp.2158.

Rameshwaran, P. and Shiono, K. (2007) ‘Quasi two-dimensional model for straight overbank flows through emergent vegetation on floodplains’, *Journal of Hydraulic Research*. International Association of Hydraulic Engineering Research, 45(3), pp. 302–315. doi: 10.1080/00221686.2007.9521765.

Reynard, N. S. *et al.* (2010) *Regionalised impacts of climate change on flood flows*. Defra.

Ricchiuto, M. and Abgrall, R. (2010) 'Explicit Runge-Kutta residual distribution schemes for time dependent problems: Second order case', *Journal of Computational Physics*. Academic Press Inc., 229(16), pp. 5653–5691. doi: 10.1016/j.jcp.2010.04.002.

Righetti, M. (2002) 'Flow resistance in open channel flows with sparsely distributed bushes', *Journal of Hydrology*.

Righetti, M. (2008) 'Flow analysis in a channel with flexible vegetation using double-averaging method', *Acta Geophysica*, 56(3), pp. 801–823. doi: 10.2478/s11600-008-0032-z.

Riis, T. and Biggs, B. J. F. (2003) 'Hydrologic and hydraulic control of macrophyte establishment and performance in streams', *Limnology and Oceanography*. American Society of Limnology and Oceanography Inc., 48(4), pp. 1488–1497. doi: 10.4319/lo.2003.48.4.1488.

Roache, P. J. (1997) 'Quantification of uncertainty in computational fluid dynamics', *Annual Review of Fluid Mechanics*. Annual Reviews Inc., 29, pp. 123–160. doi: 10.1146/annurev.fluid.29.1.123.

Roe, P. (1987) 'Upwind differencing schemes for hyperbolic conservation laws with source terms', *Nonlinear hyperbolic problems*.

Rominger, J. and Dynamics, H. N. (2011) 'Drag on Flexible, Slender Bodies Streamlined in Turbulent Flow', *APS Division of Fluid*.

Rouse, H. (1965) 'Critical Analysis of Open-Channel Resistance', *Journal of the Hydraulics Division*. American Society of Civil Engineers (ASCE), 91(4), pp. 1–23. doi: 10.1061/jyceaj.0001270.

Rowiński, P. M. *et al.* (2018) ‘How vegetation can aid in coping with river management challenges: A brief review’, *Ecohydrology and Hydrobiology*. Elsevier B.V., pp. 345–354. doi: 10.1016/j.ecohyd.2018.07.003.

Rowiński, P. and Marion, A. (2015) ‘Hydrodynamic and Mass Transport at Freshwater Aquatic Interfaces.’, in *34th International School of Hydraulics*. Springer Verlag, pp. 11–22. doi: 10.1007/978-3-319-27750-9_2.

Saggiori, S. (2010) *CFD modelling of solute transport in vegetated flow*. University of Sheffield. Master’s thesis%2C University of Sheffield (Accessed: 20 June 2021).

Sand-Jensen, K. and Pedersen, O. (1999) ‘Velocity gradients and turbulence around macrophyte stands in streams’, *Freshwater Biology*, 42(2), pp. 315–328. doi: 10.1046/j.1365-2427.1999.444495.x.

Sandercock, P. and Hooke, J. (2007) ‘Vegetation in dryland river channels and its interaction with fluvial processes’, *Progress in Physical Geography: Earth and Environment*, 31(2), pp. 107–129. doi: 10.1177/0309133307076106.

Sayers, P. *et al.* (2015) *Climate Change Risk Assessment 2017: Projections of future flood risk in the UK*, *Projections on Climate Change*.

Sayers, Penning-Rowsell and Mckenzie (2017) *Climate Change Risk Assessment 2017 Projections of future flood risk in the UK Project A: Report prepared for the Committee on Climate Change, UK*.

Schäppi, B. *et al.* (2010) ‘Integrating river cross section measurements with digital terrain models for improved flow modelling applications’, *Computers and Geosciences*. Pergamon, 36(6), pp. 707–716. doi: 10.1016/j.cageo.2009.12.004.

Schnauder, I. and Sukhodolov, A. N. (2012) ‘Flow in a tightly curving meander bend: Effects of seasonal changes in aquatic macrophyte cover’, *Earth Surface Processes and Landforms*. John Wiley and Sons Ltd, 37(11), pp. 1142–1157. doi: 10.1002/esp.3234.

Schneider, C. *et al.* (2013) ‘How will climate change modify river flow regimes in Europe?’, *Hydrology and Earth System Sciences*, 17(1), pp. 325–339. doi: 10.5194/hess-17-325-2013.

Schoelynck, J. *et al.* (2012) ‘Self-organised patchiness and scale-dependent bio-geomorphic feedbacks in aquatic river vegetation’, *Ecography*, 35(8), pp. 760–768. doi: 10.1111/j.1600-0587.2011.07177.x.

Schoelynck, J. *et al.* (2013) ‘Submerged macrophytes avoiding a negative feedback in reaction to hydrodynamic stress’, *Limnologica*.

Schwer, L. (2008) ‘Is your mesh refined enough? Estimating discretization error using GCI’, *7th LS-DYNA Anwenderforum*.

Sellin, R. H. J. and van Beesten, D. P. (2004) ‘Conveyance of a managed vegetated two-stage river channel’, *Proceedings of the Institution of Civil Engineers: Water Management*. ICE Publishing, 157(1), pp. 21–33. doi: 10.1680/wama.2004.157.1.21.

Shan, Y., Liu, C. and Nepf, H. (2019) ‘Comparison of drag and velocity in model mangrove forests with random and in-line tree distributions’, *Journal of Hydrology*. doi: 10.1016/j.jhydrol.2018.10.077.

Shimizu, Y. and Tsujimoto, T. (1994) ‘Numerical analysis of turbulent open-channel flow over a vegetation layer using a κ-ε turbulence model’, *Journal of Hydroscience and Hydraulic Engineering*. Available at: https://ci.nii.ac.jp/naid/10014854360/ (Accessed: 20 June 2021).

Simpson, I. R. and Jones, P. D. (2012) ‘Updated precipitation series for the UK derived from Met Office gridded data’, *International Journal of Climatology*, 32(15), pp. 2271–2282. doi: 10.1002/joc.3397.

Smagorinsky (1963) ‘General circulation experiments with the primitive equations: I. The basic experiment’, *Monthly weather review*.

Smakhtin, V. U. (2001) ‘Low flow hydrology: A review’, *Journal of Hydrology*. Elsevier, pp. 147–186. doi: 10.1016/S0022-1694(00)00340-1.

Sonnenwald, F., Stovin, V. and Guymer, I. (2019) ‘Estimating drag coefficient for arrays of rigid cylinders representing emergent vegetation’, *Journal of Hydraulic Research*. Taylor and Francis Ltd., pp. 591–597. doi: 10.1080/00221686.2018.1494050.

Sonnenwald, Fred *et al.* (2015) ‘Hydrodynamic and Mass Transport at Freshwater Aquatic Interfaces. 34th International School of Hydraulics’, *GeoPlanet: Earth and Planetary Sciences*. Springer, pp. 63–75. doi: 10.1007/978-3-319-27750-9_6.

Spencer, D. F., Colby, L. and Norris, G. R. (2013) ‘An evaluation of flooding risks associated with giant reed (Arundo donax)’, *Journal of Freshwater Ecology*, 28(3), pp. 397–409. doi: 10.1080/02705060.2013.769467.

Statzner, B. *et al.* (2006) ‘The debate about drag and reconfiguration of freshwater macrophytes: comparing results obtained by three recently discussed approaches’, *Freshwater Biology*, 51(11), pp. 2173–2183. doi: 10.1111/j.1365-2427.2006.01636.x.

Stephan, U. and Gutknecht, D. (2002) ‘Hydraulic resistance of submerged flexible vegetation’, *Journal of Hydrology*. Available at: https://www.sciencedirect.com/science/article/pii/S0022169402001920 (Accessed: 4 January 2020).

Stevens, A. J., Clarke, D. and Nicholls, R. J. (2016) ‘Trends in reported flooding in the UK: 1884–2013’, *Hydrological Sciences Journal*. Taylor and Francis Ltd., 61(1), pp. 50–63. doi: 10.1080/02626667.2014.950581.

Stocker, T. F. *et al.* (2013) *Climate change 2013 the physical science basis: Working Group I contribution to the fifth assessment report of the intergovernmental panel on climate change*, *Climate Change 2013 the Physical Science Basis: Working Group I Contribution to the Fifth Assessment Report of the Intergovernmental Panel on Climate Change*. Cambridge University Press. doi: 10.1017/CBO9781107415324.

Stoesser, T., Kim, S. J. and Diplas, P. (2010) 'Turbulent Flow through Idealized Emergent Vegetation', *Journal of Hydraulic Engineering*. American Society of Civil Engineers (ASCE), 136(12), pp. 1003–1017. doi: 10.1061/(asce)hy.1943-7900.0000153.

Stoesser, Thorsten *et al.* (2009) 'Large Eddy Simulation of Turbulent Flow Through Submerged Vegetation', *Transport in porous media*, 78(3 SPEC. ISS.), pp. 347–365. doi: 10.1007/s11242-009-9371-8.

Stone, B. M. and Shen, H. T. (2002) 'Hydraulic Resistance of Flow in Channels with Cylindrical Roughness', *Journal of Hydraulic Engineering*, 128(5), pp. 500–506. doi: 10.1061/(ASCE)0733-9429(2002)128:5(500).

Straatsma, M. (2009) '3D float tracking: In situ floodplain roughness estimation', *Hydrological Processes*, 23(2), pp. 201–212. doi: 10.1002/hyp.7147.

Streikoff, T. S., Clemmens, A. J. and Bautista, E. (2004) 'Field-parameter estimation for surface irrigation management and design', in *Watershed Management and Operations Management 2000*. American Society of Civil Engineers, pp. 1–10. doi: 10.1061/40499(2000)142.

Struijs, R. (1996) *A multi-dimensional upwind discretization method for the Euler equations on unstructured grids.* Technische Universiteit Delft.

Sun, X. *et al.* (2010) 'Modelling vegetation effects in irregular meandering river', *Journal of Hydraulic Research*. Taylor & Francis , 48(6), pp. 775–783. doi: 10.1080/00221686.2010.531101.

Tabata, K. K. and Hickin, E. J. (2003) 'Interchannel hydraulic geometry and hydraulic efficiency of the anastomosing Columbia River, southeastern British Columbia, Canada', *Earth Surface Processes and Landforms*. John Wiley & Sons, Ltd, 28(8), pp. 837–852. doi: 10.1002/esp.497.

Takemura, T. and Tanaka, N. (2007) 'Flow structures and drag characteristics of a

colony-type emergent roughness model mounted on a flat plate in uniform flow', *Fluid dynamics research*, 39(9–10), pp. 694–710. doi: 10.1016/j.fluiddyn.2007.06.001.

Tanaka, N. and Yagisawa, J. (2010) 'Flow structures and sedimentation characteristics around clump-type vegetation', *Journal of Hydro-Environment Research*. Elsevier, 4(1), pp. 15–25. doi: 10.1016/j.jher.2009.11.002.

Tang, C. *et al.* (2020) 'Velocity and turbulence evolution in a flexible vegetation canopy in open channel flows', *Journal of Cleaner Production*.

Tang, H. *et al.* (2014) 'Determining drag coefficients and their application in modelling of turbulent flow with submerged vegetation', *Advances in water resources*.

Tang, X. and Knight, D. W. (2009) 'Lateral distributions of streamwise velocity in compound channels with partially vegetated floodplains', *Science in China, Series E: Technological Sciences*, 52(11), pp. 3357–3362. doi: 10.1007/s11431-009-0342-7.

Tanino, Y. and Nepf, H. M. (2008) 'Laboratory Investigation of Mean Drag in a Random Array of Rigid, Emergent Cylinders', *Journal of Hydraulic Engineering*. American Society of Civil Engineers (ASCE), 134(1), pp. 34–41. doi: 10.1061/(asce)0733-9429(2008)134:1(34).

Terrier, B. *et al.* (2010) 'Influence of vegetation to boundary shear stress in open channel for overbank flow', *River Flow*.

Thiemer, K., Schneider, S. C. and Demars, B. O. L. (2021) 'Mechanical removal of macrophytes in freshwater ecosystems: Implications for ecosystem structure and function', *Science of the Total Environment*. Elsevier B.V., p. 146671. doi: 10.1016/j.scitotenv.2021.146671.

Tinoco, R. O. and Coco, G. (2018) 'Turbulence as the Main Driver of Resuspension in Oscillatory Flow Through Vegetation', *Journal of Geophysical Research: Earth*

*Surface*. Blackwell Publishing Ltd, 123(5), pp. 891–904. doi: 10.1002/2017JF004504.

Tinoco, R O and Coco, G. (2018) 'Turbulence as the Main Driver of Resuspension in Oscillatory Flow Through Vegetation', *Journal of Geophysical Research*. Earth Surface, 123(5), pp. 891–904. doi: 10.1002/2017JF004504.

Tinoco, R. O., San Juan, J. E. and Mullarney, J. C. (2020) 'Simplification bias: lessons from laboratory and field experiments on flow through aquatic vegetation', *Earth Surface Processes and Landforms*. John Wiley and Sons Ltd, 45(1), pp. 121–143. doi: 10.1002/esp.4743.

Trepel, M. *et al.* (2003) 'Influence of macrophytes on water level and flood dynamics in a riverine wetland in Northern Germany.', in *In: Proceedings of the International Conference "EcoFlood—Towards Natural Flood Reduction Strategies"*. Institute for Land Reclamation and Grassland Farming, Raszyn, Poland.

Tsavdaris, A., Mitchell, S. and Williams, J. B. (2013) 'Use of CFD to model emergent vegetation in detention ponds', *ARPN Journal of Engineering and Applied Sciences*, 8(7).

Tsavdaris, A., Mitchell, S. and Williams, J. B. (2015) 'Computational fluid dynamics modelling of different detention pond configurations in the interest of sustainable flow regimes and gravity sedimentation potential', *Water and Environment Journal*. Blackwell Publishing Ltd, 29(1), pp. 129–139. doi: 10.1111/wej.12086.

Tseng, C.-Y., Duemler, K. and Tinoco, R. (2020) 'Laboratory Study of Gravity Currents over Submerged Vegetation Canopies', in *AGU Fall Meeting*. Earth and Space Science Open Archive. doi: 10.1002/ESSOAR.10501708.1.

Tsujimoto, T. (1999) 'Fluvial processes in streams with vegetation', *Journal of Hydraulic Research*. International Association of Hydraulic Engineering Research, 37(6), pp. 789–803. doi: 10.1080/00221689909498512.

Turner, A. and Chanmeesri, N. (1984) 'Shallow flow of water through non-

submerged vegetation', *Agricultural Water Management*.

Vandenbruwaene, W. *et al.* (2011) 'Flow interaction with dynamic vegetation patches: Implications for biogeomorphic evolution of a tidal landscape', *Journal of Geophysical Research: Earth Surface*. Blackwell Publishing Ltd, 116(1). doi: 10.1029/2010JF001788.

Västilä, K. and Järvelä, J. (2018) 'Characterizing natural riparian vegetation for modeling of flow and suspended sediment transport', *Journal of Soils and Sediments*. Springer Verlag, 18(10), pp. 3114–3130. doi: 10.1007/s11368-017-1776-3.

Verschoren, V. *et al.* (2016) 'Resistance and reconfiguration of natural flexible submerged vegetation in hydrodynamic river modelling', *Environmental Fluid Mechanics*. doi: 10.1007/s10652-015-9432-1.

Verschoren, V. (2017) *Spatial pattern formation of macrophytes: an integrated model for the management of lowland rivers*.

Vidal, B. V and Wade, J.-P. D. (2012) 'Using UKCP09 probabilis-tic climate information for UK water resource planning', *Journal of Hydrology*. Elsevier, pp. 48–67. doi: 10.1016/j.jhydrol.2011.12.020ï.

Vis, C., Hudon, C. and Carignan, R. (2003) 'An evaluation of approaches used to determine the distribution and biomass of emergent and submerged aquatic macrophytes over large spatial scales', *Aquatic Botany*. Elsevier, 77(3), pp. 187–201. doi: 10.1016/S0304-3770(03)00105-0.

Wang, C. *et al.* (2015) 'Interactions between vegetation, water flow and sediment transport: A review', *Journal of Hydrodynamics*. China Ocean Press, pp. 24–37. doi: 10.1016/S1001-6058(15)60453-X.

Wang, S. *et al.* (2019) 'Long-term and inter-monthly dynamics of aquatic vegetation and its relation with environmental factors in Taihu Lake, China', *Science of The*

*Total Environment*.

Wang, W. J. *et al.* (2015) ‘Steady nonuniform shallow flow within emergent vegetation’, *Water Resources Research*. Blackwell Publishing Ltd, 51(12), pp. 10047–10064. doi: 10.1002/2015WR017658.

Watts, G. *et al.* (2015) ‘Climate change and water in the UK – past changes and future prospects’, *Progress in Physical Geography*. SAGE Publications Ltd, 39(1), pp. 6–28. doi: 10.1177/0309133314542957.

Webb, B. W. and Nobilis, F. (2007) ‘Long-term changes in river temperature and the influence of climatic and hydrological factors’, *Hydrological Sciences Journal*, 52(1), pp. 74–85. doi: 10.1623/hysj.52.1.74.

Weiming, W. and Zhiguo, H. (2009) ‘Effects of vegetation on flow conveyance and sediment transport capacity’, *International Journal of Sediment Research*.

White, B. and Nepf, H. (2020) ‘Scalar transport in random cylinder arrays at moderate Reynolds number’, *Journal of Fluid Mechanics*, 487, pp. 43–79. doi: 10.1017/S0022112003004579.

van Der A, D. *et al.* (2018) ‘Hydrodynamics under large-scale regular and bichromatic breaking waves’, in *Proceedings of the Coastal Engineering Conference*.

Van de Wiel, M. J. and Darby, S. E. (2007) ‘A new model to analyse the impact of woody riparian vegetation on the geotechnical stability of riverbanks’, *Earth Surface Processes and Landforms*, 32(14), pp. 2185–2198. doi: 10.1002/esp.1522.

Wilby, R. *et al.* (2010) ‘Evidence needed to manage freshwater ecosystems in a changing climate: turning adaptation principles into practice’, *Science of The Total Environment*.

Wilby, R. L. and Quinn, N. W. (2013) ‘Reconstructing multi-decadal variations in fluvial flood risk using atmospheric circulation patterns’, *Journal of Hydrology*.

Elsevier, 487, pp. 109–121. doi: 10.1016/j.jhydrol.2013.02.038.

Wilby, R. and Wood, R. A. (2009) *UK Climate Projections Science Report: Climate change projections*. Met Office Hadley Centre.

Wilson, C. *et al.* (2006) '3D numerical modelling of a willow vegetated river/floodplain system', *Journal of Hydrology*. Available at: https://www.sciencedirect.com/science/article/pii/S0022169405005950 (Accessed: 4 January 2020).

Wilson, C. A., Hoyt, J. and Schnauder, I. (2008) 'Impact of Foliage on the Drag Force of Vegetation in Aquatic Flows', *Journal of Hydraulic Engineering*. American Society of Civil Engineers (ASCE), 134(7), pp. 885–891. doi: 10.1061/(asce)0733-9429(2008)134:7(885).

Wilson, C. A. M. E. *et al.* (2003) 'Open Channel Flow through Different Forms of Submerged Flexible Vegetation', *Journal of Hydraulic Engineering*. American Society of Civil Engineers (ASCE), 129(11), pp. 847–853. doi: 10.1061/(asce)0733-9429(2003)129:11(847).

Wilson, C. A. M. E. *et al.* (2006) 'Application of the drag force approach to model the flow-interaction of natural vegetation', *International Journal of River Basin Management*. Taylor & Francis Group , 4(2), pp. 137–146. doi: 10.1080/15715124.2006.9635283.

Wilson, C. A. M. E. (2007) 'Flow resistance models for flexible submerged vegetation', *Journal of Hydrology*. Elsevier, 342(3–4), pp. 213–222. doi: 10.1016/j.jhydrol.2007.04.022.

Wilson, C. A. M. E. and Horritt, M. S. (2002) 'Measuring the flow resistance of submerged grass', *Hydrological Processes*, 16(13), pp. 2589–2598. doi: 10.1002/hyp.1049.

Winterwerp, J. and Kesteren, W. Van (2004) *Introduction to the physics of cohesive*

*sediment dynamics in the marine environment*.

Wohl, E. E. (1998) ‘Uncertainty in Flood Estimates Associated with Roughness Coefficient’, *Journal of Hydraulic Engineering*. American Society of Civil Engineers (ASCE), 124(2), pp. 219–223. doi: 10.1061/(asce)0733-9429(1998)124:2(219).

Wunder, S., Lehmann, B. and Nestmann, F. (2011) ‘Determination of the drag coefficients of emergent and just submerged willows’, *International Journal of River Basin Management*. Taylor & Francis , 9(3–4), pp. 231–236. doi: 10.1080/15715124.2011.637499.

Yager, E. M. and Schmeeckle, M. W. (2013) ‘The influence of vegetation on turbulence and bed load transport’, *Journal of Geophysical Research: Earth Surface*. Blackwell Publishing Ltd, 118(3), pp. 1585–1601. doi: 10.1002/jgrf.20085.

Yamasaki, T., Lima, P. de and Silva, D. (2019) ‘From patch to channel scale: The evolution of emergent vegetation in a channel’, *Advances in Water Research*. Available at: https://www.sciencedirect.com/science/article/pii/S0309170818310571 (Accessed: 22 June 2021).

Yamasaki, T. N. *et al.* (2021) ‘Feedback between vegetation, flow, and deposition: A study of artificial vegetation patch development’, *Journal of Hydrology*. Elsevier B.V., 598, p. 126232. doi: 10.1016/j.jhydrol.2021.126232.

Yan, J. (2008) *Experimental study of flow resistance and turbulence characteristics of open channel flow with vegetation*.

Yan, X. F., Wai, O. W. H. and Li, C. W. (2016) ‘Characteristics of flow structure of free-surface flow in a partly obstructed open channel with vegetation patch’, *Environmental Fluid Mechanics*. Springer Netherlands, 16(4), pp. 807–832. doi: 10.1007/s10652-016-9453-4.

Ye, C., Liu, X. nian and Wang, X. kang (2015) ‘Effects of roughness elements distribution on overland flow resistance’, *Journal of Mountain Science*. Science

Press, 12(5), pp. 1145–1156. doi: 10.1007/s11629-014-3391-8.

Zaichik, L., Alipchenkov, V. M. and Sinaiski, E. G. (2009) *Particles in Turbulent Flows*, *Particles in Turbulent Flows*. Wiley-VCH. doi: 10.1002/9783527626250.

Zhang, M. L., Li, C. W. and Shen, Y. M. (2010) 'A 3D non-linear k-ε turbulent model for prediction of flow and mass transport in channel with vegetation', *Applied Mathematical Modelling*. Elsevier, 34(4), pp. 1021–1031. doi: 10.1016/j.apm.2009.07.010.